COMPUTATIONAL FLUID DYNAMICS SIMULATIONS OF OXY-COAL COMBUSTION FOR CARBON CAPTURE AT ATMOSPHERIC AND ELEVATED PRESSURES

by

Lei Chen

M.S. Power Engineering & Engineering Thermophysics
Tsinghua University, 2006
B.S. Thermal Energy & Power Engineering
Tsinghua University, 2004

SUBMITTED TO THE DEPARTMENT OF MECHANICAL ENGINEERING IN PARTIAL FULFILLMENT OF THE REQUIREMENTS FOR THE DEGREE OF

DOCTOR OF PHILOSOPHY IN MECHANICAL ENGINEERING
AT THE
MASSACHUSETTS INSTITUTE OF TECHNOLOGY

JUNE 2013

Signature of Author . . . . . .
Department of Mechanical Engineering
February 28, 2013

Certified by. . . . . .
Ahmed F. Ghoniem
Ronald C. Crane Professor
Thesis Supervisor

Accepted by. . . . . .
Dave E. Hardt
Chairman, Department Committee on Graduate Students

Page left intentionally blank

COMPUTATIONAL FLUID DYNAMICS SIMULATIONS OF OXY-COAL COMBUSTION FOR CARBON CAPTURE AT ATMOSPHERIC AND ELEVATED PRESSURES

by
Lei Chen

Submitted to the Department of Mechanical Engineering on February 28, 2013 in partial fulfillment of the requirements for the degree of Doctor of Philosophy in Mechanical Engineering

Abstract

Oxy-fuel combustion of solid fuels, often performed in a mixture of oxygen and wet or dry recycled carbon dioxide, has gained significant interest in the last two decades as one of the leading carbon capture technologies in power generation. The new combustion characteristics in a high-O_2 environment raise challenges for furnace design and operation, and should be modeled appropriately in CFD simulation. Based on a comprehensive literature review of the state-of-the-art research on the fundamentals of oxy-coal combustion, sub-models for the critical physical processes, such as radiation and char combustion, have been properly modified for the CO_2-rich environment, and the overall performance of CFD simulation on oxy-coal combustion has been validated using Large-Eddy Simulation (LES) and Reynolds-averaged Navier-Stokes (RANS) approaches. The predicted distributions on velocity, species, and temperature were compared with experimental results from the literature in order to validate the CFD simulation. Results show that although agreeing reasonably with the measured mean axial and tangential velocity, all the RANS turbulence models used in this study underestimate the internal recirculation zone size and the turbulence mixing intensity in the char combustion zone, while LES improves the predictions of internal recirculation zone size, the entrainment of oxygen from the staging stream, and the overall flame length than the RANS approaches. Special attention was given to the CO_2's chemical effects on CO formation in oxy-fuel combustion, and its modeling approaches in CFD

simulations. Detailed reaction mechanism (GRI-Mech 3.0) identifies that the reaction $H+CO_2 \rightleftarrows OH+CO$ enhances the CO formation in the fuel-rich side of the diffusion flame due to the high CO_2 concentration, leading to a significantly higher CO concentration. Reasonable CO predictions can only be obtained using finite-rate mechanisms combining with reaction mechanisms considering the above-mentioned reaction in CFD simulations.

The validated CFD approach was used to investigate the pressure's effects in a pressurized oxy-coal combustion system. The results show that, given a fixed reactor geometry and burner velocity, the particle residence time does not change with operating pressure due to its small Stokes number; on the other hand, the coal conversion time decreases significantly because of the enhanced reaction rates at elevated pressures. Therefore, the burner can be operated at a higher burner velocity at elevated operating pressure, which results in a much higher coal throughput using the same reactor size. For instance, the thermal load can be increased from 3 MW_{th} to 60 MW_{th} using a pressurized oxy-coal reactor, when the operating pressure increases from 4 bar to 40 bar. In order to investigate the slag behaviors in the pressurized oxy-coal combustor, a first-of-its-kind three-dimensional slag model has been developed, which can be applied in slagging coal combustion/gasification with any geometry. The method couples Volume of Fluid (VOF) model and Discrete Phase Model (DPM), and fully resolves the slag's behaviors such as the slag layer buildup, multiphase flow, as well as heat transfer. The results are in good agreement with experimental observations, and can be taken as a design tool for coal furnace/gasifier development.

Thesis Supervisor: Ahmed F. Ghoniem

Title: Ronald C. Crane Professor

Acknowledgements

I would like to sincerely thank my thesis advisor, Professor Ahmed F. Ghoniem, for offering me the great opportunity to study at MIT in the area of combustion and energy conversion, which is my most interested research topic. I appreciate his guidance and support over the five years Ph.D. study, from which I learnt not only the combustion theory and computational skills, but also the way to think, solve, and communicate problems in a fundamental way. His serious attitude on scientific research has set up a high standard to my future work, and will encourage me in my whole career life.

I am grateful to my thesis committee members: Professor Janos M. Beer, Professor Yiannis A. Levendis, and Professor Alexander Mitsos, for their profound insight and constructive suggestions to my research. It is my truly honor to have the masters of clean coal and energy research in my committee.

I also would like to acknowledge Enel for the financial support during my Ph.D. study. I specially thank the colleagues of Enel Ingegneria e Innovazione S.p.A., Dr. Marco Gazzino, Mr. Stefano Sigali, Mr. Nicola Rossi, and Ms. Danila Cumbo for their supportive collaborations.

Throughout the past five years I have had the pleasure working with the talented colleagues in the Reacting Gas Dynamics Lab at MIT. First, I would like to acknowledge Dr. Jongsup Hong, Sze Zheng Yong, and Chukwunwike Iloeje, who were working on different aspects of oxy-fuel research and contributed to my research progress. I am grateful to Dr. Cheng Zhang, Dr. Mayank Kumar, Dr. Simcha Singer, Cristina Botero, Dr. Santosh Shanbhogue, and Neerav Abani, for the helpful discussions on gasification and CFD modeling. Particularly, I would like to acknowledge Simcha and Sze Zheng, with whom we worked closely to investigate the oxy-fuel combustion characteristics and had productive discussions over the past five years. Many friends in the lab gave me invaluable supports, I want to thank Dr. Guang Wu, Dr. Yixiang Shi, Zhenlong Zhao, and Professor Ghoniem's senior assistant Ms. Lorraine Rabb, for their friendships which makes the life at MIT more productive and enjoyable.

Beyond the colleagues at MIT, I would like to express my special thanks to Dr. Wenhua Li and Dr. Ligang Zheng for their encouragement to my work and life, and Dr. Genong Li at FLUENT, for his timely supports to my research.

Finally I would like to thank my parents and family, especially my wife Ling Ma and our beloved son Andrew (Xiuneng) Chen for their endless love and understanding to my study life at MIT.

Page left intentionally blank

Contents

List of Figures

List of Tables

Page left intentionally blank

Chapter 1 Introduction to Oxy-Coal Combustion

1.1. Carbon Capture Technologies for Coal-fired Power Plants

Reliable, affordable and clean energy supply is one of the basic needs of humankind. Today, our energy supply system is undergoing a long-term transition from its conventional form to a more sustainable and low carbon style, especially addressing greenhouse gas (water, carbon dioxide, methane, nitrous oxide, chlorofluorocarbons and aerosols) emissions into the atmosphere. Strong evidence suggests that both the average global temperature and the atmospheric CO_2 concentration have significantly increased since the onset of the industrial evolution, and they are well correlated [1]. Concerns over climate change have led to mounting efforts on developing technologies to reduce carbon dioxide emissions from human activities [2, 3]. Technological solutions to this problem ought to include a substantial improvement in energy conversion and utilization efficiencies, carbon capture and sequestration (CCS), and expanding the use of nuclear energy and renewable sources such as biomass, hydro-, solar, wind and geothermal energy [2].

Coal has been and will continue to be one of the major energy resources in the long term because of its abundant reserves and competitively low prices, especially for the use of base-load power generation. For instance, the share of coal in world energy consumption was 29.4% in 2009, as opposed to 34.8% for oil and 23.8% for natural gas [4]. In terms of power generation, coal continues to be the dominant fuel, contributing about 45% of the total electricity in the US in 2009 [5], and about 80% in China. Several technologies have been proposed for reducing CO_2 emission from coal-fired power generation, namely post-combustion capture, pre-combustion capture and oxy-fuel combustion capture [6]:

- *Pre-combustion capture*: Fuel is either gasified or reformed to syngas, a mixture of carbon monoxide and hydrogen, which is then shifted via steam reforming. CO_2 is then separated from the syngas by shifting carbon monoxide with steam, yielding pure hydrogen (water gas shift reaction). The Integrated Gasification Combined Cycles (IGCC) for coal is an example of pre-combustion capture system.
- *Post-combustion capture*: CO_2 is separated from the flue gases using chemical solvents [7], sorbents (such as calcium oxide [8] or carbon fibers [9]) and membranes [10] without changing the combustion process. However, the addition of a post-combustion capture unit may change the steam cycle because large quantity of low pressure steam must be extracted from the steam cycle for the solvent regeneration process.
- *Oxy-fuel combustion*: Instead of using air as oxidizer, pure oxygen (O_2) or a mixture of O_2 and recycled flue gas is used to generate high CO_2 concentration product gas; therefore, the combustion process is significantly changed. Chemical-Looping Combustion (CLC) is another combustion process that belongs to the oxy-fuel combustion category, in which pure oxygen rather than air is supplied by metal oxides for combustion, such that the mixing between CO_2 and N_2 is inherently avoided. This technology is not the primary focus of this paper, and, the reader is referred to [11-13] for more details on CLC.

In general, the technologies described above can be applied to generate energy from natural gas and coal with the exemption of some low rank coals due to unresolved engineering challenges, however, because of the important role of pulverized coal in base load electricity generation and its contribution to CO_2 emission, this study is primarily concerned with the combustion of pulverized coal, although some mention is made of other fuels as well.

Table 1-1. Representative performance and economics data for the three main capture technologies, from [14].

Performance	Supercritical PC[a]		SC[b] PC-Oxyfuel	IGCC[c]	
	w/o capture	w/ capture	w/ capture	w/o capture	w/ capture
Generating efficiency	38.5%	29.3%	30.6%	38.4%	31.2%
Efficiency penalty	CO_2 recovery (heat): -5%		Boiler/FGD: 3%	Water/Gas shift: -4.2%	
	CO_2 compression: -3.5%		ASU: -6.4%	CO_2 compression: -2.1%	
	CO_2 recovery (power): -0.7%		CO_2 compression: -3.5%	CO_2 recovery: -0.9%	
			Other: -1%		
Capital Cost ($/kWe)[e]	1330	2140 (1314)[d]	1900 (867)[d]	1430	1890
COE (c/kWh)[e]	4.78	7.69	6.98	5.13	6.52
Cost of CO_2 ($/t)[e]	40.4		30.3	24.0	

[a] PC: pulverized coal; [b] SC: supercritical; [c] IGCC: Integrated gasification combined cycle; [d] Figures in parenthesis are the expected capital cost for retrofits; [e] Based on design studies done between 2000 & 2004, a period of cost stability, updated to 2005$ using CPI inflation rate.

These three major carbon capture technologies for coal-fired power plants have been studied in terms of power generation efficiency, capital costs and costs of electricity (COE) [14-16]. Representative energy efficiency and economic performance of these technology options are compared in **Table 1-1**. All of these estimates are based on 90% CO_2 capture in rebuilt and retrofitted scenarios. The cost of CO_2 indicates the cost that is incurred to capture 1 metric ton carbon dioxide without transportation and storage. Although the absolute numbers vary by few percentage points in these studies, all reports show the same trends. In general, all three capture technologies result in an efficiency penalty, while oxy-fuel capture and pre- capture or IGCC show advantages over post-combustion capture in terms of COE and cost of CO_2. The IGCC technology yields a higher generation efficiency and a slightly lower cost than oxy-fuel combustion technology. However, all these technologies are in their early stages of development

and still have great potential for improvement.

In particular, these studies have a common conclusion that oxy-fuel combustion is the most competitive technology option for retrofitting existing coal-fired power plants, which at the moment have the largest potential for CCS. Although the number of newly-built coal power generation units declined since 1990s', there is a resurgence of new coal power plants in recent years. Moreover, about 98.7 GW or 29% of all the existing coal-fired power capacity were built after 1980 [17]. This situation is even more prominent in developing countries such as China and India, where the coal power generation capacity has been booming in the last two decades. It can safely be assumed that a sizable reduction of CO_2 emission from existing plants would come from retrofits. Oxy-fuel combustion systems have a natural advantage in retrofitting existing PC power plants because they can reuse most of the existing plant equipment. The advantages of oxy-fuel combustion as a retrofit technology are also indicated in **Table 1-1**. The capital cost for supercritical PC retrofits with oxy-fuel is $867/kWe, which is significantly lower than the capital cost of post-combustion retrofit ($1314/kWe) and of newly-built IGCC plants ($1890/kWe).

Considering the advantages of a relatively moderate efficiency penalty and the lowest retrofit capital expenditure, atmospheric oxy-fuel combustion systems have been widely accepted as a competitive carbon capture technology. More recently, it has been adopted to substitute the original IGCC plan in the U.S. DOE FutureGen 2.0 program [18]. Previous studies have reviewed its fundamentals and characteristics [6, 19-22], as well as recent developments in pilot-scale and commercial-scale demonstration plants [23]. While successful, the technology still faces many challenges, such as air leakage into the flue gas system, the relatively low energy efficiency, the need for efficient air separation and better plant integration and flue gas cleanup, among others. In particular, significant challenges are expected in the combustion process itself,

including stability and emissions, burner design and scaling, as well as determining of optimal operating conditions.

1.2. Oxy-Fuel Combustion for CCS

1.2.1. Development of the Oxy-Fuel Technology for CCS

The idea of applying oxy-fuel processes with flue gas recycle in coal-fired plants to control the CO_2 emission [24, 25] and/or produce high concentration CO_2 for enhanced oil recovery (EOR) was first proposed in 1982 [24, 26]. Following these proposals, Argonne National Laboratory (ANL) pioneered the investigation of this process in the mid and late 1980s, focusing on the system and its combustion characteristics [27-29]. Soon after, more and more researchers agreed that this system complements the two other major approaches for carbon dioxide capture, which led to a renewed interest in this technology in the 1990s. Research conducted by the International Flame Research Foundation (IFRF), CANMET, IHI, as well as other institutes and industrial parties has made considerable contributions in understanding of this process.

Along with the research and development on the air-like oxy-coal technology, pilot and large scale demonstration plants are being built around the world. Wall et al. [23] surveyed research on oxy-fuel technology, from pilot-scale tests, to industry-scale tests and full-scale demonstrations, and compiled the historical development of this technology worldwide. The year 2008 marks an important milestone with the commissioning of the world's first 30 MWth demonstration plant in Germany. More large-scale demonstrations in industry-scale coal-fired boilers have been planned or are already underway, as shown in Table 1-2 based on the work of Wall et al. [23] and Herzog [30]. Success in these demonstrations is expected to lead to wider commercial deployment.

Recent research has also focused on extending the range of operating conditions of oxy-coal combustion to improve energy efficiency, environmental performance and economics of this technology. For instance, pressurized systems have been proposed for both oxy-coal combustion with recycled flue gases [31-36] and oxy-syngas combustion in combination with solid fuel gasification technology [37]. These approaches are described in greater detail in the following sections.

1.2.2. Atmospheric Oxy-Coal Combustion Systems with Flue Gas Recycle

The atmospheric oxy-coal combustion system shown in Figure 1-1 was first introduced as a short-term solution to retrofit existing coal-fired power plant to include the option of CCS. In most oxy-coal system studies, recycled flue gases at various recycle ratios are used to control the flame temperature in the combustor and as a result, the flue gas consists primarily of steam which is later removed through condensation, and carbon dioxide which is purified before being sent for compression and sequestration. The additional equipment required, when compared with air-fired systems, is described below:

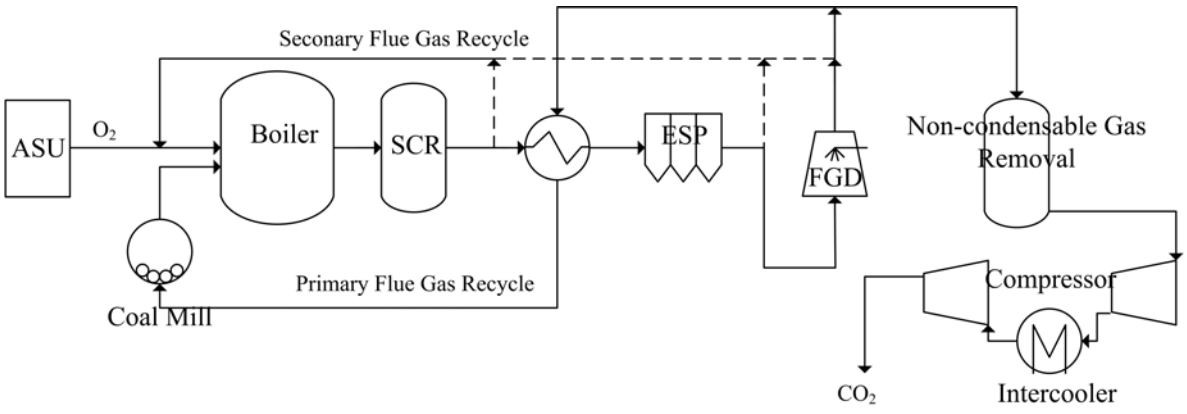

Figure 1-1. Atmospheric oxy-coal combustion system with flue gas recycle proposed for carbon ca pture in coal power plants, figures are revised based on the work in [19-21].

Table 1-2. List of ongoing and proposed large scale oxy-coal combustion demonstration projects, modified from Wall et al. [23], the CCS project database of MIT Energy Initiative [30] with current updates of these projects.

Project name	Leader	Location	Scale	Technology	MWe	New/ Retrofit	Power Gen	CO_2 Seq	Start-up
Jupiter Pearl Plant	Jupiter	USA	Pilot		22(MWth)	R	N	NA[c]	2007
B&W pilot plant	B&W	USA	Pilot	PC[a]	30(MWth)	R	N	N	2008
OxyCoal-UK	Doosan Babcock	UK	Pilot	PC[a]	40(MWth)	R	N	N	2009
Alstom Windsor Facility	Alstom	USA	Pilot	PC[a]	15(MWth)	R	N	N	2009
Schwarze Pumpe	Vattenfall	Germany	Pilot	PC[a]	10	N	N	Seq[d]	2008
Callide-A	CS Energy, IHI etc.	Australia	Pilot	PC[a]	30	R	Y	Seq[d]	2011
Compostilla (OXY-CFB-300) Phase I	ENDESA, CIUDEN and Foster Wheeler	Spain	Pilot	CFB[b]	17	N	Y	Seq[d]	2011-2012
Jamestown	Jamestown BPU	USA	Demo	CFB	43	N	N	Seq[d]	2013
Janschwalde	Vattenfall	Germany	Demo	PC[a]	250	N	Y	Seq[d]	2015
FutureGen	FutureGen Alliance	USA	Demo	PC[a]	200	R	Y	Seq[d]	2015
Compostilla (OXY-CFB-300) Phase II	ENDESA, CIUDEN and Foster Wheeler	Spain	Demo	CFB[b]	300	N	Y	Seq[d]	2015
Youngdong	KEPCO	S. Korea	Demo	PC[a]	100	R	Y	Seq[d]	2016
Black Hills Power	Black Hills Corporation	USA	Demo	PC[a]	100	N	Y	NA[c]	2016

[a] PC: Pulverized Coal; [b] CFB: Circulated Fluid Bed; [c] NA: Data Not Available; [d] Seq: Sequestration

Air Separation Unit (ASU): When retrofitting existing PC power plants, the system primarily uses existing equipment with the exception of an ASU used to produce an oxygen rich stream for combustion. Currently, the only ASU technology that can meet the volume and purity demand of a large scale coal-fired utility boiler is based on cryogenic distillation. Air is compressed, cooled and cleaned prior to being introduced into the distillation column to separate air into an oxygen-rich stream and a nitrogen-rich stream. Cryogenic air separation is energy intensive, consuming about 0.24 kWh/kg O_2 with 95% oxygen purity [15, 38]. Although the oxygen purity requirement for oxy-coal combustion (85~98%) is lower than that needed in the process industry (99.5~99.6%) [39], these cryogenic separation processes can consume more than 15% of the gross power output [15, 40-42].

Carbon Dioxide Purification Unit (CPU): CPU consists of gas cleanup units to remove water, particulate matter and other pollutant gases from the flue gas before being compressed for sequestration. Because oxy-combustion is compatible with retrofits, selective catalytic reduction (SCR), electrostatic precipitator (ESP) and flue gas desulphurization (FGD) are typically retained as means of NO_x, particulate matter and SO_x removal from the flue gases. This method is also suitable for use in conjunction with amine-type absorbents for post-combustion capture plants.

It has been widely accepted that the non-condensable impurities, such as O_2, may cause corrosion in the pipeline during transportation, and this has raised doubts about the safety of the storage sites. Therefore, after the removal of acid gases such as SO_x and NO_x, non-condensable N_2, O_2, and Ar should also be purged using a non-condensable gas purification unit. This unit is made of multi-stage compression units with inter-stage cooling in order to

separate out the inert gases. Up to the time of this review, there are still no agreed upon standards regarding the required purity of CO_2 for storage and sequestration. However, it should be noted that the acceptable degree of purity of the storage-ready CO_2 results from a trade-off between efficiency losses and operational costs during purification and the safety demands of transportation and storage. For a detailed discussion of this topic, the reader is referred to [19].

Flue Gas Recycle (FGR) System: Recycled flue gas is required to moderate the combustion temperature. Considering system efficiency and operation practices, flue gases can be recycled at different locations downstream of the economizer in the form of wet or dry recycles. In the early stages of oxy-coal system studies, the requirement on CO_2 purity was not stringent and the desulfurization and de-NO_x equipment were regarded as unnecessary [43, 44]. Therefore, all the flue gas was proposed to be extracted from a single location downstream of the ESP in wet or dry forms [43]. Later on, Dillon et al. [44] proposed flue gas recycling at different locations for the primary (used for transporting coal) and secondary streams for the sake of energy efficiency: while the primary recycle has to be dried and reheated to 250-300 ^{o}C to take up moisture from the coal feed, the secondary stream can be recycled at higher temperatures without drying to eliminate thermodynamic losses caused by cooling and re-heating [44].

Today, with a stricter requirement on CO_2 purity for pipeline transportation and storage, pollution control equipment have been again taken into account in the flue gas recycle configurations. Moreover, since SO_2 concentration in the flue gas may accumulate due to flue gas recycle, resulting in 2 or 3 times higher concentration than in conventional

air-firing systems, the primary recycle has to be at least partially desulphurized for medium and high sulphur coal, to avid corrosion in the coal mill and flue gas pipes.

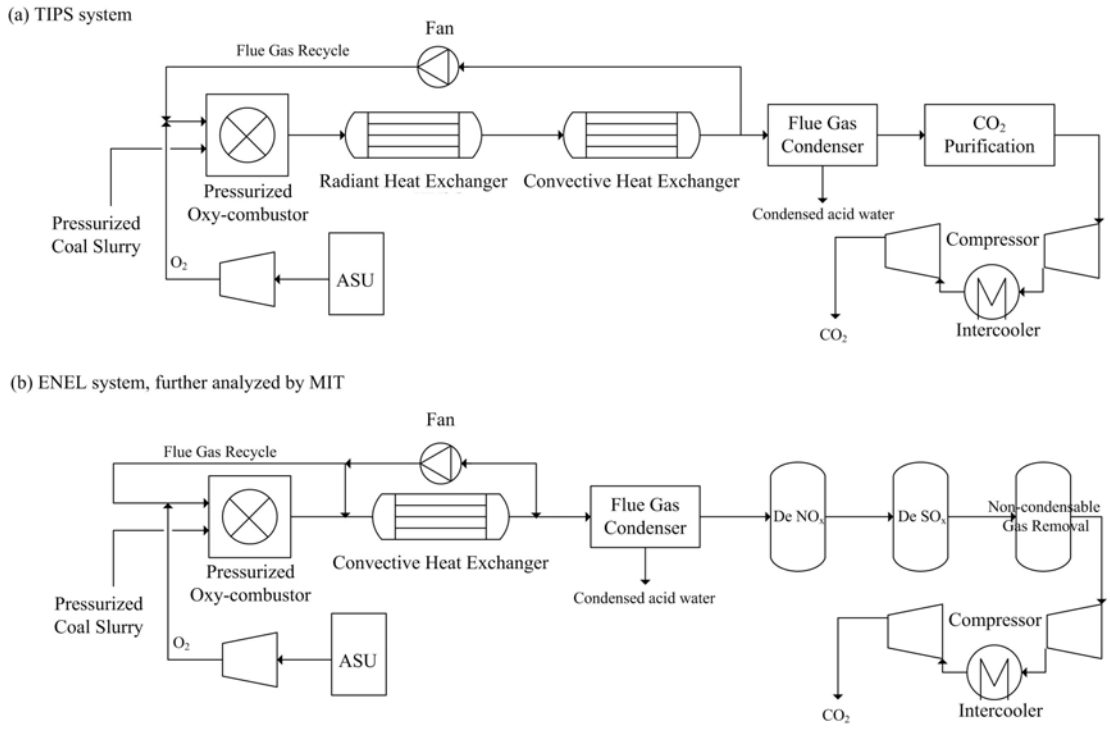

Figure 1-2. Pressurized oxy-coal combustion systems proposed for carbon capture in coal power plants, figures are revised based on the work in [35, 36, 45, 46]. (a) Schematic of the ThermoEnergy Integrated Power System (TIPS), (b) System proposed by ENEL based on a combustion process patented by ITEA, and analyzed in recent studies by MIT.

1.2.3. Pressurized Oxy-Coal Combustion Systems

Pressurized oxy-fuel combustion systems have been proposed recently, with the objective of improving the energy efficiency by recovering the latent heat of steam in the flue gas. The flue gas volume is reduced under elevated pressure, which results in smaller

components and possible reductions in capital cost for the same power output. Several studies have reported on the technical and economic feasibility of this process [31-36, 47, 48], all concluding that the overall process efficiency improves with increasing operating pressure. This is mainly because latent heat recovery from the flue gases becomes possible at higher temperatures. Other potential advantages of pressurized oxy-fuel systems are the reduction of the auxiliary power consumption such as the recycle fan work, and the elimination of air ingress into the system. However, there are challenges associated with combustion and heat transfer characteristics at elevated pressures, and hence the burners, steam/gas heat exchangers and condensing heat exchangers must be redesigned [49].

Figure 1-2 illustrates two different pressurized oxy-coal combustion systems proposed in the literature. One of the first designs is the ThermoEnergy Integrated Power System (TIPS) proposed and studied by CANMET [31, 45] and Babcock power [36]. This system (Figure 1-2a) uses a pressurized combustion unit and heat exchangers, as well as a flue gas condenser (FGC). Downstream of the radiative boiler and convective heat exchangers, steam in the flue gases is condensed in the FGC, where most of the latent heat in the flue gas is recovered by the feedwater in the steam cycle. The rest of the flue gas, which is essentially CO_2, is purified and compressed to the sequestration specifications. In contrast, in the pressurized system proposed by ENEL based on a combustion process patented by ITEA [50-52], and analyzed by MIT (Figure 1-2b) [34, 35], the hot flue gases from the pressurized combustor is quenched to about 800 ºC by the recycled cold flue gas, eliminating the need for a radiant heat exchanger and thus incurring a lower capital cost. It should be noted that in these pressurized oxy-coal systems coal is fed in the form of coal-

water slurry (CWS). Since the pressurized system takes advantage of the latent heat recovery from the steam in the flue gas, using a coal-water slurry does not significantly decrease the overall energy efficiency.

For the pressurized oxy-fuel power plants with CO_2 enriched flue gas streams, desulphurization and NO_x removal solutions have been proposed with potentially lower cost and higher energy efficiency, using lead chamber chemistry and nitric acid chemistry at elevated pressures. For instance, Air Products [53, 54] proposed utilizing two high pressure countercurrent reactive absorption columns (see Figure 1-2 (b)) while Iloeje et al. [55] combines them into a single high pressure column to remove SO_x as H_2SO_4 and NO_x as HNO_3. Both solutions claim to have significantly reduced the cost of CO_2 purification with the latter having an advantage in terms of reduced power consumption and capital cost.

1.2.4. Energy Efficiency Performance of the Oxy-Coal Combustion Systems

An important question to address at this juncture is the comparative performance of the atmospheric and pressurized oxy-fuel combustion systems described above. Figure 1-3 shows the capital expenditure ($/kWe) and efficiency (HHV%) of these systems for newly-built power plants, compared to the performance of supercritical pulverized coal systems without capture and with post-combustion capture. Data are summarized from independent studies carried out by NETL [15], MIT [14, 34, 35], CANMET [45, 56], ThermoEnergy [32, 46, 57], and Kanniche et al [16]. It is noteworthy that estimates in the open literature vary according to their assumptions and approximations. For instance, fuel type, size and configuration of the power plants, percentage of CO_2 captured, and parameters of the steam turbine, etc. Allowing for differences in modeling assumptions, the results from these

studies are averaged in Figure 1-3, with the minimum and maximum values shown as error bars; and they should only be compared qualitatively.

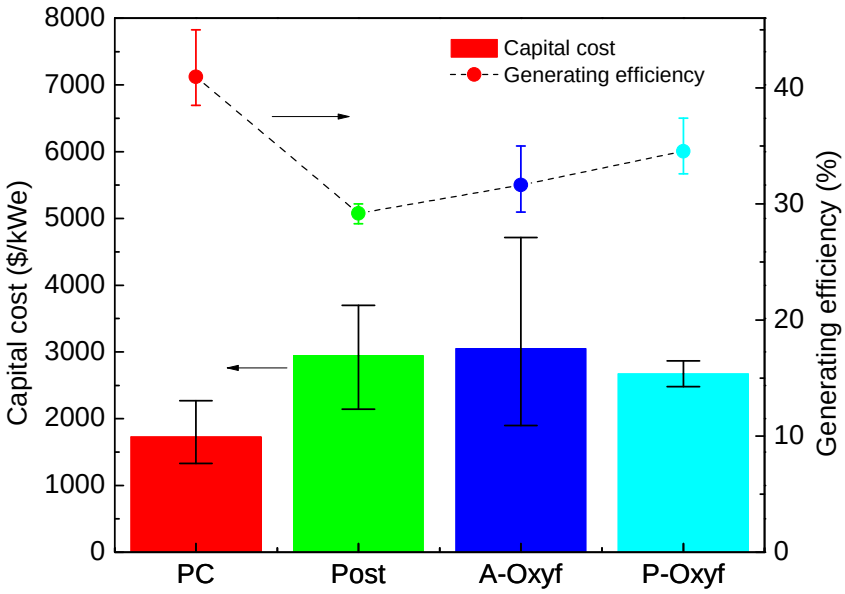

Figure 1-3. Comparison of plant generating efficiency and capital expenditure [14-16, 34, 46, 56, 57] of CO_2 capture technologies. PC: conventional PC system without capture, Post: PC with post capture, A-Oxyf: atmospheric oxy-coal with flue gas recycle, P-Oxyf: pressurized oxy-coal with flue gas recycle.

System efficiency estimates showed a loss of about 10-15% percentage points when post-combustion capture is added to the base case PC power plant. On the other hand, the atmospheric oxy-fuel combustion shows an advantage of 1-5 percentage points when compared with post-combustion capture; while the pressurized system gains a further 3 percentage points efficiency. The main advantage of pressurized oxy-fuel system is the higher saturation temperature of water at elevated pressures, which enables more thermal

energy recovery and the recuperation of latent enthalpy, as stated previously. Although the power consumption of the ASU is higher in the pressurized combustion system, the power savings in the CO_2 compression unit and in the recycled flue gas compressor is even higher, culminating in a better overall efficiency [34].

There are significant variations in capital costs estimates in these studies due to inflation since 2004. The MIT study [14] showed lower cost estimates for the PC without capture, post-combustion, and atmospheric oxy-fuel systems, because it was based on the cost of 2000-2004; while Pomalis et al. [56] estimated higher costs. The economic studies may only be viewed as relatively comparable values, but not absolute values before they are evaluated from commercial scale deployments, especially for the pressurized oxyfuel systems. It should be noted that these data are for newly-built power plants, in fact, the capital cost estimates for retrofitted atmospheric oxy-coal power plants are significantly lower than any of these options as discussed in section 1.1.

1.3. Fundamentals of Oxy-Fuel Combustion

This section reviews the thermodynamics, transport and chemistry processes that take place during oxy-fuel combustion of coal [22]. Experimental and numerical studies of single coal particles or a group of coal particles are reviewed with emphasis on the impact of a CO_2-rich environment. We start with a discussion on the heat transfer characteristics in oxy-fuel combustion and how to match the heat flux with that in the conventional air-fuel combustion, followed by a description of the stages and processes that a coal particle undergoes as it is entrained into the furnace: transportation, heating and moisture

evaporation, devolatilization, ignition and burning of the volatile matter, flame propagation, char combustion, and the CO_2's chemical effects on gas reactions. The physical properties of N_2 and CO_2 relevant to oxy-fuel combustion are summarized in Table 1-3. The effects of these properties will be discussed in greater detail in each of the following sub-sections.

Table 1-3. Comparison of selected physical properties of CO_2 and N_2 at 1 atm and 1000 K. Data are cited from [58-61].

Physical process	Physical property	Unit	CO_2	N_2	CO_2/N_2
Thermodynamic	Density	kg/m^3	0.5362	0.3413	1.57
	Specific heat capacity	kJ/kgK	1.2343	1.1674	1.06
	Volumetric heat capacity	kJ/m^3K	0.662	0.398	1.66
	Gas-water interfacial tension[a]	N/m	71.03	71.98	0.987
Momentum transfer	Kinematic viscosity	m^2/s	7.69e-5	1.2e-4	0.631
Heat transfer	Thermal conductivity	W/mK	7.057e-2	6.599e-2	1.07
	Thermal diffusivity	m^2/s	1.1e-4	1.7e-4	0.644
	Absorptivity /emissivity		0.1478	~0	-
Mass transfer	Mass diffusivity[b]	m^2/s	9.8e-5	1.3e-4	0.778

[a] Water gas interfacial tensions are evaluated for CO_2/water and air/water interfaces at 298.15 K.

[b] Mass diffusivity refers to the binary diffusion of O_2 in CO_2 and nitrogen.

1.3.1. Heat Transfer

Extensive studies have been conducted on retrofitting existing coal-fired power plants for oxy-fuel combustion. Most studies agree that the first priority in the retrofit effort is to maintain the same heat transfer characteristics in the furnace as in air-fired combustion. Matching the heat transfer in the furnace can lead to combustion stability, carbon burnout, and slagging and fouling tendencies [29].

1.3.1.1. Radiation Heat Transfer

Radiative heat transfer plays an important role in boilers and furnaces. The characteristics of radiative heat transfer in oxy-combustion are distinct from conventional air-coal combustion because the flue gas compositions are different. A simplified scaling analysis can be used to estimate the radiative heat transfer rate from an oxy-fuel combustion flame. The entire flame is considered to be a uniform source of radiation, and its total radiative energy release rate can be approximated as:

$$\dot{q}_{rad} \propto \varepsilon A_f \sigma T_f^4 \tag{1.1}$$

where ε is the average emissivity for the flame, and A_f and T_f are the flame surface and temperature, respectively. The flame temperature is the overwhelming factor because of its 4^{th} order dependence [62]. Therefore, to match the radiative heat flux between air and oxy combustion, one must achieve gas temperatures in the latter that are close to those found in the former.

On the other hand, for the same flame temperature, radiation heat transfer is enhanced when the emissivity is higher. Unlike symmetric diatomic gases such as N_2, triatomic gases such as CO_2 and H_2O are not transparent to radiation. Their partial pressures are significantly higher in oxy-fuel combustion flue gas than those in air-fuel combustion, and correspondingly, the absorptivity and emissivity of the flue gas substantially increases.

When a radiation beam of specific wavelength λ travels through a gas, a portion of the radiation intensity, α_λ, is absorbed by the gas. The change in the spectral radiation intensity, dI_λ within an infinitesimal beam length ds is:

$$dI_\lambda = -\kappa_\lambda I_\lambda ds \tag{1.2}$$

where κ_λ is the spectral absorption coefficient, which is a function of the wavelength, gas composition, gas temperature and pressure [63]. The spectral absorptivity and emissivity can be derived by integrating the above equation (1.2) over the beam length, s:

$$\alpha_\lambda = \varepsilon_\lambda = 1 - \exp\left[-\kappa_\lambda s\right] \tag{1.3}$$

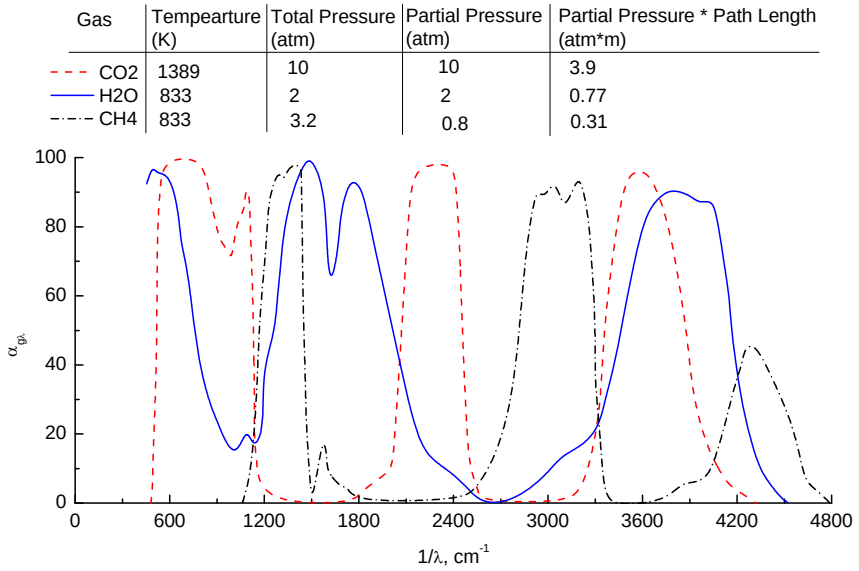

Figure 1-4. Spectral absorptivity as a function of wavenumber for water vapor, carbon dioxide and methane, reproduced from reference [64].

Figure 1-4 shows the spectral absorptivity, α_λ, of the different gas components produced in a combustion process [64]. Since triatomic gases (CO_2 and H_2O) have much higher partial pressures when flue gases are used as the diluent instead of nitrogen, the absorption and radiation in oxy-combustion are stronger than in conventional air-fuel combustion with identical gas temperatures. A close look at Figure 1-4 shows that

absorption is not continuous over the entire spectrum; instead it is concentrated in a number of moderately wide spectral bands. The effective absorptivity and emissivity of a gas mixture can be obtained by integrating the above equation over the full spectrum. However, direct computation of the gas absorptivity is difficult, and gray gas or band models are widely used in the CFD modeling, which will be discussed later.

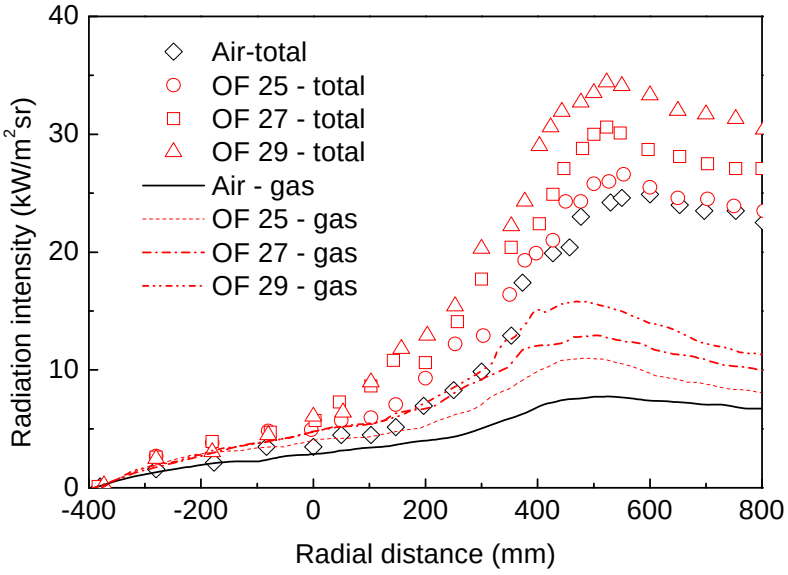

Figure 1-5. Comparison of total intensity measurements (symbols) and gas radiation modeling (lines) at 384 mm away from the burner inlet. Data cited from Andersson et al. [65].

Soot and particle (coal, char and fly ash) radiative emission and absorption play as important a role as the triatomic gases in coal combustion [66, 67]. Experimental studies in oxyfuel combustion have confirmed this trend. Andersson and coworkers [65, 68-70] investigated the radiation intensity of propane-fired and lignite coal-fired oxy-fuel flames in

the Chalmers'100 kW test facility. The total radiation intensity was measured using a narrow angle radiometer, and the gas radiation was estimated using Malkmus Statistical Narrow Band Model (SNBM). Results of the calculated gas and the measured total radiation intensities at the flame zone are shown in Figure 1-5. It can be seen that the portion of the gas radiation in the total radiation intensities under OF25 condition (OF25 denotes oxy-fuel combustion with O_2 concentration of 25% in the burner gas) is significantly higher than in air-combustion. Measurements shows that the temperature distribution in the flame zone under OF25 condition is very close to that under the air-firing condition, and that the H_2O partial pressure increases only slightly from air to OF25 condition, therefore, the higher gas radiation in oxy-fuel combustion is attributed to its 5 times higher partial pressures of CO_2. However, as another important radiation source, the particle radiation contributes about 60-70% of the total radiation in both air-fired and oxy-fired cases, which does not change much in oxy-fuel combustion. This study suggests that in lignite oxy-fuel combustion, if the gas temperature is maintained the same as in air combustion by increasing the O_2 concentration to 25% (OF25), the measured total radiation intensities are similar (OF25-total and Air-total) although gas radiation is enhanced. This is because a large fraction of radiation is emitted by particles, which have similar contribution in both combustion environments.

1.3.1.2. Convective Heat Transfer

The convective heat flux of the flue gas, q''_{conv}, can be approximated as follows:

$$q''_{conv} = h\Delta T \tag{1.4}$$

where h is the convective heat transfer coefficient, and ΔT is the temperature difference

between the bulk gas and the heated object. The convective heat transfer coefficient is influenced by the flow velocity and gas properties such as viscosity, thermal conductivity, heat capacity and density, which are also functions of temperature. The ratio of convective heat transfer coefficients of the flue gas in oxy-fuel combustion (h_{oxy}) to that in air-fuel combustion (h_{air}) can be expressed in terms of dimensionless numbers - the Reynolds number and the Prandtl number - and the fluid thermal conductivity [29]:

$$\frac{h_{oxy}}{h_{air}} = \left(\frac{\mathrm{Re}_{oxy}}{\mathrm{Re}_{air}} \right)^m \left(\frac{\mathrm{Pr}_{oxy}}{\mathrm{Pr}_{air}} \right)^n \left(\frac{k_{oxy}}{k_{air}} \right) \tag{1.5}$$

where *m* and *n* are empirical factors that vary for different geometries. The slightly higher thermal conductivity of CO_2 does not significantly change the conductive heat transfer when compared with air-combustion. However, for convective heat transfer at identical velocity, its lower kinematic viscosity results in a larger Reynolds number and thus a higher convective heat transfer coefficient.

Woycenko et al. [71, 72] studied convective heat transfer coefficients in oxy-coal and air-coal combustion. They found that the h_{oxy} / h_{air} ratio increases with increasing recycle ratio because of the changes in the thermal properties of the flue gas and the increase in the gas velocity. Moreover, this value is ~1.15 when the wet recycle ratio is 70%, at which the adiabatic flame temperatures are approximately the same.

Recall that in Equation (1.4), the convective heat flux is a function of the temperature difference (ΔT), which on average decreases with increasing recycle ratio. Therefore, an acceptable operational range of the flue gas recycle ratio exists in which one can approximately match the convective heat transfer in oxy-coal combustion to that of air

combustion [19, 73]. Thus the existing coal-fired power plant can be retrofitted to function as an oxy-coal plant without replacing the boiler or heat exchangers.

1.3.1.3. Matching the Heat Transfer in Oxy-Fuel Boilers

There are several constraints that need to be considered when retrofitting a conventional air-fired power plant to oxyfuel combustion, including the combustion temperature, the furnace outlet temperature, and the heat transfer in radiative and convective heat exchangers. Based on the above analyses, it appears that matching the gas temperature profiles in the boiler is a starting point in the effort to maintain similar heat transfer characteristics in oxy-coal combustion. A good indication that the temperature profiles are matched is when a similar adiabatic flame temperature (AFT) is achieved. Wall et al. [21] calculated the theoretical O_2 mole fraction (or flue gas recycle ratio) necessary to maintain the same AFT under air-coal and oxy-coal combustion conditions using the equilibrium approximation. Approximately 20% excess air in air-coal combustion and 3-5% excess O_2 in oxy-coal combustion are used to ensure that all the calculations are done on the same basis of about 3.3% (v/v) residual O_2 in the flue gas. Figure 1-6 shows the computational results of the AFT in air-fired and oxy-fired conditions with increasing oxygen fractions for both wet and dry flue gas recycle. The results suggest a temperature drop of about 400 K and 800 K, respectively, in wet and dry recycling oxy-fuel combustion with oxygen concentration of 21% by volume when compared with that of the air-fired condition. The authors did not indicate the coal type in their calculation; it should be noted that the results are depend on the approximate and ultimate analysis of coal.

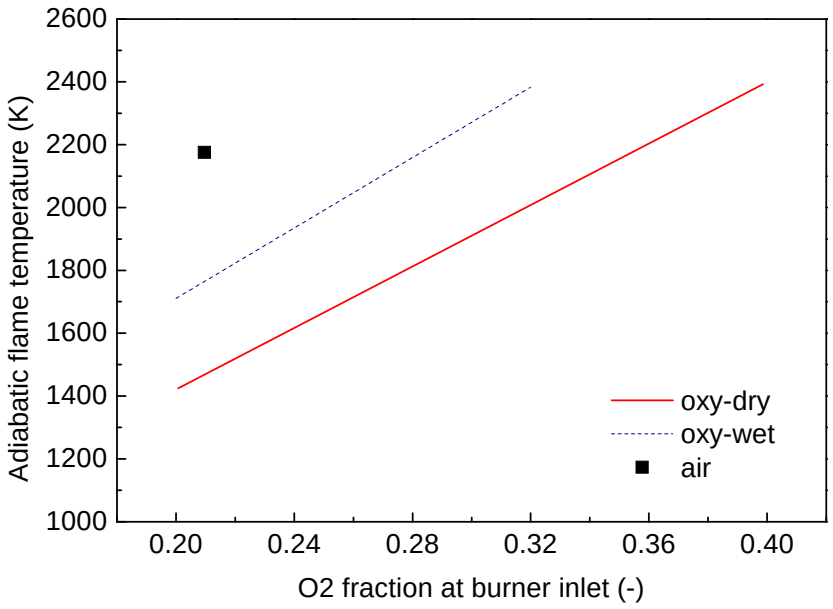

Figure 1-6. The O_2 partial pressure (fraction) required at burner inlet (to achieve similar adiabatic flame temperature as the air-fired case) for wet and dry flue gas recycle (residual O_2 mole fraction in the flue gas fixed at 3.3%) [21]. The symbol ■ indicates the AFT of air-coal combustion, the red solid line — and blue dash line --- indicate the AFT of oxy-coal combustion with dry and wet flue gas recycle, respectively.

Considering that the radiative and convective heat transfer characteristics in oxy-fuel combustion are rather different from those in air-fuel combustion, a matched gas temperature might be close to, but not precisely, the optimum operating condition in order to obtain a matched distribution of heat fluxes in different heat exchanger components. Hence, studies have also been conducted in order to find the optimum recycle ratios for a matched heat transfer distribution in the furnace (radiative section) and in the convective

section. **Table 1-4** summarizes the experimental studies on the heat transfer characteristics in oxy-fuel combustion. Based on the discussion earlier, depending on the furnace geometry, fuel type, and other operating conditions, there is an optimal flue gas recycle ratio that matches the heat transfer distribution between radiative heat exchangers for phase change and convective heat exchangers for superheat. Lower recycle ratios result in higher combustion temperatures and excess heat extraction in the radiative section, especially in the water-cooling membrane section. In this case, the required superheat and reheat temperatures of the steam cannot be attained. Conversely, higher recycle ratios result in a lower combustion temperature and a reduced steam mass flow rate that is overheated. In this case, considerable attemperation (a measure controlling the overheated steam temperature) with feedwater injection is required to reduce the steam superheat temperature, and this would reduce the boiler efficiency [29].

Table 1-4. Bench and pilot scale experimental studies on gas temperature and heat transfer in atmospheric oxy-coal combustion.

Organization	Fuel	Facility	Recycle mode	Experiment findings
Argonne National Lab/EERC[a] [27, 29]	Black Thunder Sub-bituminous Coal from Wyoming	3 MWth, vertical tower furnace	Wet/Dry FGR	Flue gas recycle ratios ((CO_2+H_2O)/O_2 in the oxidant) of 3.25 and 2.6, in wet and dry recycle respectively, matches the overall heat transfer of the air-fired furnace
Argonne National Lab/BCL [28, 29, 74]	Wage coal from Colorado	117 kWth, bench scale furnace, i.d. 0.6 m	CO_2/O_2 mixture	Dry recycling with a CO_2/O_2 molar ratio of 2.23 yields a furnace temperature distribution similar to that of air combustion.
IFRF [71, 72]	Coal	2.5 MW, 2*2 m internal square cross-section	Wet FGR	58-61% of the flue gas is recycled for stable combustion and matched convective heat transfer coefficient and radiative heat flux
University of Leeds [75, 76]	Bituminous coals from UK and international sources	Down-fired 20 kWth combustor	CO_2/O_2 mixture	When air is used as the primary stream, an O_2 concentration of 30% in the secondary stream produces matching gas temperature profiles. When an oxygen concentration of 30% is used in both primary and secondary stream, the resulting gas temperature is higher than air-coal combustion.
Chalmers University of Technology [65, 68-70]	Propane and lignite coal	100 kWth	Dry FGR	Oxy-Propane combustion: With an O_2 mole fraction of 25%, the temperature profiles in the furnace can be matched with that of air-propane combustion. Soot formation also plays an important role in the radiation intensity in air and oxy-combustion of propane. Calculated gas radiation is higher in oxy-combustion than in air combustion, but contributes only 30%-50% of the total radiation intensity. Oxy-Lignite coal combustion: With an O_2 mole fraction of 25%, the temperature distribution can be matched with that of air-fuel combustion; the flue gas temperatures at the furnace outlet are lower in all the oxy-fuel cases than in air-fuel case.
IHI [77]	Low- and medium-volatile	1.2 MWth horizontal combustion test facility	Wet/Dry FGR	When using a secondary gas stream with an oxygen mole fraction of 30%, and dry recycled flue gas as the primary gas, the gas temperature near the burner is lower in oxy-fuel combustion; the gas

	bituminous Coal			temperature is greatly increased with direct oxygen injection; drying the primary gas increases the gas temperature by 150 ºC near the burner.
RWEn power [73]	Russian and South African coals	0.5 MWth, RWEn combustion test facility	Simulated Dry FGR	Peak radiative heat flux values are inversely related to the recycle ratio. Conversely, the convective heat transfer values increase with increasing recycle ratio. A matched radiative heat transfer is established at recycle ratio between 68% and 72% for Russian coal, and between 72% and 75% for South African coal, respectively. The experimental data show that matched heat transfer characteristics can be established with about 74% dry recycle ratio for Russian coal.
CCSD/IHI [21]	Three Australian coals	1.2 MWth pilot scale vertical test facility	Wet FGR	When using an average oxygen mole fraction of 27% in the burner streams, the maximum flame temperature in oxy-fuel combustion is 100-150 ºC lower than the air-fuel flame temperature. The gas temperatures downstream of the burner are almost matched with that of air-fuel combustion.
E.ON UK/Hitachi [78]	Tselentis coal	1 MWth, horizontal firing	Dry FGR	Gas temperatures of the oxy-fuel flame with a dry recycle ratio of 76% (21.3% O_2 in the burner gas) are lower than the temperatures in air-fired flame.
IVD/Hitachi [78]	Lausitz lignite coal from Germany	500 kWth, down-shot firing	Wet FGR	Gas temperatures of the oxy-fuel flame with a wet recycle ratio of 53% (39.3% O_2 in the burner gas) are lower before the level 3 measurement port, and higher at all following levels.
CANMET [79, 80]	Bituminous, sub-bituminous, and lignite coals	0.3 MWth, vertical combustor research facility (VCRF), cylinder down-flow, 0.6 m inner diameter	CO_2/O_2 mixture, or Partial FGR with make-up CO_2	With an O_2 mole fraction of 28%-35%, the gas temperatures and heat fluxes can be matched with those of the air-coal combustion.

[a] Energy and Environment Research Corporation in Irvine, CA

1.3.2. Heating and Moisture Evaporation of Coal Particles

Grinded pulverized coal particles are heated up and partially dried by the primary air or recycled flue gas in the coal mill in order to avoid blockage of the primary pipe. To ensure drying capacity, the primary air or recycled flue gas should be reheated to above 250 ^{o}C, and maintained around 60-90 ^{o}C at the mill exit [44]. The remaining moisture content of the coal particle, or the water content in the case of CWS fuel, is evaporated in the furnace before heating, devolatilization and burning take place. Considering the different heat transfer characteristics in oxy-fuel combustion, heating and moisture evaporation processes of a single coal particle might be different, which in turn may influence the heating rate, devolatilization rate and yield, as well as the standoff distance of the flame (also denoted as lift-off distance, which is defined as the distance between the burner tip and the visible ignition of the flame).

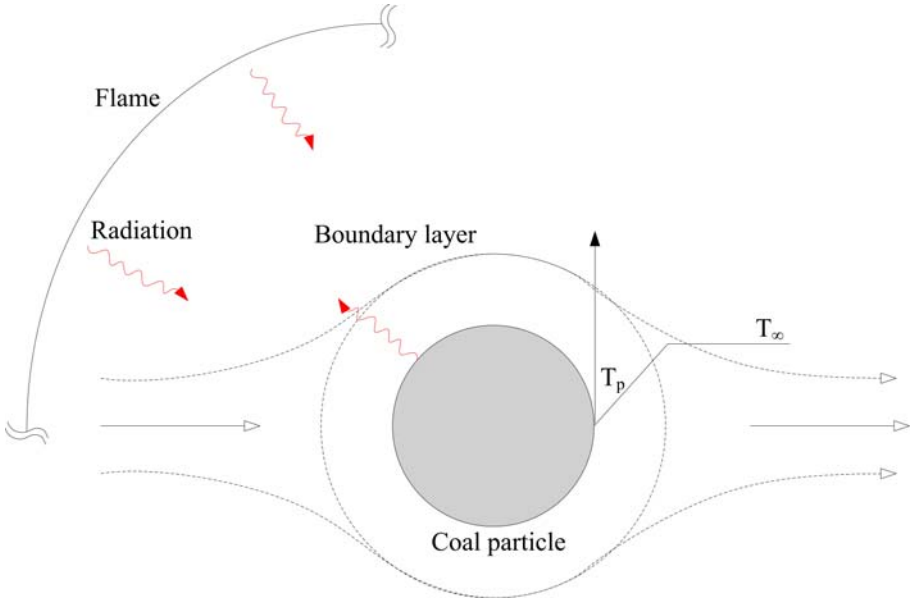

Figure 1-7. Schematic diagram of heat transfer to a single particle in coal combustion.

In this work, the impact of the gas composition on single coal particle drying and heating

processes is analyzed using a simplified heat transfer model, and the evaporation time and heating rate in air-fuel and oxy-fuel conditions are estimated. Figure 1-7 shows an illustration of a quasi-steady model that considers heat transfer between a single coal particle, the surrounding gases and the luminous flame. The energy conservation of a coal particle can be expressed as the balance of the particle internal energy and convective/radiative heat transfer:

$$\frac{4}{3}\pi r_p^3 \rho_p c_p \frac{dT_p}{dt} = 4\pi r_p^2 h\left(T_\infty - T_p\right) + 4\pi r_p^2 \sigma\left(\varepsilon_f T_f^4 - \varepsilon_p T_p^4\right) \qquad (1.6)$$

where T_∞ is the temperature of the surrounding hot gas, and T_f is the flame temperature. The heating rate is strongly determined by the temperatures of the gas and the flame. If the oxygen concentration is kept the same, the flame temperature for oxy-combustion is comparatively lower than that of the air-fuel combustion, resulting in a lower heating rate. This effect is considered in the estimation by assigning different surrounding gas tempeatures. On the other hand, the convective heat transfer coefficient of the flue gas, h, may be different, which also may result in a different heating rate and evaporation time in oxy-fuel combustion.

Water evaporation from the coal particle is a process that couples heat and mass transfer. Using the quasi-steady model of droplet evaporation [81] and the model of coal-water slurry evaporation proposed by Cen et al.[82], evaporation times for different particle sizes under both air and CO_2 conditions are calculated. The reader is referred to [22] for detailed assumptions and derivations. The drying process in the mill and the furnace, and the heating process after evaporation under both air- and oxy-combustion conditions are investigated using the model, and the parameters and properties use in the calculation are summarized in **Table 1-5**.

Table 1-5. Parameters used in estimation of the heating and drying processes of single coal particle.

	Temperature (°C)			Gas properties	Coal properties
	T_∞	T_f	T_{boil}		
Drying in mill	105	-	100	c_{pg}, μ, ρ, k for pure substances are cited from [58] at $\bar{T}_g = \frac{1}{2}(T_\infty + T_{boil})$	$\varepsilon = 0.8$, $c_p = 1500 J/kgK$ $h_{fg} = 2442 kJ/kg$ Moisture content=10%
Drying in furnace	1000	1800	100		
Heating in furnace	1000, 900, 800	1800, 1700, 1600	-	$c_{pg} = c_{H_2O}$ $k_g = 0.6k_\infty + 0.4k_{H_2O}$ [83]	

Figure 1-8 shows the required time for drying a coal particle under typical conditions in the mill and the furnace. The drying time of a 100 μm coal particles is about 1 s in the primary gas stream, and about 2.5 ms in the furnace, respectively, and it grows with increasing particle diameter. An interesting observation is that the drying times are similar in both air and CO_2 environment. For the typical size of a pulverized coal particle, the Reynolds number is small at the terminal velocity, such that the Nusselt number is close to 2, and the convective heat transfer is similar to conductive heat transfer under stagnant condition. Therefore, the thermal conductivity dominates the heat transfer rate. Given identical primary stream and combustion temperatures, the evaporation time is only slightly longer in the mill, and shorter in the furnace under CO_2-rich environment than in air. The reason is that the thermal diffusivity of CO_2 is slightly lower than air at the mill temperature, and slightly higher than air at the furnace temperature. However, the difference is negligible if the primary stream temperature in the mill, or surrounding gas and flame temperature in the furnace are identical in the two environments. Similarly, Figure 1-9 shows that the particle heating rate under CO_2-rich condition is only slightly higher than that in air.

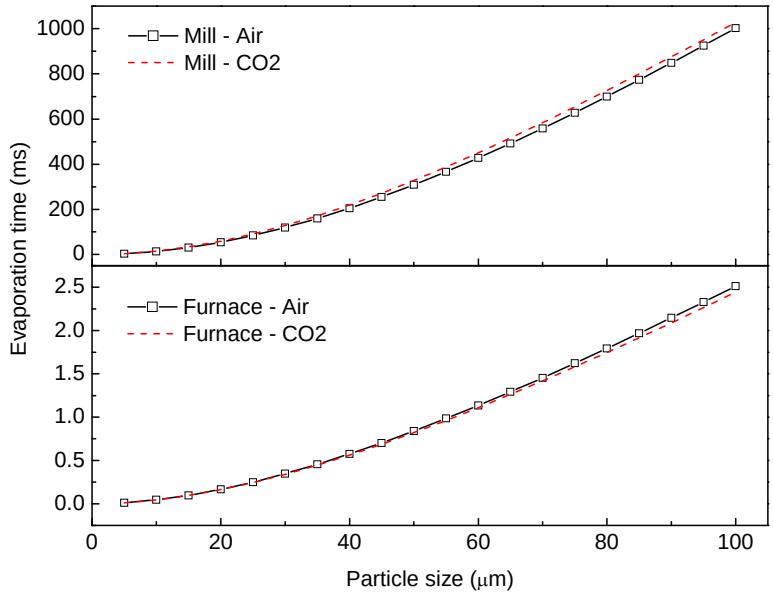

Figure 1-8. Predicted coal particle drying time as a function of particle size in air and CO_2 gas atmospheres. Drying processes in the primary duct during fuel transportation and in the furnace before combustion are estimated. The primary gas stream is set at 105 ^{o}C, and the gas and flame temperatures in the furnace are set to 1000 ^{o}C and 1800 ^{o}C, respectively.

The gas temperature and flame temperature are generally lower in oxy-coal combustion with similar oxygen concentrations. In order to investigate the impact of the potentially lower temperatures on the evaporation time, additional calculations were performed in which the temperatures in the CO_2 gas were reduced by 100 and 200 degrees from their original values, corresponding to T_∞=900 ºC and T_f=1700 ºC, and T_∞=800 ºC and T_f=1600 ºC, respectively. The results of the new calculation are also shown in Figure 1-9. The heating rate of a 100 μm coal particle decreases in the cases where the gas and flame temperatures are 100 and 200 K lower than their original values. These results indicate that the particle heating rate is more significantly influenced by combustion temperatures than by gas compositions.

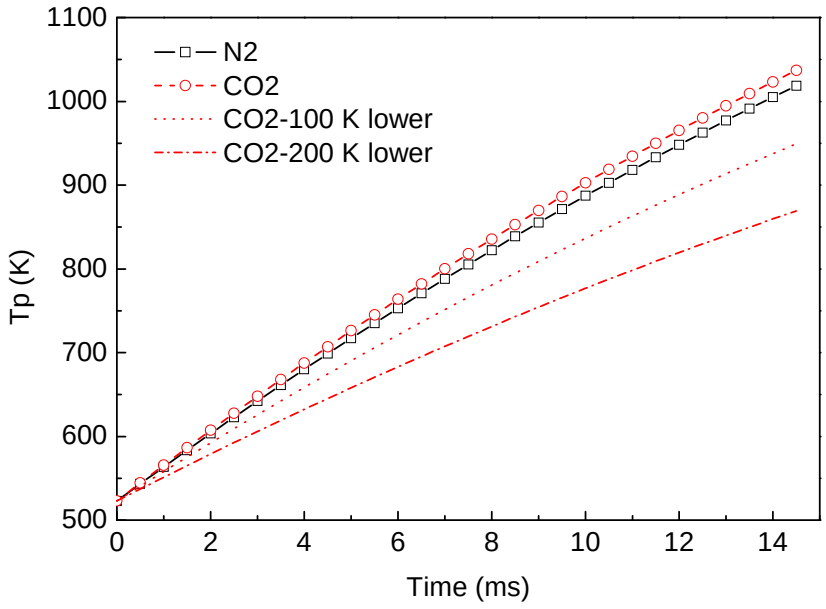

Figure 1-9. Predicted coal particle heating history in N_2 and CO_2 gas atmospheres. The gas temperature is set to 1000 ^oC and the flame temperature 1800 ^oC, respectively. The gas and flame temperature drops of 100 ^oC and 200 ^oC accounts for the possible lower temperatures under oxyfuel condition.

The analysis in this section indicate that employing a similar reheated recycled flue gas temperature will result in similar coal particle drying performance to that of air-combustion, and the evaporation time and heating rate does not change much if the combustion temperature is maintained in oxy-fuel combustion. It should also be noted that this analysis is based on isolated single particle/droplet, the more likely phenomenon of group drying may show other dependencies, and should be studied in the future.

1.3.3. Coal Devolatilization and Char Formation

During heating of the coal particles, volatile matter, including tar, light gases, and pyrolysis water, are released into the gas phase at a temperature above 300 ºC. Devolatilization is an endothermic process and its kinetics and yields are strongly governed by the temperature history (heating rate, peak

temperature, and holding time), ambient gas compositions and pressure [84-91]. Devolatilization kinetics and yields are usually investigated in inert gases, such as N_2 and helium, to avoid the interaction with ambient gases. Devolatilization in a hydrogen environment (a.k.a. hydrogasification) is also of interest for the methanation process [86, 92]. Similarly, the devolatilization characteristics in a high CO_2 concentration environment, which is typical of oxy-fuel combustion, are important and require more research.

Table 1-6. Lab/Bench scale experiments on coal devolatilization in atmospheric N_2 and CO_2 environments.

Author	Facility	Coal sample	Coal mass flow rate (g/h)	Size (μm)	Carrier gas flow rate (L/h)	Main gas flow rate (L/h)	Nominal temperature (ºC)	Residence time (s)
Rathnam [21, 93]	TGA	Coal A,B,C and D	NA	63-90	NA	NA	<1200	2400
	Drop tube furnace	Coal A,B,C and D	4-5	63-90	48	312	1400	0.62
Borrego et al. [94]	Drop tube reactor	High/Low volatile bituminous	60	36-75	300	600	1300	0.3
Al-Makhadmeh et al. [95]	Entrained flow reactor	Bituminous (KK) and lignite (LA)	500-2500	-	400	9200	700-1150	1
Brix et al. [96]	Entrained flow reactor	South American bituminous	50	90-106	18%	82%	900-1400	0.15-0.297

Experimental studies on the volatile yields at different heating rates using thermogravimetric analysis (TGA) and drop tube furnaces (DTF) are summarized in Table 1-6. The volatile yields reported by different researchers vary considerably. Some researchers observed higher volatile yields in CO_2 at high temperatures, and attributed this to the char-CO_2 gasification reaction, while others observe similar volatile yields. For example, when comparing the weight loss curves of a pulverized bituminous coal in N_2 and CO_2 atmospheres using TGA, Rathnam et al. [93] observed that coal devolatilization started at about 573 K and the weight loss history is similar for both atmospheres below 1030 K. However, the weight loss in CO_2 is significantly higher when the temperature is higher than 1030 K due to the char-CO_2 gasification reaction. They also measured the volatile yields of four coals in a DTF

with N_2 and CO_2 atmospheres at a nominal wall temperature of 1673 K. Once again, the volatile yields in CO_2 are about 5-25% higher than those in the N_2 atmosphere. Al-Makhadmeh et al. [95] have reached the same conclusion in their pyrolysis experiments on a medium volatile bituminous coal and a lignite coal using an entrained flow reactor in CO_2 and N_2 environments. To the contrary, Borrego and Alvarez [94] conducted coal pyrolysis experiments using a drop tube reactor at 1300 ºC, and reported a lower mass release in a CO_2 pyrolysis environment for both Colombian vitrinite-rich high volatile bituminous coal and Western Canadian low volatile bituminous coal. Recently, Brix et al. [96] carried out pyrolysis experiments on a South American bituminous coal using an electrically heated entrained flow reactor in N_2 and CO_2 environments. In contrast to the observations reported in the previous paragraph, they found no difference in char morphology, char N_2-BET surface area, or volatile yields in the N_2 and CO_2 environments. Brix et. al. reviewed the discrepancies from the previous experiments and suggested that the operating conditions used during these experiments, such as the mixing between cold and hot gas streams, the particle heating rate and the total particle residence times as summarized in Table 1-6, inevitably affected the results. These factors must be taken into consideration when the data are compared. They concluded that the char-CO_2 gasification reaction does increase the volatile yield during devolatilization at high gas temperature and with long residence times (0.62 s and 1 s) as reported by Rathnam et al. [93] and Al-Makhadmeh et al. [95], respectively; whereas the lower mass release in CO_2 environment reported by Borrego et al. [94] might be due to the high amount of cold entrainment gas (~1/3) and short residence time (0.3 s).

Correspondingly, the char morphology and specific surface area measurements (BET) showed different trends in these above mentioned experiments. Larger surface areas were observed for coals pyrolyzed under CO_2 devolatilization conditions in [93] and [95] to different extents. This was attributed to the char-CO_2 gasification reaction and, as mentioned before, no significant differences were detected in the char sample in [96].

1.3.4. Ignition of Coal Particles

Ignition and combustion behaviors of pulverized coal particle depend on the coal rank, particle size, heating rate and oxygen concentration in the environment. In general, two types of ignition mechanism have been observed for pulverized coal combustion: homogeneous ignition and heterogeneous ignition [97-99]. Homogeneous ignition is usually observed during high volatile bituminous coal combustion when volatile matter and O_2 are heated to the mixture auto-ignition temperature. The high surface flux of volatile products forces the reaction zone away from the solid surface, thereby preventing the solid material from oxygen attack [98]. On the other hand, sub-bituminous coal and lignite may experience heterogeneous ignition, in which ignition occurs via the oxidation of the coal surface [100], with or without fragmentation [101].

For the same coal type and operating conditions, ignition delay of single coal particles in both O_2/N_2 and O_2/CO_2 environments has been experimentally studied. A series of experiments were conducted by Molina, Shaddix and coworkers in Sandia National Lab to study the ignition behavior of an individual coal particle [102, 103] and of groups of particles [104] under O_2/CO_2 and O_2/N_2 conditions. The devolatilization time of Pittsburgh bituminous coal in different O_2 concentrations in a laminar entrained flow reactor were measured, using CCD and interference filter technology for image capture and CH^* chemiluminescence measurements. The results show that the ignition delay time (τ_i) is longer in an O_2/CO_2 environment than in an O_2/N_2 environment with similar bath gas temperature profiles along the reactor. It is also observed that under both conditions, the ignition delay time decreases with increasing oxygen concentration. Shaddix and Molina [102, 103] analyzed the trends of longer ignition delay in O_2/CO_2, and discussed several possible effects at the presence of CO_2, such as heating rate (heat transfer), homogeneous autoignition delay (heat capacity), CO_2 thermal dissociation (equilibrium), as well as chemical effect of CO_2 on the radical formation. They suggested that the longer ignition delay in O_2/CO_2 mixtures is mainly due to the higher heat capacity of CO_2, its tendency

to suppress radical formation, or a combination of both [103].

Similarly, Stivers and Levendis [105] measured the ignition delay times of four North American coals, including two lignite coals, a sub-bituminous coal and a bituminous coal, in a drop tube furnace with O_2/N_2 and O_2/CO_2 atmospheres. In their experiments, the longer ignition delay in O_2/CO_2 environment was observed not only for homogeneous ignitions of high volatile Pittsburgh bituminous coal, but also in heterogeneous ignition circumstances of lignite coals.

1.3.5. Oxy-Char Combustion

The effects of CO_2 on char combustion/gasification have been extensively discussed for air-fired coal combustion [106-109], and more recently, for oxy-fired coal combustion [93, 110-112] . CO_2 is not an inert diluent in combustion; thus, it may influence char combustion via several possible mechanisms: (a) the reduced oxygen mass transfer in CO_2, (b) the lower temperature due to the higher heat capacity of CO_2, and (c) the char-CO_2 gasification reaction [111].

Many experimental studies have been performed in recent years to investigate the effect of a CO_2-rich environment on the combustion rate of coal char. Care should be taken when interpreting these studies because experimental results are strongly dependent on the operating conditions. For instance, char oxidation may take place in different regimes, either kinetic-controlled (Zone I), diffusion-controlled (Zone III), or controlled by both (Zone II), depending on the experimental temperature range, the coal rank and particle size used in the experiments, as well as the oxygen level in the ambient gas, among other factors. As a result, the char conversion rate under oxy-fuel conditions may become higher or lower than that in air-fuel mixtures.

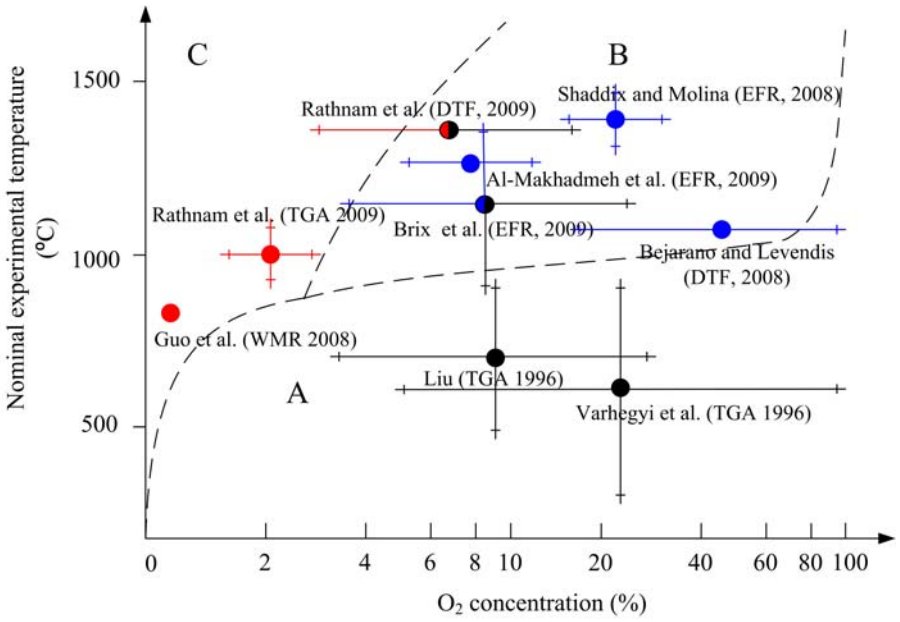

Figure 1-10. Char oxidation/gasification experiments in oxy-fuel conditions. The diagram shows three regions where the experiments were conducted. A: At low temperatures, reactions rates are the same in both O_2/N_2 and O_2/CO_2 conditions; B: At high oxygen level and high temperatures, reaction rates are lower in oxy-fuel conditions; and C: At low oxygen level and high temperatures, reaction rates are higher in oxy-fuel conditions. The error bars show the range of operating conditions, colors show unchanged (black), decreased (blue), or increased (red) char consumption rate.

With careful investigation of the experimental conditions used in the studies, the results can be classified into three regions, as illustrated in Figure 1-10, based on the oxygen concentrations and nominal temperatures in these experiments. Note that the nominal temperatures of the TGA and WMR experiments are the measured particle temperature; while in DTF and EFR experiments, because the char particle temperatures are not available in some of the studies, the nominal temperatures are the gas temperatures, which are hundreds degree lower than the burning char particle temperature, depending on the oxygen mole fraction and coal rank. For instance, the temperature difference between the char particle and the gas is 100-600 K in the Sandia EFR with an oxygen mole fraction between 12%-36%

[111], and is 400-1600 K in the Northeastern University DTF with an oxygen mole fraction between 20%-100% [110].

- *Region A- Low temperatures at any oxygen concentration*: The char oxidation reaction dominates the char consumption, which is kinetically controlled at these low operating temperatures. Most TGA experiments [113-116] fall in this region, and the experimental results show similar reaction rates in O_2/N_2 and O_2/CO_2 environments. Clearly, when the oxygen concentration approaches 100%, the difference between the two environments becomes negligible and the char consumption rate is the same even at high temperatures, as shown in the small narrow region in the top right of Figure 1-10.
- *Region B- High oxygen concentrations, high temperatures*: The char oxidation reaction dominates the char consumption, but char consumption is either in Zone II (internal diffusion controlled) or Zone III (external diffusion controlled). DTF and EFR experiments [95, 96, 103, 110, 111] are typically conducted in this region, and the results show lower char consumption rates in O_2/CO_2 conditions because of the lower oxygen diffusion rate in CO_2.
- *Region C- Low oxygen concentrations, high temperatures*: Char gasification reactions become significant at high temperatures and low oxygen concentrations. Experiments and numerical studies [117] have shown higher char consumption rates due to the gasification reactions. Similar to the exemption in Region A, the gasification reactions may also become dominant at low temperatures when the oxygen concentration approaches zero, as shown in the bottom left of Figure 1-10.

The partitioning in Figure 1-10 is only qualitative and the boundaries of different regions may differ due to the differences in apparent char combustion behavior and reactor architecture. It should be noted that the above conclusions are based on analysis using simplified models. Other mechanisms

might also affect oxy-char combustion, such as the interactions of the heterogeneous and homogeneous reactions, the multi-component diffusion within and around the porous char particle, as well as the catalytic effects of coal ash minerals. Comprehensive models are needed for a better understanding.

1.3.6. Chemical Effects of CO_2 in Gas Phase Reactions

Experimental and simulation studies have shown that CO_2 is not inert in gas phase reaction, but participates in the chemical reactions, and changes the reaction rates and species concentrations. For instance, the burning velocity of methane have been found to be significantly slower in CO_2 diluent gas than in N_2 [118]. Similarly, lower flame propagation velocity of pulverized coal in CO_2 has been reported by Kiga et al. [119] and Suda et al. [120] using the microgravity drop shaft facility in the Japan Microgravity Center (JAMIC).

Liu et al. [121] numerically investigated the burning velocities of methane and hydrogen under air-fired and oxy-fired conditions using a CHEMKIN-based model and GRI-Mech 3.0 mechanism. In their study, the kinetic effect of CO_2 was isolated by implementing a fictitious specious FCO_2 that had identical thermal and transport properties as CO_2 but was not chemical active. The results for the laminar burning velocities of CH_4 and H_2 with diluent gases of N_2, CO_2 and FCO_2 are shown in Figure 1-11. Burning velocities in three cases were calculated: fuel/O_2/N_2, fuel/O_2/CO_2 and fuel/O_2/N_2/CO_2 in which 30% N_2 in air was replaced by CO_2. Since the FCO_2 is "inert" chemically, the difference between fuel/air and fuel/O_2/FCO_2 shows the effect of the physical properties on the burning velocity, while the difference between fuel/O_2/FCO_2 and fuel/O_2/CO_2 indicates the chemical effect of CO_2. Further analysis found that the dominant reaction pathway for the chemical role of CO_2 is as follows:

$$CO+OH \leftrightarrow CO_2+H \qquad (1.7)$$

CO_2 competes for the H radicals through the reverse reaction in Equation (1.7) with the most important chain branching reaction:

$$H+O_2 \leftrightarrow O+OH \quad (1.8)$$

Thus, the presence of CO_2 significantly reduces the concentrations of important radicals, i.e. O and H radicals, leading to a reduction of the fuel burning rate [121]. Figure 1-11 indicates that CO_2's chemical effects play some role in reducing the burning velocity when replacing N_2 with CO_2. However, its physical properties have a more significant contribution.

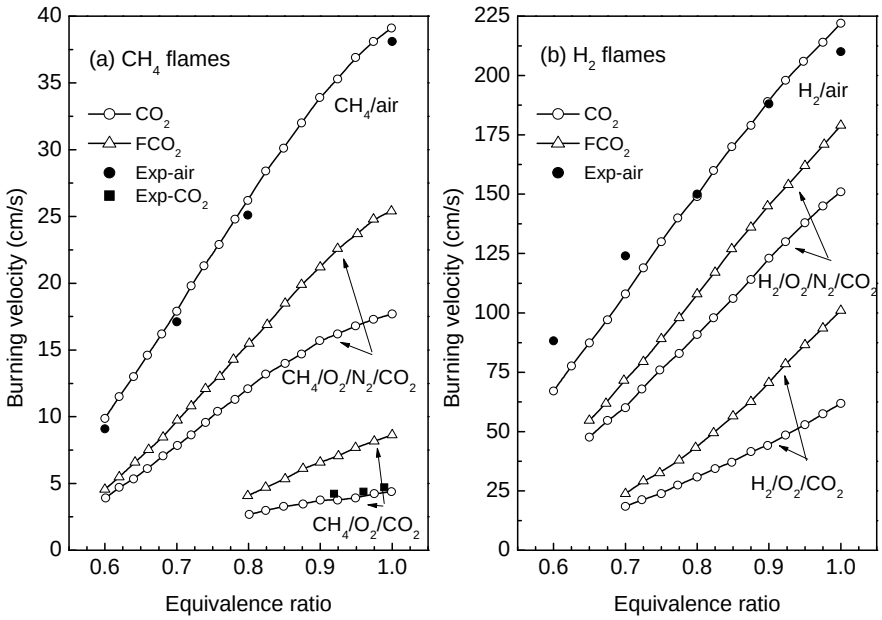

Figure 1-11. Burning velocities of methane and hydrogen mixtures at increasing equivalence ratios. Oxygen mole fraction in the oxidizer is kept at 21% in all cases. Also plotted are the experimental data of Zhu et al. [118] in methane mixture and Westbrook [122] in hydrogen mixtures as filled symbols [121]. The symbol -◯- indicates results using CO_2, -Δ- indicates results using FCO_2.

Moreover, higher CO has been observed in oxy-fuel combustion than that in traditional air combustion. CO is produced from devolatilization, the oxidation of volatile matter in the near-burner regions and char gasification reactions in the char combustion zone. From a thermodynamics point of view, the equilibrium CO concentration is governed by the following reversible reaction:

$$CO+\frac{1}{2}O_2 \leftrightarrow CO_2 \qquad (1.9)$$

Equilibrium of this reaction is shifted towards CO_2 dissociation under high temperatures and fuel rich conditions. Hence, CO concentration is expected to be higher in the flame zone of oxy-fuel combustion because of the higher CO_2 partial pressure at the same temperature.

Zheng and Furimsky [123] calculated the CO mole fraction in the equilibrium state in oxy-coal combustion and found that the CO concentration is 316 ppm at 1700 K when burning with 10% excess oxygen. This is substantially higher than that of air combustion, which has an equilibrium CO concentration of about 64 ppm at the same stoichiometric ratio. Glarborg and Bentzen [124] experimentally investigated CO concentrations during methane combustion in highly diluted environments with either N_2 or CO_2 as the diluent, in a plug-flow reactor with well-defined temperature profiles. Figure 1-12 shows the CO concentration in the product gas at the exit of the reactor under lean, stoichiometric and rich conditions in O_2/N_2 and O_2/CO_2 atmospheres. Substantially higher CO concentrations in the CO_2 diluted environment than in the N_2 diluted environment were observed in all cases. Moreover, that the CO concentration increases from fuel-lean to fuel-rich conditions in both diluent gases agrees with the trends of the equilibrium calculations in [123]. An accurate prediction of the CO concentration in the flame zone in oxy-fuel combustion becomes challenging and will be discussed in greater detail in section 2.6.

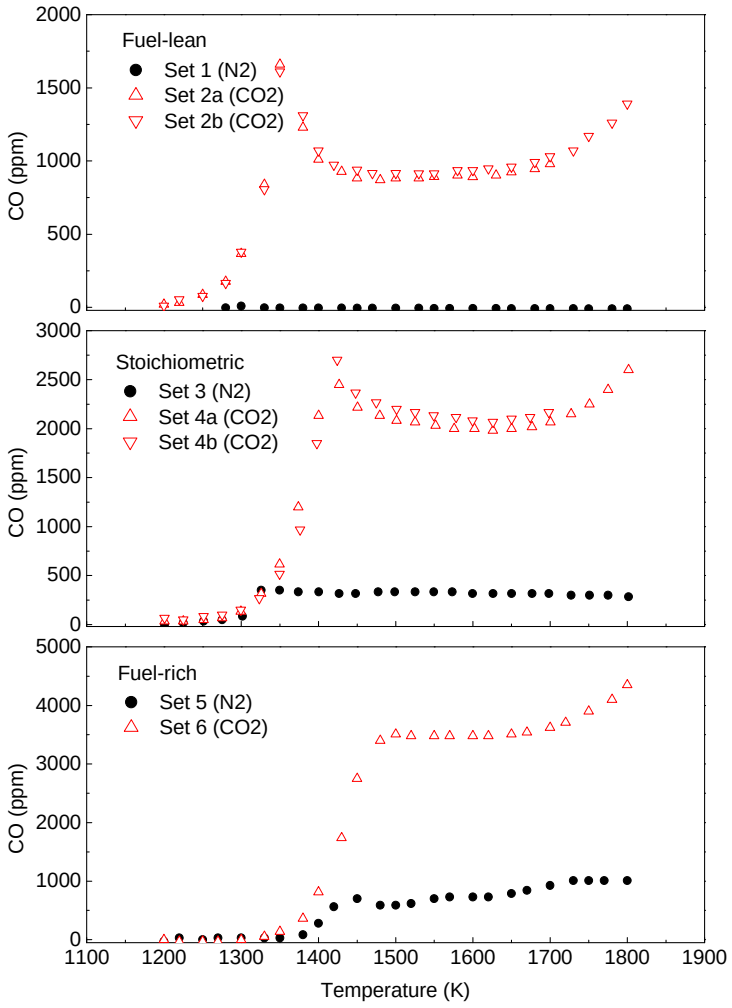

Figure 1-12. Experimental data of CO concentration in the methane combustion product gas at the outlet of a flow reactor as function of temperature and stoichiometry, with N_2 or CO_2 as bulk gas. From the top, the graphs show the CO mole fraction under lean, stoichiometric, and fuel-rich conditions [124]. The symbol ◇ indicates burning in N_2 diluent gas, while Δ and ∇ indicate burning in CO_2 diluent gas.

Higher CO concentrations in the furnace have also been reported under oxy-coal conditions. Hjartstam et al. [70] observed that CO concentrations in the combustion zone near the burner, where the gas temperature is high and fuel-rich conditions prevail, are higher under the OF27 (OF27 means

27% O_2/73% CO_2) and OF29 oxy-fuel conditions than under air-fired condition. Higher CO concentrations in the furnace were also reported in CANMET's tests at similar or higher combustion temperatures [79, 80]. Likewise, Rehfeldt et al. [78] found a significantly higher CO concentration in the oxygen lean flame region of oxy-Lausitz lignite combustion using a 0.5 MW pilot scale test facility.

However, the high CO concentration in the combustion zone does not necessarily result in higher CO emissions because of its nearly complete oxidation downstream at lower temperatures. For instance, different trends on CO emission in oxy-fuel and air-fuel modes were reported in pilot scale tests: A lower CO emission intensity (mg/MJ) in oxy-fuel mode was reported in the experiments conducted by Hjartstam et al. [70], whereas Rehfeldt [78] reported a generally higher CO concentration and emission intensity in oxy-fuel flue gas independent of the firing system, the coal rank and minor deviations in the overall stoichiometry under the operating conditions in their experiments. In general, CO emission mainly depends on the burn-out of the fuel, which is determined by the burner performance and operating conditions such as stoichiometry. Managing CO emission in oxy-coal combustion would not be a major issue if the combustion is well controlled and complete.

1.3.7. Summary

In this section, the physics and chemistry of oxy-coal combustion have been discussed in the order of the sub-processes that take place when a coal particle is burned in a CO_2 rich environment. In addition to reviewing experimental findings, simplified models were applied to identify the impact of the distinct physical properties and chemical effects of CO_2 on the combustion characteristics. The causes and effects are summarized as follows:

- *Heat transfer*: Emissivity and absorptivity of oxy-fuel combustion flue gases are enhanced due to the higher partial pressure of the triatomic gases, which results in different radiative heat transfer characteristics. Convective heat transfer coefficients are also changed due to the different flue gas

compositions. Flue gas recycle ratio is varied in the pilot scale oxy-combustion facilities to obtain matched gas temperature profiles and/or heat fluxes. The optimized recycle ratio is dependent on the wet/dry recycle strategy, the fuel type and the heat exchanger arrangement. A matched distribution of the radiative and convective heat transfer can be achieved at a slightly lower flame temperature in oxy-coal combustion than in air-coal combustion.

- *Particle heating and moisture evaporation*: Calculations using a heat transfer model show that the heating and moisture evaporation rates in CO_2-rich atmosphere in the mill and combustion zone are similar to those in air-coal combustion, given similar surrounding gases and flame temperatures. Considering the possibly lower combustion temperature in oxy-coal combustion, the heating time may be longer and ignition can be delayed.

- *Coal devolatilization*: Lab scale TGA and drop tube furnace tests under different operating conditions indicate that the weight loss might be higher or lower in a CO_2 environment than those under the N_2 conditions, depending on the gas temperature and residence time. It is believed that the higher weight loss at temperatures above 1000 K in CO_2 is due to the contribution of gasification reactions, however, there is no evident influence of the oxy-fuel environment on the devolatilization process.

- *Ignition delay*: Lab scale experiments show that ignition delay is longer in O_2/CO_2 environments than in O_2/N_2 environments for several coal types. Results from a simplified simulation on methane ignition delay with detailed reaction mechanism indicated that the high volumetric heat capacity of CO_2 is the main cause of the homogenous ignition delay.

- *Oxy-char combustion*: The effects of CO_2 on char consumption rate are two-fold. At high temperatures and sufficiently high O_2 mole fractions where reactions are diffusion controlled, the char consumption rate is lower due to the lower binary diffusivity of O_2 in CO_2; whereas at high

temperatures and deficient O_2 mole fractions, the char-CO_2 gasification reaction can increase the char consumption rate. The effect of pressure on the oxidation and gasification reactions are discussed based on the knowledge acquired in coal gasification studies.

- *Pollutant formation*: Experimental studies showed less sub-micron particulate matter in the fly ash distribution under oxy-coal combustion conditions when burning coal with an air-like oxygen mole fraction. Significantly lower NO_x emission per unit energy was reported in the literature, although NO_x concentrations in the flue gas may be comparable with [70, 78, 125], or 2 times higher than in the air-coal combustion due to flue gas recycle [79, 126]. The lower NO_x emission intensity is a result of the NO_x reduction during flue gas recycle, the lower rate of thermal and prompt NO formation, as well as the higher CO concentrations. Given similar combustion temperatures, CO concentration is significantly higher in oxy-coal combustion than in air-coal combustion due to the thermal dissociation of CO_2.

It should be noted that there are a few studies on pressurized oxy-coal combustion. However, the fundamentals derived from studies on atmospheric oxy-coal combustion can help bridge the knowledge gap and aid in the development of pressurized systems.

1.4. Thesis outline

In this study, CFD approach is used to model and investigate the oxy-coal combustion. Based on the literature review on its fundamentals in this chapter, the CFD modeling approaches, challenges, and relevant progress under the new oxy-fuel conditions will be discussed in Chapter 2. In Chapter 3, the performance of different turbulence models, i.e., the Large Eddy Simulation (LES) approach and the turbulence-viscosity models in Reynolds Average Navier-Stokes (RANS) approach, will be compared and validated in modeling a swirling flow oxy-coal burner. Chapter 4 will discuss the modeling of CO_2's chemical effects, in particular, the CO formation using appropriate reduced mechanisms.

Starting from Chapter 5, the validated CFD approach is applied to investigate the pressure's effects on oxy-coal combustion, taking the pressure's effect on the sub-processes of coal combustion into account. Slagging is an important phenomenon in pressurized coal combustion and gasification, Chapter 6 will introduce the development of a three-dimensional slag model, which is first of its kind and can be widely used for coal slagging studies with any reactor geometry.

Chapter 7 summarizes the key conclusions and findings in this study, and provides an overview of the future research needs in the CFD modeling of oxy-coal combustion.

Page left intentionally blank

Chapter 2 CFD Modeling of Pulverized Coal Combustion and the Challenges under Oxy-Fuel Conditions

2.1. Overview

CFD techniques have become the third dimension in fluid dynamics and combustion studies alongside analytical modeling and experimental diagnostics [127]. CFD provides a relatively inexpensive (when submodels are used in connection with Reynolds-averaged Navier-Stokes (RANS) or when using coarse grain large-eddy simulation (LES) models) and indispensable tool to perform comprehensive studies on the fluid flow, heat transfer and chemical reactions in combustion. Currently, CFD modeling of oxy-coal combustion utilize approaches and sub-models that are similar to those developed under air-fired conditions. With the accumulated knowledge on the fundamental differences between air-fuel and oxy-fuel combustion, some effort has gone into developing and validating sub-models for the new combustion environment.

A selection of the CFD simulation studies on oxy-fuel combustion is summarized in **Table 2-1**, which includes the sub-models used for turbulence, radiation heat transfer, char combustion and homogenous reactions. Since the existing sub-models were developed for conventional air-coal combustion, their assumptions and approximations may not be valid in the CO_2-rich environment. In the following sections, the development of CFD sub-model for an accurate prediction in oxy-coal combustion is reviewed, and the findings of these recent numerical studies are summarized.

Table 2-1. Summary of CFD simulations and their sub-models for oxy-fuel combustion.

Author	Simulated object		Modeling approaches					
	Facility	Fuel	Code	Turbulence	Radiation	Char Combustion	Homogeneous Reaction Mechanism	Chemistry-Turbulence
Wang et al. [28]	BCL Subscale combustor	Wage coal	1-DICOG (1-D)	N/A	Zone Method [128], transparent gas	$C+O_2$ $C+CO_2$ $C+H_2O$	Vilatiles combustion	Chemical Equilibrium
Khare et al. [129]	IHI 1.2 MWth vertical pilot scale test facility	Coal A	Fluent	$k-\varepsilon$	P-1 WSGG	$C+O_2$	Volatiles combustion	Chemical Equilibrium
Nozaki et al. [77]	IHI 1.2 MWth horizontal combustion test facility	Coal A/B	VEGA-3	$k-\varepsilon$	Multi-flux Radiation model [130] Three-gray-gas model	$C+O_2$ $C+CO_2$ $C+H_2O$ [131]	Volatiles combustion	EBU
Chui et al. [132]	CANMET 0.3 MWth VCRF	Western Canadian sub-bituminous coal	CFX-TASCflow	Standard $k-\varepsilon$	N/A	$C+O_2$	Volatiles combustion	EBU
Rehfeldt et al. [78]	E.ON 1 MWth horizontal firing facility and IVD 500 kWth down firing facility	Tselentis coal and Lausitz lignite coal	Fluent	Standard $k-\varepsilon$	DO	$C+O_2$ $C+CO_2$	N/A	N/A
Toporov et al. [133]	RWTH Aachen U test facility	Rhenish lignite	Fluent	$k-\varepsilon$	DO WSGG	$C+O_2$ $C+CO_2$ $C+H_2O$	Volatile breakup CO and H_2 burning [134]	Finite Rate/Eddy Dissipation
Chen et al. [62]	ISOTHERM PWR® 5 MWth pressurized test facility	Bituminous coal	Fluent	Realizable $k-\varepsilon$, $k-\omega$	DO WSGG	$C+O_2$ $C+CO_2$ $C+H_2O$	Modified JL	Finite Rate/Eddy Dissipation
Andersen et al. [135]	100 kW down-fired furnace [68]	Propane	Fluent	Realizable $k-\varepsilon$	P-1	N/A	WD [136] and Modified WD [135], JL [137] and Modified JL [135]	EDC
Vascellari et al. [138]	IFRF 2.4 MW furnace	Gottelborn hvBp coal	Fluent	Standard $k-\varepsilon$	P-1	$C+O_2$ $C+CO_2$ $C+H_2O$	Volatile decomposition, tar partially oxidation, Modified JL [139]	EDC
Muller et al.	IFK 0.5 MWth test facility	Lausitz lignite	AIOLOS	Standard	DO	$C+O_2$	JL [137]	EDC

[140]				$k-\varepsilon$	Leckner's model [141]	$C+CO_2$ $C+H_2O$		
Nikolopoulos et al. [142]	330 MWe PC boiler in Meliti power plant, Greece	Lignite from Achlada mine	Fluent	Standard $k-\varepsilon$	DO EWBM	$C+O_2$ $C+CO_2$	Volatile combustion and CO burning	Finite Rate/Eddy Dissipation
Edge et al. [143]	0.5 MWth Air- and oxy-fired combustion test facility with Doosan Babcock triple-staged low-NOx burner and IFRF Aerodynamically air-staged burner	Coal A and B	Fluent	RNG $k-\varepsilon$ and LES	DO WSGG/FSK	NA	Volatile combustion and CO burning	EDM

2.2. Governing Equations and Physical Properties

Coal combustion is typically modeled as a dilute two-phase (solid-gas) reacting flow using an Eulerian-Lagrangian approach. The mass, momentum and energy interactions between the gas phase and the solid particles are calculated using the "particle-source-in-cell" method [144] while updating the particle state along a set of particle trajectories. For the gas phase, the equations governing mass, momentum, species and energy are written in conservative form:

$$\frac{\partial(\rho\Phi)}{\partial t}+\frac{\partial(\rho u_j\Phi)}{\partial x_j}=\frac{\partial}{\partial x_j}\left(\Gamma_\Phi\frac{\partial\Phi}{\partial x_j}\right)+S_\Phi \qquad (2.1)$$

with Φ, t, u, Γ_Φ and S_Φ denoting Favre-averaged variables, time, velocity, diffusion coefficient, and source term, respectively [140]. These equations are the same in both air-coal combustion and oxy-coal combustion. However, the thermodynamics and the transport properties of the gas mixture are different.

In turbulent flows, the effects of turbulence on the transport properties, such as the turbulent viscosity, turbulent mass diffusivity, and turbulent thermal conductivity, generally dominate the laminar transport properties, resulting in a relatively insignificant contribution from the laminar properties. On the other hand, thermodynamic properties such as density and heat capacity are always important, regardless of whether it is a laminar or a turbulent flow.

2.3. Turbulent Flow

Some of the most important phenomena in a practical combustion process are dominated by turbulence, a fact that complicates the effort to predict their characteristics. Although direct numerical simulations (DNS) can resolve all the scales of the Navier-Stokes (NS) equations directly, because of its computational complexity, DNS can only be applied to simple and small geometries and at lower

Reynolds number. In situations where DNS is not feasible, turbulence models are used for approximating turbulent fluxes, turbulent dispersion and turbulent-combustion interactions. Several turbulence models have been developed; they are either based on the RANS or the LES approximations. In RANS-based models, dependent variables are decomposed into space-time averaged components and fluctuations. The resulting Reynolds fluxes are modeled by solving transport equations for the turbulent quantities, such as turbulent viscosity, turbulent kinetic energy, turbulent dissipation rate, etc., at all scales. On the other hand, LES resolves the large eddies directly, while the impact of the small eddies are modeled. In terms of the fraction of the resolved scales, LES falls between DNS and RANS [145]. CFD modeling of turbulent combustion, especially of coal or other solid fuels, is still largely based on RANS.

As can be seen in **Table 2-1**, the two-equation $k-\varepsilon$ model is widely used in oxy-coal combustion CFD simulations. These RANS simulations are reported to yield acceptable accuracy when compared with experimental data. Recently, Edge et al. [143] compared the performances of LES and RANS (RNG $k-\varepsilon$) models in their simulation of air- and oxy-fired pulverized coal combustion in a 0.5 MWth combustion test facility. The results show that LES predicts stronger recirculation zones than RANS simulations in all cases. It also yields a hotter flame edge because of its ability to resolve the large eddies of hot gas. In general, similar improvements are observed when using LES instead of RANS under air-fired and oxy-fired conditions. The study also showed that simulations using a combination of LES and a gray gas radiation sub-model overpredicts the incident radiation while the combination of RANS and a spectral gas radiation sub-model yields better comparisons. This finding further accentuates the importance of other physical sub-models.

2.4. Radiation Heat Transfer

2.4.1. Models for Radiative Properties

Radiation heat transfer is typically computed in CFD by solving the radiative transfer equation (RTE). The RTE at position $\vec{r}$ in the direction $\vec{s}$ is given by [146]:

$$\frac{dI_\lambda(\vec{r},\vec{s})}{ds} = \kappa_\lambda n^2 I_{b,\lambda} - (\kappa_\lambda + \sigma_{s,\lambda}) I_\lambda(\vec{r},\vec{s}) + \frac{\sigma_{s,\lambda}}{4\pi}\int_0^{4\pi} I_\lambda(\vec{r},\vec{s}')\Phi(\vec{s}\cdot\vec{s}')d\Omega' \quad (2.2)$$

where s is the path length, κ is the absorption coefficient, σ_s is the scattering coefficient, n is the refractive index, and I is the radiation intensity which is dependent on position $\vec{r}$ and direction $\vec{s}$. In this section, only the gaseous radiative heat transfer will be discussed. The gas mixture is considered to be an absorbing and emitting medium without scattering. In this case, the RTE is simplified to:

$$\frac{dI_\lambda(\vec{r},\vec{s})}{ds} = \kappa_\lambda n^2 I_{b,\lambda} - \kappa_\lambda I_\lambda(\vec{r},\vec{s}) \quad (2.3)$$

Integrating the radiation intensity over the whole radiation spectrum yields:

$$\frac{dI(\vec{r},\vec{s})}{ds} = \bar{a} n^2 \frac{\sigma T^4}{\pi} - \bar{a}_{incident} I(\vec{r},\vec{s}) \quad (2.4)$$

The Planck-mean absorption coefficient, $\bar{a}$, and the incident mean absorption coefficient, $\bar{a}_{incident}$, are absorption coefficients averaged over the whole spectrum weighted by radiation intensity. Therefore, these properties are functions of gas composition, temperature and pressure; additionally, the incident mean absorption coefficient, $\bar{a}_{incident}$, also depends on the incident radiation. An accurate calculation of the gas radiation property must consider the spectral absorption of CO_2 and H_2O, and also the overlap between these radiating gas components. As discussed in section 1.3.1.1, since direct prediction of the absorption coefficient is computationally complex, models for absorption properties, such as the gray gas or the band models, will have to be employed in the radiation heat transfer model.

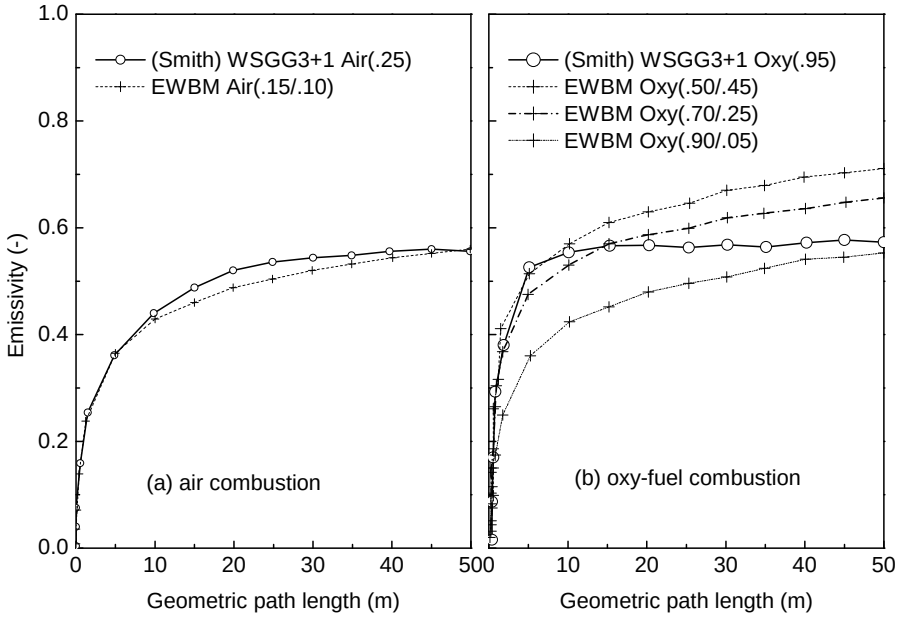

Figure 2-1. Predicted total emissivity of gas mixture of carbon dioxide and water vapor at 1500 K for: (a) conventional air combustion and (b) oxy-fuel combustion using the EWBM and the WSGG models. Values in parentheses show the molar fraction of carbon dioxide / water vapor [147].

The most commonly used gray gas model in CFD is the weighted sum of gray gases (WSGG) model proposed by Smith et al. [148]. In this model, the gas is assumed to consist of a transparent gas and several gray gases without any wavelength dependence, and the model parameters are based on the radiation properties of air-fired flue gases. In contrast, when using the band models, spectral calculations are performed by dividing the entire wavelength spectrum into several bands and assuming that the absorption characteristics of each species remain either uniform or change smoothly according to a given functional form over these bands [149]. One example of this type of radiation models is the Exponential Wide Band model (EWBM) proposed by Edwards and Menard [150], which assumes exponential functions of the line intensity around a band center. Band models are believed to be applicable in oxy-fuel combustion because of their theoretical soundness in non-gray radiation.

However the use of band models is usually computational expensive, and the model is typically used to calibrate the gray gases model [147, 151].

2.4.2. Modification of the Gray-Gas Model

In the WSGG model, the Planck-mean absorption coefficient of the gas mixture over a path length, s, is determined by:

$$\bar{a} = -\ln(1-\varepsilon)/s \tag{2.5}$$

where s is the radiation beam length, and ε, the gas emissivity. The latter is calculated from:

$$\varepsilon = \sum_i a_{\varepsilon,i}(T)\left(1-\exp(-\kappa_i p_i s)\right) \tag{2.6}$$

where $a_{\varepsilon,i}$ is the emissivity weighting factor for gray gas i, κ_i and p_i are the pressure absorption coefficient ($\frac{1}{m \cdot atm}$) and partial pressure (atm) of the absorbing gas i, respectively.

The emissivity weighting factors used in the previous equation (2.6) are polynomial correlations that can be given as a function of the gas temperature:

$$a_{\varepsilon,i} = \sum_j b_{\varepsilon,i,j} T^{j-1} \tag{2.7}$$

The coefficients of the polynomial correlations, $b_{\varepsilon,i,j}$, and the absorption coefficients of the gray gas, κ_i, are derived from experimental data of oil and methane stoichiometric combustion, in which the CO_2 partial pressure is around 0.1 atm, and the partial pressure ratio of H_2O and CO_2 is in the range of 1 to 2, with a path length of less than 10 m [147]. It is worth noting that the CO_2 and H_2O partial pressures and their relative ratio in oxy-coal combustion are not within the applicable range.

Rehfeldt et al. [147] compared the predicted emissivity of the flue gases in both air-fuel and oxy-fuel combustion conditions at 1000 K and 1500 K using both the WSGG model and EWBM, and the results are shown in Figure 2-1. Both models predict similar gas emissivities for the air-fuel conditions.

However, the agreement between the two models is poor for oxy-fuel combustion conditions, especially at high CO_2/H_2O ratios.

Therefore, when using the WSGG model, the coefficients of the polynomial correlations should be modified to reflect the conditions found in oxy-fuel combustion. Direct use of the gray gases model for the radiative properties in oxy-fuel combustion may cause errors and should be avoided [146]. In order to adapt the WSGG model to oxy-fuel conditions, Johansson et al. [151] modified its parameters by fitting the emissivity to a Statistical Narrow Band (SNB) model. The absorption coefficients are constant for each gas, while the weights are calculated from temperature-dependent relations. The two new parameter sets are applicable in oxy-fired conditions with dry or wet recycle, in a temperature range of 500-2500 K and for path lengths between 0.01 and 60 m.

Likewise, Rehfeldt et al. [147] developed a four gray gases plus one clear gas approach. Instead of providing different parameters for specified H_2O mole fractions as done in reference [151], the molar ratio of H_2O to CO_2 (ϕ) was considered as a variable in the emissivity weighting factor correlations:

$$a_{\varepsilon,i} = \sum_j \left[\sum_m c_{\varepsilon,i,j,m} \phi^{m-1} \right] T^{j-1} \qquad (2.8)$$

where $c_{\varepsilon,i,j,m}$ is the coefficient of the correlation which is derived by curve fitting with the EWBM predictions in the range of 600 K to 2400 K and molar fractions of carbon dioxide in the range of 0.3 to 0.9. A comparison between the predictions of radiative heat flux in a furnace using both the WSGG model with these new parameters and the EWBM shows good agreement.

2.5. Heterogeneous Reactions

Oxy-char combustion characteristics have been reviewed in Section 1.3.5, which showed that the kinetics of char oxidation and gasification reactions are not significantly different from those in air-combustion. However, the mathematical model used in CFD simulations should reflect the effects of

the slower oxygen diffusion and the contributions of gasification reactions in a CO_2-rich atmosphere.

2.5.1. Modeling the Diffusivity's Effect

When approaching higher combustion temperatures while maintaining a high oxygen concentration in oxy-fuel combustion, the operating conditions transit from kinetics control to diffusion control (also see Figure 1-10). In this region, the char-O_2 oxidation reaction still dominates, however, char oxidation (char+O_2) becomes progressively more diffusion controlled with increasing char particle temperatures, and for larger particle sizes. Therefore, oxygen diffusion turns out to be the controlling process in determining the char consumption rate in this region.

Measurements of *temperatures and burnout times* of single char particles have been conducted in both N_2 and CO_2 diluent gases. Bejarano and Levendis [110] investigated the burning of bituminous coal, lignite coal, and a spherical synthetic char at increasing oxygen concentrations in both N_2 and CO_2 diluent gases. They conducted particle temperature and burnout time measurements in a 4.2 kW electrically heated laminar flow DTF using a three-color pyrometer at relatively high oxygen concentrations (20%-100%) and high temperatures (1400 K and 1600 K). The experimental results showed that the coal particle temperatures are lower, and the burnout times are longer, in O_2/CO_2 than in O_2/N_2. Similarly, Shaddix and Molina [103, 111] measured the char particle temperature of a Pittsburgh high-volatile bituminous coal and a Powder River Basin subbituminous coal in Sandia's EFR at a gas temperature of 1700 K over an oxygen concentration range of 12-36% in N_2 and CO_2 diluent gases. Lower char particle temperatures and burning rates were observed for both coals in the O_2/CO_2 environment. After accounting for the diffusion limitation of oxygen through the particle's boundary layer, the deduced intrinsic kinetics of the char oxidation reactions were found to be the same for O_2/N_2 and O_2/CO_2 conditions.

The *carbon conversions* of sampled char particles during oxy-char combustion in entrained flow

reactors also show the same trend. Brix et al. [96] measured the char conversion profiles in an EFR under O_2/N_2 and O_2/CO_2 conditions with a coal feeding rate of 50 g/h. At the lower temperature range of 1173-1373 K and with an oxygen concentration of about 6%-28%, they observed no significant difference in the char conversion rate between the two environments, which confirms the trends in region A. When increasing the wall temperatures to 1673 K, where char oxidation is controlled by diffusion, the char conversion rates in CO_2 were lower.

A simplified model for char particle combustion is used to investigate the impact of mass transfer on char oxidation in both air-fired and oxy-fired environments. Studies on carbon or coal char combustion are voluminous, and various models, such as the Single Film Model (SFM) and Double Film Model (DFM), have been proposed to describe the mass and heat transfer in the boundary layer surrounding a combusting char particle. The difference between these models is mainly the approximation of CO burning locations [152]. Mitchell et al. [153] modeled the CO oxidation process in coal boundary layers and suggested that little CO_2 is formed in the boundary layer when the char diameter is smaller than 100 μm, which warrants the applicability of SFM for the size range of pulverized coal combustion. Therefore, SFM is applied in this study to examine the fundamentals of single char particle combustion in O_2/N_2 and O_2/CO_2, and the experimental results in [110] are used to verify the calculations from this model.

The char particle is described as a shrinking homogenous sphere particle surrounded by a chemically frozen boundary layer [154], and the burning process is considered to be quasi-steady in a stagnant gas environment (O_2/N_2 or O_2/CO_2 with increasing O_2 mole fractions). Oxygen diffuses towards the char particle through the dilution gas (either N_2 or CO_2) and reacts at a finite rate with the char surface to produce CO and CO_2. Based on their experimental findings, Tognotti et al. [155] suggested that the CO_2/CO ratio formed by the heterogeneous reaction on the char surface is less than 0.1 at normal combustion temperatures. Therefore, the simulation only considers CO as the combustion

product, which diffuses away from the char surface. Diffusion and reactions inside the char particle are neglected.

Following the derivation in [81], the reaction heat release from char surface is balanced by thermal conductive and radiative heat transfer to the surrounding gas:

$$\dot{m}_C \Delta h = -k_g 4\pi r_s^2 \left.\frac{dT}{dr}\right|_{r_s} + \varepsilon_s 4\pi r_s^2 \sigma \left(T_s^4 - T_{sur}^4\right) \tag{2.9}$$

where the temperature gradient at the particle surface is given by:

$$\left.\frac{dT}{dr}\right|_{r_s} = \frac{\dot{m}_C c_{pg}}{4\pi k_g r_s^2} \left[\frac{\left(T_\infty - T_s\right) \exp\left(\frac{-\dot{m}_C c_{pg}}{4\pi k_g r_s}\right)}{1 - \exp\left(\frac{-\dot{m}_C c_{pg}}{4\pi k_g r_s}\right)} \right] \tag{2.10}$$

The O_2 mass transfer in the particle boundary layer follows Fick's Law:

$$\dot{m}_C = \frac{4\pi r^2 \rho D}{\left(1 + Y_{O_2}/\nu_{O_2}\right)} \frac{d\left(Y_{O_2}/\nu_{O_2}\right)}{dr} \tag{2.11}$$

where ν_{O_2} is the oxygen to fuel mass ratio. Char consumption rate is estimated using a first order surface reaction:

$$\dot{m}_C = 4\pi r_s^2 k_C P_{O_2,s} \tag{2.12}$$

where the partial pressure of oxygen at the particle surface is $P_{O_2,s} = P Y_{O_2,s} \frac{MW_{mix}}{MW_{O_2}}$, and the kinetics of char-O_2 surface reaction rate, k_C, is taken from the experimental results of Field [156]:

$$k_C = 0.8596 \exp\left[\frac{-17967}{T_s}\right] \tag{2.13}$$

Note that the pre-exponential factor in k_C is different from the original reference due to unit conversion. The diffusivities used in the mass diffusion equations are for the binary diffusion of O_2 in the N_2 or CO_2 bath gases (see Table 1-3).

The differential equation (2.9), (2.11) and (2.12) with appropriate boundary conditions are solved simultaneously to find the char consumption rate, $\dot{m}_C$, char surface temperature, T_s, and the char surface oxygen mass fraction, $Y_{O_2,s}$ for a fixed radius, r_s, in quasi-steady state.

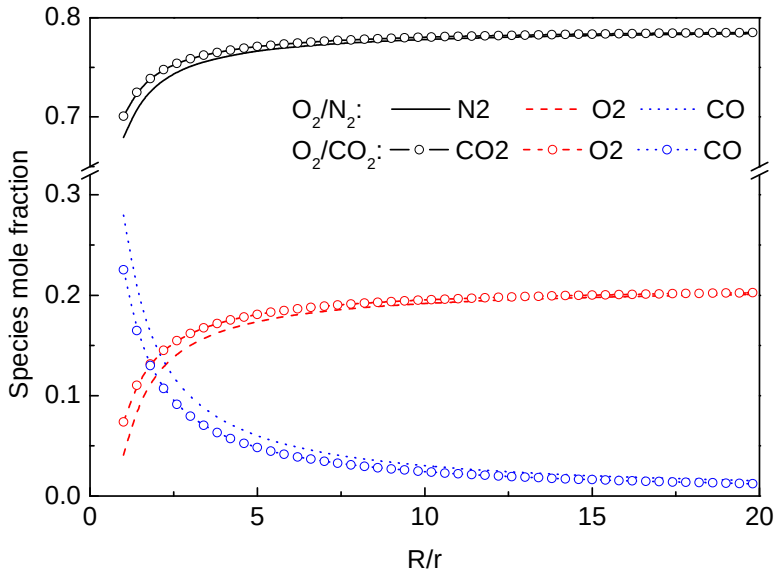

Figure 2-2. Species (O_2, N_2, CO, and CO_2) mole fraction profiles in the boundary layer around a 50 um burning char particle in the outward radial direction, predicted using the Single Film Model in air-fired and 21% O_2/CO_2 conditions.

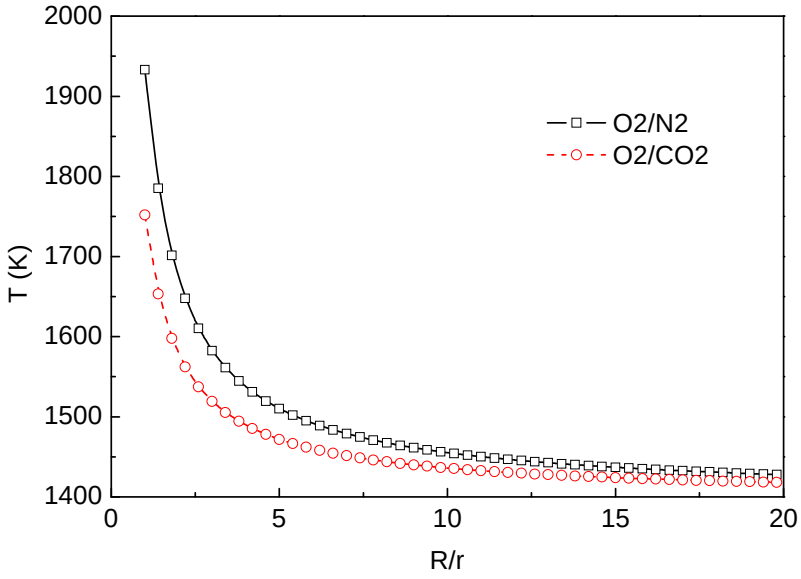

Figure 2-3. Temperature profiles in the boundary layer around a 50 um diameter burning char particle with radial coordinate, predicted using the Single Film Model in air-fired and 21% O_2/CO_2 conditions.

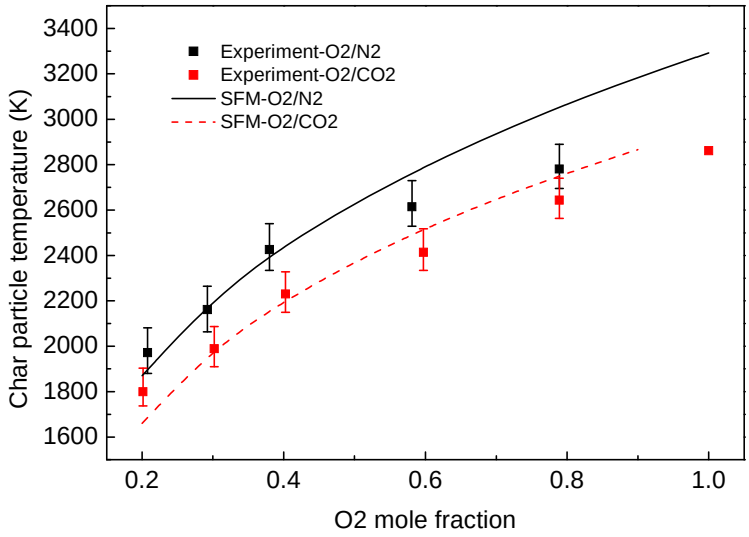

Figure 2-4. Particle surface temperature of a 50 um char particle in O_2/N_2 and O_2/CO_2 mixtures at $T_{furnace}$=1400 K. Lines show the predicted results using the Single Film Model, and markers show the experimental data in [110]. Continuous lines — and broken lines --- correspond to O_2/N_2 and O_2/CO_2 conditions, respectively.

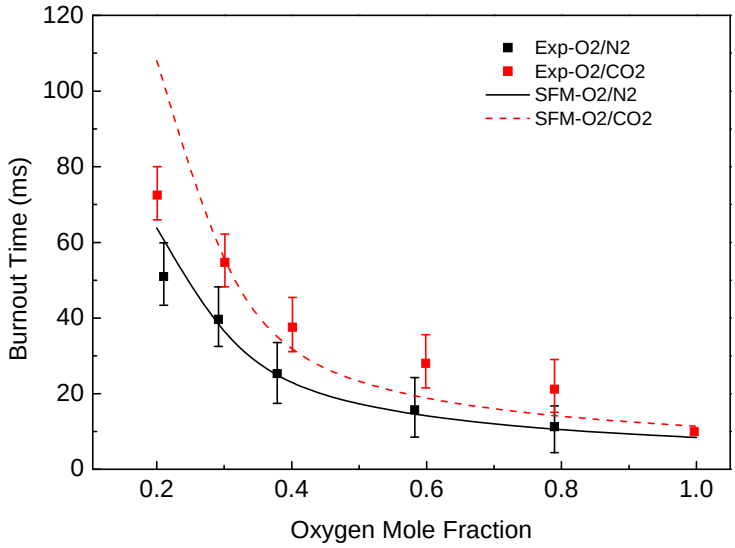

Figure 2-5. Burnout times of a 50 um char particle in O_2/N_2 and O_2/CO_2 mixtures at $T_{furnace}$=1400 K. Lines show the predicted results using the Single Film Model, and markers show the experimental data in [110]. Continuous lines — and broken lines --- correspond to O_2/N_2 and O_2/CO_2 conditions, respectively.

Figure 2-2 to Figure 2-5 show the experimental and simulation results using the SFM model, from which the effect of diffusivity in N_2/O_2 and O_2/CO_2 combustion can be seen. Figure 2-2 illustrates the simulation results for species mole fraction profiles under both environments with an O_2 concentration of 21%. Oxygen diffuses towards the particle in the bath gas (N_2 or CO_2), as shown in the figure. Recalling that the O_2 diffusivity in CO_2 is 0.78 times that in N_2 (see Table 1-3), the oxygen diffusion flux, and thus the carbon consumption rate is correspondingly lower in the CO_2-rich environment. Figure 2-3 shows the predicted temperature profile in the boundary layer of the particle. Lower temperatures, especially at the particle surface (R/r_p=1), is observed under oxy-fuel combustion condition when compared with the temperatures in air combustion. The char surface temperature in 21% O_2/CO_2 is about 190 K lower than that in air-fired combustion. The temperature profile results from a balance between the reaction heat release and the conductive and radiation heat transfer at the particle surface during char burning process, and it reflects the extent of the char burning intensity. A lower O_2 diffusion rate in oxy-fuel combustion translates into a lower char consumption and heat

release rate. Therefore, the particle surface temperatures are lower than in air combustion.

Figure 2-4 and Figure 2-5 show the measured and predicted particle surface temperatures and burnout times, respectively, under O_2/N_2 and O_2/CO_2 conditions with increasing O_2 mole fraction. Both the experimental results from Bejarano and Levendis [110] and the modeling results show lower particle temperatures and longer burnout times under O_2/CO_2 conditions. Similar trends have been reported by Shaddix and Molina [111] in their entrained flow reactor (EFR) experiments: the combusting char temperature is lower in CO_2 than in N_2 at the same gas temperature (1500-1750 K) and O_2 concentrations (12%, 24% and 36%). The predicted particle surface temperatures under O_2/N_2 conditions match well with the experimental data. However, the predictions overestimate the particle surface temperatures by about 200-400 K under O_2 enriched conditions (oxygen mole fraction higher than 0.8). This discrepancy may be because the simulation did not consider the dissociation reactions and equilibrium at very high combustion temperatures. Moreover, the assumptions such as CO as the sole heterogeneous reaction product and ignoring its oxidation in the boundary layer may not be valid at high particle temperatures and high oxygen mole fractions [153, 155]. The gasification reactions may also become important at high char temperatures [112, 157]. A more comprehensive consideration of the physics and chemistry fundamentals in O_2/CO_2 conditions is needed.

It should be noted that although the different diffusivity has significant impacts on the temperature and burnout time of char particles, its effect may not change the mean gas phase temperature distribution within the boiler in the same degree. For instance, Nikolopoulos et al. [142] have shown in their full scale 330 MWe PC boiler CFD modeling, that the mean temperature differences are less than 5 K with considering the different diffusivity in the bulk diffusion.

2.5.2. Modeling the Gasification Reactions

Taking the gasification reactions into account improves the prediction of char consumption rate,

especially in the flame zone and the later stages of oxy-combustion. Therefore, in some CFD simulations [78, 142], the Boudouard reaction was considered. Kuhr et al. [158] simulated char combustion in both O_2/N_2 and O_2/CO_2 atmospheres in a vertical once-through 20 kW furnace at the Institute of Combustion and Power Plant Technology (IFK). The CFD study compared the performance of an intrinsic model based on Smith's approach [159] against a surface reaction model. Figure 2-6 shows the experimental and numerical simulation results of the O_2 and CO mole fraction profiles along the reactor. It should be noted that the operating condition shown in Figure 2-6 is 5% O_2 with a wall temperature of 1300 °C, which falls between Region B and C of Figure 1-10 where the Boudouard reaction contributes to the char consumption rate. As seen in Figure 2-6(a), the intrinsic char oxidation model, which only considers the oxidation reaction, can predict the gas species distribution well for the O_2/N_2 condition. However, when a surface reaction model that consists of only the oxidation reaction is used for the O_2/CO_2 condition, it underpredicts the char consumption rate and overpredicts the O_2 mole fraction as shown in Figure 2-6(b). Adding the Boudouard reaction increases the char consumption rate and improves the O_2 profile prediction. Additionally, since the partial pressure of H_2O is substantially higher under wet recycle conditions, most other CFD simulation studies [62, 77, 133, 138, 140] implemented both the char-CO_2 and char-H_2O gasification reactions in the char consumption model, where the char-H_2O gasification reaction is considered to take place in parallel with the oxidation reaction and Boudouard reaction.

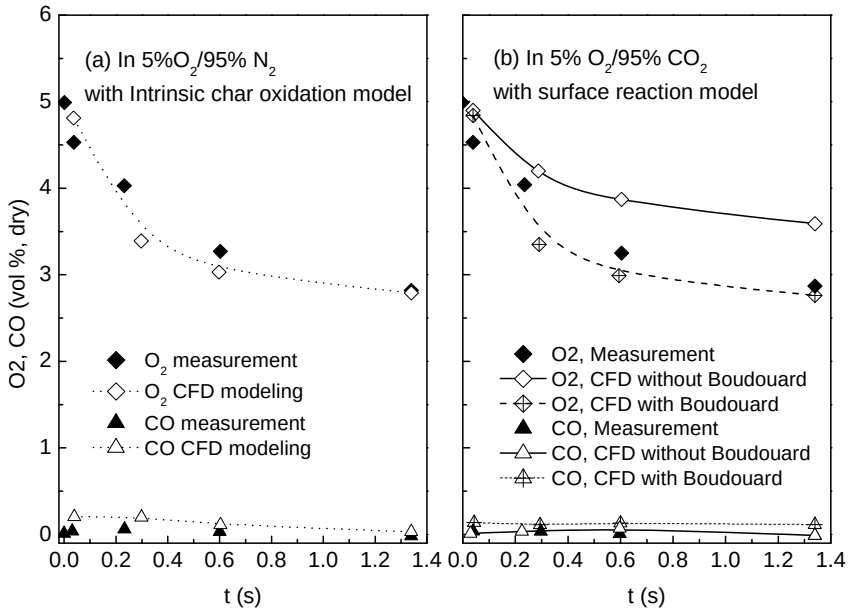

Figure 2-6. Measured and calculated species volume fractions for the lignite-char burning with a wall temperature of 1300 °C. (a) CFD predictions using intrinsic char oxidation model under 95% N_2 and 5% O_2 condition. (b) CFD predictions using surface reaction model under 95% CO_2 and 5%O_2 conditions [158].

The reaction rates of the three heterogeneous reactions discussed above are determined by both surface reaction kinetics and external oxidizer diffusion. Based on the assumption that the global reaction kinetics do not change in oxy-fuel combustion [111], the kinetic parameters are usually taken from air-coal combustion kinetics for similar ranks.

For computational simplicity, oxy-char combustion sub-models are usually simplified in CFD simulations. Important processes such as the internal diffusion and reactions within the porous char particles, the CO flame sheet around the char particles and the interactions of gas species diffusion in the boundary layer are usually ignored. Therefore, advanced sub-models that are accurate and yet computationally inexpensive need to be developed for the oxy-char combustion.

2.6. Gas Phase Reactions

Gas phase reactions play an important role in coal combustion and gasification. Light gases, hydrocarbon gases (alkenes and alkyls) and tar are produced alongside CO_2 and pyrolysis H_2O during coal devolatilization [91]. CO and H_2 produced from the char particle gasification reactions are also burned in the free stream outside the coal particle boundary layer for typical pulverized coal particle sizes [160]. In a CO_2-rich environment, the global reaction rates might be different from the conventional air-fuel combustion due to the chemical effects of CO_2. Therefore, the modeling of gas phase reactions should be modified as well. This includes both the reaction mechanism and the turbulence-chemistry interaction model.

2.6.1. Reduced Reaction Mechanisms

Detailed reaction mechanisms for hydrocarbon combustion such as the detailed chemical kinetic model (DCKM) presented by Glarborg and Bentzen [124], and the GRI-Mech 3.0 used previously in this work have been shown to be valid under oxy-fuel combustion conditions. However, it is computationally expensive to apply these detailed reaction mechanisms in CFD modeling of coal combustion. Alternatively, reduced hydrocarbon combustion mechanisms have been proposed. Reduced reaction mechanisms and models used in CFD studies of oxy-fuel combustion are summarized in **Table 2-1**. In early numerical simulations of oxy-coal combustion, volatile matter combustion was simplified to a one-step global reaction. For instance, Wang et al. [28] simulated the oxy-coal combustion in the Battelle Columbus Laboratory subscale combustor using an infinitely fast reaction rate and local chemical equilibrium. The simulation results showed similar trends to the experimental data for the temperature and major composition distributions. On the other hand, the model failed to predict the CO concentration because of the assumptions of one-dimensional well-mixing and infinitely fast reactions.

Toporov et al. [133] proposed a simplified reaction mechanism for volatile combustion in the CFD simulation of oxy-coal combustion, which consists of volatile decomposition and irreversible combustion of CO and H_2:

$$C_xH_yO_lS_nN_m+\left(\frac{x}{2}+n-\frac{l}{2}\right)O_2 \rightarrow xCO+\frac{y}{2}H_2+nSO_2+\frac{m}{2}N_2 \qquad (2.14)$$

$$CO+0.5O_2 \rightarrow CO_2 \qquad (2.15)$$

$$H_2+0.5O_2 \rightarrow H_2O \qquad (2.16)$$

The simulation results showed agreement with experiments for the temperature and O_2 species. The CO concentration measurement was not available, and hence the accuracy of the CO prediction using this mechanism was not verified.

Multi-step reaction mechanisms, such as the two-step mechanism proposed by Westbrook and Dryer (WD) [136] and the four-step mechanism proposed by Jones and Lindstedt (JL) [137], were suggested for the homogeneous reactions under conventional air-fired conditions, and have been successfully used in CFD modeling of coal combustion and gasification [161, 162]. Since the WD mechanism considers the reversible CO_2 dissociation reaction, and the JL mechanism consists of the reversible water gas shift reaction, they are expected to yield a more accurate CO concentration prediction than the irreversible reaction mechanisms. However, since the kinetics of these global reactions were deduced from air-combustion experimental data, Andersen and coworkers [135] concluded that these mechanisms cannot be expected to work as well under oxy-fuel conditions as they do for conventional air-fuel combustion. Therefore, they further modified the two-step WD and four-step JL mechanisms for methane combustion by calibrating their kinetics parameters with the ignition delay and the final product concentration results predicted by the DCKM reaction mechanism under oxy-fuel conditions. Both modified mechanisms are claimed to perform better than the original mechanisms for CO and flame temperature predictions in the CFD modeling of oxy-propane combustion.

Coal combustion involves complicated hydrocarbon species, including both tar and gases that depend on the rank and property of the fuel, resulting in a large range of gas compositions. Although the reduced mechanisms are reasonably well established for natural gas and other gas fuels, and have been applied in air-coal combustion, their accuracies in oxy-coal combustion simulation remain a subject of investigation.

2.6.2. Turbulence-Chemistry Interactions

For laminar flows, the reaction rates can be computed using the laminar finite-rate model. However, in the case of turbulent flames, turbulent fluctuations becomes important and chemistry-turbulence interactions must be modeled while considering the effects of turbulent fluctuations on the source term of the species equation. The description of the interaction between turbulence and chemistry, therefore, becomes another concern in accurate modeling the gas phase reaction under oxy-fuel conditions.

The eddy dissipation model (EDM) [163] was used in some numerical studies of oxy-coal combustion [77, 132] in which the chemical reaction is governed by the large-eddy mixing time scale based on the eddy break-up (EBU) model proposed by Spaling [164]. As a further development, the finite rate/eddy dissipation model was proposed, in which the reaction rate is taken to be the lower of the Arrhenius reaction rate and eddy dissipation rate. In the flame zone, the eddy dissipation rate is generally smaller than the Arrhenius rate, and reactions are limited by the extent of mixing. Based on the assumption that the reaction rate is limited by both the mixing of the reactants and the heating of the reactants through the mixing with hot reaction products, the net rate of production of species i due to reaction r, $R_{i,r}$, is given by the smaller of the reactant mixing rate (first term) and product mixing rate (second term):

$$R_{i,r} = \min\left(\nu'_{i,r} M_{w,i} A\rho \frac{\varepsilon}{k} \min_R \left(\frac{Y_R}{\nu'_{R,r} M_{w,R}} \right), \nu'_{i,r} M_{w,i} AB\rho \frac{\varepsilon}{k} \frac{\sum_P Y_P}{\sum_j^N \nu''_{j,r} M_{w,j}} \right) \quad (2.17)$$

where A and B are model constants. Note that in oxy-fuel combustion, the CO_2 and H_2O partial pressures in the burner streams are already high before mixing with hot product gases. Therefore, using the same model constants A and B for air-fuel combustion may over-estimate the second term, and thus over-estimate the reaction rate of oxy-fuel combustion.

Another drawback of eddy dissipation based models is that they cannot deal with multi-step chemical mechanisms and reversible reactions, such as CO_2 dissociation. The reason is that multi-step mechanisms are based on reaction rates which occur at different time scales, whereas in these models, every reaction has the same turbulent rate, and therefore, the same reaction rate [145]. CFD modeling of an oxy-natural gas flame has shown that the mixed-is-burned nature of the eddy dissipation model results in a failure to predict CO accurately [165].

The eddy dissipation concept (EDC) model was developed as an extension to the eddy dissipation model to incorporate multi-step chemical mechanisms in turbulent flows [166], where the reactions are assumed to occur in a turbulence-characterized fine-scale reactor governed by Arrhenius rates. Multi-step reaction mechanisms have been implemented in this model for air-methane combustion [139, 167] as well as air-coal combustion [168], and are believed to be more accurate than the eddy dissipation based models. Recently, Vascellari and Cau [138] applied this model with a modified JL mechanism which is taken from air-fuel combustion, to simulate oxy-coal combustion in the IFRF 2.4 MWth furnace. However they did not show a comparison with experimental data. Similarly, Muller et al. [140] also used the same approach for the gas phase reactions in their simulation of oxy-coal combustion in the IFK 0.5 MWth test facility, and the CO prediction agrees well with their experimental data.

2.7. Summary

Based on the overview of the state-of-the-art development of CFD simulation on oxy-coal combustion, CFD approaches have been used in some studies to better understand the flowfield and combustion processes in oxy-coal combustion, and extensive applications of CFD are expected in the scale up and advanced design of oxy-coal combustion facilities. However, distinct characteristics in oxy-coal combustion necessitate modifications of CFD sub-models because the approximations and assumptions for air-fuel combustion may no longer be valid. Therefore, development and validation of more accurate sub-models are still needed. Several problems remain that need to be resolved to achieve a higher predictive accuracy of combustion characteristics in a CO_2-rich environment, such as:

- *Turbulence models*: While swirling flows and their impact on mixing via the establishment of inner recirculation zones near burners and injectors are important in all combustors, they take on a more significant role in the case of oxy-combustion. Better predictive models for rotating and swirling flows are thus needed, such as RANS and LES.
- *Radiation models*: Radiation heat transfer plays a major role in the furnace, and it also governs the energy equation in combustion. Sub-models for the turbulence-radiation interaction and gas emittance/absorptance are needed to improve the simulation of the temperature field.
- *Oxy-char combustion sub-models*: The models should take into account the effect of physical (heat capacity and mass transfer) and chemical (its interaction with heterogeneous and homogenous reactions) properties of CO_2 and be able to predict the burning rate in the different operating condition regions (see section 1.3.5).
- *Gas phase reaction mechanisms*: High-fidelity reduced gas combustion mechanism should capture the chemical effect of CO_2 in oxy-combustion, and provide accurate predictions of minor species and pollutant formations.
- *Pressure's effects*: At higher operating pressure, the physical properties of sub-processes can be

changed significantly, such as the boiling point, transport phenomena, and surface kinetics. Appropriate modeling of the pressure's effects is required in the pressurized oxy-coal combustion.

- *Slag flow models*: Slagging combustion and gasification is widely used in combustors and gasifiers using coal as the feedstock, in particular for the pressurized systems because of its advantage in removing the ash from the flue gas or syngas. However advanced slag models are required to develop to describe the complicated multiphase flow problem.

Therefore, this study will focus on the development and modification of key submodels, and their validation as a whole for oxy-coal combustion in a high-CO_2 concentration environment. The validated CFD approach will be used to further investigate the oxy-coal combustion at elevated operating pressures, based on which a guideline for the optimal operating conditions will be proposed at high pressure.

Page left intentionally blank

Chapter 3 Validation of the Turbulence Models for Oxy-Coal Combustion

Starting from this chapter, we will introduce the CFD simulations of oxy-fuel combustion: its submodel development, the validation using experimental measurements, and the analysis of the simulation results in order to gain insights into the combustion process. In this capture, we focus on the performances of turbulence models, including RANS turbulent-viscosity models and Large Eddy Simulations, in prediction of the combustion field with a swirl oxy-coal burner.

3.1. Overview

Turbulence is one of the most challenging and critical processes in turbulent combustion modeling, because of its role in establishing the flow, mixing, and combustion processes. RANS approaches, especially turbulent-viscosity models such as the $k-\varepsilon$ model, the $k-\omega$ model and their variations [113, 169, 170], are widely applied in the modeling of turbulent combustion because of their low computational cost. Specifically in oxy-coal combustion computational fluid dynamics (CFD) simulations, the standard $k-\varepsilon$ model has been extensively used [77, 78, 129, 133, 140, 142, 171, 172]. For instance, Toporov et al. [133] chose the standard $k-\varepsilon$ model in their CFD modeling of the 100 kW_{th} oxy-coal combustion test at RWTH Aachen University, and Al-Abbas et al. [172] used the same turbulence model to investigate air-fired and oxy-fuel coal combustion in a similar scale test facility at Chalmers University of Technology. CFD simulations of a full-scale (330 MW_e) [142] pulverized coal-fired furnace have also been conducted using the standard $k-\varepsilon$ model. Reasonably good agreements were observed when comparing the temperature and species distributions in these studies. However, the impact of turbulence models on the discrepancy between experimental and simulation results have not been fully assessed.

The $k-\varepsilon$ model has been shown to perform rather poorly in shear layers with strong pressure gradients, while the $k-\omega$ model performs better for many flows [173]. Based on a literature review on the performance of the RANS models in coal gasification, Kumar and Ghoniem [174, 175] demonstrated that the shear-stress transport (SST) $k-\omega$ model performs better than the $k-\varepsilon$ models in swirling flows. They conducted simulation using the standard and the realizable $k-\varepsilon$ models, the SST $k-\omega$ model and LES to predict the flow in a sudden expansion, and showed that the SST $k-\omega$ model yields the most satisfactory predictions in swirling and nonswirling canonical flow cases. We note here that although swirling flows are widely used in coal burner designs, there are few applications of the $k-\omega$ model in oxy-coal combustion simulations.

In recent years, LES has attracted more interests in CFD simulation. LES can capture the time-dependent large-scale flow dynamics, and is less dependent on the assumed turbulence model. However, it is computationally more expensive. LES has been applied to model oxy-coal combustion, and results showed better agreement with experiments. For instance, Edge et al. [143] compared the performance of LES and RANS (renormalization-group (RNG) $k-\varepsilon$) models in their simulations of air-fired and oxy-fuel pulverized coal combustion in a 0.5 MW_{th} test facility. Gharebaghi et al. [176] modeled a 1 MW_{th} industrial test facility using LES and RANS (standard $k-\varepsilon$). Both studies suggest that LES improves the prediction of the recirculation zones and flame shape. It has also been realized that the radiation model needs to be modified in order to improve the prediction of the temperature field and the heat transfer characteristics.

In this study, both RANS (standard $k-\varepsilon$ model, RNG $k-\varepsilon$ model, SST $k-\omega$ model) and LES approaches, along with improved sub-models for gas radiation properties and char consumption in a CO_2-rich environment, are performed to investigate the oxy-fuel combustion of lignite coal in a pilot-scale test facility at RWTH Aachen University. Velocity, species concentration, gas and particle temperature measurements are used to examine the accuracy of the CFD simulations. In particular, the

study focuses on assessing the performance of RANS turbulence models and LES approaches in a typical swirling flow burner equipped with multiple staging streams. Based on the simulation results, some of the mechanisms of oxy-combustion, such as the stabilization mechanism and the oxy-char combustion characteristics, are also discussed.

3.2. Experimental Studies

3.2.1. Furnace and Burner Geometry

The geometry and operating conditions of the oxy-lignite coal combustion experiments in a 100 kW_{th} test facility [133, 177] at the Institute of Heat and Mass Transfer of RWTH Aachen University was used in this numerical study. The axial and tangential mean velocities, averaged oxygen and temperature distributions were measured at different locations downstream of the burner. These results are used to examine the accuracy of the CFD simulations. Figure 3-1(a) shows the geometry of the cylindrical furnace. The length of the combustion chamber is 2.1 m and its inner diameter is 0.4 m. The burner shown in Figure 3-1(b) is a swirl burner with an annular orifice through which the primary stream is supplied with coal particles. The secondary stream is swirled with a velocity ratio $\frac{v_{\tan}}{v_{axial}} = 1$, and it is injected into the combustion chamber through an annulus surrounding the primary stream inlet. According to a geometry-based correlation for the vane-type swirler in an axial tube proposed by Beer and Chigier [178], the swirl number of the secondary stream is close to 0.96. A more accurate calculation using the CFD simulation results shows that the swirl number of the secondary stream is 1.06, which takes the pressure gradient into account. Moreover, the CFD calculated swirl number at the burner quarl outlet is 0.81 combining the non-swirled primary and the swirled secondary stream flow. A tertiary stream can be injected through an annulus enclosing the quarl. Another gas stream, the staging fluid, enters the furnace through an annulus at the outer diameter of the furnace. Its main purpose is to

reduce the amount of gas injected through the other inlet openings, thus reducing the axial velocities and maintaining local fuel-rich stoichiometry at the burner.

(a) (b)

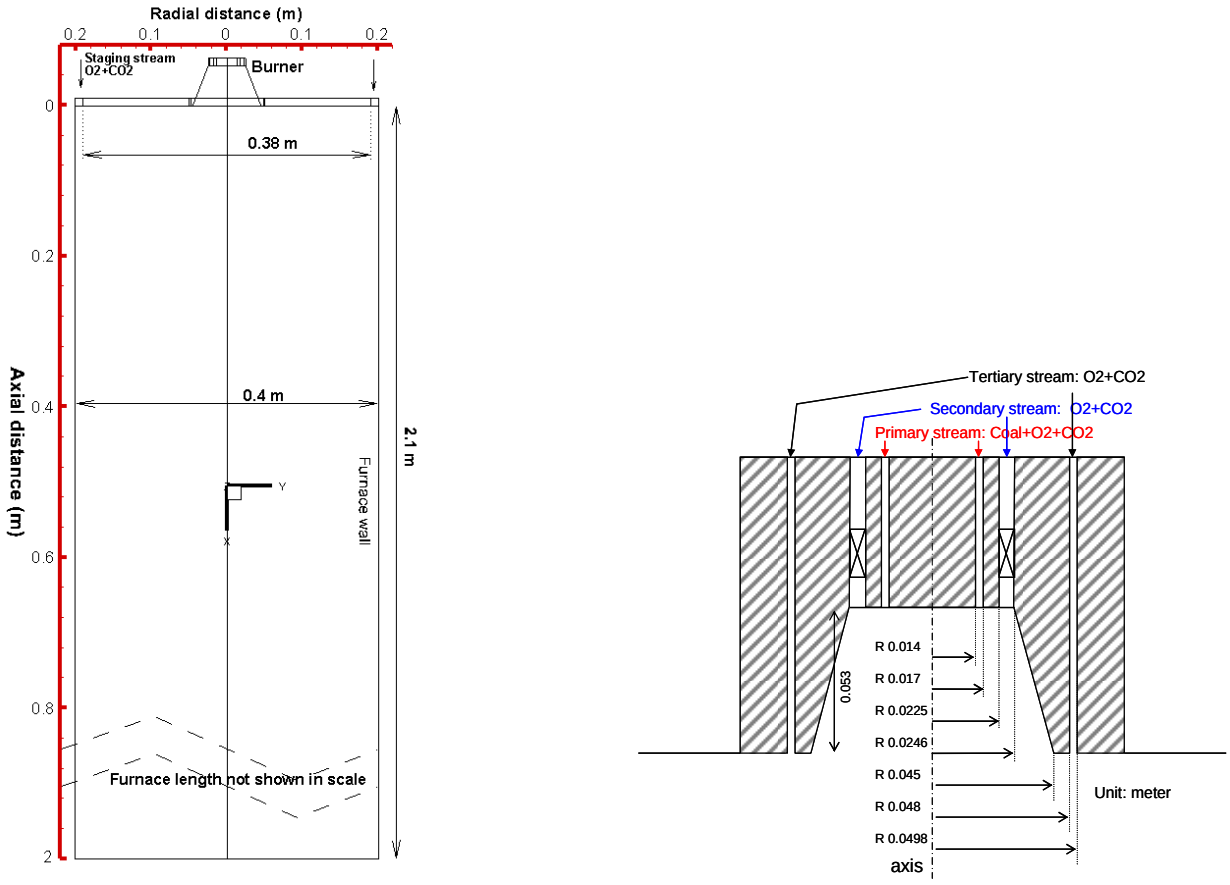

Figure 3-1. The geometry of (a) RWTH Aachen University 100 kW_{th} test facility and (b) swirl burner, in meter. The mass flow rate, composition and temperature of the burner streams are summarized in Table 3-1.

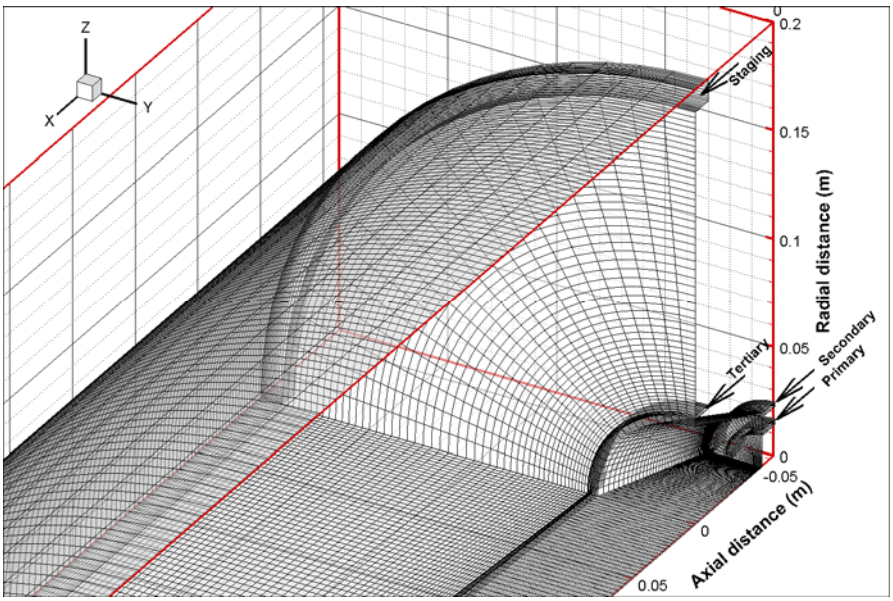

Figure 3-2. The three-dimensional mesh for RWTH Aachen' 100 kW_{th} oxyfuel combustion test facility. Figure shows only the part in the vicinity of the burner.

Based on the burner and the furnace geometry, a three-dimensional mesh was generated for one quadrant taking advantage of the axisymmetric character of the furnace and burner. Figure 3-2 shows part of the mesh where local refinement was used to improve the resolution near the burner. The mesh consists of 383,420 cells, and only hexahedron cells are used in order to minimize numerical diffusion. A mesh-independent study was performed by comparing the RANS simulation results with those obtained from a finer two-dimensional axisymmetric mesh consisting of 24,000 quadrangular cells, and those from another three-dimensional mesh consisting of 590,800 cells. The differences of the predicted velocity and species concentrations between these meshes were negligible.

3.2.2. Operating Conditions and Measurement Techniques

In the RWTH Aachen University oxyfuel combustion experiment, the oxidizer mixture was provided by a gas mixing unit instead of flue gas recycle. The compositions and mass flow rates of the four streams are shown in Table 3-1. The overall oxygen/fuel ratio described by the stoichiometry value

($\frac{\text{oxygen/fuel}}{(\text{oxygen/fuel})_{st}}$) was 1.3 while the local stoichiometry value at the burner (with oxygen provided by primary, secondary and tertiary streams only) was set to 0.6, the remaining oxidizer mixture was injected through the staging stream. A pre-dried Rhenish lignite coal was used in the experiment, and its properties are shown in Table 3-2. The experimentally tested particle size distribution (PSD) of the pulverized lignite coal is shown in Figure 3-3. This PSD is represented using 6400 particles with a size range of 5-100 μm in the CFD simulations. The 6400 particles follow a Rosin-Rammler distribution with a mean diameter of 35.2 μm and spread parameter of 1.218, that are least-square regressed from the experimental measurement.

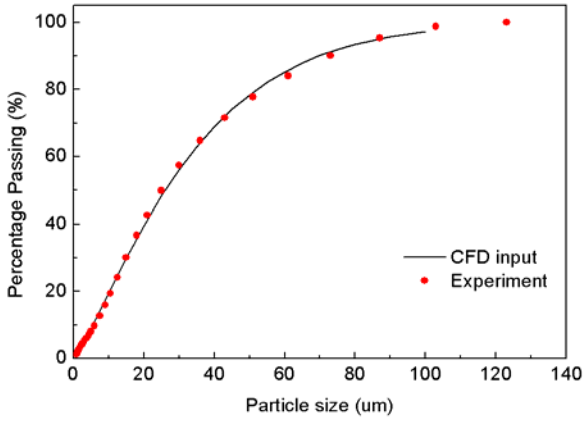

Figure 3-3. The particle size distribution of the coal used in experiment and CFD simulations.

Table 3-1. The operating conditions of the oxy-coal combustion experiment at RWTH Aachen University.

	Mass flow rate kg/h	O_2 content vol%	CO_2 content vol%	Temperature ^oC
Coal	6.5			
Primary stream	17.6	19	81	40
Secondary stream	26.6	21	79	60
Tertiary stream	1.5	21	79	60
Staging stream	54.9	21	79	900

Table 3-2. The proximate and ultimate analysis of the Rhenish lignite used in the RWTH Aachen University experiments.

	As received	Dry	DAF
Proximate Analysis (wt%)			
Water	8.40		
Ash	4.10	4.48	
Volatiles	46.60	50.87	53.26
Char	40.90	44.65	46.74
Ultimate Analysis (wt%)			
Water	8.40		
Ash	4.10	4.48	
Carbon	67.40	73.58	77.03
Hydrogen	4.24	4.63	4.85
Oxygen	14.70	16.05	16.80
Nitrogen	0.86	0.94	0.98
Sulfur	0.30	0.33	0.34

Multiple techniques were used in order to measure the velocity, gas and particle temperature, as well as the gas composition during the experiments. Laser Doppler anemometry (LDA) was applied for the nonintrusive measurements of the axial and tangential velocities. Coal and ash particles in the coal flame were used as tracers, with the assumption that the slip velocity between the particles and the gas was negligible for the small coal particles used in the experiment ($D_{p90} < 75$ μm). Gas samples were collected using a water-cooled suction probe with a ceramic tip, and the concentration of oxygen was measured by a magnetomechanical analyzer. The gas temperature was measured using a PtRh/Pt thermocouple mounted within a ceramic tip ($D_{outer} = 27$ mm) of a water-cooled stainless steel traversable suction probe, while the particle temperature was measured by a two-color pyrometer. The reader is referred to [133] for more detail on the measurement techniques and processes.

3.3. Modeling Approaches

This section briefly introduces the approaches and sub-models used in the CFD simulations, including the turbulence sub-models in RANS and LES, the combustion models for coal and gas phase reactions, as well as the modified sub-models for radiative heat transfer.

3.3.1. Modeling Turbulence: RANS Simulation

In variable-density problems such as compressible flows and reacting flows, the Favre-averaged Navier-Stokes equations are solved. Taking density weighted time average of the instantaneous continuity and momentum equations, we obtain the Favre-averaged Navier-Stokes equations as:

$$\frac{\partial \overline{\rho}}{\partial t} + \frac{\partial}{\partial x_i}\left(\overline{\rho}\tilde{u}_i\right) = 0 \tag{3.1}$$

$$\frac{\partial}{\partial t}\left(\overline{\rho}\tilde{u}_i\right) + \frac{\partial}{\partial x_j}\left(\overline{\rho}\tilde{u}_i\tilde{u}_j\right) = -\frac{\partial \overline{p}}{\partial x_i} + \frac{\partial}{\partial x_j}\left[\mu\left(\frac{\partial \tilde{u}_i}{\partial x_j} + \frac{\partial \tilde{u}_j}{\partial x_i} - \frac{2}{3}\delta_{ij}\frac{\partial \tilde{u}_k}{\partial x_k}\right)\right] + \frac{\partial}{\partial x_j}\left(-\overline{\rho u_i' u_j'}\right) \tag{3.2}$$

where $\tilde{u}_i$, $\tilde{u}_j$, $\tilde{u}_k$ are the Favre-averaged velocity components, and u_i' and u_j' are their fluctuations in the Cartesian coordinate, $\overline{\rho}$ and $\overline{p}$ are the standard time-averaged density and statistic pressure, and μ is the molecular viscosity of the fluid.

The Reynolds stresses $-\overline{\rho u_i' u_i'}$ are unknown. In turbulent-viscosity models, such as the $k-\varepsilon$ and the $k-\omega$ model, the Reynolds stresses are related to the mean velocity gradients and turbulent viscosity, μ_t, using the Boussinesq hypothesis:

$$-\overline{\rho u_i' u_j'} \approx \mu_t\left(\frac{\partial \tilde{u}_i}{\partial x_j} + \frac{\partial \tilde{u}_j}{\partial x_i} - \frac{2}{3}\delta_{ij}\frac{\partial \tilde{u}_k}{\partial x_k}\right) - \frac{2}{3}\overline{\rho}k\delta_{ij} \tag{3.3}$$

In the standard $k-\varepsilon$ model [169], the turbulent viscosity, μ_t, is modeled as a function of the turbulent kinetic energy, k, and its dissipation rate, ε:

$$\mu_t = \overline{\rho} C_\mu \frac{k^2}{\varepsilon} \tag{3.4}$$

which are obtained by solving two transport equations:

$$\frac{\partial}{\partial t}\left(\overline{\rho}k\right) + \frac{\partial}{\partial x_i}\left(\overline{\rho}k\tilde{u}_i\right) = \frac{\partial}{\partial x_j}\left[\left(\mu + \frac{\mu_t}{\sigma_k}\right)\frac{\partial k}{\partial x_j}\right] + G_k + G_b - \rho\varepsilon - Y_M \tag{3.5}$$

$$\frac{\partial}{\partial t}(\bar{\rho}\varepsilon)+\frac{\partial}{\partial x_i}(\bar{\rho}\varepsilon\tilde{u}_i)=\frac{\partial}{\partial x_j}\left[\left(\mu+\frac{\mu_t}{\sigma_\varepsilon}\right)\frac{\partial \varepsilon}{\partial x_j}\right]+C_{1\varepsilon}\frac{\varepsilon}{k}(G_k+C_{3\varepsilon}G_b)-C_{2\varepsilon}\bar{\rho}\frac{\varepsilon^2}{k} \tag{3.6}$$

where G_k and G_b are the generation of turbulence kinetic energy due to the mean velocity gradients and buoyancy, respectively; Y_M represents the contribution of the fluctuating dilatation in compressible turbulence to the overall dissipation rate; σ_k and σ_ε are the turbulent Prandtl numbers for k and ε; $C_{1\varepsilon}$, $C_{2\varepsilon}$, $C_{3\varepsilon}$, C_μ, σ_k, σ_ε are default model constants. The RNG $k-\varepsilon$ model [170] has a similar transport equation form for k and ε, but it includes the effect of swirl on turbulence.

In the $k-\omega$ model [179], the turbulent viscosity is computed as a function of k and the specific dissipation rate $\omega \equiv \frac{\varepsilon}{k}$:

$$\mu_t=\alpha^*\frac{\bar{\rho}k}{\omega} \tag{3.7}$$

and again k and ω are obtained from two transport equations:

$$\frac{\partial}{\partial t}(\bar{\rho}k)+\frac{\partial}{\partial x_i}(\bar{\rho}k\tilde{u}_i)=\frac{\partial}{\partial x_j}\left[\left(\mu+\frac{\mu_t}{\sigma_k}\right)\frac{\partial k}{\partial x_j}\right]+G_k-Y_k \tag{3.8}$$

$$\frac{\partial}{\partial t}(\bar{\rho}\omega)+\frac{\partial}{\partial x_i}(\bar{\rho}\omega\tilde{u}_i)=\frac{\partial}{\partial x_j}\left[\left(\mu+\frac{\mu_t}{\sigma_\omega}\right)\frac{\partial \omega}{\partial x_j}\right]+G_\omega-Y_\omega \tag{3.9}$$

where a^* is the damping coefficient for turbulent viscosity, G_k and G_ω are the generation of k and ω, while Y_k and Y_ω represent the dissipation of k and ω due to turbulences. The SST $k-\omega$ model [180] retains the $k-\omega$ model formulation in the near-wall region and switches to the standard $k-\varepsilon$ model in the far field region using an appropriate blending function and a "cross-diffusion" term. The modification makes the SST model more accurate in adverse pressure gradient flows and swirling flows [174].

3.3.2. Modeling Turbulence: Large Eddy Simulation

Different from the RANS approach in which turbulence is modeled at all scales, in LES, the time-dependent Navier-Stokes equations are filtered in physical or wave-number space. Therefore, in principle, the large eddies that transport most of the momentum, mass and energy, are directly resolved, while the small subgrid-scale eddies that dissipate energy are modeled [181]. A filtered variable is defined by:

$$\overline{\phi}(x) = \int_D \phi(x') G(x, x') dx' \tag{3.10}$$

where D is the fluid domain and G is the filter function that determines the scale of the resolved eddies. The filter function is applied in the finite-volume discretization scheme:

$$G(x, x') = \begin{cases} 1/V, & x' \in \nu \\ 0, & x' \notin \nu \end{cases} \tag{3.11}$$

where ν is the computational cell, and V is the volume of the cell. The filtered variable becomes:

$$\overline{\phi}(x) = \frac{1}{V} \int_\nu \phi(x') dx', \; x' \in \nu \tag{3.12}$$

The Favre-filtered Navier-Stokes equations are :

$$\frac{\partial \overline{\rho}}{\partial t} + \frac{\partial}{\partial x_i}\left(\overline{\rho} \tilde{u}_i\right) = 0 \tag{3.13}$$

$$\frac{\partial}{\partial t}\left(\overline{\rho} \tilde{u}_i\right) + \frac{\partial}{\partial x_j}\left(\overline{\rho} \tilde{u}_i \tilde{u}_j\right) = -\frac{\partial \overline{p}}{\partial x_i} + \frac{\partial}{\partial x_j}\left[\mu\left(\frac{\partial \tilde{u}_i}{\partial x_j} + \frac{\partial \tilde{u}_j}{\partial x_i} - \frac{2}{3}\delta_{ij}\frac{\partial \tilde{u}_k}{\partial x_k}\right)\right] - \frac{\partial \tilde{\tau}_{ij}}{\partial x_j} \tag{3.14}$$

The over bar and tilde in the variables represent standard-filtered and Favre-filtered value, respectively. The subgrid-scale stress, $\tilde{\tau}_{ij}$, is defined by:

$$\tilde{\tau}_{ij} \equiv \overline{\rho}\left(\widetilde{u_i u_j} - \tilde{u}_i \tilde{u}_j\right) \tag{3.15}$$

Similar to the RANS model, the subgrid-scale turbulent stresses are assumed to have the form:

$$\tilde{\tau}_{ij} = \frac{1}{3}\tilde{\tau}_{kk}\delta_{ij} - 2\mu_t \hat{S}_{ij} \tag{3.16}$$

where $\tilde{\tau}_{kk}$ is the isotropic part of the subgrid-scale stresses, $\hat{S}_{ij}$ is the rate-of-strain tensor for the resolved scale defined by:

$$\hat{S}_{ij} \equiv \frac{1}{2}\left(\frac{\partial \tilde{u}_i}{\partial x_j} + \frac{\partial \tilde{u}_j}{\partial x_i} \right) \tag{3.17}$$

The subgrid-scale turbulent viscosity μ_t is modeled using the Smagorinsky-Lilly model [182], in which the eddy-viscosity is computed from:

$$\mu_t = \bar{\rho} L_s^2 \left| \hat{S} \right| \tag{3.18}$$

where $\left| \hat{S} \right| \equiv \sqrt{2\hat{S}_{ij}\hat{S}_{ij}}$ and L_s is the mixing length for subgrid scales calculated from:

$$L_s = \min\left(\kappa d, C_s \Delta \right) \tag{3.19}$$

where κ is the von Kármán constant, d is the distance to the closest wall, C_s is the Smagorinsky constant and Δ is the local grid scale defined as $V^{1/3}$ [181]. It is also assumed that the centroid of the wall-adjacent cell falls within the logarithmic region of the boundary layer, and the law-of-the-wall is employed as the near-wall treatment.

Since the LES approach resolves the evolution of the large scale eddies, it is believed to be more accurate. However, it requires refined time and space discretization and involves significantly higher computational cost.

3.3.3. Coal Combustion Sub-Models

Pulverized coal combustion is modeled as a dilute two-phase (solid-gas) reacting flow using an Eulerian-Lagrangian approach. The mass, momentum and energy interactions between the gas phase and the solid particles are calculated using the "particle-source-in-cell" method [144] while updating the particle state along a set of particle trajectories. In total, 6400 particle representing 20 sizes between 5-100 μm were tracked in the simulations starting at the primary stream inlet of the burner. No

apparent changes can be observed when the number of tracked particles was doubled or halved. The particle size follows the Rosin-Rammler distribution shown in Figure 3-3.

3.3.3.1. Modeling Coal Devolatilization

The single kinetic rate devolatilization model was used to describe the thermal decomposition rate of dry coal particles:

$$-\frac{dm_p}{dt} = k\left[m_p - \left(1-f_{v,0}\right)\left(1-f_{w,0}\right)m_{p,0}\right] \quad (3.20)$$

where m_p and $m_{p,0}$ are the current and initial particle mass, $f_{v,0}$ is the mass fraction of volatiles on a dry basis, and $f_{w,0}$ is the mass fraction of moisture initially present in the coal particle as received, respectively. The rate constant, k, is given by

$$k = Ae^{-\left(E/R_u T_p\right)} \quad (3.21)$$

where $R_u = 8314\, J/\left(kmol \cdot K\right)$ is the ideal gas constant, T_p is the particle temperature. Since the devolatilization kinetics data for this lignite coal are not provided in the experimental study, kinetics parameters were taken from the literature. The activation energy, E, was taken from Badzioch and Hawksley [47] ($E = 4.64e7$ J/kmol) and the pre-exponential factor, A, was taken to be 20,000 as suggested by Al-Abbas et al. [172].

3.3.3.2. Modeling Oxy-Char Combustion

Char combustion in a CO_2 rich environment has been investigated in recent years. Bejarano and Levendis [110], and Shaddix and Molina [103] found that, when the oxygen concentrations in the gas are the same, the char burning temperatures are lower, and burnout times are longer under O_2/CO_2 conditions than in O_2/N_2. Using a detailed single particle combustion model, Shaddix and co-workers discussed the effect of CO_2 on oxy-char combustion and attributed the differences to CO_2's distinct

physical properties, such as the diffusivity and volumetric heat capacity, as well as the char-CO_2 and char-H_2O gasification reactions [112, 157]. The different physical properties and chemical effects of CO_2 should be considered when modeling oxy-char burning process in CFD simulations.

In conventional air-fired combustion, the Single-Film Model (SFM) is appropriate for the burning of char with typical pulverized coal particle sizes. Mitchell et al. [153] modeled the CO oxidation process in the coal particle boundary layer and suggested that little CO_2 is formed in the boundary layer when the char diameter is smaller than 100 μm. For oxy-fuel combustion, Chen et al. [22] showed that the SFM along with appropriate diffusivity can capture the trends of lower char temperature and reaction rates in oxy-char combustion. Hecht et al. [157] found that the SFM is adequate for the simulation of a 130 μm diameter particle burning when oxygen mole fraction is below 12%. These facts warrant the applicability of SFM for the size range of pulverized coal combustion in the present study.

On the other hand, gasification reactions may play a role in determining the char particle temperature and burning rate. The char-CO_2 gasification reaction may enhance the overall char consumption rate for oxygen concentrations up to 24%, while it reduces the overall consumption rate in environments with greater than 24% oxygen due to the endothermicity of the gasification reaction [157]. In this study, three heterogeneous reactions are considered on the char external surface:

$$2C(s)+O_2 \rightarrow 2CO \qquad (3.22)$$

$$C(s)+CO_2 \rightarrow 2CO \qquad (3.23)$$

$$C(s)+H_2O \rightarrow CO+H_2 \qquad (3.24)$$

In the oxidation reaction (Equation (3.22)), only CO is considered as the combustion product, which diffuses away from the char surface and reacts with oxygen to form carbon dioxide in the computational cell. This assumption is valid because the CO_2/CO ratio formed by the heterogeneous reaction on the char surface is less than 0.1 at normal combustion temperatures [155].

The char reaction rate, $\dot{m}_{p,i}$, by heterogeneous reaction i depends on the external diffusion rate, D_i, and the surface reaction kinetic rate, R_i:

$$\dot{m}_{p,i} = -A_p p_i \frac{D_i R_i}{D_i + R_i} \tag{3.25}$$

where A_p is the external surface area of the char particle, p_i is the partial pressure of species i in the bulk gas. The kinetic rate of the char external surface reactions, R_i, is represented in an Arrhenius form:

$$R_i = A_i T_p^{\beta_i} \exp\left[\frac{-E_i}{R_u T_p}\right] \tag{3.26}$$

where the kinetics parameters were taken from empirical data for low-rank coal char in references [133, 183, 184]. Diffusion often controls the char-O_2 reaction rate at high temperatures. Following the approach described in [159], the mass transfer limited reaction rate, D_i, can be expressed as:

$$D_i = C_i \frac{\left[\left(T_p + T_\infty\right)/2\right]^{0.75}}{d_p} \tag{3.27}$$

where T_∞ is the gas temperature in the cell, d_p is the particle diameter. C_i is the mass diffusion limited constant expressed as a function of the binary diffusivity, heterogeneous reaction stoichiometric coefficients, as well as the operating pressure [22]:

$$C_i = \nu_i MW_c \cdot \frac{1}{R_u T_0^{1.75}} \cdot Sh \cdot DF_{i,0} \frac{P_0}{P} \tag{3.28}$$

where ν_i is the stoichiometric coefficient of carbon relative to the gas phase reactant *i* in the oxidation and gasification reactions (Equation (3.22)-(3.24)); MW_c is the molecular weights of carbon. T_0 and P_0 are the reference temperature and pressure for the binary diffusivity $DF_{i,0}$. P is the operating

pressure of the furnace. R_u is the gas constant, and Sh is the Sherwood number. The oxy-char sub-model is implemented into the CFD code in the form of a User Defined Function (UDF). The parameters and coefficients used for the heterogeneous reactions are listed in Table 3-3.

Table 3-3. The kinetics parameters and diffusion coefficients for the oxy-char surface reactions.

Reaction	A_i $kg/(m^2 sPa)$	E_i kJ/mol	β_i	C_i $s/K^{0.75}$	Ref.
Equation (3.22)	0.005	74	0	4.41×10^{-12}	[133, 156]
Equation (3.23)	0.00635	162	0	2.47×10^{-12}	[133, 184]
Equation (3.24)	0.00192	147	0	2.47×10^{-12}	

3.3.4. Modeling Gas Phase Reaction

In the flame zone, gas phase reactions are mostly limited by the extent of mixing, because the turbulent mixing rate is generally slower than the kinetic rate. The eddy dissipation model (EDM) [163, 164] was used in this study, in which the chemical reaction is governed by the large-eddy mixing time scale, k/ε, proposed by Spalding [164]. Based on the assumption that the reaction rate is limited by both the mixing of the reactants and the heating of the reactants through the mixing with the products, the net rate of production of species i due to reaction r, $R_{i,r}$, is given by the smaller of the reactant mixing rate (first term) and product mixing rate (second term):

$$R_{i,r} = \min \begin{pmatrix} \nu'_{i,r} M_{w,i} A \rho \dfrac{\varepsilon}{k} \min\limits_R \left(\dfrac{Y_R}{\nu'_{R,r} M_{w,R}} \right), \\ \nu'_{i,r} M_{w,i} AB \rho \dfrac{\varepsilon}{k} \dfrac{\sum_P Y_P}{\sum_j^N \nu''_{j,r} M_{w,j}} \end{pmatrix} \quad (3.29)$$

where $\nu'_{i,r}$ and $\nu''_{j,r}$ are the stoichiometric coefficient for reactant i and product j in reaction r, M_w is the molecular weight, Y_R and Y_P are mass fraction of any reactant and product species,

respectively. $A = 4.0$ and $B = 0.5$ are empirical model constants.

Three gas phase reactions were considered:

$$\text{volatile} + \nu_1 O_2 \rightarrow \nu_2 CO + \nu_3 H_2O + \nu_4 N_2 + \nu_5 SO_2 \quad (3.30)$$

$$CO + 0.5O_2 \rightarrow CO_2 \quad (3.31)$$

$$H_2 + 0.5O_2 \rightarrow H_2O \quad (3.32)$$

taking the burning of volatiles, carbon monoxide and hydrogen into account. The coefficients ν_i in reaction (3.30) are calculated using the coal proximate and ultimate analysis data in Table 3-2 according to mass and element balance. It should be noted that the EDM does not incorporate finite rate kinetics. Therefore, this model can only be used to predict the major products species for stable diffusion flames in which the reaction rates are controlled by turbulent mixing. Since the simplified gas phase reaction scheme in reaction (3.30)-(3.32) could not reflect the chemical effect of CO_2 on hydrocarbon oxidation [124, 135], it should not be expected to show accurate prediction of intermediate species such as CO and H_2 in oxy-fuel combustion. Validation of the reaction mechanisms for oxy-fuel combustion remains a subject of investigation.

3.3.5. Modeling Radiative Heat Transfer in Oxy-Fuel Combustion

Radiation dominates the heat transfer in the combustion environment, especially within the flame zone, and it is modeled by solving the radiative transfer equation (RTE). The RTE at position $\vec{r}$ in the direction $\vec{s}$ takes the form [146]:

$$\frac{dI_\lambda(\vec{r},\vec{s})}{ds} = \kappa_\lambda n^2 I_{b,\lambda} - (\kappa_\lambda + \sigma_{s,\lambda}) I_\lambda(\vec{r},\vec{s}) + \frac{\sigma_{s,\lambda}}{4\pi}\int_0^{4\pi} I_\lambda(\vec{r},\vec{s}')\Phi(\vec{s}\cdot\vec{s}')\,d\Omega' \quad (3.33)$$

where s is the path length, κ is the absorption coefficient, σ_s is the scattering coefficient, n is the refractive index, and $I_\lambda(\vec{r},\vec{s})$ is the spectral radiation intensity which is dependent on position $\vec{r}$ and direction $\vec{s}$.

Thermal radiation is directional in the wavenumber space. In this study, the Discrete Ordinates (DO) model [185, 186] is used to solve the RTE. Each octant of the angular space 4π is discretized into 3×3 solid angles, and a total of 72 RTE equations are solved in the three dimensional space. It is computationally expensive to solve radiative heat transfer in each wavelength band, and gray gas models such as the weighted-sum-of-gray-gas model (WSGGM) [187] are used to calculate the absorption coefficient of the participating gas mixture. In WSGGM, the absorption coefficient of the gas mixture is assumed to be the weighted-average of several (3 or 4) gray gases and a transparent gas, therefore it is a function of the H_2O and CO_2 concentrations and gas temperature. The model coefficients are derived from experimental data for oil and methane stoichiometric combustion, in which the CO_2 partial pressure is around 0.1 atm, and the partial pressure ratio of H_2O and CO_2 is in the range of 1 to 2, with a path length of less than 10 m [148]. However, it is worth noting that the CO_2 and H_2O partial pressures and their relative ratio in oxy-coal combustion are not within the applicable range. Johansson et al. [151] modified the coefficients of the three gray-one clear gases model by fitting the emissivity to a Statistical Narrow Band (SNB) model. The new parameters are applicable under oxy-fuel conditions with dry or wet flue gas recycle in the temperature range of 500-2500 K and for path lengths between 0.01 and 60 m. Similar to the method in reference [188], the modified WSGGM was implemented in the CFD simulation in the form of UDF. In the modified three gray-one clear WSGGM, the Planck-mean absorption coefficient of the gas mixture over a path length, s, is determined by:

$$\bar{a} = -\ln\left(1-\varepsilon\right)/s \tag{3.34}$$

where s is the radiation beam length, and ε, the gas emissivity. The former is estimated to be ~0.6 m based on an average dimension of the furnace domain; while the latter is calculated from:

$$\varepsilon = \sum_i a_{\varepsilon,i}\left(T\right)\left(1-\exp\left(-\kappa_i p_i s\right)\right) \tag{3.35}$$

where $a_{\varepsilon,i}$ is the emissivity weighting factor for gray gas i, κ_i and p_i are the pressure absorption

coefficient ($\frac{1}{\text{Pa}\cdot\text{m}}$) and partial pressure ($\text{Pa}$) of the absorbing gas i, respectively. The emissivity weight factors $a_{\varepsilon,i}$ used in the previous equation (2.6) are polynomial correlations which are given as a function of the gas temperature:

$$a_{\varepsilon,i} = \sum_j b_{\varepsilon,i,j} \left(\frac{T}{T_{ref}} \right)^{j-1} \tag{3.36}$$

where $T_{ref} = 1200$ K is a reference temperature. The coefficients of the polynomial correlations, $b_{\varepsilon,i,j}$, and the pressure absorption coefficients of the gray gas, κ_i, are summarized in Table 3-4.

Table 3-4. The coefficients used in the three gray-one clear gases WSGG model for oxy-fuel combustion, adapted from reference [151].

Gray gas i	$\kappa_i \times 10^5 \left(\frac{1}{\text{Pa}\cdot\text{m}} \right)$	$b_{\varepsilon,i,1}$	$b_{\varepsilon,i,2}$	$b_{\varepsilon,i,3}$
1	0.0992	0.4995	-000170	-0.0393
2	2.6589	0.3418	-0.1701	0.0196
3	88.1078	0.1273	-0.0726	0.0101

Moreover, the contribution of the particles (coal, char and ash) to the radiative heat transfer is also considered by modeling its absorption and scattering coefficient in the RTE.

3.3.6. Boundary Conditions

Mass flow rate boundary conditions are used for the burner inlets, i.e., the primary, secondary, tertiary and staging streams. The pressure outlet boundary condition is used at the furnace outlets. Measured wall temperatures are used for all the thermal boundary conditions in the simulation. Temperature ($T_{wall} = 1000$ ^{o}C) and heat flux ($q'' = 0$) thermal boundary conditions are used for the furnace wall and burner surfaces, respectively, with emissivity of 0.7 and 0.2 as suggested in the experimental study [172].

3.3.7. Solution Strategy

FLUENT 12.1 was used as the computation platform for this CFD study. For the RANS simulation, the three-dimensional pressure-based solver with double precision was chosen to solve the steady-state governing equations. Second-order upwind scheme is used for the momentum, species transport, energy and radiation equations. A converged solution was obtained for the cold flowfield with species transport after about 5000 iteration steps, and the Lagrangian tracking of coal particles, gas phase reactions and radiative heat transfer sub-models were added to the system of equations. Converged solutions for the reacting flow were obtained after about 50,000 iteration steps. The RANS simulations were performed on the Pharos computing cluster of MIT, using 8 parallel AMD Magny-Cours 12-core 2.2 GHz processor cores. It takes about 90 hours clock time for each of the RANS simulation until convergence is achieved.

In the LES, a second-order bounded central differencing scheme is applied to solve the momentum equation, and second-order upwind scheme is used for the species transport, energy and radiation equations. The time dependent terms are discretized using a second-order implicit scheme with an initial time step of 0.2×10^{-4} second, such a value guarantees that the Courant number is smaller than 1 in most of the computational cells. After obtaining a stable combustion field, the time step was increased to 1×10^{-4} second progressively. The LES starts with the converged RANS reacting flow solutions, and the unsteady calculation takes about 4-5 flow residence times, or about 1.5 second flow-time, to achieve fully developed reacting flow. The time-averaged statistics were obtained with another 0.5 second flow-time simulation. In general, for unsteady simulation of 1 second flow time, it takes about 300 hours clock time using 32 parallel processor cores on the same computing cluster.

3.4. Results and Discussions

In this section, the CFD predictions are compared with the measurements in the test facility, especially in the vicinity of the burner where oxygen and fuel particle mix and the volatiles flame is stabilized. In particular, the performance of the different RANS turbulence models and the LES are compared, and their impacts on the mixing and reaction processes are discussed.

(a) (b)

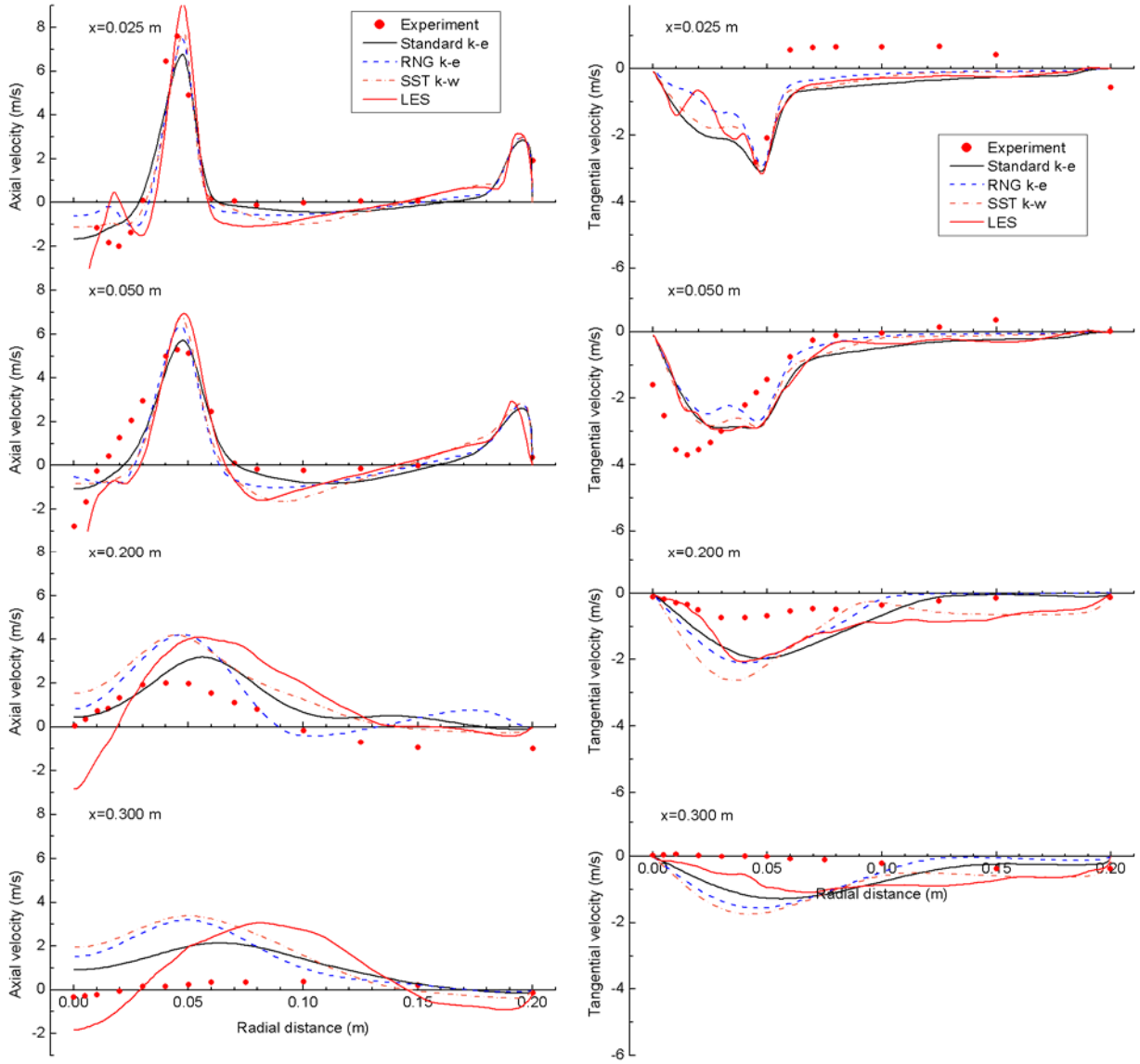

Figure 3-4. Comparison between the measured (scatters) and predicted (lines) velocity profiles at 0.025, 0.05, 0.2 and 0.3 m away from the burner outlet. (a) Axial velocity, and (b) tangential velocity.

3.4.1. Velocity Field

Figure 3-4 shows a comparison between the experimental measurements and the CFD simulations for the axial and tangential velocity profiles. In general, RANS and LES results capture the overall trends of the flowfield. However, they perform differently in terms of predicting the internal recirculation zone size and the mixing intensity between the burner streams and the staging stream. From Figure 3-4(a), it can be seen that all the turbulence models show an internal recirculation zone along the centerline downstream of the burner outlet, a positive axial velocity peak of 6-9 m/s at around 0.05 m in the radial direction, and an external recirculation zone at around 0.07-0.15 m in the radial direction. The swirling secondary burner stream is responsible for establishing the internal recirculation zone, along with the bluffbody and quarl geometries. Another axial velocity peak is observed near the outer diameter of the furnace where the staging stream is injected. In Figure 3-4(b), all the simulation models show that the peak tangential velocity is reached at the burner outlet, and this peak decays in both the axial and radial directions.

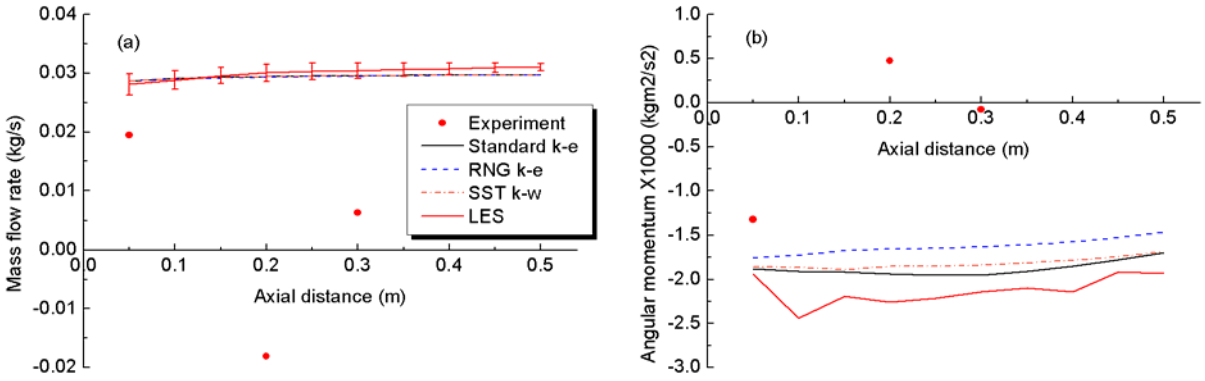

Figure 3-5. Comparison between the measured (scatters) and predicted (lines) gas phase mass flow rate and angular momentum along the axis: (a) mass flow rate in (kg/s), and (b) angular momentum in (kgm^2/s^2). The error bar with the LES results shows the velocity and density covariance term in mass flow rate calculation.

Discrepancies between the simulation and the measured results are found downstream, at 0.2 and 0.3 m away from the burner exit. The simulation results show higher axial and tangential velocity magnitudes than the experimental results. In order to identify a possible source of the discrepancy, we calculated the total gas mass flow rate and the total angular momentum in the experimental and simulation results. Figure 3-5 shows the measured and CFD calculated average gas phase mass flow rate, $\bar{\dot{m}}$, and angular momentum, $\bar{G}_\varphi$. For the experimental results, these quantities are defined as:

$$\bar{\dot{m}} = \int_0^R 2\pi r \bar{\rho}\bar{u} dr \tag{3.37}$$

$$\bar{G}_\varphi = \int_0^R 2\pi r \bar{\rho}\bar{u}\left(\bar{w}r\right) dr \tag{3.38}$$

where $\bar{u}$ and $\bar{w}$ are the measured mean axial and tangential velocity, respectively. Piecewise-polynomial representations of $\bar{u}$ and $\bar{w}$ were obtained by curve-fitting the measured mean velocity profiles in Figure 3-4. The gas density $\bar{\rho}$ is calculated using the measured mean gas temperature profiles (in Figure 3-9(b)) and the ideal gas state equation. The measured $\bar{\dot{m}}$ and $\bar{G}_\varphi$ were calculated by substituting the piecewise-polynomial curves and integrating Equation (3.37)-(3.38) at different axial locations. Similarly, the mass flow rate and angular momentum can also be integrated at different cross sections along the axis using the simulation results. We note that the mean mass flow rate contains a density-velocity covariance term due to turbulence,

$$\bar{\dot{m}} = \int_0^R 2\pi r \bar{\rho}\bar{u} dr + \int_0^R 2\pi r \overline{\rho' u'} dr \tag{3.39}$$

which is omitted in Equation (3.37). The magnitude of this covariance term was estimated using the LES results and shown in Figure 3-5. It is negligible comparing to the first term because of the stable combustion dynamics.

The comparison in Figure 3-5 indicates several points:

- Figure 3-5(a) shows that the measured mass flow rate downstream is significantly lower than the total burner mass flow rate, which is 0.028 kg/s. The measured mass flow rate at x=0.2 m is negative, which indicates that the measured positive velocity in the inner radial section was lower, or the measured negative velocity in the external recirculation section (0.1 m<R<0.2 m) was higher than the actual value. On the other hand, the simulation solution satisfies gas phase mass conservation, as well as the mass exchange from coal particle (combustibles) to the flue gas.
- Figure 3-5(b) shows that the measured angular momentum decays faster than the predicted results.

The low measured axial and tangential velocities in the downstream sections may be partially due to the fact that coal/char particles were used as trace particles in the experimental measurement. We also note that the measured tangential velocity at the axis 0.05 m away from the burner shows a non-zero value. According to the experimental study, this might be due to "the minor misalignment between the burner and the furnace axes, or the procedure for alignment of the optical axis of the LDA system with the burner axis"[133].

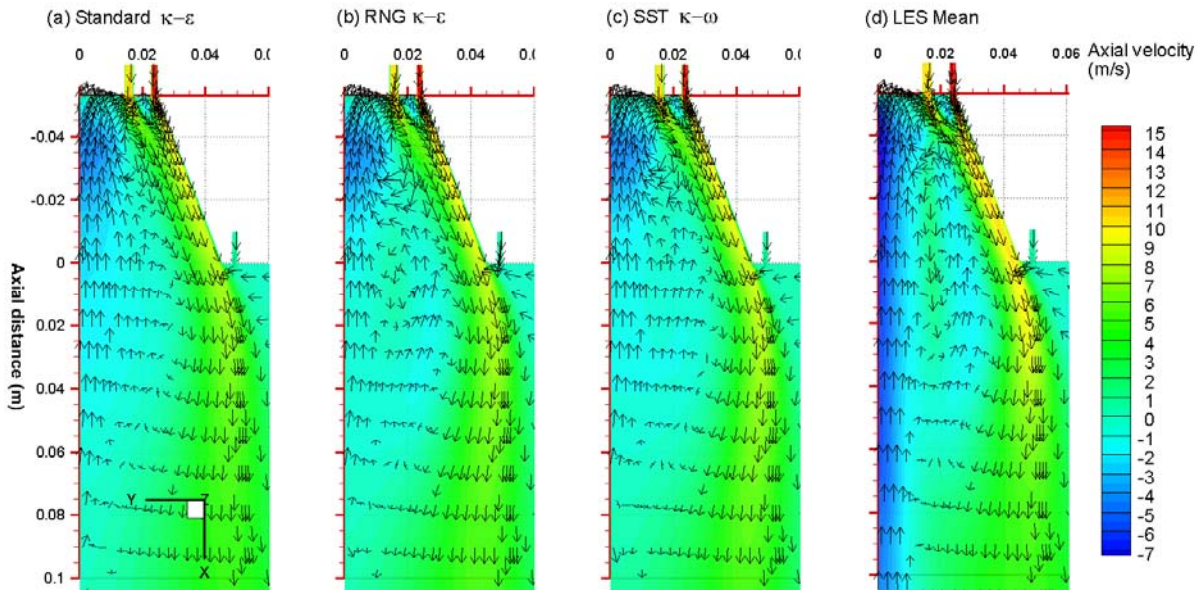

Figure 3-6. The predicted velocity distribution in the burner quarl using uniform vector length, colored by axial velocity. The results from (a) Standard $k-\varepsilon$ model, (b) RNG $k-\varepsilon$ model (c) SST $k-\omega$ model, and (d) LES

mean values, show different internal recirculation zone sizes and peak reverse velocity.

Although all the simulations show the same overall trends, the turbulence models perform differently with regard to the near-burner internal recirculation zone and its peak velocities, and the external recirculation zone.

- The internal recirculation zone: At 0.05 m away from the burner, LES reproduces the reverse velocity of about -3 m/s near the centerline (see Figure 3-4(a)), while the RANS simulations underestimate the peak reverse velocity. The experimental results at 0.3 m show that a reverse flow remains at the centerline, and only the LES can show this trend. It should be noted that the measured centerline axial velocity at x=0.2 m is inconsistent with the measurements upstream and downstream. As mentioned previously, the velocity profile at this cross section does not conserve the mass flow rate. Figure 3-6 shows the internal recirculation zones predicted by the different turbulence models. Again, all RANS models underestimate the internal recirculation zone size, while a significantly longer recirculation zone with higher reverse velocities is predicted by the LES. As a result, more hot gases are recirculated back to mix with the unburned burner stream and stabilize the coal flame in the quarl, which results in a higher turbulent mixing between the burner streams and the staging stream as will be shown later.
- The external recirculation zone: At x=0.2 m and x=0.3 m, the measured axial velocity shows negative values (see Figure 3-4(a)), indicating an external recirculation zone. Only the SST $k-\omega$ model and LES predict the external recirculation zone. This external recirculation zone is induced by the strong entrainment of the staging stream, and it has an impact on the oxygen distribution, which will be discussed in the next section.

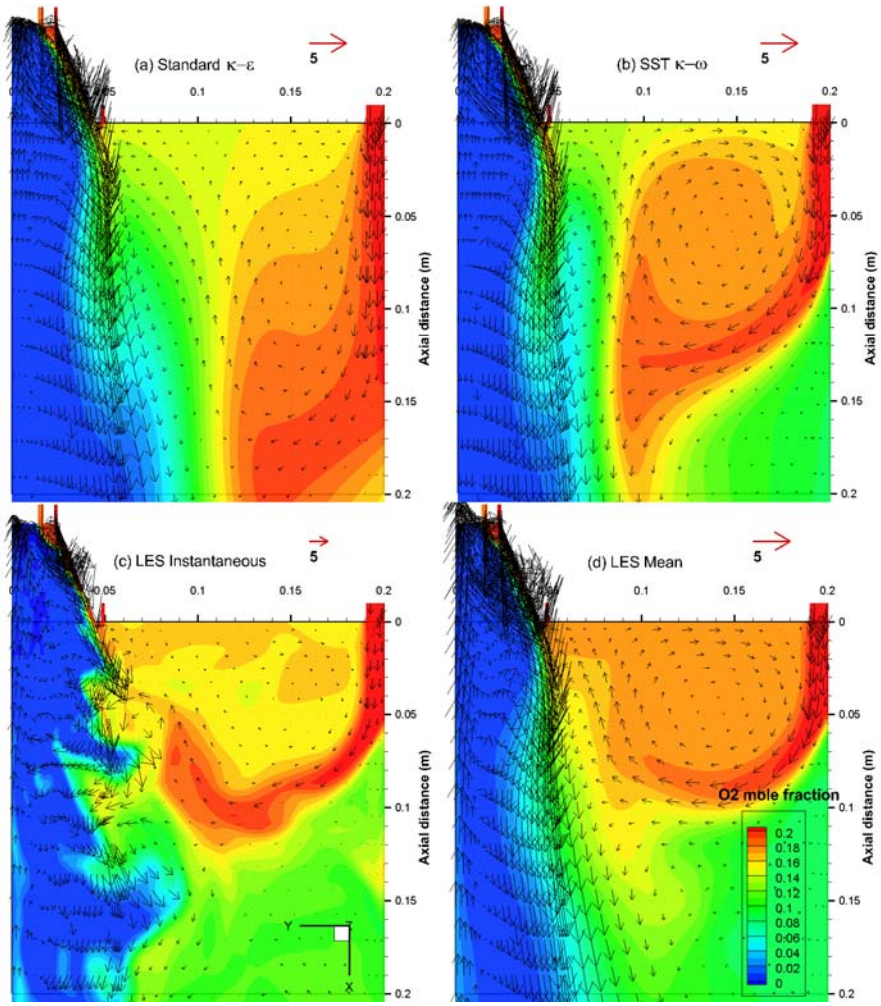

Figure 3-7. RANS and LES predicted velocity (scaled vector) and oxygen concentration (colored contour) distribution in the near-burner region, showing the mixing between the staging stream and the burner streams. The figures show the results from (a) Standard $k-\varepsilon$ model, (b) SST $k-\omega$ model, (c) LES in an instantaneous moment, and (d) LES mean values. Note that the LES instantaneous velocity vector scale is different from others because the instantaneous velocity magnitudes are larger than the mean values.

In general, the best match with the experimental results in terms of the velocity profiles is obtained using LES. Although the RNG $k-\varepsilon$ model accounts for the swirl effect in the turbulence viscosity calculation, it shows similar trends as those of the standard $k-\varepsilon$ model. The SST $k-\omega$ captures the external recirculation zone almost as close as the LES does, and it performs the best

among the RANS models.

3.4.2. Mixing and Oxygen Diffusion

The radial velocity profiles were not reported in the experimental study. These are, however, critical to the mixing between the burner streams and the staging stream. Figure 3-7 shows the predicted velocity and oxygen concentration distributions in the vicinity of the burner using the standard $k-\varepsilon$ model, SST $k-\omega$ model and LES. For the latter, both instantaneous results and time-averaged values are shown. The RNG $k-\varepsilon$ model results are similar to those obtained using the standard $k-\varepsilon$ model, therefore are not shown here. As discussed previously, an internal recirculation zone is predicted by both the RANS and LES approaches. However, significant differences can be observed in the entrainment of the staging stream and its mixing with the burner streams. In the standard and RNG $k-\varepsilon$ models (see Figure 3-7(a)), the staging stream flows parallel to the burner streams, while the SST $k-\omega$ model (see Figure 3-7(b)) predicts a different flow: the staging stream separates from the wall, forming a wall recirculation zone which results in a better mixing with the burner streams. The unsteady LES simulation (see Figure 3-7(c)) shows more detail regarding the turbulent structure and shear layer at the burner exit, where the staging stream is entrained into and mixes with the fuel-rich stream. In all the tested RANS turbulence models, only the SST $k-\omega$ model shows this mixing process as that observed in the LES time-averaged results (see Figure 3-7(d)).

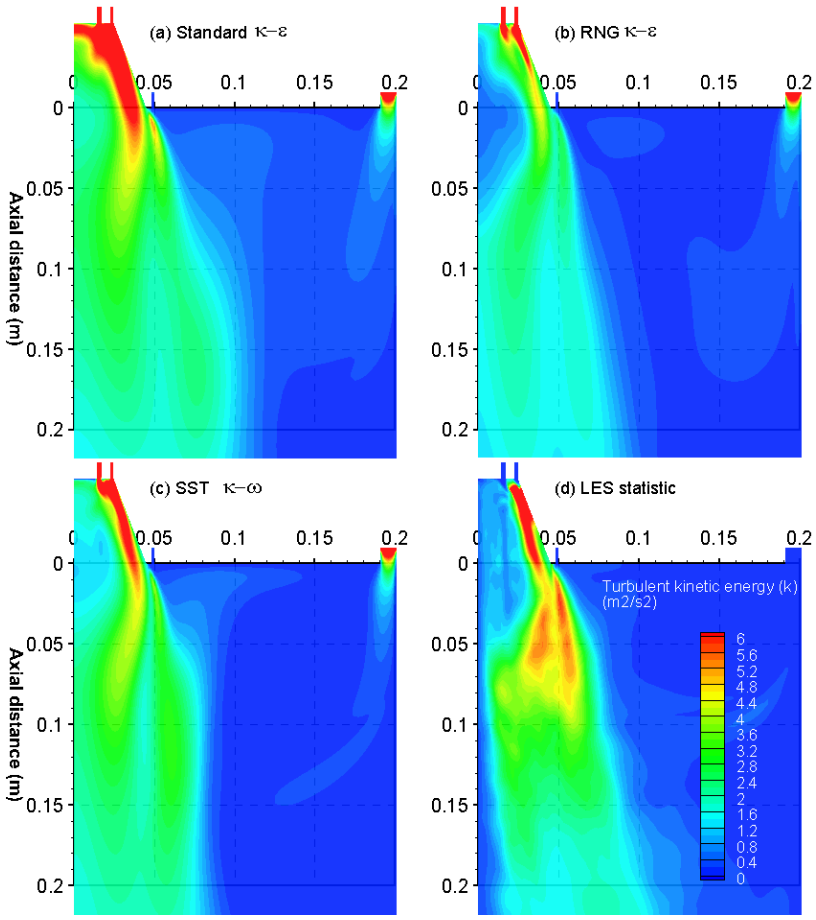

Figure 3-8. The predicted turbulent kinetic energy k in the near-burner region. The figures show the results from (a) Standard $k-\varepsilon$ model, (b) RNG $k-\varepsilon$ model, (c) SST $k-\omega$ model, and (d) LES statistic values.

Besides the mean velocity predictions, the other important quantity in turbulent flows is the velocity fluctuation, because of its role in mixing. Figure 3-8 compares the turbulent kinetic energy k predicted by the RANS and LES approaches. The turbulent kinetic energy is the mean kinetic energy per unit mass associated with the unsteadiness or the eddies in turbulent flow. It is defined as the square of the root-mean-square velocity fluctuations in three dimensions:

$$k = \frac{1}{2}\left(\overline{u_i'^2} + \overline{u_j'^2} + \overline{u_k'^2}\right) \qquad (3.40)$$

As discussed in section 3.3.1 and 3.3.2, in the RANS approaches, k is modeled using a transport equation; while in LES, the time dependent velocity is explicitly resolved, and k is calculated using the statistic results. Although all turbulence models show similar mean velocity profiles, they perform

differently in predicting the turbulence intensity. The turbulent kinetic energy predicted by the LES approach is marginally higher than those predicted by the RANS models in the burner exit region, indicating more intense turbulence and better mixing between the staging and the burner streams.

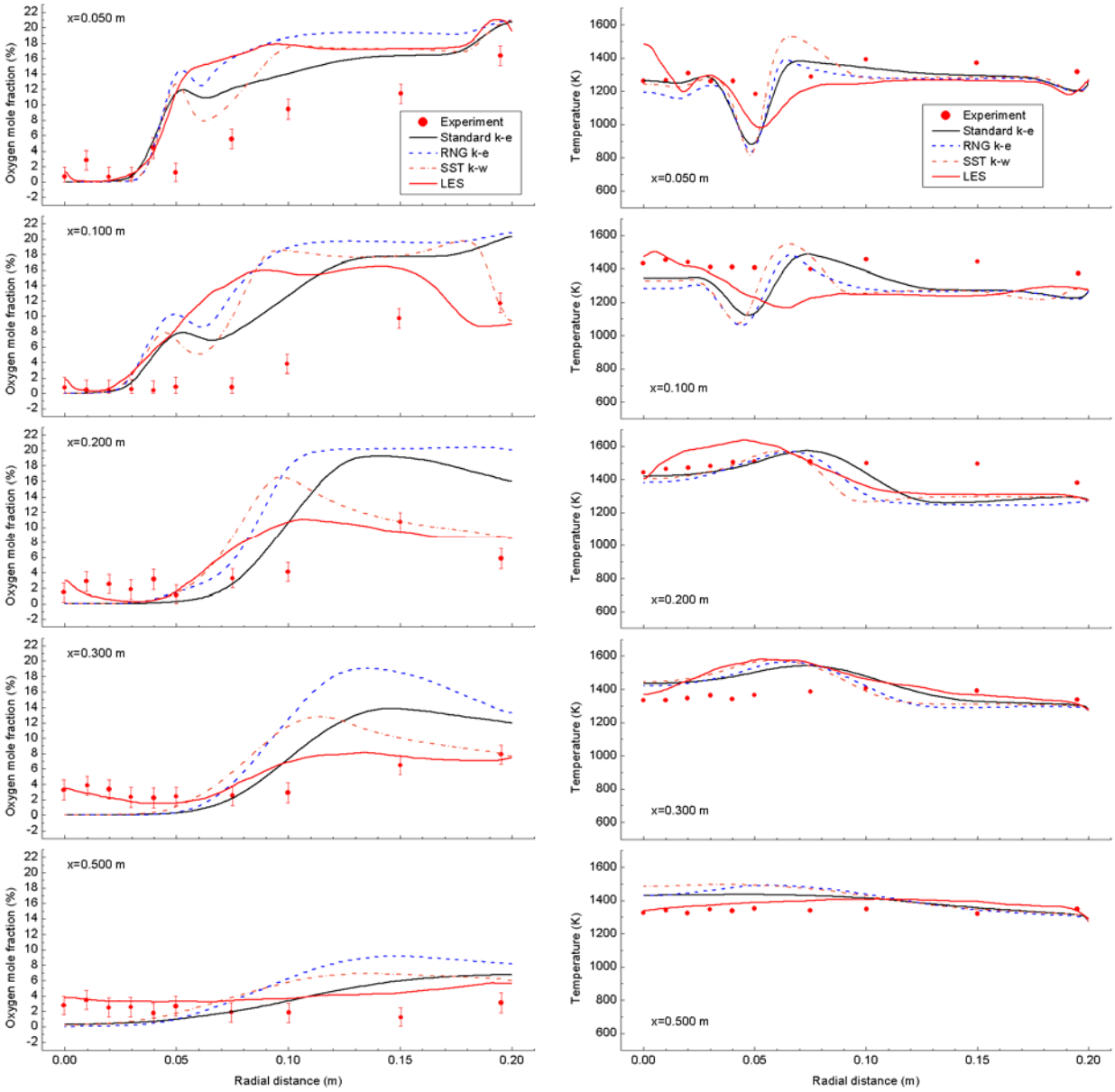

Figure 3-9. Comparison between the measured (scatters) and predicted (lines) oxygen mole fraction (left) and gas temperature (right) at 0.05, 0.1, 0.2, 0.3 and 0.5 m away from the burner. The error bar of the experimental results indicates two standard deviations.

Figure 3-9(a) shows the oxygen mole fraction profiles at 0.05, 0.1, 0.2, 0.3 and 0.5 m away from

the burner. As a result of the different predicted flowfield and mixing processes, significantly different oxygen mole fraction distributions are observed when applying different turbulence models. For instance, the oxygen concentrations in the standard and RNG $k-\varepsilon$ model deviate from the measured results significantly in the outer radial section, especially at 0.2 and 0.3 m away from the burner. The same results have also been reported in previous numerical studies using standard $k-\varepsilon$ model [133, 188]. The RNG $k-\varepsilon$ model predictions agree poorly with the measured results, since it under-predicts the turbulent intensity in this region, as shown in Figure 3-8. On the other hand, the SST $k-\omega$ model and LES show better match in these regions as they better predict the flowfield and the mixing process. Both the experimental and simulation results show low oxygen concentration near the axis, and higher oxygen mole fraction in the outer region. Recalling that the stoichiometry in the burner region is set to 0.6, low oxygen mole fraction near the axis should be expected in the fuel-rich zone. The remaining oxygen is supplied by the staging stream for char burning in the downstream, and that will be discussed in greater detail later.

In summary, we show that although similar mean axial and tangential velocity profiles are predicted by all the turbulence models, the standard and RNG $k-\varepsilon$ model fail to predict the burner streams turbulence intensity and its mixing with the staging stream in the burner exit region, thus underestimating the downstream oxygen diffusion process. To the contrary, the SST $k-\omega$ model and LES can capture the formation of the recirculation zones induced by the staging stream, and hence show better match with the experimental results.

3.4.3. Temperature Distribution

Figure 3-10 compares the predicted temperature distribution in the furnace using the standard $k-\varepsilon$ model, the SST $k-\omega$ model and LES. The results show similar trends but different flame lengths. The standard and RNG $k-\varepsilon$ models show longer flames because they underestimate the mixing of the staging stream. Although the SST $k-\omega$ model captures most of the average flow

structures, it still underestimates the turbulent intensities as discussed previously. Intense mixing and temperature fluctuations in the char combustion zone are illustrated in the LES instantaneous result in Figure 3-10 (c). The LES time-averaged results match the experimental observations best in terms of the flame length, which can be seen more clearly in the comparison between the simulation and experimental results in Figure 3-9(b).

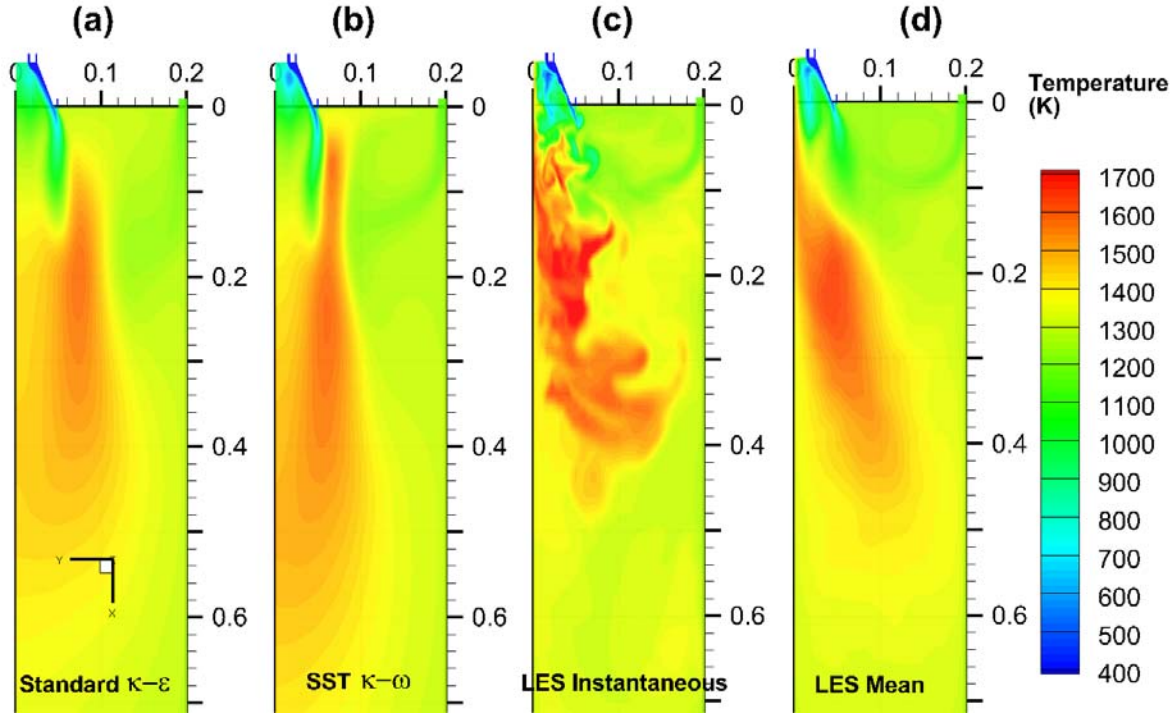

Figure 3-10. The predicted temperature distributions using RANS and LES. (a) Standard $k-\varepsilon$ model, (b) SST $k-\omega$ model, (c) LES in an instantaneous moment, and (d) LES mean values.

Although predicting apparently different flowfield, the three RANS turbulence models predict similar temperature profiles in the furnace, while LES performs marginally better. For instance, at 50 mm away from the burner, the predicted gas temperature by all the turbulence models closely follows the experimental results. However, in RANS, the minimum temperature at 0.05 m off axis is 300 K lower than the measured data, likely to be due to the burner cold stream penetration, while LES show a

marginally improved result. This is because the RANS models underestimate the turbulent mixing between the staging stream and the burner streams. Similar trend has been reported by Gharebaghi et al. [176] who compared the temperature predictions by the standard $k-\varepsilon$ model and LES in an industrial coal combustion facility: they found that the RANS simulation was not able to predict the turbulence structures downstream the burner, leading to a longer and narrower flame than that predicted by LES and observed in the experiment. LES shows better temperature predictions at 0.05 ma and 0.1 m away from the burner, indicating that it models the turbulent mixing and reaction rates in the burner downstream more accurately. This is also shown at x=0.5 m where the LES results match the temperature measurements, while the RANS approaches overestimate the flame length.

All the simulation underestimated the gas temperature in the outer radial region (0.1 m<R<0.2 m) at 0.1 and 0.2 m away from the burner: the predicted gas temperatures are about 200 K lower than the measured results. Recalling that all simulations over-predict the oxygen concentration in the same location, this might be partially due to the gas phase reaction model, the assumed coal devolatilization and char combustion kinetic parameters, or the deviation on particle trajectory predictions. The discrepancy may also be partially due to the experimental errors. Note that the diameter of the suction pyrometer tip is ~1/8 of the furnace radius, which may disturb the flowfield and average out the radial profiles.

3.4.4. Flame Stabilization and Oxy-Char Combustion

The CFD provides some insight into the coal combustion process, in particular the volatile flame stabilized in the vicinity of the burner, and the oxy-char combustion downstream.

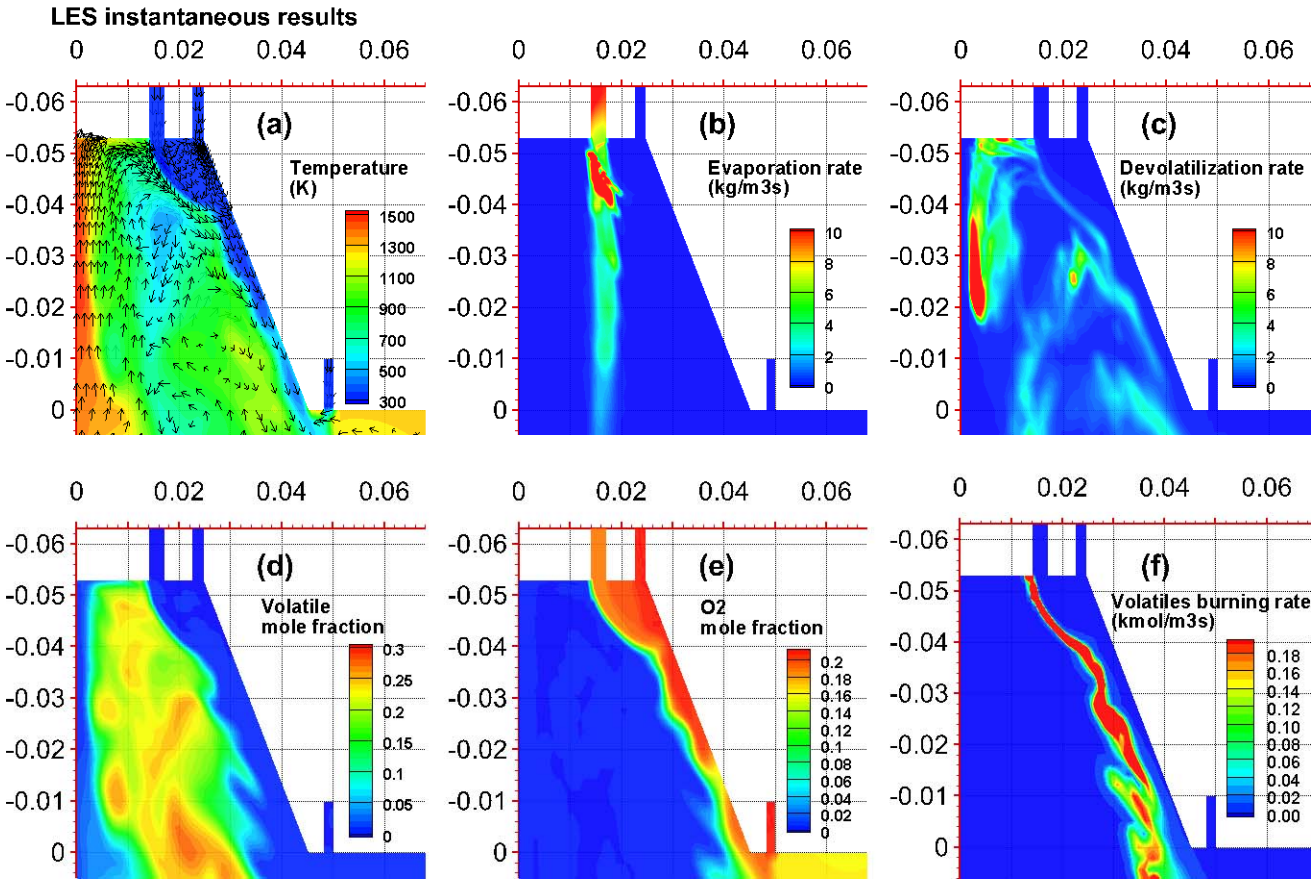

Figure 3-11. The LES instantaneous results, showing the flame stabilization mechanism in the burner quarl. (a) Gas temperature is shown using colored contour, and velocity is shown using uniform length vector, (b) coal particle moisture evaporation rate, (c) coal particle devolatilization rate, (d) volatiles mole fraction, (e) O_2 mole fraction, and (f) volatiles burning rate in the quarl structure.

Flame destabilization has been reported in oxy-coal combustion due to the different thermodynamic and transport properties [189]. Maintaining flame stability and keeping the heat transfer characteristics in oxy-fuel combustion similar to those in air combustion may be achieved by adjusting the flue gas recycle ratio [70], partitioning of the gas volume and oxygen contents in different burner streams [190, 191], as well as using advanced burner design. The swirl burner used in the test facility was specifically designed for oxy-coal combustion with low oxygen concentrations and has demonstrated favorable aerodynamics features in the experiment [177]. Using unsteady LES simulation,

the flame stabilization mechanism can be revealed. Combustion in this case is characterized by an attached flame, sufficient mixing between the recirculated hot gas and unburned burner streams, and stable coal particle devolatilization and ignition. Figure 3-11(a) shows the gas temperature and velocity distribution in the burner quarl. A stream of hot gas up to 1500 K is recirculated to the primary and secondary stream inlets along the centerline, which maintains the high temperature in the burner quarl. Figure 3-11(b) shows the coal de-watering processes: because of the fine particle size used in the experiment, the evaporation process takes place early in the primary stream duct, and nearly all the particles are dried out as soon as they are injected into the high temperature zone. Figure 3-11(c) shows the volatile release rate in the quarl: coal particles start releasing volatiles following the de-watering process, some of the coal particles are recirculated back following the gas flow while continuing the devolatilization process. Figure 3-11(d) and (e) show the volatile and oxygen concentration distributions in the quarl. A volatile mole fraction up to 30% shows that volatile matters are concentrated in the recirculation zone. Figure 3-11(f) shows the volatiles burning rate (reaction in Equation (3.30)). The volatiles are burned by the oxygen supplied from the primary and secondary streams. The wrinkled interface between the volatile and oxygen streams shows that a turbulent diffusion flame is stabilized near the burner quarl wall, which agrees well with the experimental observations.

(a)

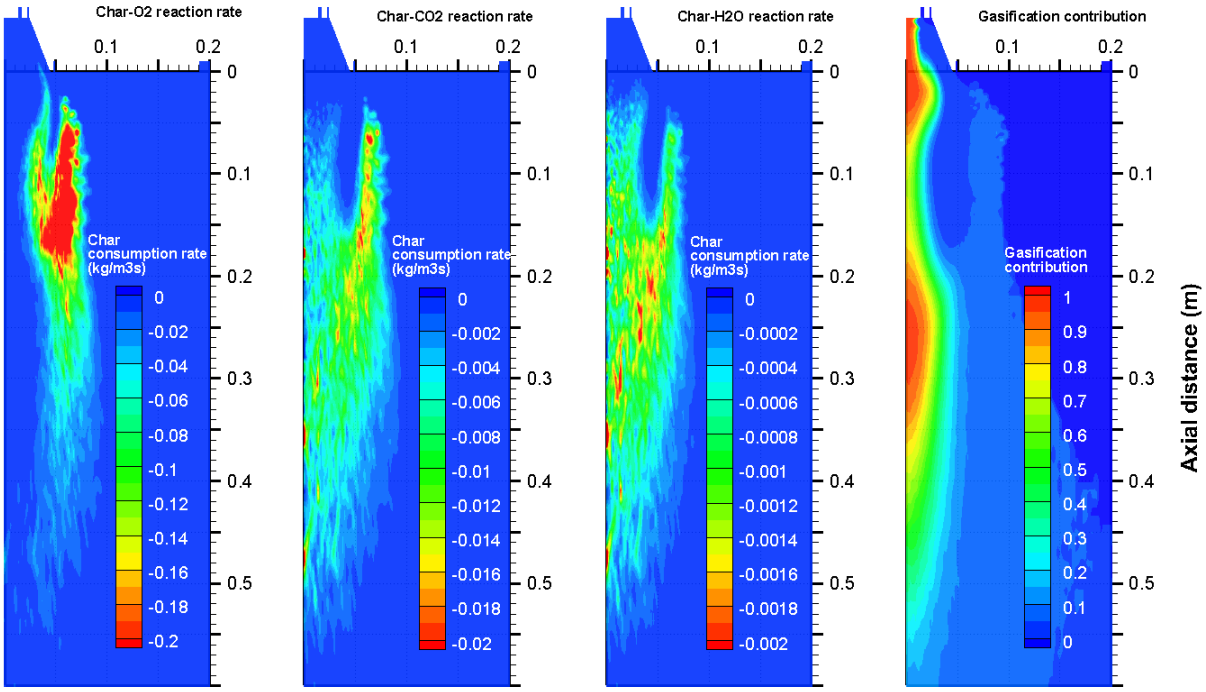

(b)

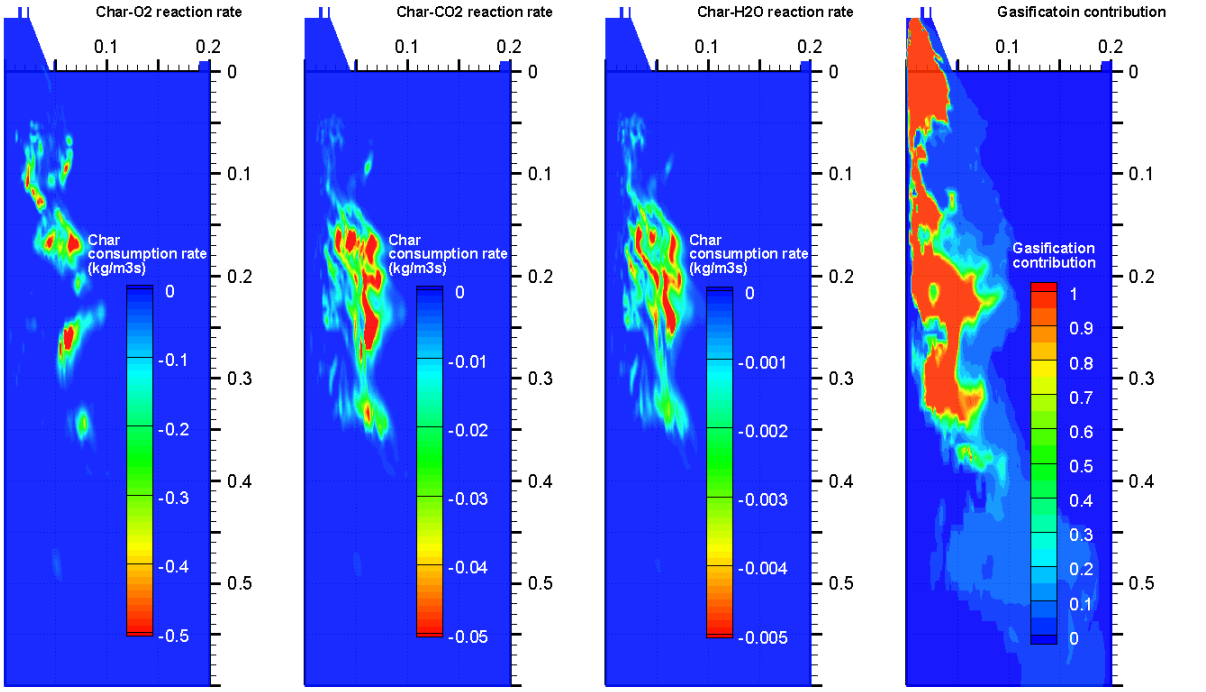

Figure 3-12. Predicted char consumption rate by oxidation and gasification reactions, and the gasification reaction's contribution. (a) SST $k-\omega$ model, (b) LES in an instantaneous moment.

Following volatiles combustion, char particles are burned further downstream using mostly the oxygen supplied from the staging stream. Figure 3-12 shows the char consumption rates due to the char oxidation and gasification reactions predicted by the SST $k-\omega$ model, and the instantaneous result predicted by LES. Following the trajectory of the coal particles, char is burned using the oxygen supplied by the stating stream at the burner outlet where intense mixing takes place due to the local turbulence, as discussed in section 3.4.2. The char-O_2 reaction occurs mainly within 0.3 m away from the burner, in accordance with the experimental observations [133]. On the other hand, the char-CO_2 and char-H_2O gasification reactions can be observed across a broader region. However, noting the different contour ranges used in the figures, the gasification reaction rates are one to two orders of magnitude lower than the oxidation reaction because of their higher activation energies. In oxy-fuel combustion, char consumption is dominated by the oxidation reactions because of their higher reaction rates. The contributions of the char-O_2, char-CO_2 and char-H_2O reactions to char consumption are 91.9%, 7.46%, and 0.68%, respectively. However, the gasification reactions may become important locally where the gas temperature is high and the oxygen concentration is low [22]. As shown in the last chart of Figure 3-12(a) and (b), the gasification reactions' contribution reaches up to 90% in the fuel-rich zone of the volatile-flame and the char-combustion regions, where the gas temperature is high and oxygen concentration is low. It should be noted that, because the calculations are based on a simplified oxy-char combustion model and global reaction kinetics, the relative contributions of oxidation and gasification reactions are only qualitative. They may vary depending on the coal rank, burner designs, and operating conditions such as overall stoichiometry, dry or wet flue gas recycle, as well as the flue gas recycle ratio.

The experimental study also measured the particle temperature distribution at several axial locations. Figure 3-13 shows a comparison between the measurement and the CFD simulations. It should be noted that the two-color pyrometry method used in the experiment is based on optical

measurement of the infrared radiation intensity of the hot coal particle at two selected wavelengths, and only particles which are hotter than the background gas are detected. The same criteria were used when the particles were sampled in the CFD analysis. Figure 3-13 shows that the computed particle temperature follows the same trends as those observed in the experiment. However, the simulation results are significantly lower than the measured particle temperature at 0.05 m away from the burner, showing less burning intensity in a mean statistical sense, while the simulation results at 0.2 m away from the burner match the experimental results well. This may be due to the fact that only few char particles are burned at 0.05 m (see Figure 3-12), where the experimental result might have a higher uncertainty because hotter particles can be detected with higher probability.

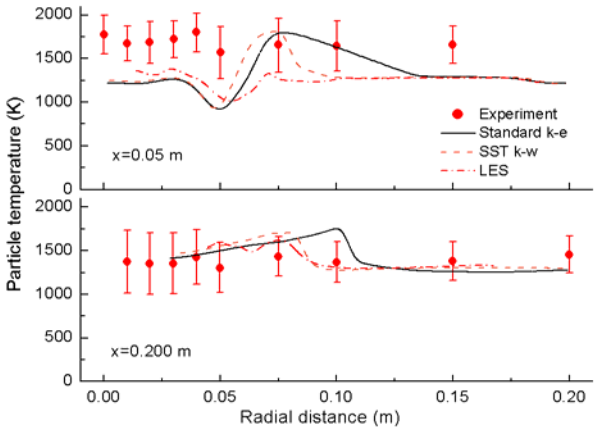

Figure 3-13. Comparison between the measured (scatters) and CFD predicted (lines) particle temperature at 50 and 200 mm away from the burner.

3.5. Conclusion

In this chapter, three-dimensional CFD simulations were performed for oxy-fuel lignite coal combustion in a 100 kW_{th} pilot-scale combustion unit using RANS and LES approaches, as well as radiation and char-combustion sub-models modified specifically for a high CO_2 concentration oxy-combustion environment. The predicted velocity, species and temperature distributions using different turbulence models, such as standard $k-\varepsilon$ model, RNG $k-\varepsilon$ model, SST $k-\omega$ model and LES

model, were compared with experimental results. These turbulence models show different performance in predicting the turbulent flowfield, which significantly impacts the prediction of oxygen diffusion, coal combustion and temperature distribution. The main conclusions are as follows:

(1) All turbulence models show the overall trends of the measured mean axial and tangential velocity profiles, and capture the internal and external recirculation zone formed by the swirling burner stream. However, the RANS models underestimate the internal recirculation zone size and the turbulent intensity at the burner exit. LES shows better performance in predicting the turbulent structure and flowfield, and match well with the experiment.

(2) The different performance of these turbulence models lead to different oxygen concentration predictions: the standard $k-\varepsilon$ model and RNG $k-\varepsilon$ model fail to predict the entrainment and mixing of the staging stream, while SST $k-\omega$ model can capture the corresponding flow structures and improve the oxygen concentration prediction. Nevertheless all the RANS models underestimate the turbulence intensity downstream in the char combustion zone, while LES shows intense mixing and oxygen diffusion, which also improves the prediction of the flame length and temperature field.

(3) LES provides insights into the flame stabilization mechanism. The swirling flow forms strong internal recirculation zone along with the bluffbody and quarl geometry, which stabilizes the volatiles diffusion flame in the quarl.

(4) Char-O_2 reaction contributes up to 91.9% of the char consumption and dominates the char combustion process in oxy-fuel combustion. However, gasification reactions can become important locally at the fuel-rich zone of the volatile-flame and char-combustion regions, where the gas temperature is high and oxygen concentration is low.

Page left intentionally blank

Chapter 4 Modeling the CO_2 Chemical Effects in Gas Phase Reactions

In last chapter, we validated the CFD approach as a whole in predicting oxy-coal combustion. Note that a relatively simple combustion model (Eddy Dissipation model) was used, with which only the major species, such as oxygen, carbon dioxide, and steam, can be predicted. However, CO_2 has its chemical effects on homogeneous reactions, which may significantly change the reaction rates and intermediate species such as CO under specific conditions. In this chapter, we will focus on these chemical effects and validate the appropriate modeling method in CFD simulations.

4.1. Overview

Higher CO concentration has been reported in oxy-fuel combustion tests, as compared to conventional air-fired combustion. For instance, increased CO level within the flame zone was reported in the experimental study performed in the IFRF 2.5 MWth furnace by Woycenko et al. [72]. Likewise, Rehfeldt et al. [78] found significantly higher CO concentration in the fuel-rich flame region of oxy-Lausitz lignite coal combustion using a 0.5 MW_{th} pilot scale test facility. Andersson et al. [68, 69] and Hjartstam et al. [70] measured the CO concentrations in a 100 kW_{th} test facility using propane or lignite coal fuels, and they observed consistently higher CO concentrations in the combustion zone near the burner under oxy-fuel conditions than under air-fired conditions when the combustion temperatures are maintained the same.

The mechanism responsible for the higher CO concentration observed in the diffusion flames is still under investigation. It has been widely accepted that the different CO level is due to the CO_2 chemical effects in homogeneous and/or heterogeneous reactions [19, 22], because CO_2 is not inert but it participates in the chemical reactions [113]. In a thermodynamic point of view, CO_2 can be

dissociated into CO and O_2 through $CO_2 \rightleftarrows CO+0.5O_2$, and the equilibrium concentrations are dependent on temperature, pressure, as well as the stoichiometry value. In reality, the majority of the CO formation in the flame zone is not from the dissociation reaction, but through elementary reactions between CO_2 and intermediate species. Liu et al. [192] investigated the chemical effect of CO_2 by modeling the ethylene diffusion flame using a detailed mechanism, CO_2 was added in the fuel side or oxidizer side with a mole fraction of 20%. The simulation showed higher CO concentrations with CO_2 addition in both sides, while introducing CO_2 on the oxidizer side has a more significant chemical effect than on the fuel side. The reaction $CO_2+H=CO+OH$ and $CO_2+CH=HCO+CO$ are shown to be responsible for the chemical effects of CO_2 addition. In order to understand the chemical effect of CO_2 on CO formation, Gloarborg and Bentzen [124] measured the CO concentration from highly diluted methane (~0.1%) premixed combustion at the exit of a plug-flow reactor in N_2 or CO_2 bulk gases under different equivalence ratios. Substantially higher CO concentrations were observed in the case of CO_2 compared to those in N_2, moreover, the difference increases significantly from the fuel-lean to the fuel-rich conditions. Simulations with a detailed mechanism again identify the CO_2/H and CO_2/hydrocarbon fragment reactions as the major pathways responsible for the higher CO concentration. In oxy-coal combustion, the char-CO_2 and char-H_2O gasification reactions may also contribute to the higher CO in the fuel-rich region of the diffusion flame where oxygen concentration is low and temperature is high. This heterogeneous pathway is not discussed in the present study, and the reader is referred to other relevant studies [117, 193].

Therefore, an accurate prediction of the CO formation in oxy-fuel combustion requires appropriate modeling of the CO_2's chemical effects in computational fluid dynamics (CFD) simulations [22]. However, the widely-used global reaction mechanisms used in CFD simulation are developed for traditional air-fired combustion, and they may not capture the chemical effects of CO_2 in a high CO_2 concentration environment. Andersen et al. [135] reviewed two global combustion mechanisms,

namely the Westbrook and Dryer two-step mechanism (WD2) and Jones and Lindstedt four-step mechanism (JL4), and modified the kinetic parameters by calibrating the peak and equilibrium CO predictions in a plug flow reactor using a detailed mechanism under oxy-fuel conditions. The modified global mechanism improved the CO predictions, but there are still discrepancies between the measurements and simulations.

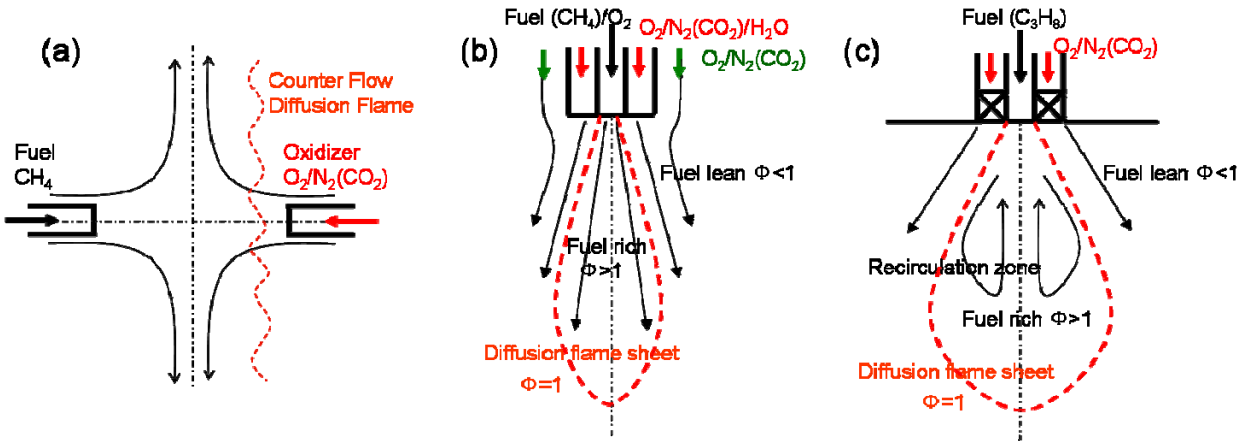

Figure 4-1. Schematic of three diffusion flames in the present study: (a) A counter flow laminar diffusion flame, (b) a jet flow turbulent partial premixed flame, and (c) a swirling flow turbulent diffusion flame.

The objective of this study is to investigate the mechanisms responsible for the higher CO concentrations in oxy-fuel diffusion flames, and the appropriate approaches to model them in CFD simulations. The paper begins with chemical equilibrium calculations, gaining a thermodynamic perspective of the CO_2 chemical effects. A basic 1-D counter-flow diffusion laminar flame was calculated using a detailed mechanism GRI-mech 3.0, in order to understand the fundamental differences between air-fired and oxy-fuel combustions. Based on the analysis, two turbulent diffusion flames with increasing fluid dynamics complexities, namely the Sandia Flame D burning methane and a swirling flow flame burning propane, were modeled using CFD approaches under both air-fired and oxy-fuel conditions. Figure 4-1 shows the schematics of the three air-fired and oxy-fuel diffusion flames investigated in this paper. The performances of the detailed, reduced, quasi-global, and global

mechanisms are compared in the 1-D simulation and CFD modeling of the diffusion flames, their uses and limitations in predicting the overall flame structure and CO concentration are discussed.

4.2. Literature Experimental Results

Many oxy-fuel combustion tests have been carried out in pilot scales since 1980s [29, 73, 77, 80, 93, 96, 133, 189], however, available experimental measurements of CO concentration in flame region with detailed burner geometry and operating conditions are scarce. Therefore, available experimental results for air-fuel and oxy-fuel combustions are used in this study in order to test the performance of the combustion models and reaction mechanisms.

4.2.1. Sandia Flame D

Sandia Flame D [194-196] is a well-documented jet flow non-premixed turbulent flame. As shown in Figure 4-1(b), it consists of three concentric flows: a jet fuel/air flow in the center with an inner diameter of 7.2 mm, an annular hot pilot flow with an inner diameter of 7.7 mm and outer diameter of 18.2 mm, and the wind tunnel flow outside supplying oxygen for the diffusion flame. It should be noted that the partial-premixed jet flow was used to eliminate soot formation and produce a robust flame, the mixing rates are high enough that the flame burns as diffusion flame [195]. The measured scalars include temperature, mixture fraction, and species including N_2, O_2, H_2O, H_2, CH_4, CO, CO_2, OH and NO measured by Raman scattering and LIF (Laser-Induced Fluorescence). The CO mass fraction measured by LIF is used for comparison with simulation results because of its higher accuracy. With similar operating conditions but a O_2/CO_2 environment, the oxy-fuel flame of methane in 35% O_2/65% CO_2 (labeled as OF35) is calculated and the performance of these mechanisms is compared. The operating conditions under air-fired and oxy-fuel conditions are shown in **Table 4-1**.

Table 4-1. The operating conditions of the Sandia Flame D under air-fired and oxy-fuel conditions [194, 195].

	Temperature (^oC)	Volume flow rate (m3/s) and species mole fraction (vol%) Air	OF35[a]
Jet flow	21	2.02e-3 CH_4/Air=25/75	1.41e-3 CH_4/(35%O_2+65%CO_2) =35.71/64.29
Pilot flow	1635	2.43e-3 $O_2/N_2/CO_2/H_2O/CO$ =4.88/73.50/6.97/14.25/0.40	1.67e-3 $O_2/N_2/CO_2/H_2O/CO$ =7.09/0/69.16/23.75/0
Wind tunnel	18	6.34e-2 Air	3.80e-2 35%O_2+65%CO_2

[a]: Experimental unavailable

4.2.2. Chalmers Swirling Flow Diffusion Flame

Andersson and coworkers [68, 69] investigated propane flames under both air-fired and oxy-fuel combustion conditions using the Chalmers'100 kW_{th} test unit. Comprehensive temperature and gas composition measurements were carried out at different locations downstream of the burner. The test furnace consists of a swirl burner, a cylindrical refractory-lined furnace with an inner height of 2.4 m and an inner diameter of 0.8 m, a fabric filter, as well as a flue gas recycle system. Figure 4-1(c) shows a schematic of the swirl burner in the test facility: the burner consists of a fuel lance (i.d.=34 mm), surrounded by cylindrical primary and secondary feed-gas registers. The primary register is equipped with 45^o swirl vanes and with an outer diameter of 52 mm, whereas the secondary register has a more moderate swirl number with a fin angle of 15^o and outer diameter of 92 mm. In the air-fired case, air is used in the primary and secondary streams; while in the oxy-fuel cases, two different flue gas recycle rates (hence different oxygen fractions in the feed gas) were used. The oxygen mole fraction was 21% and 27% in the primary and secondary stream under the cases labeled OF21 and OF27, respectively, balanced by recycled dry flue gas consisting of mainly CO_2. In this study, we calculated the air-fired case and the OF27 case for their similar combustion temperatures and flame characteristics, and the stoichiometry was kept constant at stoichiometry of $\lambda = 1.15$. Details of the gas compositions and mass flow rates under the air-fired and oxy-fuel operating conditions are summarized in **Table 4-2**.

Table 4-2. The operating conditions of the propane combustion experiment under air-fired and oxy-fuel conditions.

Streams	Temperature ^{o}C	Mass flow rate (kg/s) and mole fraction (vol%) in O_2:N_2:CO_2	
		Air	OF27
Fuel lance	25	1.67e-3 (Propane)	1.67e-3 (Propane)
Primary stream	25	1.22e-2 (21:79:0)	1.33e-2 (27:2:71)
Secondary stream	25	1.78e-2 (21:79:0)	1.93e-2 (27:2:71)

4.3. Modeling Approaches

4.3.1. One-Dimensional Modeling of the Counter-Flow Diffusion Flame

The counter flow diffusion flame is modeled using the 1-D opposed-flow diffusion flame model in CHEMKIN 4.0. The fuel (methane) and oxidizer streams (either O_2/N_2 or O_2/CO_2) are injected from two concentric, circular nozzles directed towards each other, as shown in Figure 4-1(a). Mass, momentum and energy equations in the axisymmetric coordinate are solved using the stead state solver TWOPNT.

4.3.2. CFD Modeling of the Jet-Flow and Swirling-Flow Diffusion Flames

FLUENT 12.1 was used for the CFD simulations. A 2-D axisymmetric mesh with 5580 quadrilateral cells and a 3-D mesh with 400,000 hexahedral cells were used for the simulations of Sandia Flame D and Chalmers swirling flow flame, respectively. The mesh independence was checked by comparing the cold and reacting flow results using double-size meshes. For instance, the results from the 3-D mesh were compared with meshes with 1,000,000 cells. The 400,000-cell mesh with 1 mm resolution in the burner region showed satisfactory accuracy at moderate computational cost.

The realizable $k-\varepsilon$ model was used for modeling the turbulence in Sandia Flame D, and the SST $k-\omega$ model [180] was used for the swirling flow turbulence modeling because of its better performance in swirling flows based on our previous studies [193]. The Discrete Ordinates (DO) model

[185, 186] was used to solve the radiative transfer equation (RTE) for radiative heat transfer, and the absorption coefficient of the participating gas mixture was modeled using weighted-sum-of-gray-gas model (WSGGM) [187] with modified parameters for oxy-fuel combustion as proposed by Johansson et al. [151]. The modified WSGGM was implemented in the CFD simulation in the form of user defined functions (UDFs) [197]. Unlike the Sandia Flame D which eliminates soot formation by the partial premixed jet stream, soot formation is observed and plays a significant role in radiative heat transfer in the Chalmers experiments [68, 113]. Therefore, soot formation was modeled in the latter case using a one-step model [198], and the effect of the soot particles on the radiative heat transfer is considered by modeling its absorption coefficient in the RTE.

Two gas-phase reaction models, namely the eddy dissipation model (EDM) and eddy dissipation concept (EDC) model, were used in this study to model the turbulence-chemistry interaction. In the EDM [163, 164], the chemical reaction is governed by the large-eddy mixing time scale, defined as turbulence kinetic energy over its dissipation rate (k/ε), proposed by Spalding [164]. Based on the assumption that the reaction rate is limited by the mixing of the reactants and the heating of the reactants through the mixing with the products, the net rate of production of species i due to reaction r, $R_{i,r}$, is given by the smaller of the reactant mixing rate (first term) and product mixing rate (second term):

$$R_{i,r} = \min \left(\begin{array}{l} \nu'_{i,r} MW_i A \rho \dfrac{\varepsilon}{k} \min_R \left(\dfrac{Y_R}{\nu'_{R,r} MW_R} \right), \\ \nu'_{i,r} MW_i AB \rho \dfrac{\varepsilon}{k} \dfrac{\sum_P Y_P}{\sum_j^N \nu''_{j,r} MW_j} \end{array} \right) \quad (4.1)$$

where ρ is density, $\nu'_{i,r}$ and $\nu''_{j,r}$ are the stoichiometric coefficient for reactant i and product j in reaction r, M_w is the molecular weight, Y_R and Y_P are mass fraction of any reactant and

product species, respectively. $A = 4.0$ and $B = 0.5$ are empirical model constants. Hydrocarbon combustion is assumed to take place in two irreversible steps:

$$C_nH_m + \left(\frac{2n+m}{4}\right)O_2 \rightarrow nCO + \frac{m}{2}H_2O \quad (4.2)$$

$$CO + 0.5O_2 \rightarrow CO_2 \quad (4.3)$$

It should be noted that the EDM does not incorporate finite-rate kinetics, and the simplified gas phase reaction scheme in Equation (3.32)-(3.31) does not reflect the chemical effect of CO_2 on hydrocarbon oxidation discussed previously. Therefore, this model can only be used to predict the major products species in stable diffusion flames in which the reaction rates are controlled by turbulent mixing, but not be expected to show accurate prediction of intermediate species such as CO and H_2 in oxy-fuel combustion. This will be discussed in more details later.

In the EDC model [163, 166], the reactions are assumed to occur in small turbulent structures, or fine scales associated with the length fraction as a function of the average turbulence intensity:

$$\xi^* = C_\xi \left(\frac{\nu\varepsilon}{k^2}\right)^{1/4} \quad (4.4)$$

where * denotes fine-scale quantities, ν, k and ε are kinematic viscosity, turbulence kinetic energy and its dissipation rate, respectively. $C_\xi = 2.1377$ is the volume fraction constant. The volume fraction occupied by the fine structure is ξ^{*3}. The mean residence time τ^* of the fluid within the fine structures is modeled by:

$$\tau^* = C_\tau \left(\frac{\nu}{\varepsilon}\right)^{1/2} \quad (4.5)$$

where $C_\tau = 0.4082$ is a time scale constant. Combustion at the fine scales is assumed to occur in a constant pressure reactor, with initial conditions taken as the current species and temperature in the cell. The overall reaction rate of species i is modeled as

$$R_i = \frac{\rho\left(\xi^*\right)^2}{\tau^*\left[1-\left(\xi^*\right)^3\right]}\left(Y_i^* - Y_i\right) \qquad (4.6)$$

where Y_i and Y_i^* are the mass fraction of species i in the surrounding and fine scale, and Y_i^* is calculated by integrating the laminar reaction rate of the reaction mechanism over time scale τ^* using the ISAT algorithm [199]:

$$Y_i^* = Y_i + \frac{MW_i}{\rho}\int_0^{\tau^*}\sum_{r=1}^{N_R}\Gamma\left(\nu''_{i,r} - \nu'_{i,r}\right)\left(k_{f,r}\prod_{j=1}^{N}\left[C_{j,r}\right]^{\eta'_{j,r}} - k_{b,r}\prod_{j=1}^{N}\left[C_{j,r}\right]^{\nu''_{j,r}}\right)dt \qquad (4.7)$$

where Γ represents the effect of third bodies on the reaction rate, $\left[C_{j,r}\right]$ is the mole concentration of species j, $\nu'_{i,r}$ and $\nu''_{i,r}$ are the stoichiometric coefficient for reactant i in reaction r as defined previously, $\eta'_{j,r}$ is the rate exponent for species j in reaction r, $k_{f,r}$ is the forward reaction rate constant for reaction r in the Arrhenius form:

$$k_{f,r} = A_r T^{\beta_r} e^{-\frac{E_r}{RT}} \qquad (4.8)$$

and the backward reaction rate constant, $k_{b,r}$, is calculated using the equilibrium constant, K_r, as follows:

$$k_{b,r} = \frac{k_{f,r}}{K_r} \qquad (4.9)$$

For global reaction mechanisms where the rate exponents are different from the stoichiometric coefficients, the backward reaction rate is computed using individual kinetic parameter sets which are obtained by calculating the backward reaction constant at a series of temperatures to guarantee chemical equilibrium.

The EDC model can incorporate detailed chemical mechanisms, and it is possible to predict intermediate species, such as CO and H_2, given that appropriate reaction mechanisms are used.

4.3.3. Reaction Mechanisms

Table 4-3 summarizes the mechanisms that were tested in this numerical study, including detailed, skeletal, quasi-global, and global mechanisms. Detailed reaction mechanisms for hydrocarbon combustion have been shown to be valid under oxy-fuel combustion conditions. For instance, Glarborg and Bentzen [124] validated the detailed chemical kinetic model (DCKM) on CO prediction in a plug-flow reactor. In our previous work [22], we have demonstrated that the GRI-Mech 3.0 is valid on predicting the burning velocity under both air-fuel and oxy-fuel conditions. Therefore, GRI-Mech 3.0 [200] consisting of 53 species and 325 elementary reactions for CH_4 combustion was used in the 1-D counter flow diffusion flame modeling. A skeletal mechanism for methane combustion consisting of 17 species and 58 reactions [201] was used in the CFD simulation of Sandia Flame D. These two mechanisms have been tested in previous studies and serve as benchmarks in the simulation.

Table 4-3. A summary of the mechanisms tested in this study.

Mechanism	Species	Reactions	Calculated Cases	Reference
GRI-mech 3.0	53	325	1-D Counter flow	[200]
Skeletal	17	58	Sandia Flame D	[201]
WDmult	12	22	1-D Counter flow, Sandia Flame D, Chalmers Swirling Flow	[122, 136]
WD2	5	2	1-D Counter flow, Sandia Flame D, Chalmers Swirling Flow	[122, 134, 136]

However, it is computationally expensive to apply detailed reaction mechanisms in CFD modeling. Alternatively, quasi-global or global hydrocarbon combustion mechanisms have been proposed. Westbrook and Dryer [122, 136] proposed several simplified reaction mechanisms for the oxidation of hydrocarbon fuels in premixed flames, namely the WD one-step (WD1), WD two-step (WD2) and WD multi-step (WDmult) mechanisms. Later on, based on the analysis of premixed and diffusion flame structures, Jones and Lindstedt [137] proposed a four-step global reaction scheme (JL4) for hydrocarbon combustion. The features and limitations of these global and quasi-global mechanisms are as follows:

- ***WD1*** contains one step hydrocarbon oxidation reaction

$$\left(\text{R.WD1-1}\right)\ \mathrm{C_nH_m}+\left(n+\frac{m}{4}\right)\mathrm{O_2}\rightarrow n\mathrm{CO_2}+\frac{m}{2}\mathrm{H_2O}\quad(4.10)$$

This global mechanism, with empirical kinetic parameters for different hydrocarbons, agrees well with the laminar burning velocity over a range of equivalence ratio However, it cannot predict CO or H_2.

- ***WD2*** contains two step reactions:

$$\left(\text{R.WD2-1}\right)\ \mathrm{C_nH_m}+\left(\frac{2n+m}{4}\right)\mathrm{O_2}\rightarrow n\mathrm{CO}+\frac{m}{2}\mathrm{H_2O}\quad(4.11)$$

$$\left(\text{R.WD2-2}\right)\ \mathrm{CO}+\frac{1}{2}\mathrm{O_2}\rightleftarrows\mathrm{CO_2}\qquad(4.12)$$

This mechanism recognizes the fact that the hydrocarbons are partially oxidized to CO, and these two global reactions often proceed at different time scales. The rate of the CO oxidation (forward reaction in (R.WD2-2)) was taken from Dryer and Glassman [134], and a reverse reaction rate was proposed in order to reproduce the proper heat of reaction and the CO concentration at equilibrium. The reversible reaction (R.WD2-2) takes the CO_2 dissociation into account in a global thermodynamic manner.

- ***WDmult*** consists of an initiation reaction, in which CO and H_2 are produced in hydrocarbon partial oxidation, and a 21 skeletal elementary reactions for CO-H_2-O_2 system. The initiation reaction is in the form of:

$$\left(\text{R.WDmult}-1\right)\ \mathrm{C_nH_m}+\frac{n}{2}\mathrm{O_2}\rightarrow n\mathrm{CO}+\frac{m}{2}\mathrm{H_2}\quad(4.13)$$

The CO-H_2-O_2 mechanism includes 11 species (H, O, H_2, O_2, OH, H_2O, N_2, CO, CO_2, HO_2 and H_2O_2) and 21 elementary reactions. The advantage of this mechanism is that it includes the critical elementary reactions in which CO_2 participates, hence no special treatments are required for the CO-H_2-O_2 system in a high CO_2 concentration environment.

Another global mechanism is the JL4 consisting of two initiation reactions, along with one reversible reaction for H_2 oxidation, and the reversible water gas shift reaction. The water gas shift reaction partially represents the CO_2 chemical effects in a global reaction manner, which may improve the CO concentration predictions. However, as has been discussed by Andersen et al [135], a negative reaction order has to be assigned to H_2 for the reverse reaction in order to satisfy the equilibrium constant, hence numerical difficulties were encountered under fuel-lean conditions where hydrogen concentration approaches zero.

Table 4-4. The reduced, quasi-global, and global reaction mechanisms used for CH_4 and C_3H_8 combustion under air- and oxy-fuel conditions (Units are in m-sec-kmol-J-K).

Reaction No.	Reaction	A_r	E_r	β_r	Reaction orders
Skeletal [201]					
Skeletal-1-58	CH_4-O_2 system	See reference [201]			
WD Multi-Step [122, 136]					
WDmult-1	$CH_4+0.5O_2 \rightarrow CO+2H_2$	7.54e11	2.00e8	0	$[CH_4]^{0.7}[O_2]^{0.8}$
	$C_3H_8+1.5O_2 \rightarrow 3CO+4H_2$	3.38e10 (8.44e9)[a]	1.25e8	0	$[C_3H_8]^{0.1}[O_2]^{1.65}$
WDmult-2-22	CO-H_2-O_2 system	See reference [136]			
WD 2-Step [134, 136]					
WD2-1	$CH_4+1.5O_2 \rightarrow CO+2H_2O$	5.03e11	2.00e8	0	$[CH_4]^{0.7}[O_2]^{0.8}$
	$C_3H_8+3.5O_2 \rightarrow 3CO+4H_2O$	5.62e9	1.25e8	0	$[C_3H_8]^{0.1}[O_2]^{1.65}$
WD2-2f	$CO+0.5O_2 \rightarrow CO_2$	2.24e12	1.67e8	0	$[CO]^{1}[O_2]^{0.25}[H_2O]^{0.5}$
WD2-2r	$CO_2 \rightarrow CO+0.5O_2$	5.00e8	1.67e8	0	$[CO_2]^{1}$

[a] The global reactions parameters shown in brackets are for oxy-fuel combustion.

Based on the review of the reduced reaction mechanisms, the skeletal mechanism, quasi-global mechanism WDmult, and global mechanism WD2 were incorporated in the EDC model for modeling the turbulent flames, because of their capability on predicting CO and numerical robustness in commercial CFD software, and their formulations and rates are summarized in **Table 4-4**. We note that the initiation reactions for methane and propane are different and list them separately.

4.4. Results and Discussions

4.4.1. Thermodynamic Analysis of the CO Concentration in Oxy-Fuel Combustion

In a previous study, Zheng and Furimsky [123] calculated the CO emission from coal combustion in O_2/N_2 and O_2/CO_2 at chemical equilibrium state. Under O_2/CO_2 condition, the CO concentration is 316 ppm at 1700 K when burning with 10% excess oxygen, which is higher than that found in air combustion (64 ppm) at the same stoichiometry. The CO yield increases significantly to 2010 ppm at stoichiometry under O_2/CO_2 condition. However, the difference between the O_2/N_2 and O_2/CO_2 cases (0.025%-0.2%) is insignificant compared to that observed in the fuel-rich zone in the experiments (up to several percentage points) [68, 78]. Therefore, the apparent CO concentration difference must be associated with specific stoichiometry in the diffusion flame.

In this study, we calculated the equilibrium compositions in methane/air and methane/(O_2+3.76CO_2) systems over a expanded range of stoichiometry. Figure 4-2 shows the CO mole fraction as a function of gas temperature and stoichiometry at equilibrium state. CO mole fraction increases with increasing the gas temperature and decreasing the stoichiometry under both air- and oxy-conditions, while the stoichiometry plays a more significant role. When the air/fuel ratio, λ, is higher than unity, there are rarely CO remaining in both cases. At $\lambda = 1.05$ which is a typical overall air/fuel ratio for combustion processes, the CO mole fraction difference between the air-fired and oxy-fuel environment is less than 1% up to 2000 K.

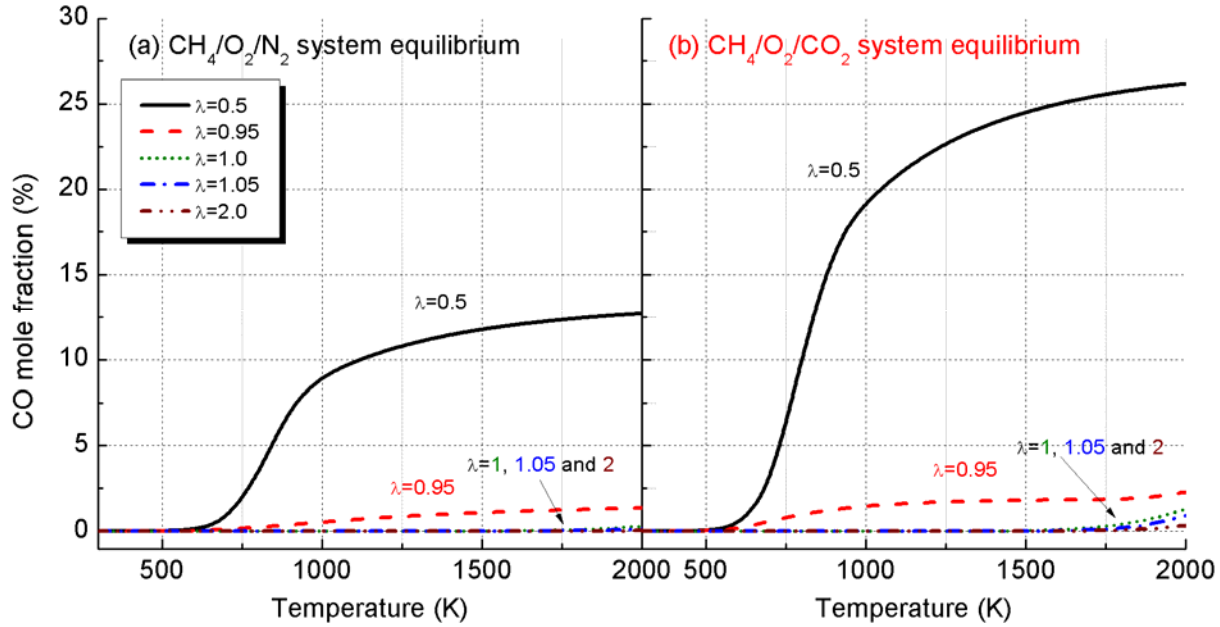

Figure 4-2. The CO mole fraction at thermodynamic equilibrium in $CH_4/O_2/N_2$ and $CH_4/O_2/CO_2$ systems as a function of temperature and stoichiometry.

However, under fuel-rich conditions, the difference increases drastically at high temperatures, showing that the CO_2 chemical effect is more prominent under fuel-rich conditions. The equilibrium CO mole fraction is up to 26% at 2000 K, significantly higher than the maximum CO that can be produced from the methane partial oxidation (~15%). Similar results have been reported in the experiment performed by Glarborg et al. [124]. The equilibrium results indicate that the higher CO concentration observed in oxy-fuel flames can be attributed to the CO_2 thermal dissociation under fuel-rich conditions rather than oxidizer-rich conditions from a thermodynamic point of view. However, the pathways through which CO is formed can only be identified using kinetics calculation with detailed mechanism, which is discussed in the following sub-section.

4.4.2. One-Dimensional Counter Flow Flames

The one-dimensional counter-flow diffusion flame structures under CH_4/Air and $CH_4/O_2/CO_2$ conditions were calculated using detailed mechanism GRI-Mech 3.0. The oxygen mole fraction in the oxy-fuel oxidizer jet was set to be 30% in order to maintain a similar peak combustion temperature

(2002 K) as that of the air-fired case (2067 K). Figure 4-3 shows the predicted species mole fraction profiles. Under a strain rate of ~60 s^{-1}, the peak temperature is stabilized at about 1.12 and 1.02 cm away from the fuel nozzle outlet under air-fired and oxy-fuel conditions, respectively, indicating a slightly higher burning rate in the air-fired case. It can be seen that the CO concentration is significantly higher, and the H_2 concentration is slightly lower, in oxy-fuel flame than in air-fuel flame.

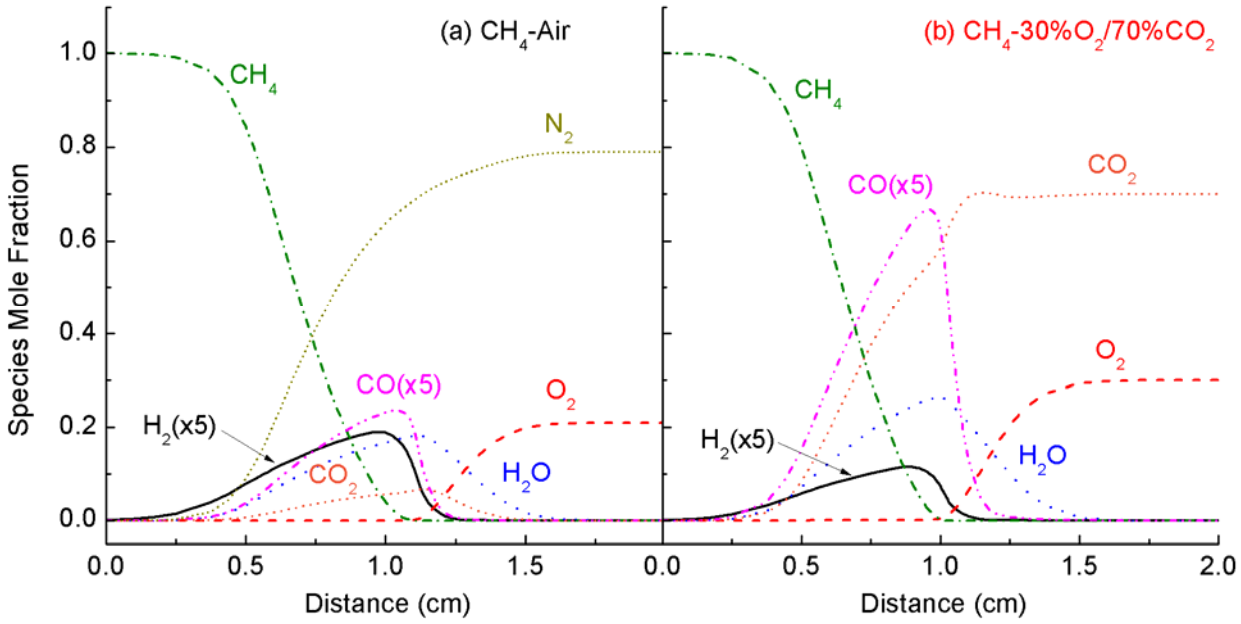

Figure 4-3. Counter flow diffusion flame structures in (a) air-fired and (b) oxy-fuel combustion under a strain rate of 60 s^{-1}. Results are predicted using GRI-mech 3.0 detailed mechanism. Note that CO and H_2 mole fractions are enlarged 5 times in the figure.

An analysis on the CO production rates show that CO is mainly produced via two pathways in both cases. The first pathway is the reactions between intermediate hydrocarbon and active radicals, including

$$(\mathrm{R.167})\ \mathrm{HCO+M \rightleftarrows H+CO+M} \qquad (4.14)$$

$$(\mathrm{R.79})\ \mathrm{H+HCCO \rightleftarrows CH_2(s)+CO} \qquad (4.15)$$

$$(\mathrm{R.23})\ \mathrm{O+C_2H_2 \rightleftarrows CO+CH_2} \qquad (4.16)$$

$$(\mathrm{R.153})\ \mathrm{CH_2(s)+CO_2 \rightleftarrows CO+CH_2O} \qquad (4.17)$$

$$(\mathrm{R.284})\ \mathrm{O+CH_3 \rightleftarrows CO+H+H_2} \qquad (4.18)$$

$$(\text{R.140})\ \text{CH}_2+\text{CO}(+\text{M}) \rightleftarrows \text{CH}_2\text{CO}(+\text{M}) \quad (4.19)$$

$$(\text{R.132})\ \text{CH}+\text{CO}_2 \rightleftarrows \text{HCO}+\text{CO} \quad (4.20)$$

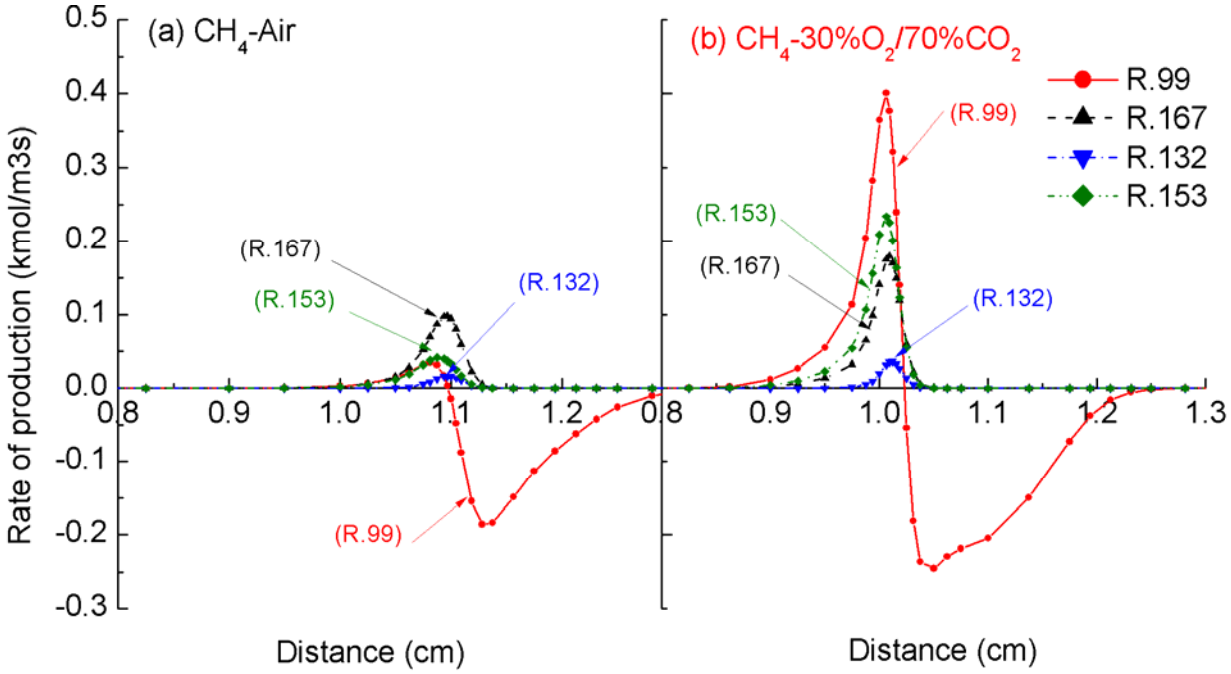

Figure 4-4. CO rate of production due to reactions (R.99), (R.167), (R.132), and (R.153) under (a) air-fired and (b) oxy-fuel conditions. Results are predicted using GRI-mech 3.0 detailed mechanism, and the strain rate is 60 s^{-1}.

We note that CO_2 participates in some of the above reactions directly, such as (R.153) and (R.132), or in the form of a third-body (M), such as (R.167), (R.140), which produces CO at high CO_2 concentration. The second pathway is the reaction between CO_2 and H radical

$$(\text{R.99})\ \text{OH}+\text{CO} \rightleftarrows \text{H}+\text{CO}_2 \quad (4.21)$$

Figure 4-4 compares the CO rate of production by these elementary reactions in air-fuel and oxy-fuel flames. The total CO production rate increases significantly from 0.5 kmol/m^3s in the air-fuel flame to 1.3 kmol/m^3s in the oxy-fuel flame, when the diluent changes from N_2 to CO_2. As discussed above, the higher total CO production rate in oxy-fuel flame are mainly attributed to hydrocarbon reactions in which CO_2 participates, such as (R.167), (R.153) and (R.132), and the backward reaction

of the second pathway (R.99). Moreover, the second pathway reaction (R.99) dominates the CO production in the oxy-fuel flame, it contributes about one third of the total CO in the fuel-rich side of the flame sheet. It also dominates the CO oxidation in the fuel-lean side under both conditions.

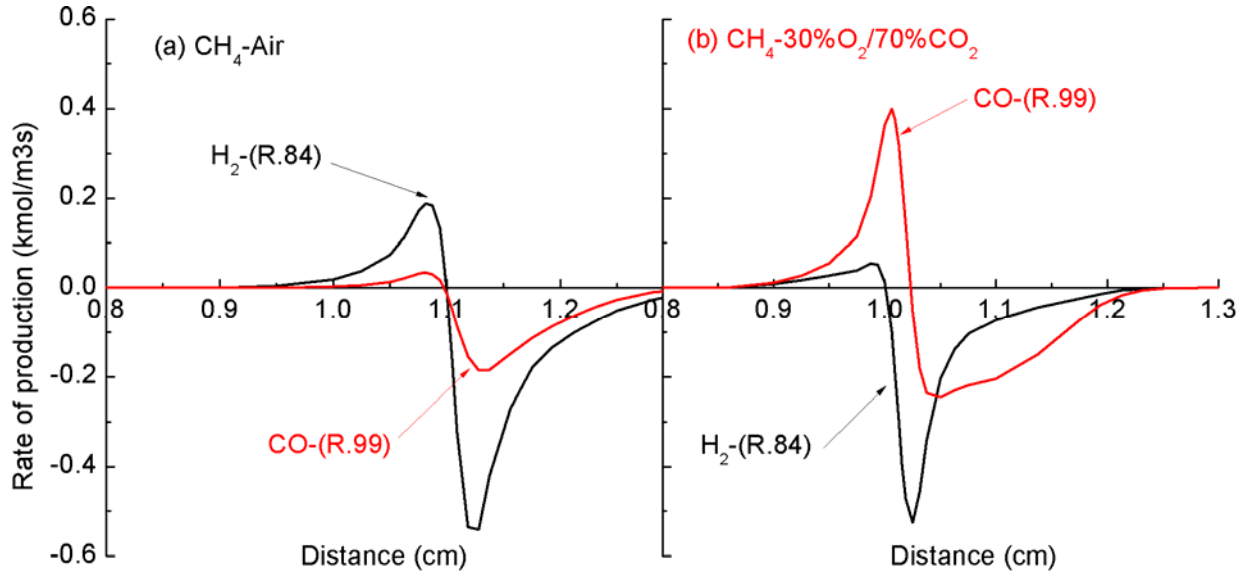

Figure 4-5. H_2 and CO rate of production due to reactions (R.84) and (R.99) under (a) air-fired and (b) oxy-fuel conditions. Results are predicted using GRI-mech 3.0 detailed mechanism, and the strain rate is 60 s^{-1}.

Another interesting result in Figure 4-3 is the lower H_2 and higher H_2O concentrations in the oxy-fuel flame. Analysis shows that the elementary reaction

$$(\text{R.84})\ \text{OH}+\text{H}_2 \rightleftarrows \text{H}+\text{H}_2\text{O} \qquad (4.22)$$

dominates H_2 production in the fuel-rich side, and H_2 oxidation in the fuel-lean side. In the fuel-rich side of the oxy-fuel flame, we have shown that the higher CO_2 concentration promotes the backward reaction of (R.99), which leads to a higher OH and lower H concentration in the radical pool. Consequently, the reaction (R.84) is pushed forward, and H_2 is shifted to produce H_2O. Figure 4-5 compares the H_2 rate of production due to (R.84), along with the CO rate of production due to (R.99), between the air-fuel and oxy-fuel flames. The results show that the backward reaction of (R.84) is inhibited in the oxy-fuel flame, which leads to lower H_2 production rate. Moreover, different from the

air-fuel flame in which CO and H_2 are produced and consumed simultaneously in the fuel-rich and fuel-lean sides, there is a region between 1.00 and 1.02 cm in the flame sheet, where CO is produced through (R.99) and H_2 is consumed through (R.84). The combined effect of these two elementary reactions is the backward water gas shift reaction

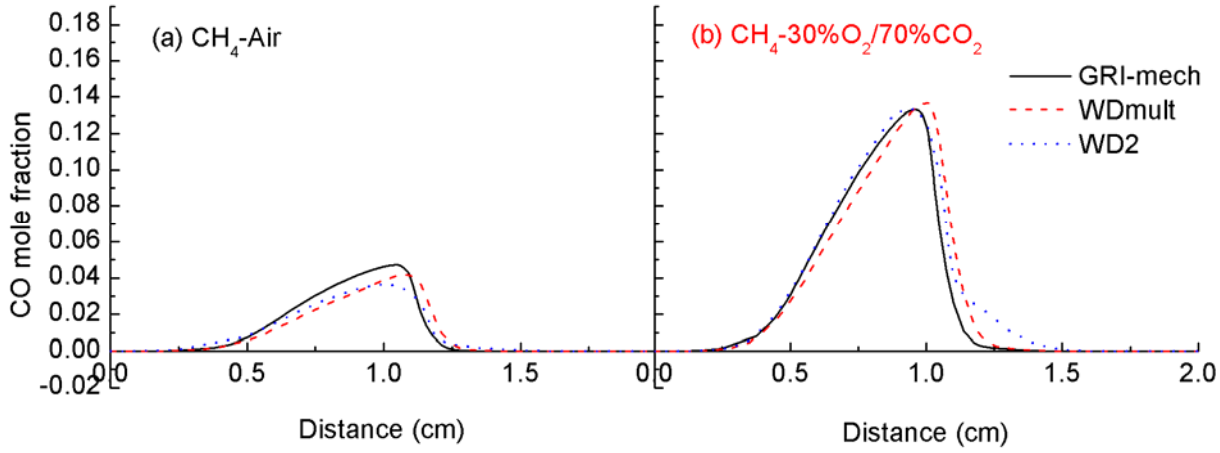

Figure 4-6. Comparison of the predicted CO mole fractions in 1D counter flow diffusion flame using GRI-mech 3.0, WDmult and WD2 mechanisms under (a) air-fired and (b) oxy-fuel conditions. The strain rate is 60 s^{-1}.

$$CO+H_2O \rightleftarrows CO_2+H_2 \qquad (4.23)$$

In a global reaction perspective, the higher CO_2 concentration moves the equilibrium of the water gas shift reaction, leading to lower H_2 but higher CO and H_2O concentrations in the fuel-rich side of the diffusion flame sheet.

The performances of the quasi-global mechanism WDmult and the global mechanism WD2 are tested and compared with the benchmark GRI-mech 3.0. Figure 4-6 shows the predicted CO mole fractions under CH_4-Air and CH_4-O_2/CO_2 conditions using these mechanisms. It is interesting to see that both reduced and global mechanisms perform reasonably and show the higher CO concentration trend in oxy-fuel combustion. In the WDmult mechanism, the critical elementary reactions responsible to the CO_2 chemical effects have been included, therefore, it can represent the higher CO trend in oxy-fuel combustion. While the WD2 mechanism models the CO concentration through the reversible

reaction $(\text{R.WD2-2})\ \text{CO}+\frac{1}{2}\text{O}_2 \rightleftarrows \text{CO}_2$. At high temperature, both forward and backward reaction rates are high enough to ensure the chemical equilibrium, hence the higher CO concentration under oxy-fuel condition is predicted as well.

In summary, the analysis has identified the reaction pathways in which higher CO_2 concentration influences CO formation in the oxy-fuel diffusion flames: it interacts with hydrocarbon fragments, and promotes the $\text{H}+\text{CO}_2 \rightleftarrows \text{OH}+\text{CO}$ reaction, resulting in a higher CO concentration. Combined with the $\text{OH}+\text{H}_2 \rightleftarrows \text{H}+\text{H}_2\text{O}$ reaction, higher CO_2 also leads to lower H_2 and higher H_2O concentration. This has implications regarding the use of the reduced mechanisms. To capture the first pathway, appropriate kinetic parameters should be used for the initiation reaction, taking the chemical effect of CO_2 on hydrocarbon-CO_2 reactions into account. Regarding the second pathway, either critical elementary reactions, such as $\text{H}+\text{CO}_2 \rightleftarrows \text{OH}+\text{CO}$ and $\text{OH}+\text{H}_2 \rightleftarrows \text{H}+\text{H}_2\text{O}$, should be calculated directly as the WDmult mechanism does; or the CO/CO_2 equilibrium should be modeled using global reversible reactions as the WD2 mechanism does. Although the reduced mechanism and global mechanism capture the CO trends in the relatively simple one-dimensional laminar diffusion flame, their performances for turbulent diffusion flames should be further investigated because of the turbulence-chemistry interactions and the multi-scale nature of the chemical reactions.

4.4.3. Jet Flow Diffusion Flame (Sandia Flame D)

Based on the validation in the 1-D diffusion flame, three reaction mechanisms, namely the reduced methane skeletal mechanism, the quasi-global WDmult mechanism, and the global WD2 mechanism, were tested in modeling the Sandia Flame D under both air-fired and oxy-fuel conditions. Following the validation study using air-fired experiment results, the performance of these mechanisms are compared under a conceived oxy-fuel operating condition.

Figure 4-7 and Figure 4-8 compare the CFD predicted temperature and CO mole fraction distributions under air-fired and oxy-fuel conditions, using the EDC model with (a) skeletal, (b) WDmult, and (c) WD2 mechanisms. Results using EDM with infinite-fast reaction rates were also compared. All these approaches predict the jet flow diffusion flame shape as observed in the experiment: a diffusion flame sheet is developed starting from the root of the burner stabilized by the hot pilot stream, and the peak temperature and CO concentration are observed in the flame sheet zone.

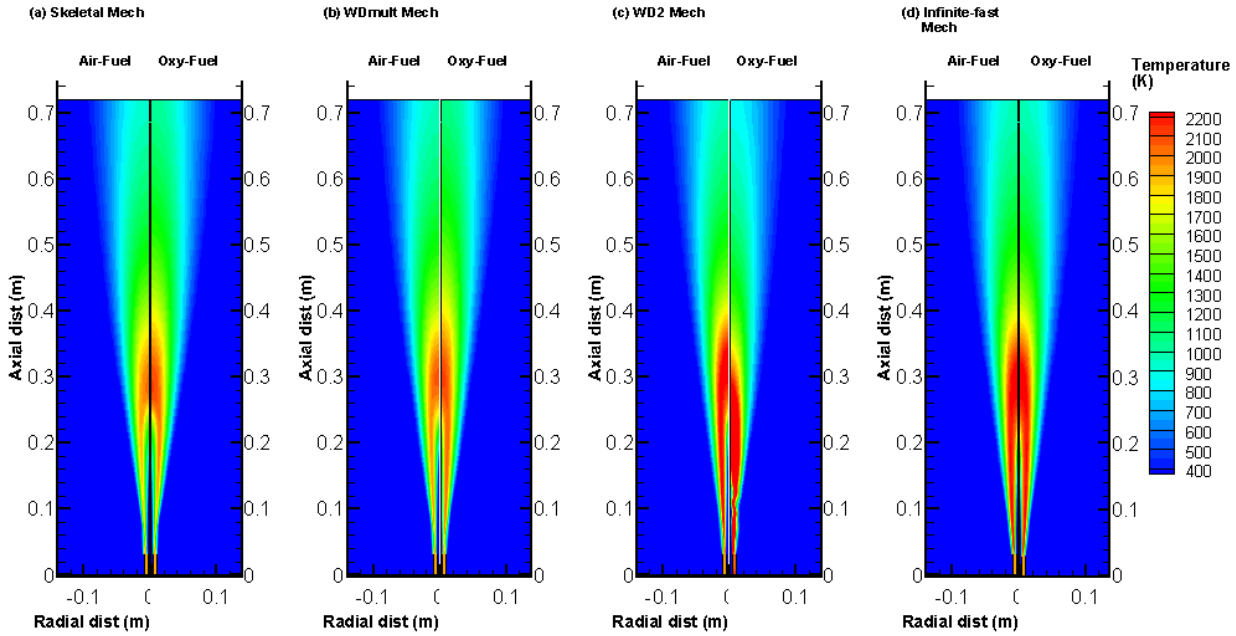

Figure 4-7. Comparison of the predicted temperature distribution in jet flow partial premixed flames (Sandia Flame D) using skeletal, WDmult, WD2 mechanisms, as well as the infinite fast chemistry model under air-fired (left) and oxy-fuel (right) conditions.

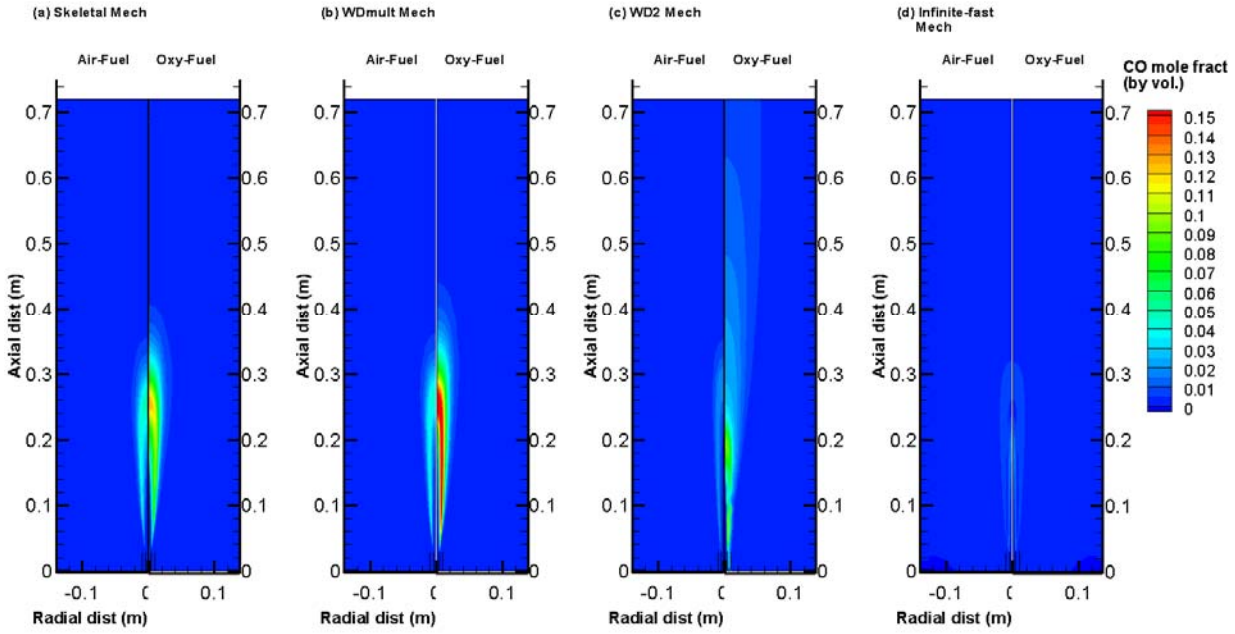

Figure 4-8. Comparison of the predicted CO mole fraction distribution in jet flow partial premixed flames (Sandia Flame D) using skeletal, WDmult, WD2 mechanisms, as well as the infinite fast chemistry model under air-fired (left) and oxy-fuel (right) conditions.

Figure 4-9(a) compares the measured and the predicted axial profiles of temperature and species in air-fuel combustion. All the simulation approaches agree reasonably with the measured results for temperature and major species such as CH_4 and O_2, however their performances are distinct in the intermediate species predictions, such as CO and H_2. The skeletal and quasi-global mechanism WDmult show significantly better agreements with the measurement, while the WD2 mechanism underestimates the CO concentration. Similar trends are observed in Figure 4-9(b), in which the predicted counterpart scalars in oxy-fuel combustion are compared. Moreover, the WD2 mechanism shows significant deviations from the benchmark simulation.

Figure 4-10 compares the measured and predicted radial CO mole fraction at different distances from the burner exit. As it can be seen from Figure 4-8 and Figure 4-10, the performances of different mechanisms on CO predictions are distinct:

- All EDC model based finite-rate mechanisms capture the higher CO concentration in oxy-fuel combustion as they do in the 1-D diffusion flame, while the EDM fails to capture this trend because it assumes the reactions are turbulent mixing controlled and neglects the CO_2 chemical effects.
- The WDmult mechanism predicted CO concentration agrees well with measurement and the benchmark skeletal mechanism in the air-fuel case, while it slightly overpredicts the CO concentration in the oxy-fuel case than the benchmark skeletal mechanism.
- The WD2 mechanism underestimates the peak CO concentration significantly in both cases. However, it shows an overpredicted ~1% CO mole fraction downstream because the forward and backward kinetic parameters of reaction (R.WD2-2) lead to a slight deviation from equilibrium [135].

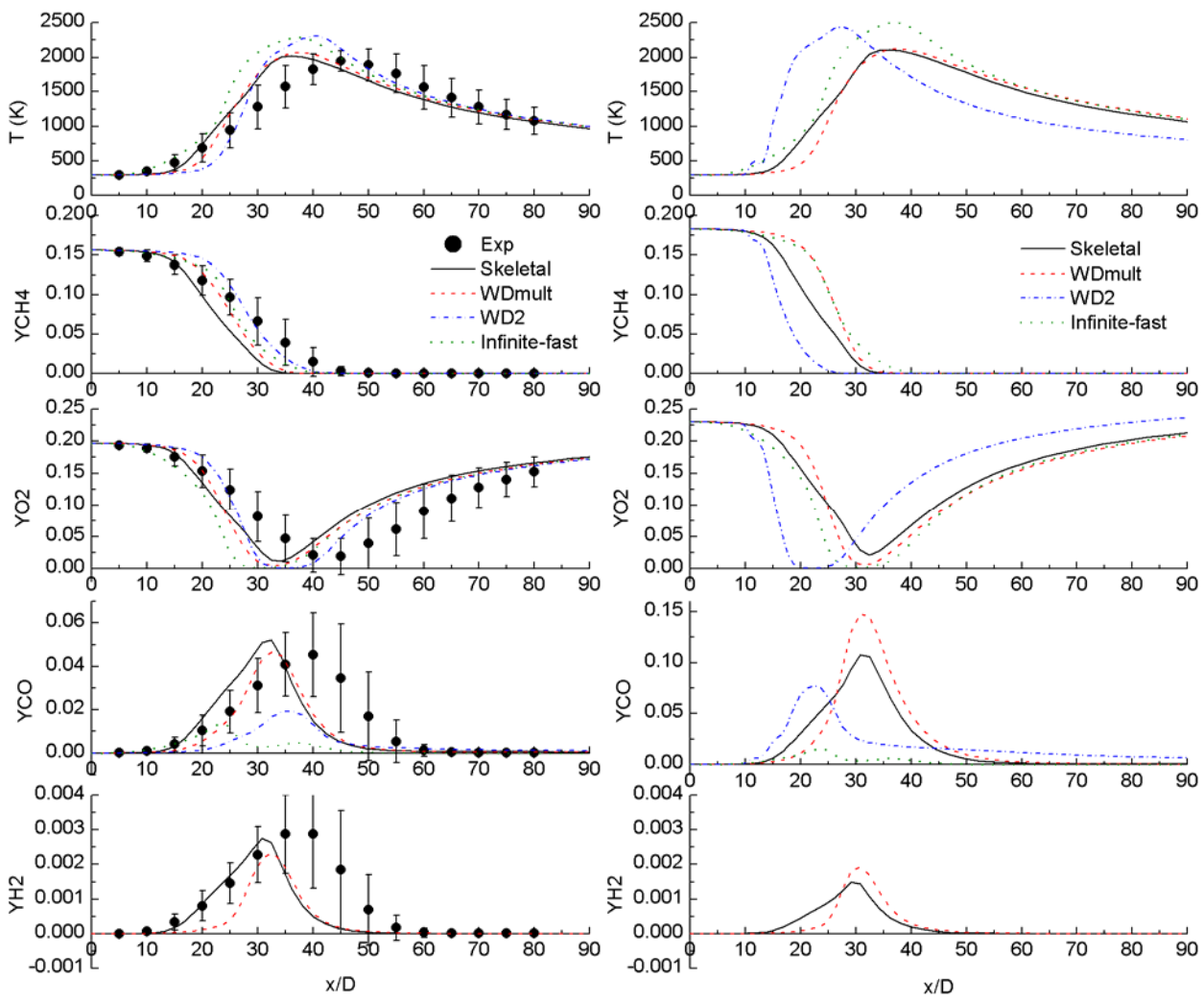

Figure 4-9. Comparison of the measured (scatters) and predicted (lines) axial profiles of temperature, CH_4, O_2, CO and H_2 mass fractions in the Sandia Flame D using skeletal, WDmult, WD2 mechanisms, as well as the infinite fast chemistry model under (a) air-fired and (b) oxy-fuel conditions. Results are shown as function of normalized axial distance (x/D) with a jet flow diameter D=7.2 mm.

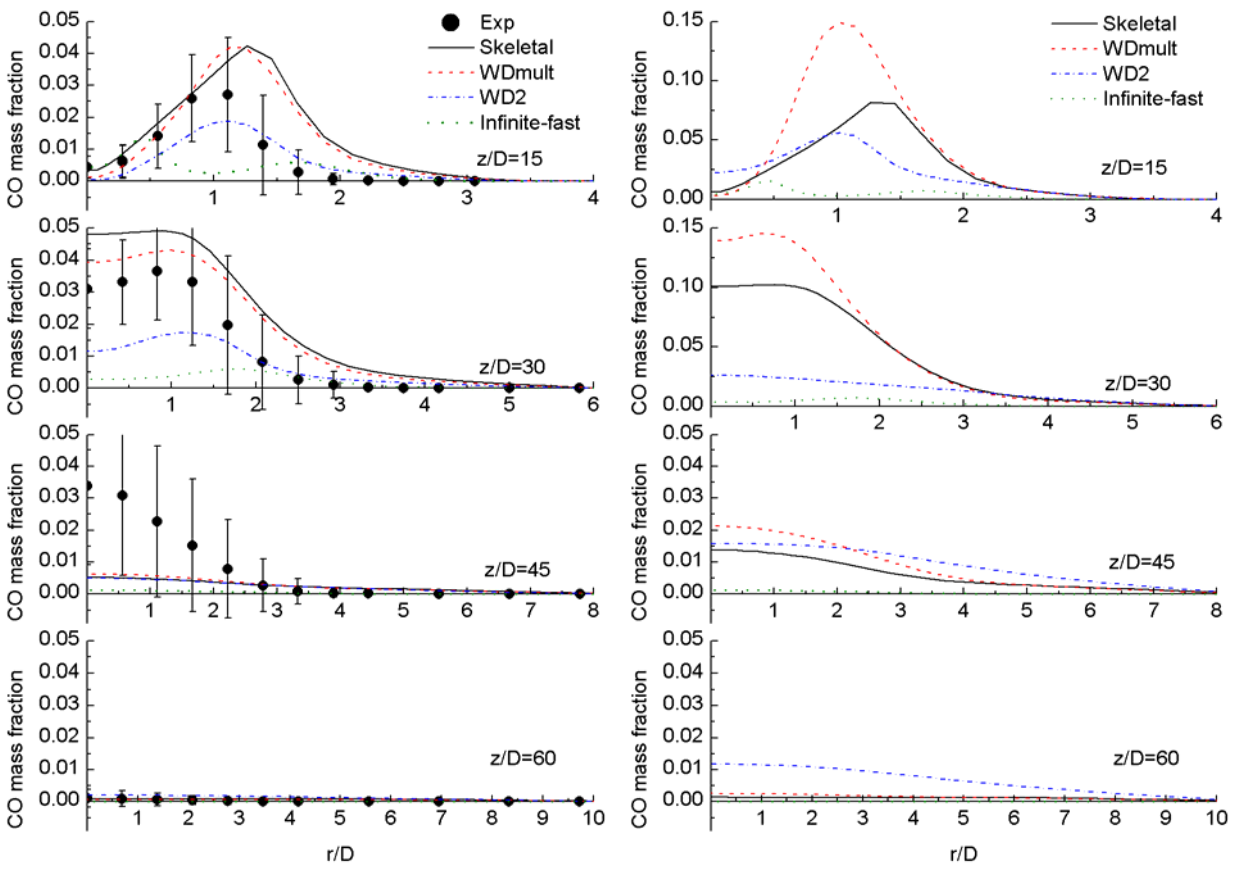

Figure 4-10. Comparison of the measured (scatters) and predicted (lines) radial profiles of CO mass fraction in the Sandia Flame D using skeletal, WDmult, WD2 mechanisms, as well as the infinite fast chemistry model under (a) air-fired and (b) oxy-fuel conditions. Results are shown as function of normalized radial distance (r/D) with a jet flow diameter D=7.2 mm.

The results show that although all the mechanisms can predict the CO concentration in simple one-dimensional diffusion flame, their performances in the turbulent diffusion flame are apparently different. With the qualitative comparison in the Sandia Flame D, the two quasi-global (WDmult) and global (WD2) mechanisms are further tested and their predictions are compared with experimental results in a swirling flow oxy-fuel diffusion flame in the following sub-section.

4.4.4. Swirling Flow Diffusion Flames

The aerodynamics of swirling flow is distinct from the free jet flow. As shown in Figure 4-1(c), in swirling flow combustion, reverse pressure gradient is generated along the axis forcing the hot gas to recirculate and mix with unburned streams in an internal recirculation zone (IRZ), which increases the flame intensity and stabilizes the diffusion flame. Therefore, it has been widely used in gaseous fuels and pulverized coal combustion [178]. The internal recirculation zone features high temperature and fuel-rich stoichiometry, which is favorable for CO formation as discussed in the thermodynamic analysis. In this section, the predicted temperature and species distribution are compared with measurements in the Chalmers 100 kWth test facility. Special attention is given to the CO formation mechanism in a swirling flow diffusion flame, and the performances of different combustion models and reaction mechanisms in such a case.

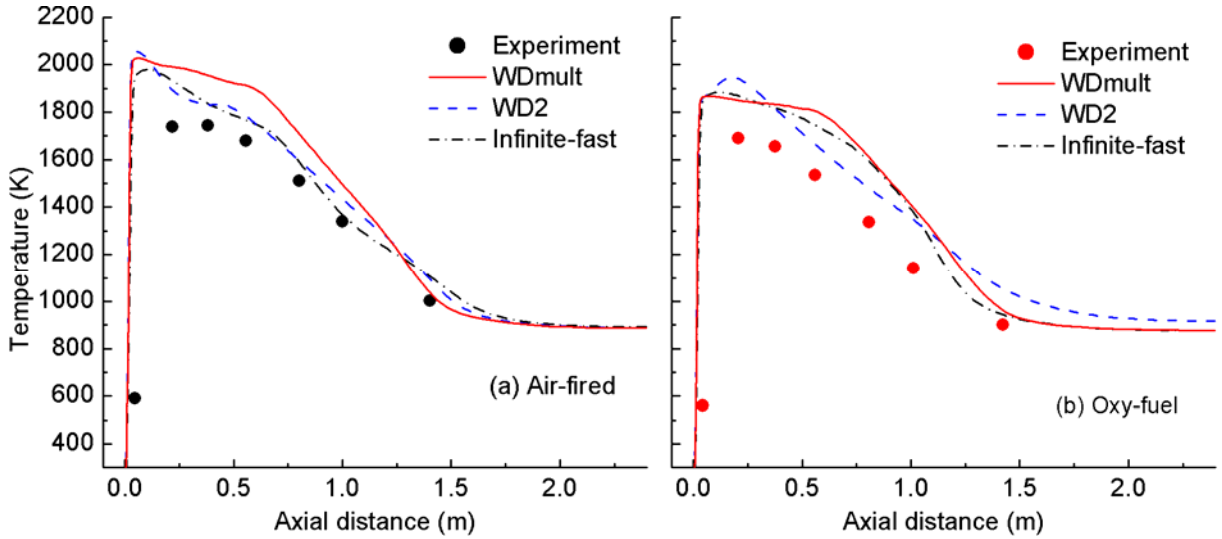

Figure 4-11. Comparison between the measured (scatters) and predicted (lines) radial temperature in (a) air-fired, and (b) oxy-fuel combustion. Simulation results were obtained using different gas phase reaction models and reaction mechanisms. Infinite-fast represents EDM with infinite fast chemistry).

Figure 4-11 show a comparison between the measured and predicted gas temperature along the axis of the furnace under air-fired and oxy-fuel conditions. Satisfactory agreements are obtained with all

approaches. For instance, all the predictions show the temperature rise at the flame zone, which is stabilized near the swirl burner, and a similar declining temperature profile due to mixing and heat transfer downstream. It should be noted that the temperature profiles were improved when the soot formation and its radiation were modeled in both air-fired and oxy-fuel combustion, as also has been shown in ref. [202]. Moreover, the predicted gas temperatures are all slightly higher than the measurements, especially in the flame region, probably because of the fact that not all minor radicals were calculated in the species transport and energy equations.

Figure 4-12 shows a comparison between the measured and predicted oxygen mole fraction radial profiles at x=0.215 and x=0.384 m away from the burner. The EDM shows good match with the measurements under both air-fired and oxy-fuel conditions. On the other hand, the finite-rate mechanisms also agree with the measurement in the air-fired combustion, but slightly lower than those from the EDM, which translates to faster oxygen consumption rates. In the oxy-fuel combustion case, the WD2 mechanism over-predicts the oxygen mole fractions at 0.215 and 0.384 m away from the burner. This again might be due to the non-equilibrium backwards reaction rate [135], whose effect is magnified by high CO_2 concentrations. While the WDmult mechanism shows much better match with the measurement.

(a) Air-fired (b) Oxy-fuel

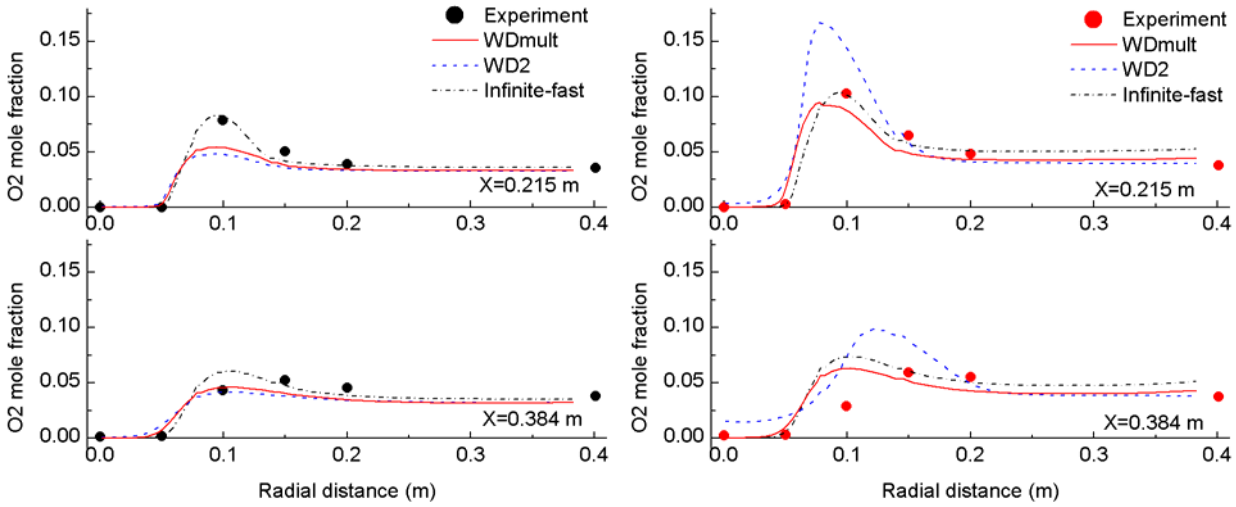

Figure 4-12. Comparison between the measured (scatters) and predicted (lines) oxygen mole fractions (dry basis) at 0.215 and 0.384 m away from the burner in (a) air-fired, and (b) oxy-fuel combustion.

(a) Air-fired (b) Oxy-fuel

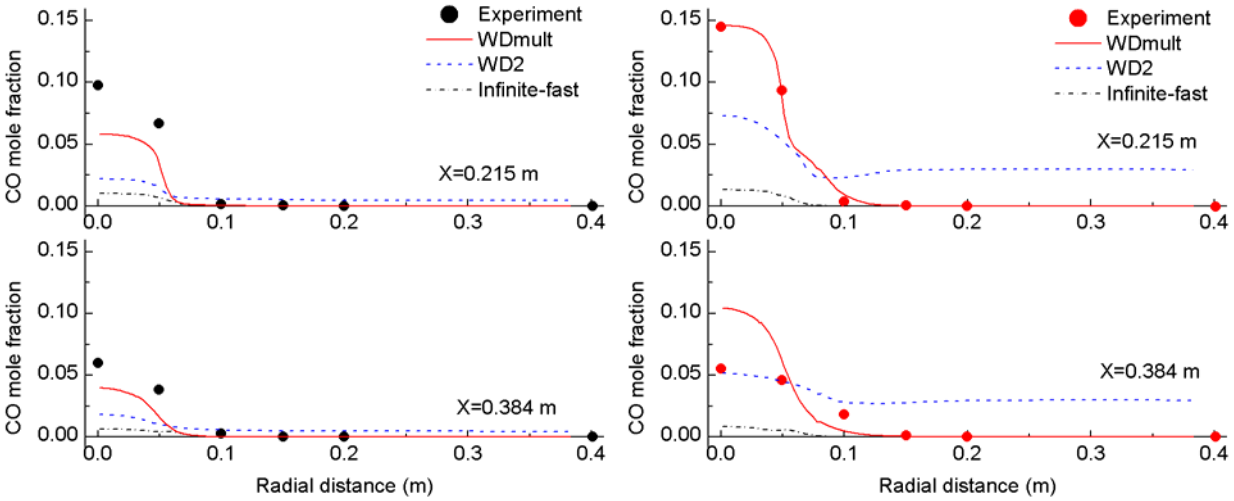

Figure 4-13. Comparison between the measured (scatters) and predicted (lines) CO mole fractions (dry basis) at 0.215 and 0.384 m away from the burner in (a) air-fired, and (b) oxy-fuel combustion.

Similar to that observed in the jet flow diffusion flame simulation, the performances of EDM and EDC models with various reduced mechanisms on CO concentration predictions are apparently different. Figure 4-13 shows the measured and predicted CO radial profiles at x=0.215 and x=0.384 m. Again, the EDM significantly underpredicts the CO concentrations in both air-fired and oxy-fuel combustion, and it cannot show the higher CO trend in oxy-fuel combustion because the reaction rates are assumed to be controlled by the turbulent mixing only, while the chemical kinetics are neglected. The WD2 mechanism improves the CO predictions and shows the higher CO trend in oxy-fuel combustion. However, it still underestimates the CO concentrations in both cases. Note that the original WD2 mechanism cannot approach chemical equilibrium and leads to 1% and 3% residual CO (~1%) in the furnace under air-fired and oxy-fuel combustion, respectively, which has been shown by Andersen et al. [135]. In contrast, the WDmult mechanism significantly improves the CO predictions in both air-fired and oxy-fuel combustion, because it includes the critical reactions discussed in section 4.4.2. These results are consistent with those observed in the jet flow diffusion flame.

We have shown in the 1-D diffusion flame calculation that the $H+CO_2 \rightleftarrows OH+CO$ reaction dominates the higher CO production rate and leads to higher CO concentration in oxy-fuel combustion. This is demonstrated by the EDC model with the WDmult mechanism in the CFD simulation. Figure 4-14 shows the predicted species, velocity, and reaction rates distributions in the air-fired and oxy-fuel flames. The vector flowfield shows that an IRZ is formed by the swirled primary and secondary oxidizer streams (air or O_2/CO_2), which stabilizes the flame in the vicinity of the burner. Similar to the jet flow flame, reactions take place mostly at the diffusion flame sheet between the fuel-rich zone and the oxidizer-rich streams (see Figure 4-14(a)). CO and other active radicals are produced in the fuel-rich side of the diffusion flame sheet (shown in Figure 4-14(b)), and recirculated back to the burner along with the burned hot gases. Figure 4-14(b) compares the reaction rate of $OH+CO \rightleftarrows H+CO_2$ in the air-fuel and oxy-fuel flames. The significantly higher backward reaction rate of $OH+CO \rightleftarrows H+CO_2$ in

the oxy-fuel flame leads to its substantially higher CO concentration in the IRZ.

(a)

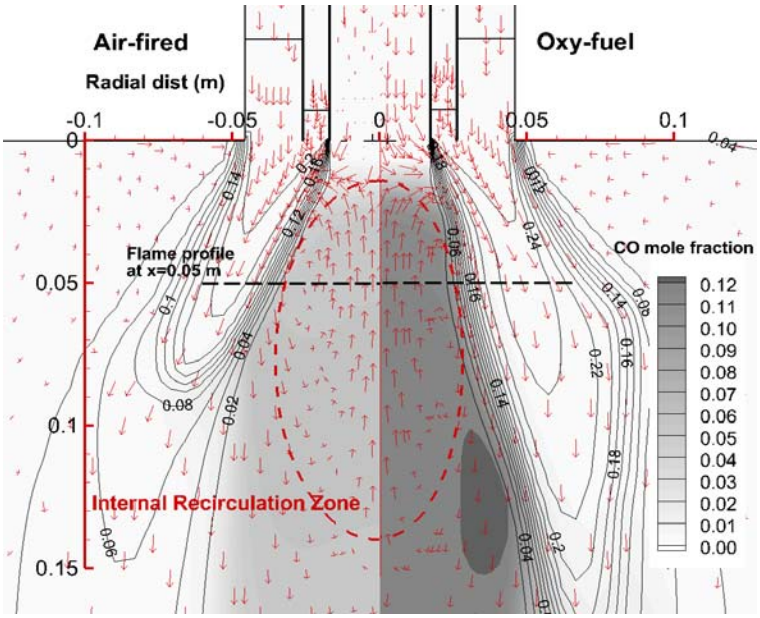

(b)

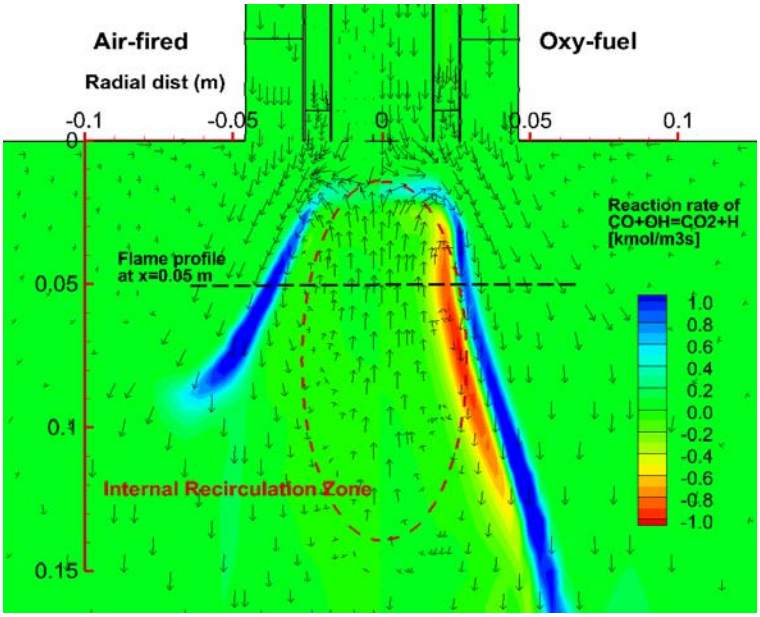

Figure 4-14. Comparison between air-fired (left) and oxy-fuel (right) combustion: (a) the oxygen mole fractions and the carbon monoxide mole fraction shown in isoline and gray contour, respectively; and (b) the reaction rate of $OH+CO \rightleftarrows H+CO_2$ shown in color contour in the vicinity of the swirl burner. The velocity field is shown using

uniform vectors. Results are obtained using the WDmult reaction mechanism.

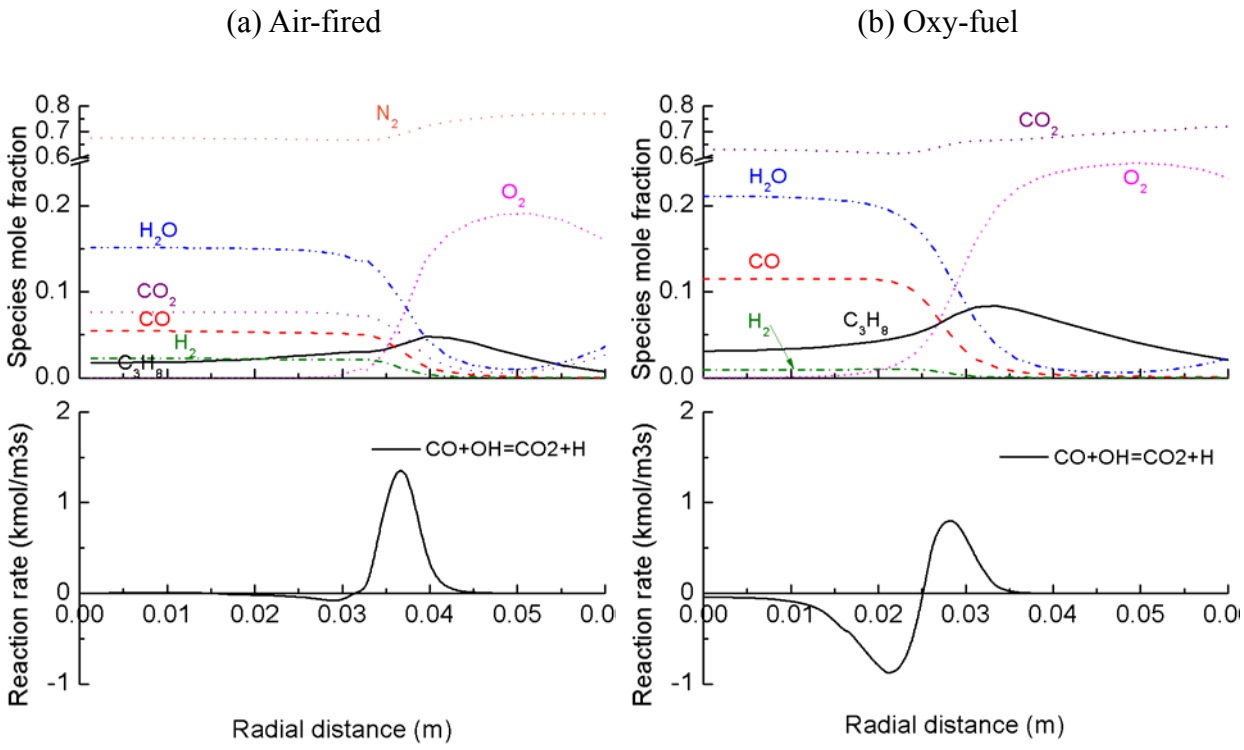

Figure 4-15. Comparison of the flame structures at x=0.05 m away from the burner in (a) air-fired and (b) oxy-fuel swirling flow diffusion flames. Figures show the predicted profiles of species mole fractions and rates of the reaction $OH+CO \rightleftarrows H+CO_2$. Results are obtained using the WDmult reaction mechanism.

Figure 4-15 shows the predicted flame structures at 0.05 m away from the burner under the two operating conditions (the profile location is also illustrated in Figure 4-14). Unlike the jet flow diffusion flame, the species concentrations are uniform around the centerline due to the strong mixing in the IRZ. The species mole fraction profiles indicate a diffusion flame sheet in the interface between the fuel-rich recirculation zone and the surrounding oxidizer streams. Note that higher CO and H_2O, and lower H_2 concentrations are observed in the recirculation zone under oxy-fuel condition. The backward reaction rate of $OH+CO \rightleftarrows H+CO_2$ in the oxy-fuel flame sheet is about 1 kmol/m^{3}s, significantly higher than that (almost 0) in the air-fuel flame, which explains the higher CO concentration in oxy-fuel

combustion. Similar to the 1-D diffusion flame, the high CO_2 concentration also impacts the reaction $OH+H_2 \rightleftarrows H+H_2O$, and results in lower H_2 in the oxy-fuel flame.

4.5. Conclusion

Higher CO concentrations have been observed in oxy-fuel combustion than the traditional air-fuel combustion by previous experimental studies [68, 70]. In this section, the CO_2 chemical effects on CO formation have been investigated using detailed mechanism in a 1-D simulation of the counter flow laminar diffusion flame, and the performances of reduced, quasi-global and global reaction mechanisms have been compared with experimental results in the CFD simulation of jet flow and swirling flow turbulent diffusion flames. The main findings are as follows:

(1) From a thermodynamic point of view, the higher CO concentration observed in oxy-fuel flames can be attributed to the CO_2 thermal dissociation under fuel-rich conditions rather than oxidizer-rich conditions.

(2) The 1-D counter flow diffusion flame simulation using detailed reaction mechanism identifies two reaction pathways through which CO formation is enhanced by the high CO_2 concentration under oxy-fuel condition: (a) the hydrocarbon fragment-CO_2 reactions and (b) the $OH+CO \rightleftarrows H+CO_2$ reaction. The latter one dominates the CO formation, and impacts the $OH+H_2 \rightleftarrows H+H_2O$ reaction, leading to lower H_2 and higher H_2O in the reaction region. The combination effect of the above reactions may be partially represented in the form of water gas shift reaction $CO+H_2O \rightleftarrows CO_2+H_2$ in the fuel-rich side.

(3) The Eddy Dissipation Model with infinite-fast chemistry can be used to predict the temperature and major species in the jet flow and swirling flow turbulent diffusion flame under both air-fired and oxy-fuel conditions, however it fails to predict CO reasonably.

(4) Detailed and reduced mechanisms, such as GRI-mech 3.0 and the skeletal methane mechanism used in this study, fully resolve the CO_2 chemical effect and agree well with the measured CO concentrations. The WD2 global reaction mechanism models the CO_2 chemical effect through the CO_2 dissociation and can capture the higher CO concentration trend in the 1-D diffusion flame. However, it consistently underestimates the CO concentrations in the CFD simulations. The WDmult quasi-global reaction mechanism contains critical elementary reactions, and it is able to capture the chemical effects of CO_2 in oxy-fuel combustion, showing improved performance in both air-fuel and oxy-fuel flame CFD simulations.

Page left intentionally blank

Chapter 5 Pressure's Effects on Oxy-Coal Combustion

In the last two chapters, we have introduced the CFD numerical approaches and submodels, and validated the turbulence models and combustion models specifically for oxy-coal combustion at atmospheric pressure. In this chapter, the validated CFD approach will be "extrapolate" to broader operating conditions under elevated pressures, with appropriate adaption of the submodels taking into account the physics at high pressures. We will focus on the pressure's effects on oxy-coal combustion, and investigate the optimal operating conditions at high pressures.

5.1. Introduction to the Pressurized Oxy-Coal Combustion

Pressurized oxy-coal combustion has been proposed for improved power plant thermal efficiency [34, 48, 203]. Moreover, it is possible that combustion performance could be improved at higher pressure because of the faster reaction kinetics. Enel has carried out experimental studies on the pressurized oxy-coal combustion in a 3 MW_{th} pilot-scale experimental furnace under an operating pressure of 4 bar. Preliminary measurements on the heat transfer, pollutant emissions and flame stability were evaluated while varying the amount of flue gas recycled back to the furnace, the oxygen excess and the burner settings. The experimental tests demonstrated that oxy-fuel combustion can be performed with low-NO_x burners designed for air combustion under the investigated operating conditions, without having any stability problems.

Based on different system configurations and assumptions, previous studies [35, 36, 46] have shown optimal system thermal efficiencies at significantly higher operating pressure (10-80 bar) than

the current tested operating conditions. However, to our knowledge, the effects of elevated pressure on oxy-coal combustion have not been fully investigated. The objective of this study is to examine the effect of pressure on oxy-coal combustion, such as flow patterns, coal conversion time, heat transfer, and slag behaviors. The validated CFD approaches [193] were used to simulate the oxy-combustion under elevated pressures (20 bar and 40 bar), with the distinct physical properties and char reaction kinetics considered in the modeling. Since the conversion time could be different at higher pressure, progressively increasing feeding rates were used in order to find an optimal thermal load at elevated pressures.

5.2. Pilot Scale Experimental Facility

5.2.1. The Test Facility Geometry

The ISOTHERM® pressurized oxy-fuel combustion system was developed by ITEA Spa and Enel and introduced elsewhere [34]. Figure 5-1 shows the schematic geometry of the 5 MWth pressurized CWS oxy-fuel combustion pilot scale test rig (the thermal capacity is 3 MWth in this study). It consists of a partial swirl burner, and a CWS atomizer located a small distance off the axis of the central bluffbody, as shown in Figure 5-2. The flue gas duct and the molten ash port are located at the top and bottom end of the combustor. The refractory wall lined cylindrical combustor is mounted horizontally with a 1.5 degrees slope. The experiments on this test rig showed good environmental performance [204].

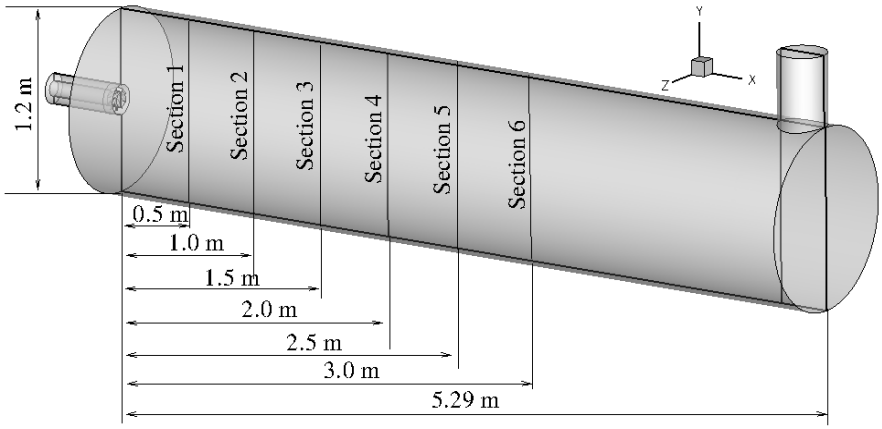

Figure 5-1. Geometry of the pressurized CWS oxy-fuel combustor. The center X-Y plane and vertical traverse lines are highlighted in this figure, showing the cross section where contours and velocity fields are plotted.

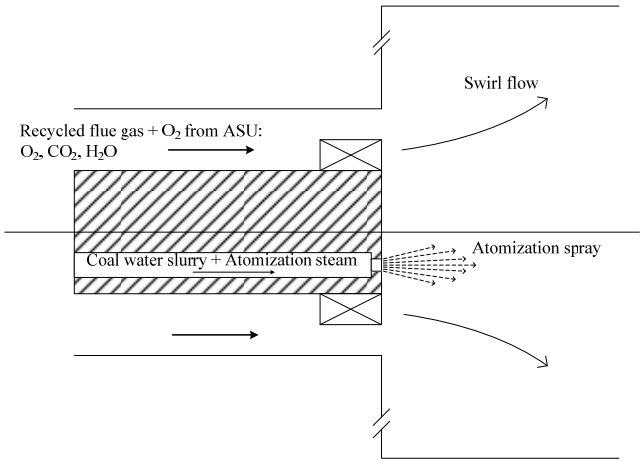

Figure 5-2. Schematic diagram of the swirl burner and coal water slurry effervescent atomizer.

5.2.2. Operating Conditions

A bituminous coal was adopted in this numerical study. Its properties, including approximate and ultimate analysis, are shown in Table 5-1. The base case operating conditions for the burner and CWS atomizer are consistent with those in system analysis [33, 34], while scaled down to 3 MW_{th} for the pilot-scale combustor CFD study, and the details are shown in Table 5-2.

Table 5-1. Coal properties used in this study.

	Unit	Value
Proximate analysis (as received)		
HHV	kJ/kg	29153
Moisture	%	6.4
Ash	%	7.0
Volatile matter	%	33.1
Fixed carbon	%	53.5
Ultimate analysis (dry ash free)		
Carbon	%	82.1
Hydrogen	%	5.43
Oxygen	%	10.5
Nitrogen	%	1.39
Sulphur	%	0.58

Table 5-2. Operating conditions of the oxy-coal burner and atomizer.

	Composition	Mole (Mass) fraction %	Mass flow rate kg/s	Pressure bar	Temperature ºC
Burner stream	O_2	21.9	0.29	4	280
	N_2	3.37	0.038		
	CO_2	36.3	0.56		
	H_2O	38.3	0.24		
CWS	Coal	(65)	0.1	8	37.22
	Water	(35)	0.054		
Atomization gas	Steam	-	0.01	18	265

The combustor is lined with three-layer refractory wall inside of the steel shell, and a water cooling jacket outside of the steel shell. The conductive heat transfer in the refractory wall and the convective heat transfer by the external cooling water were modeled in the CFD thermal boundary condition. The parameters used in the heat transfer model are shown in Table 5-3. Since the convective heat transfer coefficient, *h*, of water cooling tubes is not known, for the case of forced convection by water, it is in the range of 50-10,000 [205]. A convective heat transfer coefficient of 200 W/m^2K was used as an estimated value in the boundary condition.

Table 5-3. Parameters of the refractory wall and cooling system of ISOTHERM combustor

	Parameters	Unit	Value
Refractory wall, ceramic fiber insulation	Thermal conductivity	W/mK	1.13
	Thickness	m	0.221
Cooling water	Temperature	C	45
	Convective heat transfer coefficient	W/m^2K	200

5.2.3. Scaling Strategy at Elevated Operating Pressure

There are several variables in the pressure parametric study: the operating pressure, the mass flow rate, the burner velocity, and the geometry of the burner and reactor, and they are independent when the operating pressure changes. For instance, the gas density increases proportionally at elevated pressure based on the ideal gas law, which results in a reduced velocity and increased residence time, if the geometry and the mass flow rates remain the same. Therefore, two equivalent strategies are reasonable to operate the reactor under elevated pressures:

- Dimension scaling: Fix the mass flow rate (or the thermal load), while reduce the dimension of the burner and reactor under higher operating pressures;
- Mass flow rate scaling: Fix the geometry of the burner and reactor, and increase the mass flow rate progressively under higher operating pressure.

In the present study, we adopted the latter strategy, so that re-scaling the reactor and burner geometry is avoided, and the results can be more comparable with a fixed geometry. Special attention is paid to the coal particle residence time, in order to ensure a high carbon conversion under higher operating pressures. With the objective of optimizing the thermal load of the combustor in mind, simulations with increasing mass flow rates (or burner velocity) were carried out under 20 bar and 40 bar. The low mass flow rate (termed as LV) cases were chosen to match the reference design's axial momentum flux at 4 bar; and the median mass flow rate (termed as MV) cases maintain the identical axial burner velocity in the reference design; the high mass flow rate (termed as HV) cases are aggressive designs, with a burner velocity that doubles the reference case burner velocity. The operating conditions of the seven CFD cases are listed in Table 5-4, showing the mass flow rate of the burner oxidizer, coal water slurry, as well as the steam used for atomization.

The same burner oxidizer composition and overall stoichiometry ($\lambda \approx 1.057$) is used for all the

simulation cases for comparison. Similarly, identical atomization steam to CWS mass flow rate ratio was used in all the simulation cases in order to ensure a good atomization effect. However, the atomization stream pressure has to be increased by ~20 bar higher than the reactor pressure in order to maintain choked condition, and the steam has to be heated up to 327 ^{o}C and 427 ^{o}C at 20 bar and 40 bar, respectively, in order to avoid condensation during the atomization process. Moreover, the coal water slurry droplet size distributions were assumed to be the same with the reference 4 bar case.

Table 5-4. Operating conditions of the burner and atomizer under elevated pressures

Case	Ref. case	20-LV[a]	20-MV[a]	20-HV[a]	40-LV[a]	40-MV[a]	40-HV[a]
Operating pressure (bar)	4	20	20	20	40	40	40
Burner velocity (m/s)	Median	Low	Median	High	Low	Median	High
Nominate thermal load (MW)	3	7	15	30	10	30	60
$\dot{m}_{oxidizer}$ (kg/s)	1.148	2.566	5.738	11.475	3.629	11.475	22.950
$\dot{m}_{CWS}$ (kg/s)	0.154	0.344	0.769	1.538	0.486	1.538	3.077
$\dot{m}_{\text{atom steam}}$ (kg/s)	0.01	0.022	0.05	0.1	0.032	0.1	0.2
Stoichiometry[b]	1.187	1.187	1.187	1.187	1.187	1.187	1.187

a LV/MV/HV: Low/Median/High burner Velocity

b This is the stoichiometry in the combustor, taking the recycled oxygen into account.

5.3. Numerical models

5.3.1. Modeling Approaches

FLUENT 12.0.16 was used in this study, with the validated submodels described in our previous oxy-coal combustion validation study [193]. A 3D mesh including 266,717 hexahedral and tetrahedral elements was constructed coupling the flow field in the burner duct, the flow across the swirlers, and the combustion chamber together, so that the effects of the swirlers on pressure drop and turbulence can be captured in the simulation.

The Realizable $k-\varepsilon$ model of the Reynolds Average Navier Stocks (RANS) approach was chosen for turbulence modeling because of its higher accuracy for weak swirling flows [206], and the

SIMPLE algorithm was used for pressure-velocity coupling. The eddy dissipation model was used to compute the gas phase reaction source term, in which the reaction rate is determined by the turbulent mixing, while detailed chemical kinetics were neglected. This assumption is valid for stable combustion, but it has limitations on predicting intermediate species such as CO and H_2. Detailed introduction on the CFD framework is presented in reference [193], and is left out in this report. The ideal gas law was used to calculate the gas density at the elevated operating pressures.

It should be mentioned that the pressure influences physical properties and char combustion kinetics, correspondingly, related submodels were modified, taking the pressure's effects into account in the CFD simulations, which is discussed in greater detail below.

5.3.2. Modeling the Coal Water Slurry Atomization

An effervescent CWS atomizer is used in the combustor, and its properties such as the spray angle, droplet velocity and droplet size distribution were calculated using experimental observations and correlations by Sojka and Lefebvre [207] and Sovani et al. [208]. The estimated CWS droplet velocity is 50.11 m/s, with a Sauter Mean Diameter (SMD) of 134 micron.

A total of 3000 atomized CWS droplets with 50 different sizes sampled from a Rosin-Rammler distribution are tracked using Lagrangian approach. Since experiments showed that the coal particles in a CWS droplet tend to agglomerate [209, 210], each droplet is modeled as a one phase sphere consisting of water and an agglomerated coal particle. The water content evaporates and boils at the saturation temperature (for instance, 143 ºC at 4 bar pressure) before devolatilization and burning occur.

5.3.3. Modeling the Physical and Chemical Processes at High Pressure

Higher operating pressures have significant effects on the physical properties and chemical kinetics, which may result in different turbulence intensity, heat and mass transfer, and heterogeneous

reaction rates. For instance:

- Increased gas density, and increased drag force on the particles;
- Increased saturation temperature and delayed slurry droplet evaporation/boiling process;
- Retarded volatiles mass diffusion in coal porous structure, secondary pyrolysis reactions and decreased total volatile yields;
- Saturation of the active sites for heterogeneous reactions on the char surface and reduced reaction order at higher pressure;

The different physical properties (density and saturation temperature) were modeled using the ideal gas law and piece-wise linear formula in the simulation. The reduced volatile yield effect was captured by the CPD model [211] using a pre-processing approach. Similar to the oxy-char combustion model used in Chapter 3, three surface reactions were taken into account as follows:

$$2\mathrm{C(s)}+\mathrm{O_2} \rightarrow 2\mathrm{CO} \qquad \text{(R.1)}$$

$$\mathrm{C(s)}+\mathrm{CO_2} \rightarrow 2\mathrm{CO} \qquad \text{(R.2)}$$

$$\mathrm{C(s)}+\mathrm{H_2O} \rightarrow \mathrm{CO}+\mathrm{H_2} \qquad \text{(R.3)}$$

The total reaction rate for each of the heterogeneous reactions, r_i, is computed by:

$$r_i = \pi d_p^2 \frac{r_{kin,i} r_{diff,i}}{r_{kin,i} + r_{diff,i}} \qquad (5.1)$$

where d_p is the char particle diameter, and $r_{kin,i}$ and $r_{diff,i}$ are the kinetics controlled and bulk diffusion controlled reaction rates, respectively, for reaction i. The kinetics controlled reaction rate is calculated using the N^{th} order equation:

$$r_{kin,i} = A_i T_p^{\beta_i} \exp\left(\frac{-E_i}{R_u T_p}\right)\left(\frac{p_i}{10^5}\right)^{n_i} \qquad (5.2)$$

where T_p is the particle temperature, p_i is the partial pressure for species i, R_u is gas constant. A_i,

β_i, and E_i are pre-exponential factor, temperature order, and activation energy for reaction i, respectively, taken from literature for high pressure char oxidation and gasification [206], which are summarized in Table 3-3.

Table 5-5. The kinetics parameters and diffusion coefficients for the oxy-char surface reactions.

Reaction	A_i $kg/\left(m^2 sPa^n\right)$	E_i kJ/mol	β_i	n_i
R.1	300	130	0	0.65
R.2	2224	220	0	0.6
R.3	42.5	142	0	0.4

The diffusion controlled reaction rate is calculated by:

$$r_{diff,i} = C_i \frac{\left[\left(T_p + T_\infty\right)/2\right]^{0.75}}{d_p} p_i \qquad (5.3)$$

where T_∞ is the temperature of the surrounding gas, and the diffusion constant, C_i, is calculated by:

$$C_i = \nu_i MW_c \frac{1}{R_u T_0^{1.75}} Sh \cdot DF_{i,0} \frac{P_0}{P} \qquad (5.4)$$

where ν_i is the stoichiometric coefficient of carbon relative to the gas phase reactant i, MW_c is the molecular weights of carbon. T_0 and P_0 are the reference temperature and pressure for the binary diffusivity DF_0. P is the operating pressure of the reactor. Sh is the Sherwood number for the sphere particle. Note that C_i is inversely proportional to the operating total pressure.

The char consumption model was implemented into the CFD platform as user defined function (UDF), which is provided as Appendix of the report.

5.4. Results and Discussions

5.4.1. Reference Case at 4 bar

5.4.1.1. Flowfield

The velocity vector fields in the central cross-section of the combustor in XY and XZ planes are plotted in Figure 5-3. Figure 5-3(a) shows that in the vertical XY plane, a strong turbulent jet enters the combustor with a velocity magnitude of 20 m/s, which generates a large reversed flow zone at the top part of the combustion chamber through the length of the reactor. In contrast, the velocity distribution in the horizontal XZ plane shown in Figure 5-3(b) is more symmetric.

A close look at the velocity distribution in vicinity of the burner is shown in Figure 5-4. The oxidizer flow (mixture of O_2 and recycled flue gas) from the partial-swirl burner couples with the coal water slurry atomization spray, and this forms a high velocity jet in the along the axis. Since the tangential velocity is not high, no internal recirculation zone is observed in the burner flow downstream. The tangential momentum and its swirling effect will be discussed in greater detail later. Again, the vectors show an evident recirculation zone in the top part of the reactor space (Y>0).

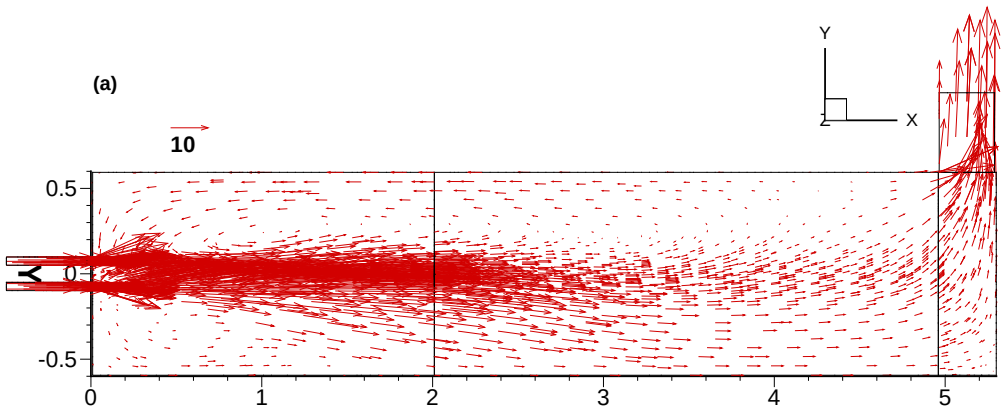

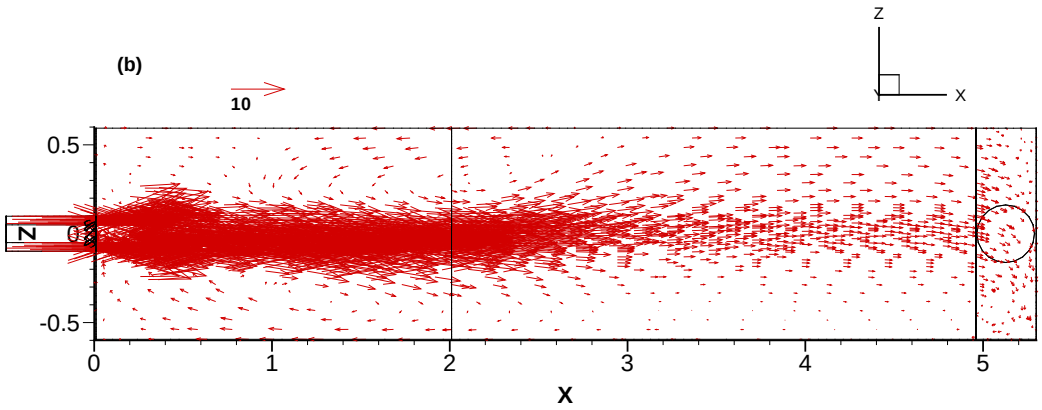

Figure 5-3. Gas velocity vector field in the combustor: (a) central cross section in XY plane. (b) central cross section in XZ plane.

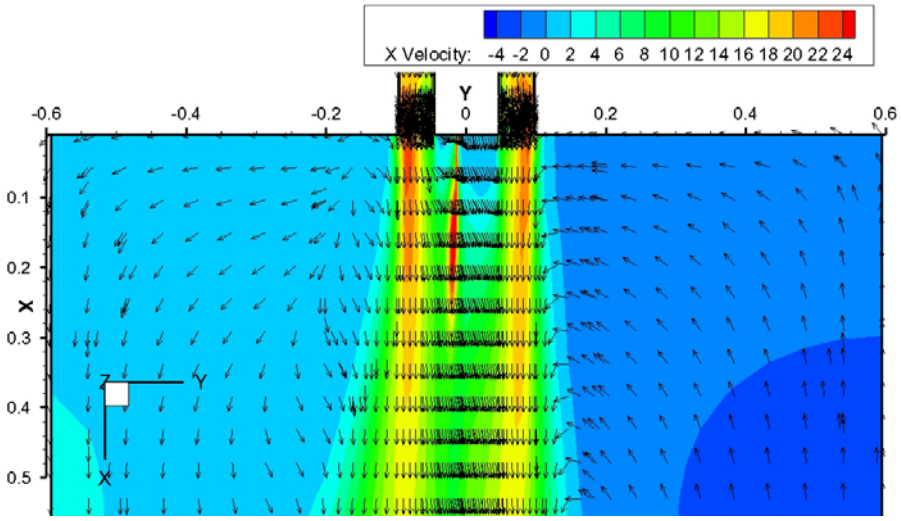

Figure 5-4. Gas velocity vector field in vicinity of the burner. Vectors of uniform length show the flow directions, and background color show the magnitude of the axial velocity (V_x).

The axial and tangential velocity distribution along the vertical traverses at different axial locations (i.e., the section 1-6 in Figure 5-1) is shown in Figure 5-5: the axial velocity is high in vicinity of the burner and it decays due to the entrainment of the recirculated gas. The negative velocity at the topside shows the maximum reversed flow velocity is ~5 m/s. This asymmetric flow field is caused by the asymmetric geometry of the flue gas duct arrangement, and was experimentally observed during the tests at the pilot plant.

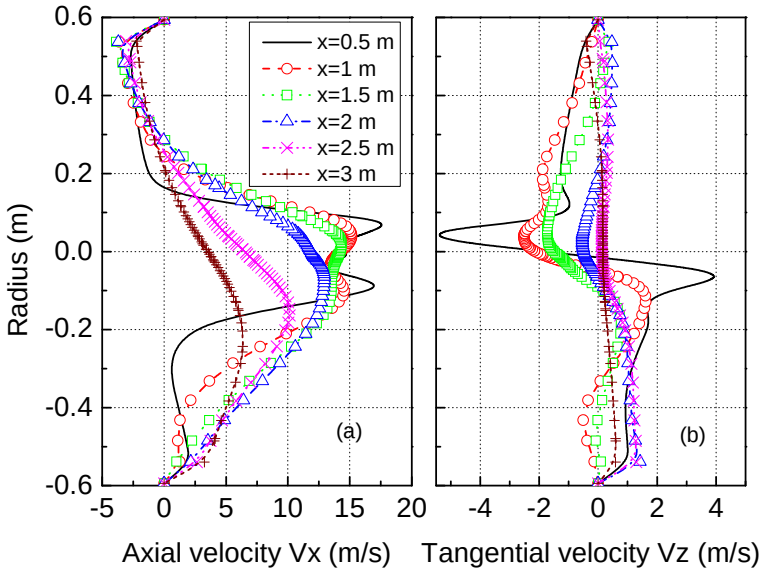

Figure 5-5. Axial (a) and tangential (b) gas velocity profiles of traverses at different axial locations.

The burner implements partial axial swirl blades to generate tangential momentum and enhance the mixing between oxidizer stream and the CWS spray. The swirl number (S') characterizing the effect of the swirl flow is defined as [178]:

$$S' = \frac{G_\varphi}{G_x' R} = \frac{2\pi \int_0^R (Wr)\rho U r dr}{2\pi \int_0^R \rho U^2 r dr \cdot R} \qquad (5.5)$$

Based on the 3D CFD simulation results, it is ~0.18, indicating that it is a relatively weak swirling flow. The tangential velocity shown in Figure 5-5(b) decays faster than the axial velocity: the maximum tangential velocity decreases from 15 m/s at the burner outlet to 5 m/s at x=0.5 m.

Figure 5-6 shows the mass flow rate and sensible enthalpy flow rate of gas phase at different axial locations. The net gas phase mass flow rates increase from ~1.2 kg/s to ~1.3 kg/s due to the evaporation of water and consumption of carbon in coal, while the recirculated mass flow rate (shown as negative in Figure 5-6(a)) varies from 0.4-1.0 kg/s. The recirculated mass contains ~2.5 MW sensible enthalpy, which is entrained and mixed with the unburned gas stream. The hot gas recirculation speeds up the evaporation of the water content in the CWS droplets, and facilitates the ignition of the volatiles.

The flow field in the ISOTHERM oxy-coal reactor governs the combustion characteristics. As it will be discussed in greater detail in the following sections, the hot gas recirculation in the reactor creates even temperature and species distributions, dilutes the reactions and results in some MILD combustion effects.

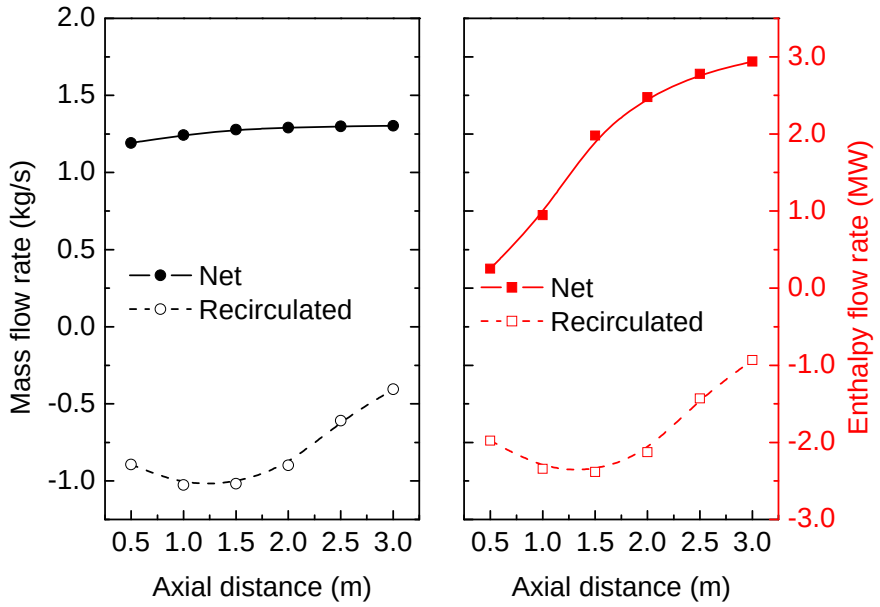

Figure 5-6. Net and recirculated gas phase mass and enthalpy flow rate of the YZ cross-sections at different axial locations.

5.4.1.2. Gas temperature Distribution

Figure 5-7 shows the temperature distribution in the combustor. The cold burner stream core is enveloped by hot burned gas in vicinity of the burner, and the high temperature gradient indicates a diffusion and combustion zone up to about 3 m downstream the burner exit. The gas temperature increases from 500-600 K to 1700 K at x=2.5 m, and remains at ~1800 K for most of the combustion chamber. Similar to that observed in the flowfield, Figure 5-7(a) shows an asymmetric temperature distribution: the cold unburned stream goes down towards the bottom of the combustor because of the asymmetric arrangement of the flue gas exit. On the other hand, the temperature distribution in the horizontal plane as shown in Figure 5-7(b) is much more symmetric.

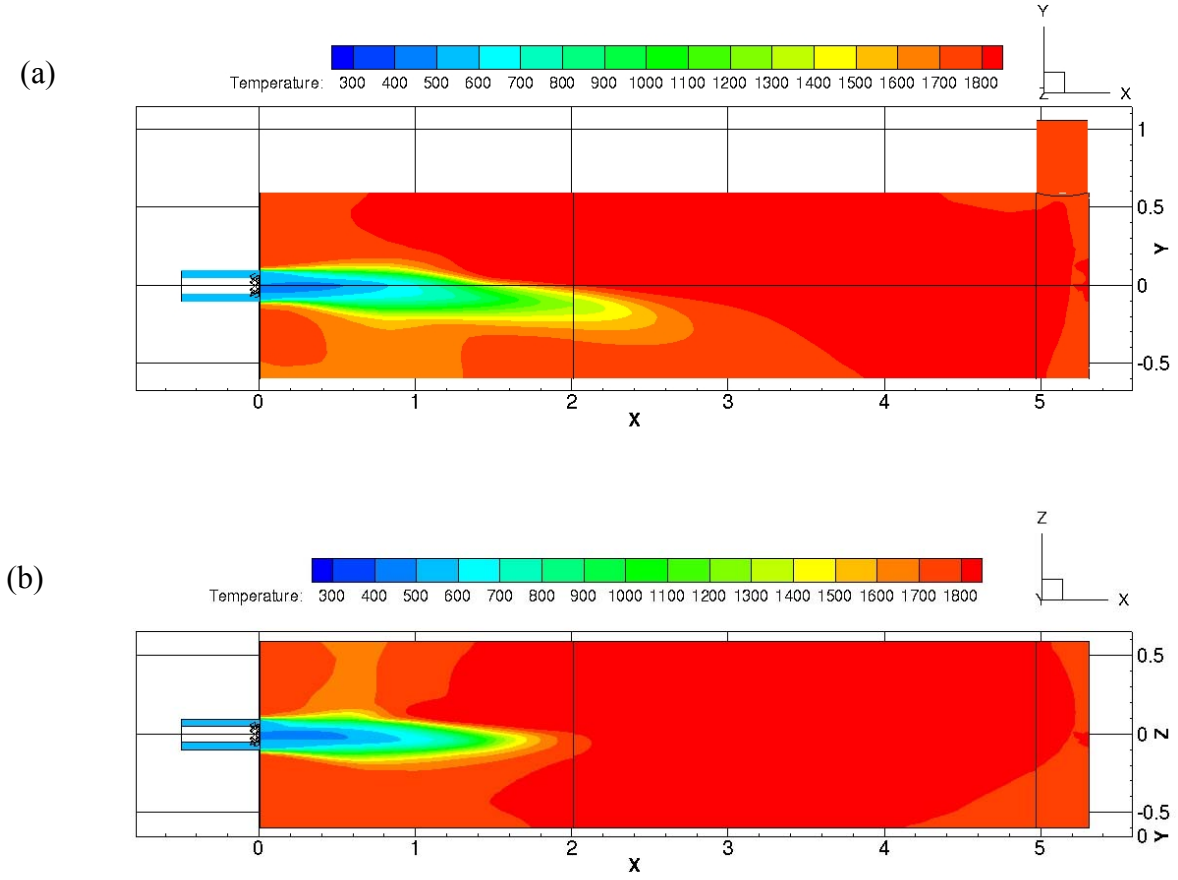

Figure 5-7. Gas temperature distribution in the central XY and YZ cross-sections in the combustor.

It is notable that the temperature distribution is so even that there are no extremely high temperature regions in the combustor. This is a result of the large volume hot gas recirculation as discussed in 5.4.1, and it indicates a potentially low NO formation. Further studies on the pollutant formation are needed in the future.

5.4.1.3. Species Distribution

Figure 5-8(a) to (f) shows the distribution of gas species in the combustor, and indicates the reaction processes during the oxy-coal combustion. As shown in Figure 5-8(a), the volatiles begin to be released at about 0.5 m, and the maximum mass fractions ($\sim 1.5 \times 10^{-2}$) are at ~1 m away from the atomizer. The volatile distribution indicates the location where most of the coal water slurry is dried out and devolatilization occurs. The volatiles exist throughout a distance of 0.5 to 2 m because the

evaporation times vary with particle sizes. For small particle, the evaporation time is shorter and its velocity decays faster, so its devolatilization occurs faster compared with large particles. Figure 5-8(b) and Figure 5-8(c) show the H_2 and CO distributions produced by decomposition of the volatiles, the secondary pyrolysis of tar, as well as the char combustion and gasification reactions. The major source of CO is the char oxidation since its concentration is higher than volatiles. The CO mass fraction is above 4×10^{-3} at a wide range from ~1 m to 3 m downstream the burner, showing where the char burning reactions take place. The maximum CO mass fraction is about 1.2×10^{-2}, which is lower than the values reported in other oxy-coal combustion experimental studies [70, 78] (typically ~10%). The lower maximum species fraction is attributed to the dilution by the burned gas at vicinity of the burner. The O_2 concentration, therefore, decreases due to the consumption of volatile and H_2/CO oxidation and char burning, as shown in Figure 5-8(d).

Figure 5-8(e) and Figure 5-8(f) show that CO_2 dominates the gas phase throughout the whole combustor, and it increases from 50% in the burner stream to 64% at the flue gas duct, while H_2O concentration increases from 26% in the burner stream to 29% at x=1.5 m due to the water evaporation of the CWS, the mixing with the atomization steam and the combustion product of the hydrogen contents of coal. Triatomic gases consist of more than 70% of the gas throughout the combustion environment, and even higher (92%) at the end of the combustion process. Since the total emissivity of the triatomic gases increases with increasing temperature, the partial pressure of the gases, and the beam length, the elevated partial pressure of CO_2 and H_2O in the oxy-fuel combustor substantially enhances the radiative heat transfer compared to the air combustion. The radiation characteristics are discussed in a second paper (Part II) of this study.

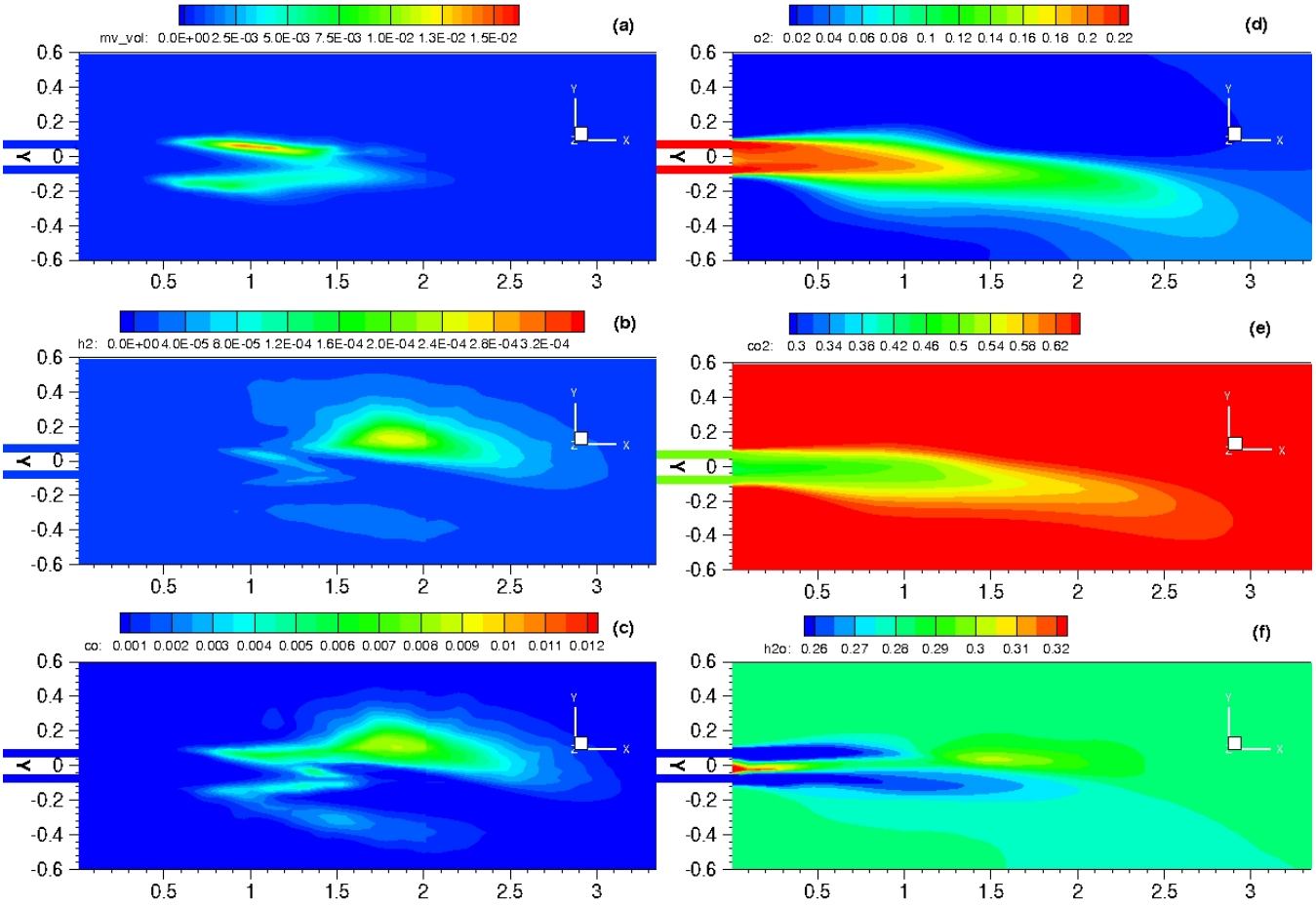

Figure 5-8. Distribution of mass fractions for gaseous species: volatile, H_2, CO, O_2, CO_2, and H_2O in the central X-Y cross-section. Figures only show axial range of 0-3.3 m where combustion reactions take place.

5.4.1.4. Coal Water Slurry Droplet Fate

Coal water slurry droplets were injected into the computational domain in accordance with the experimental correlations as introduced in section 5.3.2. The motion of particles is calculated in a Lagrangian reference frame using force balance:

$$\frac{du_p}{dt} = F_D\left(u - u_p\right) + \frac{g_x\left(\rho_p - \rho\right)}{\rho_p} \qquad (5.6)$$

where u and u_p are velocities, and ρ and ρ_p are the densities of the gas and particle, respectively. The gravity is considered in the second term on the right side, while the drag force to the particle, F_D, is considered as:

$$F_D = \frac{18\mu}{\rho_p d_p^2} \frac{C_D \mathrm{Re}}{24} \qquad (5.7)$$

where C_D is the drag coefficient taken from [212], μ is the molecular viscosity of the fluid, and d_p is the particle diameter. Re is the relative Reynolds number, defined as:

$$\mathrm{Re} = \frac{\rho d_p \left| u_p - u \right|}{\mu} \qquad (5.8)$$

Therefore, the particle trajectories depend on particle size and density, its initial velocity, as well as the surrounding gas environment (velocity and compositions). Figure 5-9 shows 3 typical trajectories of 100 um droplet/particle, and the effect of particle size on its velocity decay is shown in Figure 5-10.

It can be seen in Figure 5-10 that all particles start from a velocity of about 52 m/s at the orifice of the atomizer, however, the velocity decays at different rates for different sizes. Smaller droplets/particles decay faster, and large particles slower, because larger particles has a higher initial momentum, with which they can penetrate a longer path downstream the burner. The distinct trajectories also influence the drying, devolatilization and reaction process of the coal water slurry droplets and coal particles.

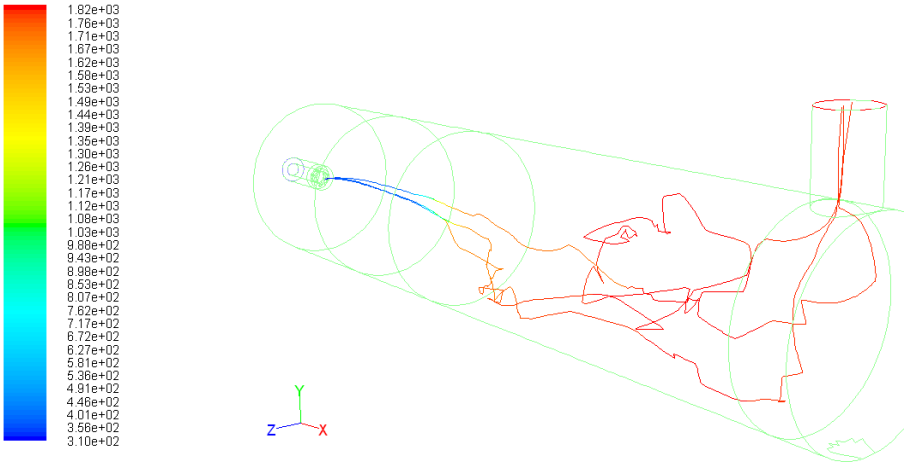

Figure 5-9. Trajectories of sampled coal water slurry droplets (100um) in the reactor. Color shows the particle temperature (K).

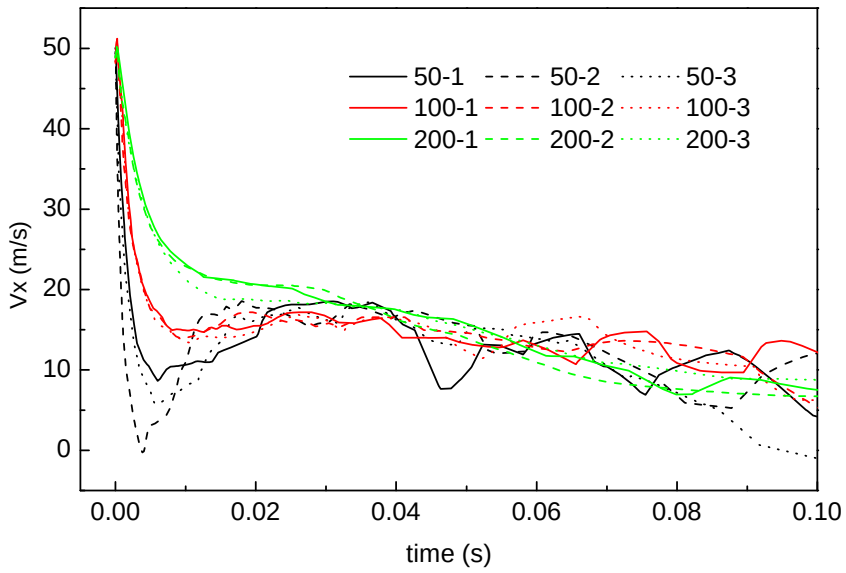

Figure 5-10. Axial velocity decay of sampled coal water slurry droplets with different initial diameters. 3 samples were presented in the figure for each diameter.

The mass and temperature histories of sampled droplets with four typical sizes (50, 100, 200, and 500 μm) are compared in Figure 5-11. The weight loss shows the evaporation/boiling, inert heating, devolatilization and char burning processes with corresponding time scales. Larger droplets take significantly longer to heat up, dry out, and burn. The 50 μm droplet burns out within 0.3-0.4 s, during which the water content evaporation and devolatilization takes as much time as char burning; the 200 μm droplet, however, burns out in about 1 s, and char oxidation takes most of the time (0.9 s). It is notable that agglomeration [209, 210] and fragmentation [213] has been discovered in previous experimental studies on CWS combustion. Since the particle history (velocity, temperature, and mass loss) depends on particle size, the above phenomena responsible for altering particle size should be considered in future development of the model.

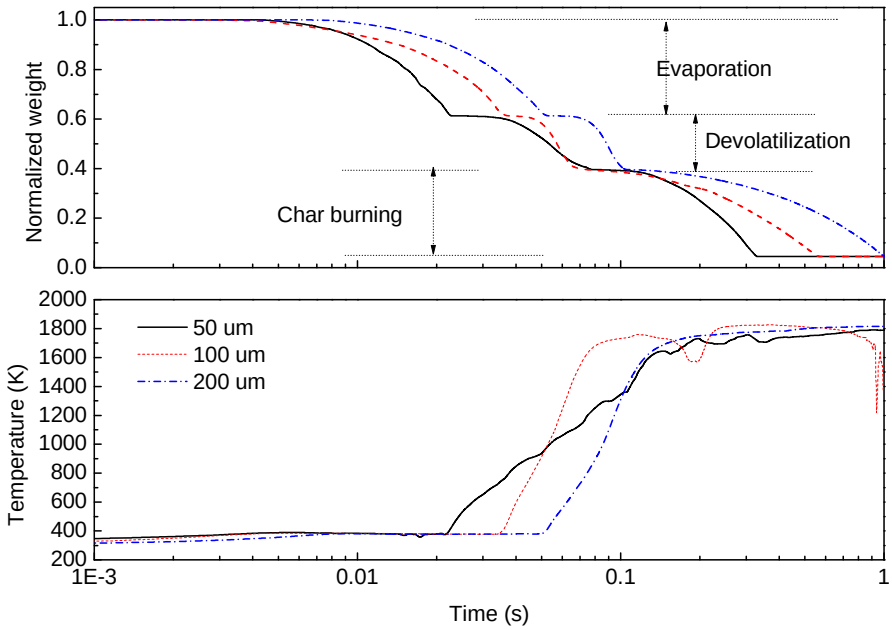

Figure 5-11. Mass and temperature histories of sampled CWS droplets in different sizes show the evaporation, devolatilization, and char burning time scales.

A statistic study of the time needed for moisture content evaporation, devolatilization, and 95% char conversion of the CWS droplet was carried out based on sampled discrete phase trajectories in the CFD modeling. The carbon conversion is defined as the proportion of carbon contents converted to gas phase in raw coal particle. Figure 5-12 shows the time average and its standard deviations calculated from 300 stochastic trajectories of specific sizes. It can be seen that the conversion time increases almost linearly with the increasing CWS droplet size: the average total conversion times are about 0.3 s, 0.6 s, and 1.4 s, for 50, 100 and 200 μm diameter coal water slurry droplets, respectively. And the conversion time is dominated by char conversion.

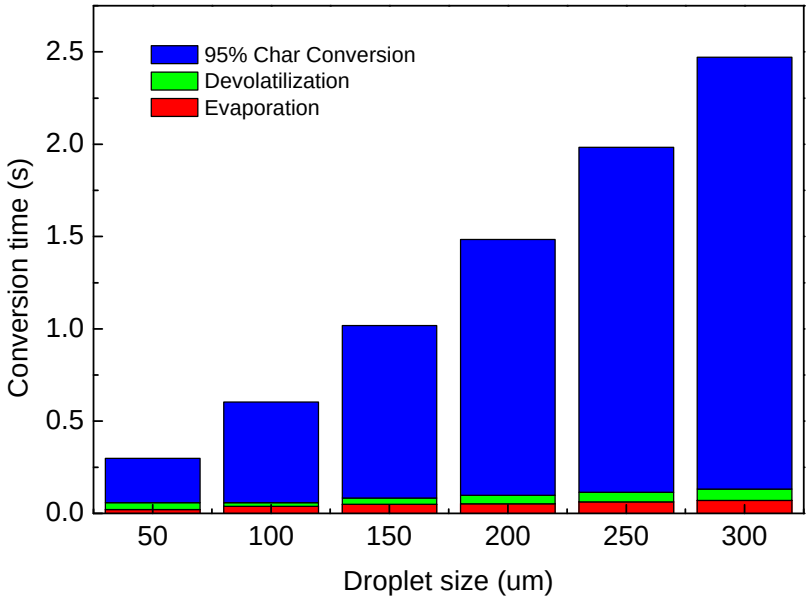

Figure 5-12. Statistic of the time for evaporation, devolatilization, and 95% carbon conversion of the coal particle, as a function of the CWS droplet size.

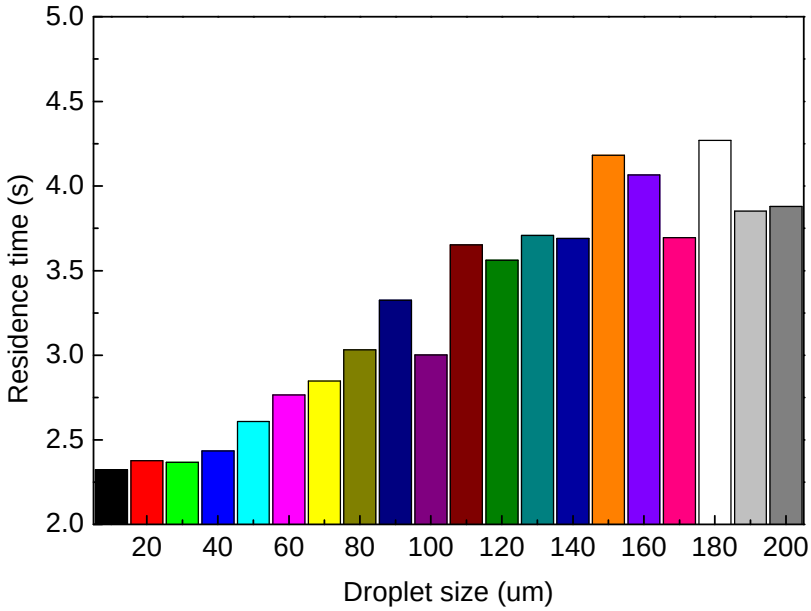

Figure 5-13. Average residence time of CWS droplets as a function of the droplet size.

Comparing with the 95% carbon conversion times, the residence times of the particles are long enough for a high conversion ratio. Figure 5-13 shows the residence time of coal water slurry particles as a function of the particle size. The average residence times are above 2 s for all the particle sizes, while

they increase with the increasing particle size.

5.4.2. Oxy-Coal Combustion at Elevated Pressures

In the previous study, the oxy-coal combustion characteristics under the identical tested operating conditions have been investigated using CFD, such as the flowfield, gas temperature and species distribution, coal water slurry droplet and char particle oxy-combustion processes. Results show a uniform distribution of chemical reactions and gas temperature with high carbon conversion under the reference operating conditions. In the following sections, the flowfield, gas temperature distribution, oxy-char combustion processes, residence time, heat transfer, and slag behaviors are compared under the investigated operating conditions. Special attention is given to the effects of pressure and burner velocity on the oxy-coal combustion processes, and the optimal operating conditions at elevated pressure.

5.4.2.1. Flow field and temperature distribution

As discussed in Part I and Part II report, the ISOTHERM flowfield is a confined jet flow with external recirculation, formed by the burner and atomizer injection confined by the cylindrical wall boundaries in this combustor. Figure 5-14 compares the axial velocity contour of the computed cases. It can be seen that the overall flowfield characteristics are similar to the reference case at 4 bar for all the 20 bar and 40 bar cases, while pressure does not change the flow significantly. However, the flow pattern is apparently different depending on the burner velocity. Higher velocity magnitude, longer jet penetration depth, and larger recirculation zone size are observed at higher burner velocities.

It is interesting to see in the bottom of Figure 5-14, that the jet flow becomes stronger and more uniform under the high burner velocity operating conditions than the reference case (with median burner velocity). The high burner axial velocity of 40 m/s from the burner has a stronger axial momentum, which results in longer penetration in the centerline of the reactor, and more uniform

flowfield in the combustor.

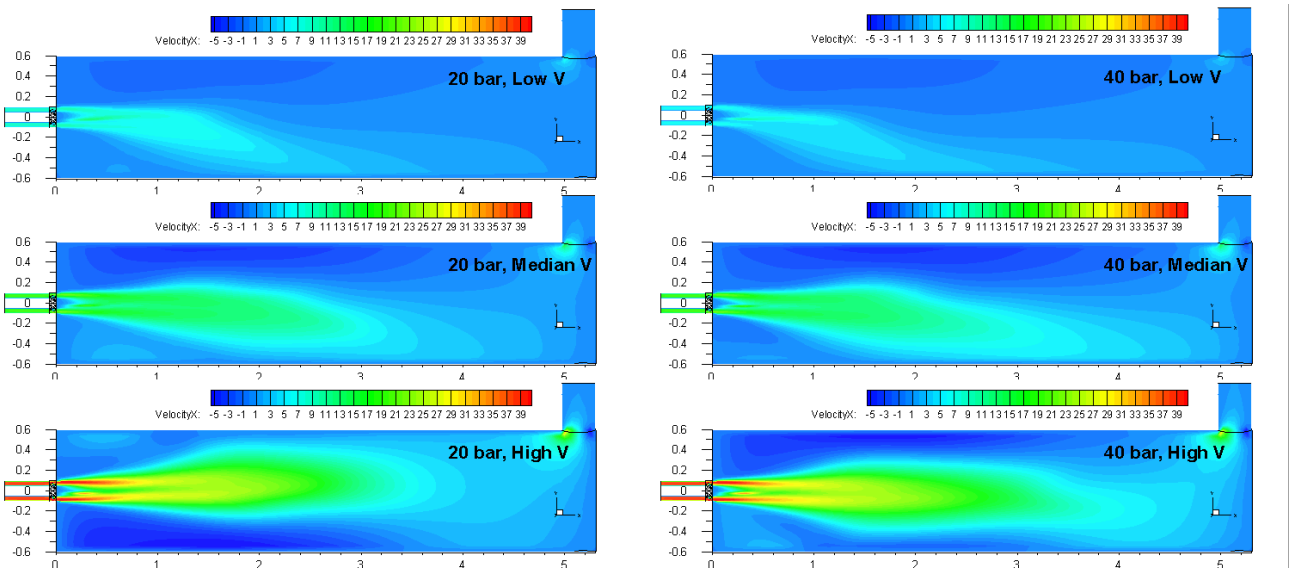

Figure 5-14. Comparison of the axial velocity (m/s) distributions among cases with low/median/high velocity under 20 bar and 40 bar operating pressures.

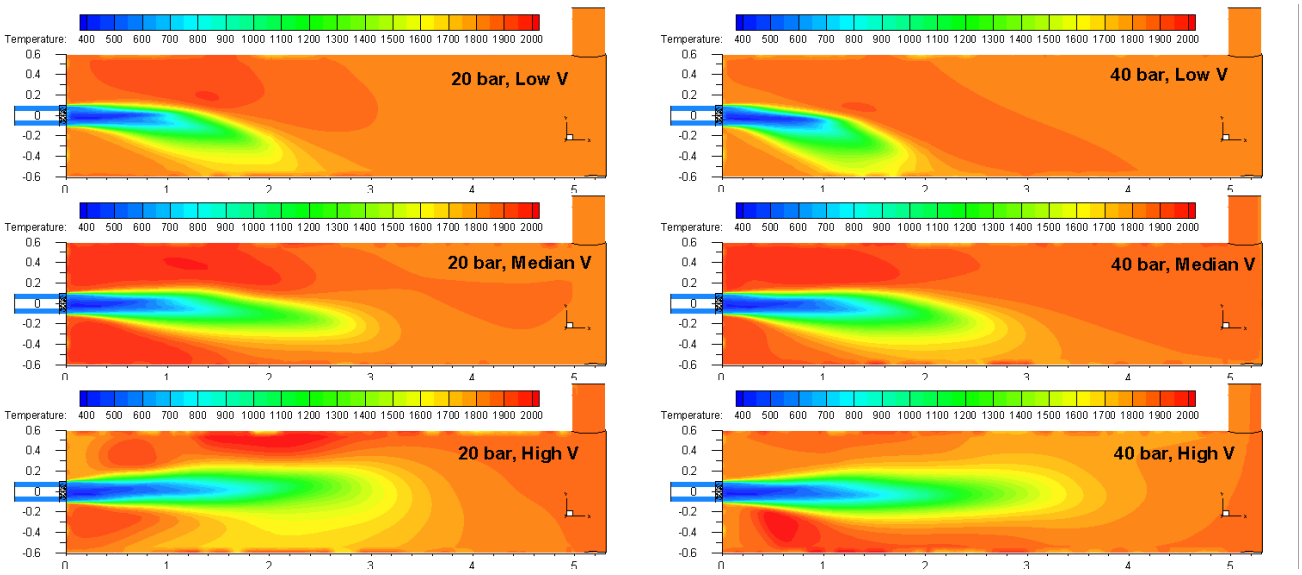

Figure 5-15. Comparison of the temperature (K) distributions among cases with low/median/high velocity under 20 bar and 40 bar operating pressures.

Similar trend was observed in the temperature distribution as well. Figure 5-15 shows the gas phase temperature contour of the tested cases. Again, due to the same adiabatic flame temperature in all cases, the peak temperatures are similar in all cases, and the pressure does not have significant effects on the

temperature distribution. However, it is significantly affected by the burner velocity. Comparing to the high burner velocity cases at 20 and 40 bar, the low and median burner velocity scenarios show a shorter burner flow penetration depth and non-uniform distribution. To the contrary, a high burner velocity improves the uniformity of the temperature distribution, and makes use of the reactor length for maximum thermal load.

5.4.2.2. Coal combustion processes

The char combustion process in pressurized oxy-fuel combustion under the reference 4 bar operating conditions has been discussed previously in report Part I, especially for the effects of CO_2 on char combustion/gasification. In the current study, special attention is given to the effect of elevated pressure on coal combustion kinetics, its spatial distribution, and burnout time.

Figure 5-16 and Figure 5-17 show the spatial distribution of char-O_2 oxidation reaction and char-CO_2 gasification reaction rates in the ISOTHERM oxy-combustor. As has been discussed previously, the spatial distribution mainly depends on the burner velocity: more uniform distribution was observed in the median and high burner velocity cases at both 20 bar and 40 bar. Moreover, given the same burner velocity, the volumetric reaction rate increases significantly from 4 bar to 20 bar and 40 bar, due to the doubled thermal load. The results indicate that, given the assumed char oxidation and gasification kinetics, a high burner velocity (~40 m/s) is possible for the current combustor design, which significantly increases the thermal load to ~60 MW_{th} at 40 bar. However, with a further increased burner velocity and feeding rate, the reactor length might be not long enough for the char conversion. This will be discussed in greater detail using the conversion time and residence time results later.

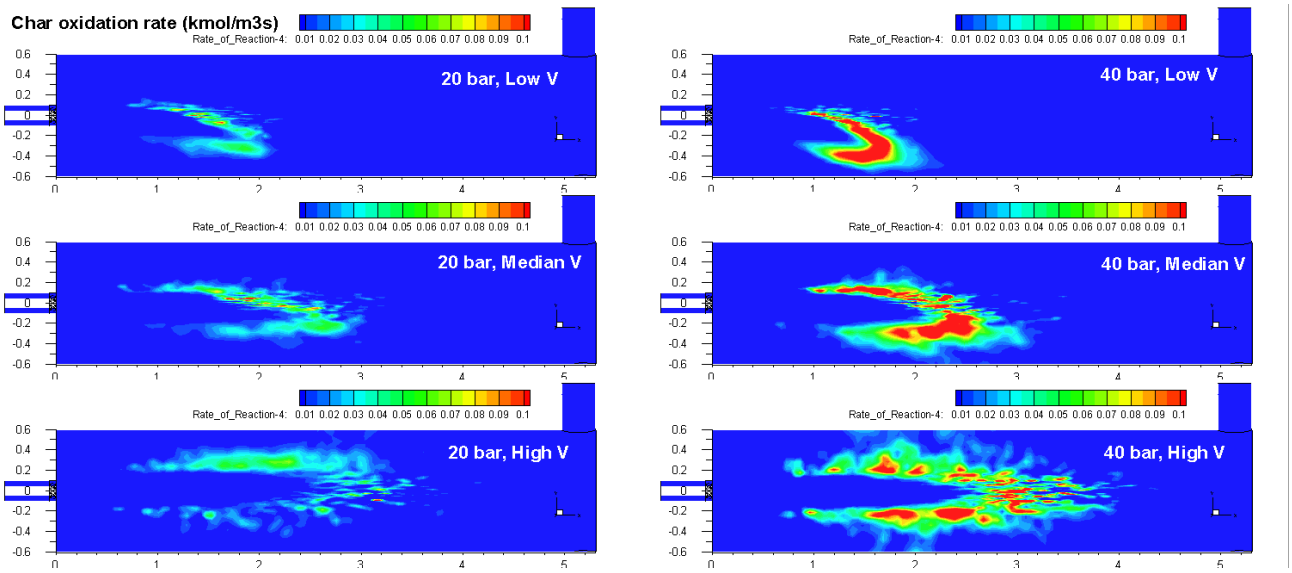

Figure 5-16. Comparison of the char oxidation ($C+O_2$) rate distribution among cases with low/median/high velocity under 20 bar and 40 bar operating pressures.

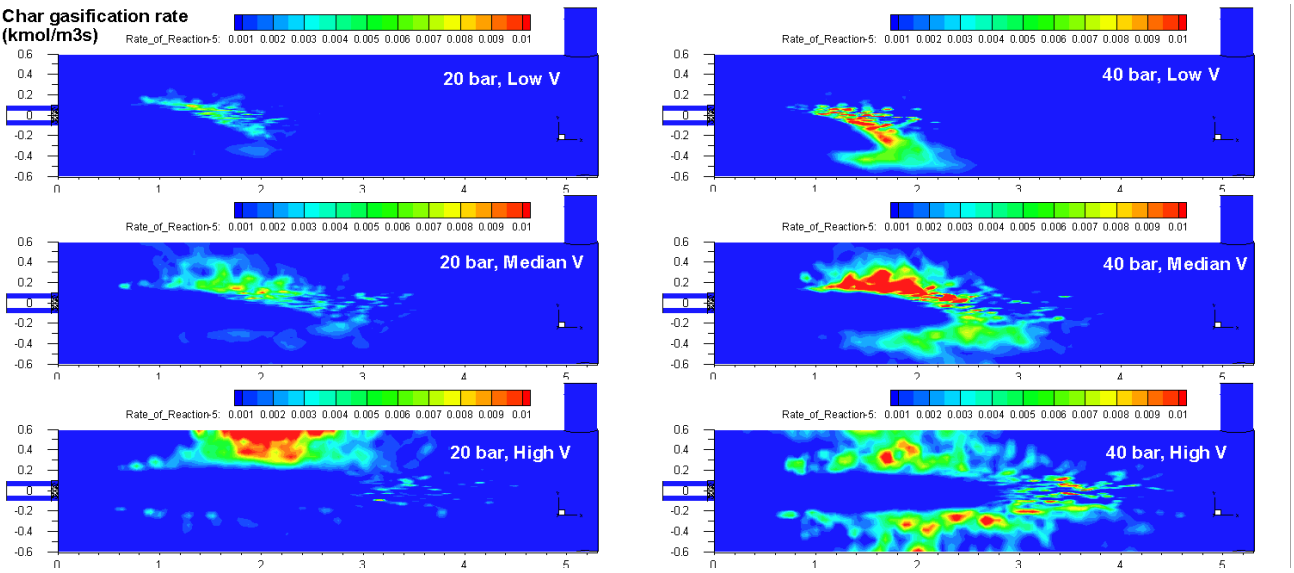

Figure 5-17. Comparison of the char gasification ($C+CO_2$) rate distribution among cases with low/median/high velocity under 20 bar and 40 bar operating pressures.

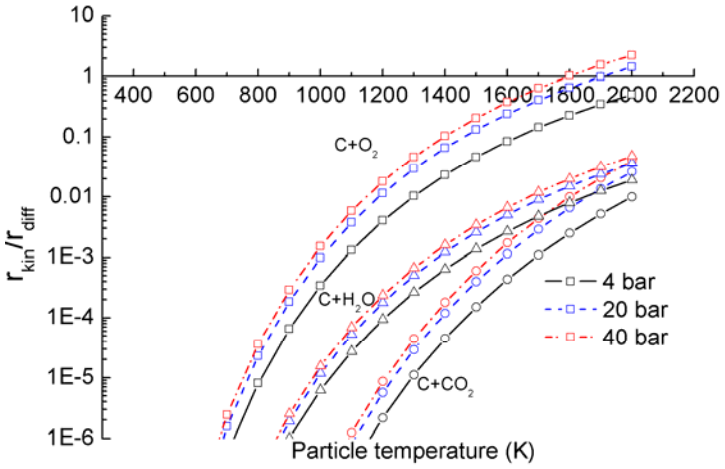

Figure 5-18. Comparison of the char surface reaction rates at 4 bar, 20 bar, and 40 bar operating pressures with 10% O_2, 40% CO_2 and 40% H_2O (by vol.). Results indicate that the oxidation reaction ($C+O_2$) becomes diffusion controlled at high temperatures, in particular at elevated pressure. Gasification reactions are kinetics controlled within the ISOTHERM reactor, and the reaction rates are times higher at 20 bar and 40 bar than the reference case.

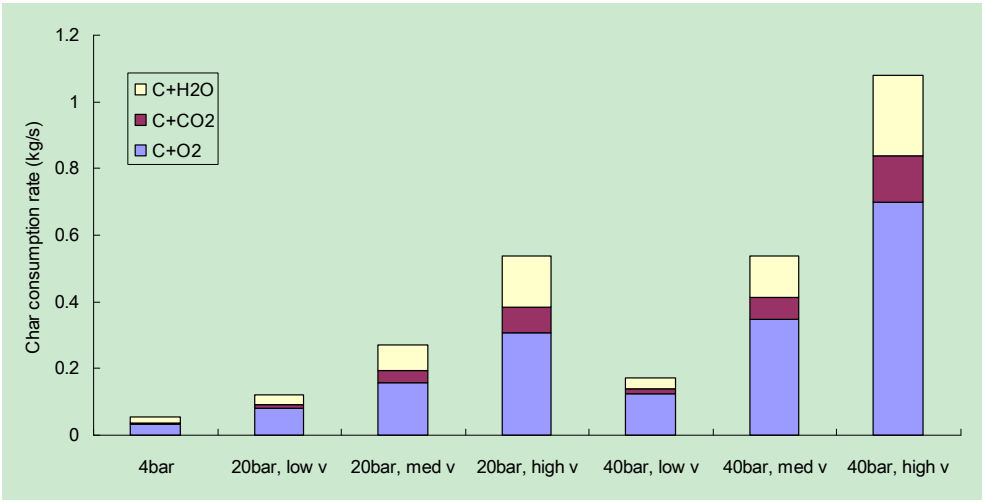

Figure 5-19. Char consumption rate due to the oxidation and gasification reactions in the investigated cases.

One of the research interests is the contribution of gasification reactions to char conversion at elevated pressure in oxy-fuel combustion. Through the analysis of the "oxy-base" case in Part I paper, it has been shown that the oxygen mass fraction reduces down to 6% due to the entrainment of the recirculated hot flue gas, while the mass fraction of CO_2 (> 60%) and H_2O (> 27%) are much higher at

most of the spaces. Therefore, the gasification reactions can contribute significantly to the overall char conversion in the ISOTHERM oxy-combustor, and this trend might become more prominent at higher operating pressure because of the enhanced gasification reaction rates.

Figure 5-18 shows the ratio of the kinetics reaction rate and the diffusion rate for the char surface reactions, as an indicator of the reaction regimes (kinetics control or diffusion control) under the tested operating conditions. An order of magnitude analysis shows that the bulk diffusion rate does not change significantly when the total pressure increases [22], therefore, the results indicate the relative kinetic rate change along with pressure. It can be seen that based on the char reaction kinetics from the literature, kinetic rates of all the heterogeneous reactions are enhanced by the increased gas partial pressure. The kinetic rates increase more significantly from 4 bar to 20 bar, because the reaction order is less than unity. Moreover, the oxidation and gasification reactions are in different regimes at typical reactor temperature (1800 K): the oxidation reaction ($C+O_2$) approaches bulk diffusion control above ~1800 K, and it becomes more diffusion control under higher pressures. In contrast, the gasification reactions ($C+CO_2$ and $C+H_2O$) are still kinetics controlled in the typical environment of ISOTHERM reactor. Figure 5-19 compares the char consumption rates by the three heterogeneous reactions under different operating conditions. The gasification reactions contribute 30-40% of the total char conversion in all cases. The char-H_2O reaction has a higher impact than the char-CO_2 reaction due to its higher kinetics. However, it is interesting that overall contribution of the gasification reactions does not show significant increase as a function of the operating pressure. This might be due to the fact that the reaction order for the gasification reactions are smaller (see Table 3-3), therefore the gasification rates increase less prominently under higher total pressure.

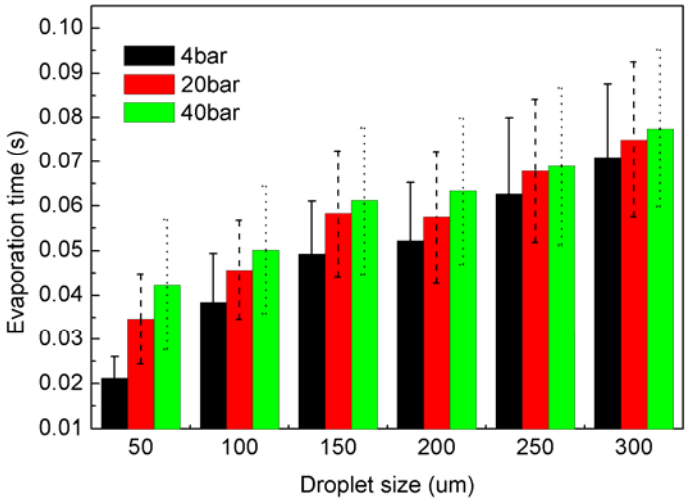

Figure 5-20. Statistics of water evaporation time as a function of droplet diameter in 4 bar, 20 bar, and 40 bar operating pressures with identical median burner velocity (~20 m/s). Results are the average and standard deviation values calculated using 300 droplet particle trajectories in the reactor.

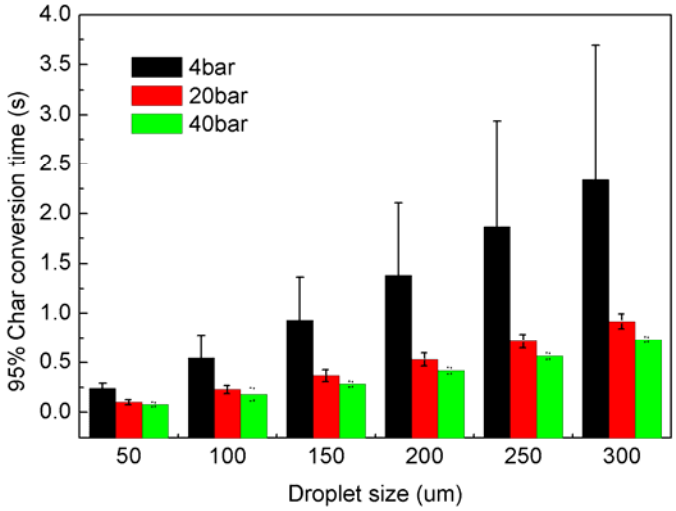

Figure 5-21. Statistics of 95% char conversion time as a function of droplet diameter in 4 bar, 20 bar, and 40 bar operating pressures with identical median burner velocity (~20 m/s). Results are the average and standard deviation values calculated using 300 char particle trajectories in the reactor.

The conversion time is a critical indicator for the furnace and reactor design. For coal combustion, the conversion time is usually within seconds depending on the burner configuration, operating conditions, as well as the heat transfer characteristics. We put special attention on the effect of pressure

on coal particle combustion process, especially evaporation, devolatilization, as well as char conversion.

Figure 5-20 shows the statistics of the evaporation time as a function of droplet size under 4 bar, 20 bar, and 40 bar with median burner velocity. As expected, the drying time increases with the increasing CWS droplet size in all cases, and increases slightly (<0.01 s) with the elevated pressure. We have shown that the heat transfer to the droplets in the furnace is dominated by convective heat transfer [22], and if the ambient gas temperatures are similar, the heat transfer rate is controlled by thermal conductivity, k. The thermal conductivity is a weak function of pressure, for instance, k_{CO_2} increases only slightly from 0.0706 W/mK at 4 bar to 0.0711 W/mK at 40 bar [58]. Therefore, the heat transfer rate should not be changed significantly at higher operating pressure. However, the saturation temperature increases significantly from 143.6 ^{o}C at 4 bar to 250.4 ^{o}C at 40 bar. The delayed boiling process is the major reason for the longer droplet evaporation time.

However, the increase in the evaporation time is negligible when comparing to the change in the char conversion time. Figure 5-21 compares the time for 95% char conversion at 4 bar, 20 bar, and 40 bar operating pressure with median burner velocity. The conversion time reduces significantly from 4 bar to 20 bar, and slightly from 20 bar to 40 bar. For instance, the conversion times at 20 bar and 30 bar is only 50% and 40% of those at 4 bar, even with 5 times and 10 times higher fuel feeding rate. Moreover, the smaller standard deviation at high pressures indicates a stable and uniform combustion.

The significantly reduced coal particle conversion time is because of the enhanced char reaction kinetics as discussed previously in Figure 5-18. Again the conversion time does not decrease linearly with pressure increase because the reaction order is less than 1, and the reaction rates become less sensitive to the reactant partial pressure. The results indicate that an even higher feeding rate is possible (such as the 40 bar high velocity case), because less time is required to burn the coal water slurry fuel. However, one has to ensure that the residence time is higher than the conversion time, for a high carbon conversion ratio and minimum residue carbon in the ash particles.

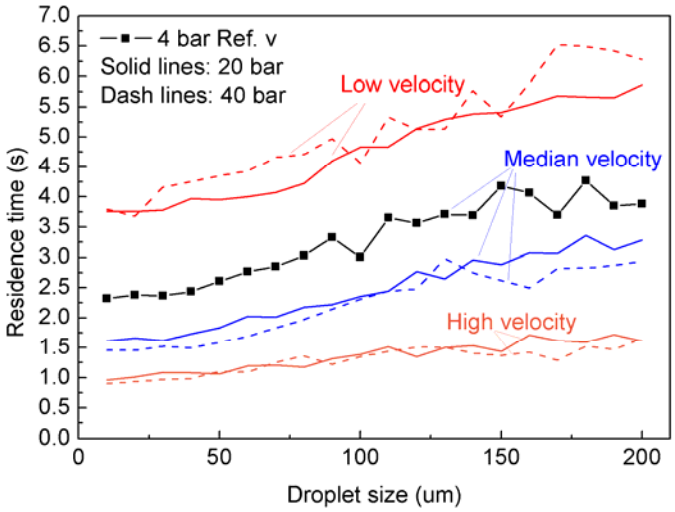

Figure 5-22. Statistic results of particle residence time in the oxy-combustor under different operating conditions.

5.4.2.3. Particle residence time

Figure 5-22 shows the statistics for the coal particle residence time in the reactor as a function of the coal water fuel droplet size. The results show that larger particles tend to stay longer in the reactor than small particles, probably due to larger stokes number. The residence time is mainly determined by the overall flow velocity, and it is almost inversely proportional to the burner velocity. For instance, the average residence time for 100 um droplets is 4.56 s, 2.31 s, and 1.35 s, respectively under a burner velocity of ~10 m/s, 20 m/s, and 40 m/s at 40 bar. To the contrary, the operating pressure has a much less impact on the residence time, especially for high pressure cases. The residence time for 100 um droplets decreases from 3.0 s at 4 bar to 2.35 s at 20 bar, and decreases slightly to 2.31 s at 40 bar.

Compared to the conversion time shown in Figure 5-21, at 4 bar, the residence time with a median burner velocity is longer than the char conversion time, while the residence time with a high burner velocity might be too short for a high char conversion. However, if the operating pressure is raised to 20 bar and 40 bar, the residence time with a high burner velocity is still longer than the char conversion time. This shows the advantages of pressurized oxy-coal combustion: that is the possibility to increase the thermal load significantly.

5.4.2.4. Heat loss

Another point of interest is the heat loss from the oxy-coal reactor. The reactor is built with three-layer refractory wall with the objective of reducing heat loss and ensuring good combustion performances. In this study, the same thermal boundary conditions were applied in the tested cases: the conductive heat transfer in the refractory wall and ceramic fiber material and the convection heat transfer of the external cooling water to the steel shell are calculated in the CFD simulations.

Figure 5-23 shows the heat loss rate through the refractory wall under 4 bar, 20 bar, and 20 bar with a median burner velocity. The total heat loss increases slightly from 0.158 MW to 0.169 MW as the operating pressure increases from 4 bar to 20 and 40 bar, due to the high heat resistance of the refractory wall. As a result, the heat loss over the total thermal load reduces from 6.1% to 1.2% and 0.62%, respectively, when the operating pressure increases.

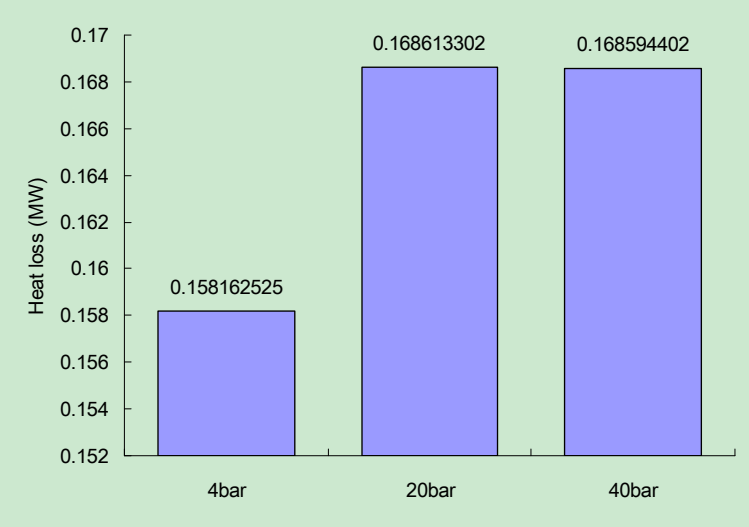

Figure 5-23. Comparison of the total heat loss rate (MW) through the refractory wall under an operating pressure of 4 bar, 20 bar, and 40 bar with identical median burner velocity (~20 m/s).

5.4.2.5. Slag behaviors

The slag flow behaviors have also been investigated under the tested operating conditions, taking advantage of the one dimensional slag model [113] developed previously in the ENEL-MIT oxy-

combustion research program. Due to the limitation of the current slag model, the reactor is assumed to be vertically-oriented, and only the slag flow in the axial direction driven by gravity was modeled.

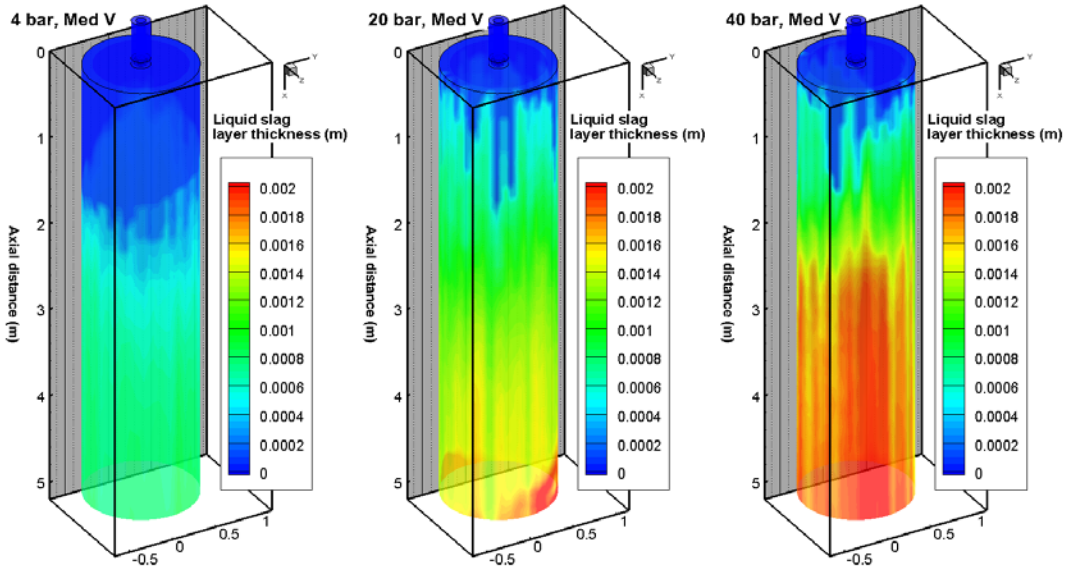

Figure 5-24. Molten slag thickness (m) under an operating pressure of 4 bar, 20 bar, and 40 bar, with identical median burner velocity (~20 m/s).

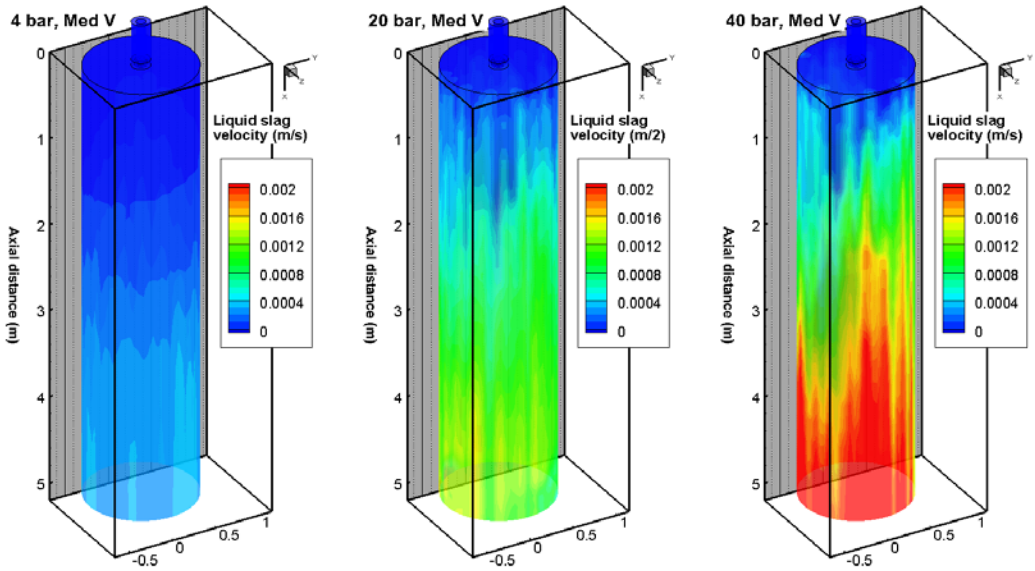

Figure 5-25. Molten slag flow velocity (m/s) under the same operating conditions above.

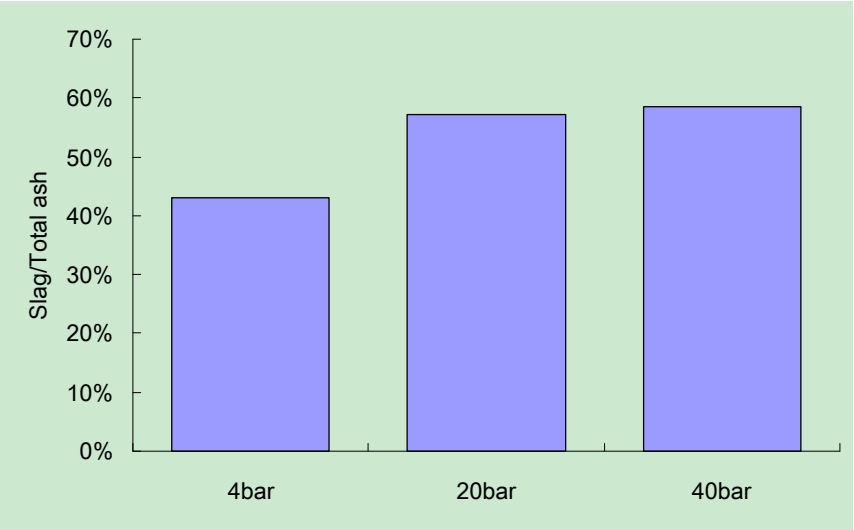

Figure 5-26. Ash that captured on the side refractory wall in the form of molten slag over the total ash mass flow rate under an operating pressure of 4 bar, 20 bar, and 40 bar, with identical median burner velocity (~20 m/s).

Figure 5-24 and Figure 5-25 shows the steady-state molten slag thickness and molten slag flow velocity distribution on the side wall under 4 bar, 20 bar, and 40 bar operating pressures with a median burner velocity. Similar slag flow characteristics were observed in these cases because of the similar gas phase flowfield as shown in Figure 5-14. However, slag thickness becomes significantly higher, from 0.8 mm at 4 bar to 1.2 mm at 20 bar, and 2.0 mm at 40 bar. This is mainly because of the significantly higher coal throughput. As a result, the slag flow velocity increases accordingly, governing by the gravity driven flow characteristics.

The slagging tendency becomes more prominent at higher operating pressures, or, at higher coal throughputs. Figure 5-26 shows the captured slag mass flow rate over the total ash mass flow rate in the 4 bar, 20 bar, and 40 bar cases with median burner velocity. We can see that the slag to total ash mass flow rate ratio increases from ~43% in the reference case to ~57% and 58% in the high pressure cases. The reason may be because of the thicker slag layer, which increases the capture probability, in particular at the near burner region.

5.5. Conclusions

The pressure effects on oxy-coal combustion in a pilot scale combustor have been studied using CFD approach with validated submodels, the physical and chemical effects under elevated pressure were also considered and modeled in the CFD simulations. With a fixed reactor and burner geometry, the operating pressure is increased up to 20 and 40 bar with progressively increasing burner velocities. A comparison between the results of reference case and high pressure cases shows that:

(1) Similar flowfields are maintained with the identical burner velocity at high pressures, which results in similar gas temperature and coal conversion spatial distributions in the reactor. Coal particle residence time is mainly determined by the burner velocity as well.

(2) High pressure enhances the char reaction kinetics and reduces the char conversion time significantly. At 20 and 40 bar, the char conversion time decreases to about 40-50% of that in the reference 4 bar case, which makes higher burner velocity and coal throughput possible at high pressure.

(3) It is possible to operate the current reactor at 60 MW thermal load at 40 bar, taking advantage of the enhanced char conversion kinetics.

(4) The heat loss through the reactor wall does not change significantly due to the high thermal resistance of the refractory wall, and the relative heat loss rate reduces significantly at high pressures with high coal throughput.

(5) Molten slag thickness and velocity increases significantly at high pressures due to the higher coal throughput.

We note that the results in this study are based on coal reactivity kinetics data taken from the literature, and therefore the conclusions are only qualitative. However, it shows the trends of the oxy-coal combustion at elevated pressure, and can be taken as instructive guideline for pressurized oxy-coal

combustor design.

Page left intentionally blank

Chapter 6 Development of 3-D Slag Model

Following the pressure study conducted in last chapter, we will look closer to an important phenomenon in the pressurized oxy-coal combustor – slagging. Slagging and fouling are not unique in oxy-coal combustion, but widely observed in all combustion and gasification facilities dealing with coal, which contains inorganic matters (or ash content) that may form slag on the refractory wall or heat exchanger surfaces. Some of the furnace and gasifiers are intended to be operated with slag film formation on the wall, so called slagging combustion or slagging gasification. In this chapter, a first-of-its-kind three-dimensional slag model will be introduced, and its predictions on the slagging behaviors in the ISOTHERM oxy-coal reactor will be compared with experimental observations.

6.1. Overview

6.1.1. Slagging Oxy-Coal Combustion

Coal contains inorganic mineral content, when burned or converted in industrial furnace and reactors, these mineral residuals are discharged from the flue gas or synthetic gas in the forms of fly ash, bottom ash and slag. Slagging combustion and gasification is intended to operate at temperatures above the ash fusion temperature, in which the ash content is molten and deposited along the wall, forming a slag layer. Up to 90% of the ash can be discharged as molten slag from the bottom of the furnace or reactor to a water quenched slag hopper, where it forms crystal pellets. Advantages of slagging combustion and gasification include higher energy efficiency, broader fuel flexibility, compact heat exchangers, as well as higher value of the low-carbon content slag residuals for utilization [214, 215]. However, challenges associated with slag behavior have been identified on slagging combustors and gasifiers operating. If the operating conditions are not optimum, problems may damage the reliability and safety [216-218], such as excessive corrosion of the refractory wall and water membrane by molten

slag, and slag discharging difficulties due to solidification. Therefore, a better understanding of the char-slag interaction and slag flow behavior is imperative for the reactor design and optimization.

Pressurized oxy-fuel combustion systems have been proposed recently, with the objective of improving the energy efficiency by recovering latent heat of the steam in the flue gas. The flue gas volume is reduced under elevated pressure, which results in smaller components size and possible capital cost for the same power output. Several studies have reported on the technical and economic feasibility of this process [31-36], which all concluded that the overall process efficiency improves with increasing operating pressure. This is mainly because latent heat recovery from the flue gases becomes possible at higher temperatures. However, one of the operating challenges for pressurized coal combustion system is the ash removal in the flue gas. Slagging combustion is favorable because most of the coal ash can be discharged in the form of molten slag in the combustor. As a pilot scale study of the ISOTHERM® pressurized oxy-fuel combustion system [34], a 5 MW_{th} oxy-coal combustion test facility was operated under slagging combustion conditions, and experiments on this test rig showed good combustion characteristics and environmental performance [204]. Figure 6-1 shows the slagging behaviors in the test facility during shut-down condition, and it can be seen that the slagging behavior can be complicated in different locations. The molten slag covers the top and side refractory wall of the reactor, and flows down to the bottom driven mainly by gravity. The thickness of the slag is not uniform, but depends on the gas phase flowfield, temperature distribution, as well as the particle depositions in the reactor.

(a) (b)

Figure 6-1. The slagging behaviors in the 5 MW_{th} oxy-coal reactor, pictures were taken from the end of the reactor during shut-down period. (a) shows the frozen slag on the ceiling of the reactor, and (b) shows the slag on the side and bottom wall of the reactor.

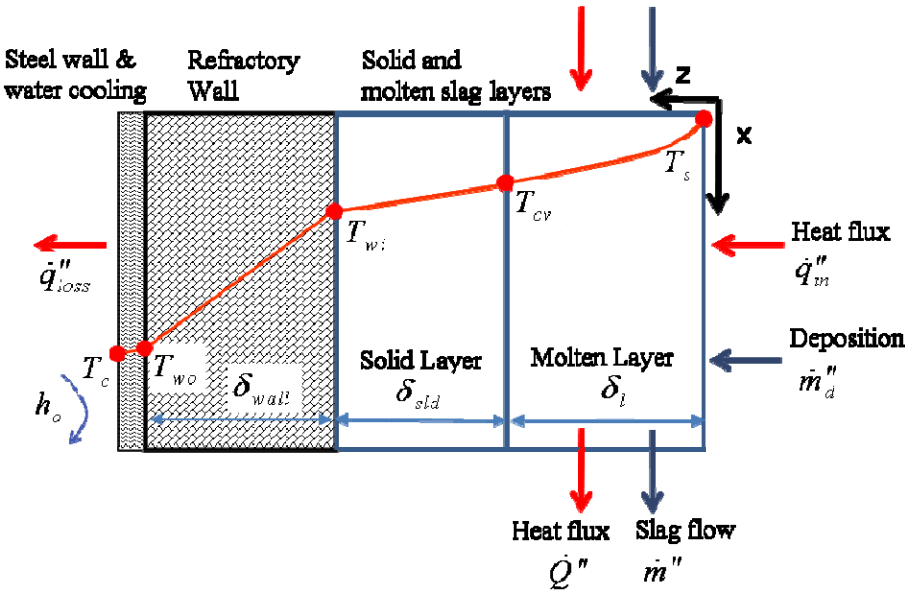

Figure 6-2. A schematic diagram of the slag flow on refractory wall, with steel wall and water cooling outside. Figure is cited and modified from reference [219]. Red color arrows and curves show the heat transfer process, and dark blue arrows indicate mass transfer process.

Figure 6-2 shows a schematic diagram of the slag layer with mass and heat transfer processes.

Molten ash particles are trapped and deposited on the refractory wall, which build up a dynamic balanced slag layer flowing down driven by gravity. Depending on the operating temperature, ash fusion temperature and heat transfer characteristics on the refractory wall, a solid slag layer may form between the molten slag and the refractory wall. In the current study, this solid slag layer is not modeled because the operating temperature is above the ash fusion temperature, and the reactor is refractory wall lined. Outside the refractory wall, a water-jacketed steel shell is used to support the reactor structure and operating pressure.

6.1.2. CFD Modeling of the Slag Flow in Coal Combustion and Gasification

The slag flow model in Computational Fluid Dynamics (CFD) simulation has been developed in previous studies [113, 219-221]. One approach is the one-dimensional slag model along the axial direction on the reactor wall. Seggiani [219] developed a one-dimensional time-varying slag flow model for a Prenflo entrained-flow gasifier and integrated it into a three-dimensional gasifier code. The gasifier wall was discretized to 15 cells in the vertical direction. In each of the cells, perimeter averaged analytical solutions derived from conservation equations are calculated to get the slag velocity, molten and solid slag thickness, and temperature distributions, with the particle mass deposition rate, gas temperature and heat flux from the three-dimensional code as input variables. Wang et al. [220, 222] developed another one-dimensional steady state model for the slag flow in a coal-fired slagging combustor. Compared to the Seggiani model, this model considers the wall-burning sub-process when particles are trapped on the slag surface and its effects on the char conversion and heat transfer near the wall region. In recent years, insights have been gained into the char-slag interaction and char capture sub-process by experimental and numerical approaches [218, 223, 224]. Yong et al. [113] proposed a set of particle trap criteria for the slag-particle interaction and applied it in the one-dimensional slag flow modeling.

However, the one-dimensional slag models developed by Seggiani [219], Wang et al. [220, 222],

and Yong et al. [113] average the variables in the circumference, which can not resolve the non-axisymmetric slag behavior in the azimuthal direction. Based on previous works, Bockelie et al. [225] and Chen et al. [226] expand the one-dimensional slag model into the two-dimensional wall surface in coal gasifier and coal combustor respectively, with the assumption that slag flow only in one direction. This two-dimensional approach captures the spatial distribution of ash particle deposition due to the gas phase flowfield, thus further improves the accuracy of the slag modeling in three-dimensional CFD simulation. However, this approach cannot fully resolve the three-dimensional flow behavior in the cases of horizontally-oriented reactors, or reactors with complicated geometry, with the limitations stemming from the one-dimensional model.

In order to fully resolve the slag flow and its interactions with ash particle deposition and heat transfer, multiphase flow model has been used in slag flow modeling as a different approach. Liu and Hao [227] modeled the slag flow in an entrained flow gasifier using the Volume of Fluid (VOF) model. The computational domain is a two-dimensional near wall region, and a constant ash deposition of 0.5 $\mathrm{kg}/(\mathrm{m}\cdot\mathrm{s})$ was used as mass input to the free surface of the slag. Ni et al. [221] applied the same approach to model the slag flow in the entrained flow gasifier slag throat region, similarly to Liu and Hao's work, a two-dimensional axisymmetric mesh and a constant ash deposition rate was used in the simulation. It should be noted that in these models, the ash deposition rate spatial distribution due to gas phase flowfield was neglected.

In this work, a fully three-dimensional slag model was developed coupling two multiphase flow models: the VOF model and the Discrete Phase Model (DPM). This model fully resolves the three-dimensional characteristics of char/ash deposition, slag flow, as well as heat transfer through the slag layer, and it is general to be applied in coal slagging gasification and combustion with any reactor geometry. The slag behavior in the 5 $\mathrm{MW_{th}}$ pressurized oxy-fuel coal combustor was investigated using the slag model, and the simulation results were compared with the experimental observations.

6.2. Reactor Geometry and CFD Mesh Refinement

The geometry of a pressurized oxy-fuel combustor developed by ITEA Spa and ENEL has been introduced in Chapter 5. Figure 6-3 shows the schematic geometry of the 5 MW_{th} pressurized Coal Water Slurry (CWS) oxy-fuel combustion pilot scale test rig. Since the flow of molten slag is fully resolved by the VOF model, a fine mesh size is required near the wall boundary layer regions. Based on our previous study [226], the average slag thickness is in the scale of several millimeter. Therefore, the first layer of the three-dimensional mesh was refined to be 0.01 mm, about 2 orders of magnitude lower than the slag layer in order to get a high resolution of the slag thickness. The mesh consists of 1.6 million hexahedral cells in total.

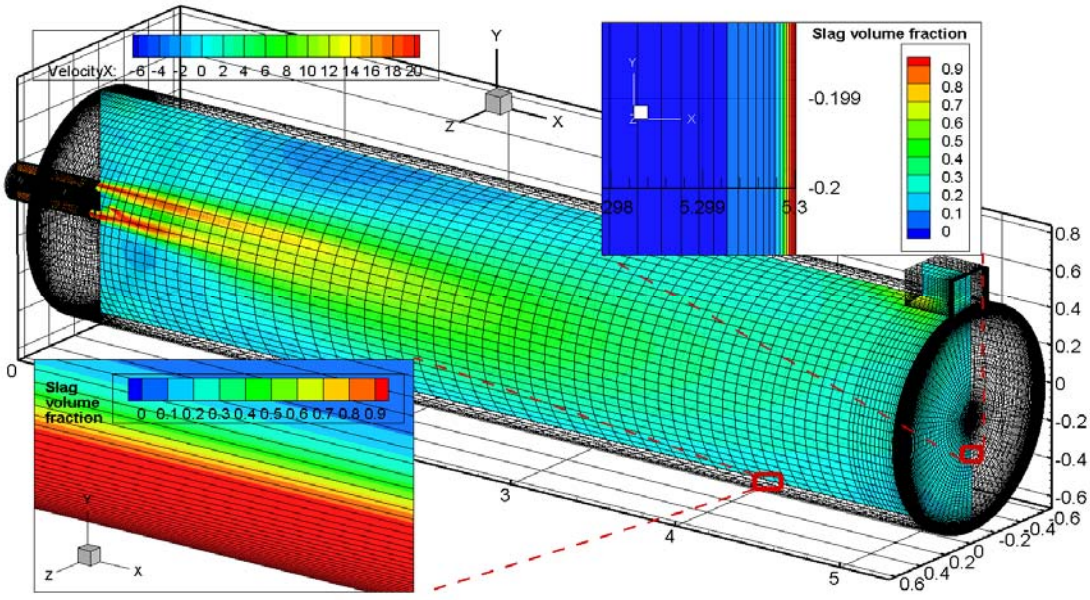

Figure 6-3. The geometry and three-dimensional mesh of the 5 MW_{th} oxy-coal test unit. The axial velocity contour is shown in a XY cross section, and the slag volume fraction distributions were emphasized with the refined mesh in the near-wall region at the bottom and the back wall of the reactor.

6.3. Mathematical Models

In this study, the oxy-coal combustion in the reactor is simulated using a three-dimensional commercial CFD code FLUENT 12.1.4. The three-dimensional slag model couples two multiphase methods: the VOF model and the DPM. The VOF model is an Eulerian-Eulerian approach used to model the gas phase and slag phase and their volume fraction in the computational cells; while the DPM is an Eulerian-Lagrangian approach used to model the coal particle trajectories in the reacting gas phase. The slag model was implemented in the form of User Defined Functions (UDF). In this section, the conservation equations for the VOF model and DPM are introduced, followed by a description on the coupling of these two models. Implementation of the slag model with the CFD framework and its solving strategy are discussed as well.

6.3.1. The Volume of Fluid (VOF) Model

The VOF model [228] is a multiphase flow method that tracks the interfaces among immiscible fluids. It solves a continuity equation of volume fraction for each fluid, α_i, in the computations cells. For the molten slag flow in coal combustion, the gas phase (primary phase) and slag phase (secondary phase) are two non-interpenetrating fluids, with their volume fractions α_g and α_s, respectively. There are three conditions for α_s in the multiphase flow:

- $\alpha_s = 0$: The cell is full of gas phase.
- $\alpha_s = 1$: The cell is full of slag.
- $0 < \alpha_s < 1$: The cell contains an interface between the gas and slag phase, which is the most interesting for free surface tracking.

The tracking of the interface is achieved by solving the continuity equation of the slag volume fraction in the computational domain:

$$\frac{1}{\rho_s}\left[\frac{\partial}{\partial t}\left(\alpha_s\rho_s\right)+\nabla\cdot\left(\alpha_s\rho_s\vec{v}_s\right)=S_{\alpha_s}+\dot{m}_{gs}-\dot{m}_{sg}\right] \qquad (6.1)$$

where ρ_s is the slag density, $\vec{v}_s$ is the velocity of the fluid, S_{α_s} is the source term due to ash particle deposition, and $\dot{m}_{gs}$ and $\dot{m}_{sg}$ are the mass transfer rate between gas and slag phase due to phase change.

Since the slag is hardly evaporated at the operating temperature, the last two terms due to phase change are neglected in the modeling. However, the source term S_{α_s} due to particle deposition should be modeled when a ash particle or molten slag droplet is captured by the wall or the slag film on the wall. This is accomplished by coupling the DPM and the VOF model, which will be described in greater detail in 6.3.3.

A single momentum is solved throughout the domain, and the resulting velocity field is shared among the phases:

$$\frac{\partial}{\partial t}\left(\rho\vec{v}\right)+\nabla\cdot\left(\rho\vec{v}\vec{v}\right)=-\nabla p+\nabla\cdot\left[\mu\left(\nabla\vec{v}+\nabla\vec{v}^{\mathrm{T}}\right)\right]+\rho\vec{g}+\vec{S}_{ash} \qquad (6.2)$$

where ρ and μ are the density and viscosity of the fluid mixture in the cell, $\vec{g}$ is the gravity acceleration, and $\vec{S}_{ash}$ is the momentum source term due to particle deposition.

Similarly, the energy equation is also shared all phases, is solved as:

$$\frac{\partial}{\partial t}\left(\rho E\right)+\nabla\cdot\left(\vec{v}\left(\rho E+p\right)\right)=\nabla\cdot\left(k_{eff}\nabla T\right)+S_h \qquad (6.3)$$

where E is the sensible energy of the fluid, k_{eff} is the effective thermal conductivity, and the source term, S_h, again is due to the particle deposition.

6.3.2. The Discrete Phase Model (DPM)

The motion of coal water slurry droplets and coal particles are modeled with the Discrete Phase Model (DPM) using an Eulerian-Lagrangian approach. The velocity of the particle is determined by

drag force, gravity force, and other body forces as formulated in the following equation:

$$\frac{d\vec{v}_p}{dt} = \frac{18\mu_g}{\rho_p d_p^2}\frac{C_D \mathrm{Re}}{24}\left(\vec{v}_g - \vec{v}_p\right) + \frac{\vec{g}\left(\rho_p - \rho_g\right)}{\rho_p} + \vec{F} \qquad (6.4)$$

where $\vec{v}_p$ and $\vec{v}_g$ are the particle and gas velocity, μ_g is the gas viscosity, d_p is the particle diameter, C_D is the drag coefficient, and $\vec{F}$ is other body forces which are neglected in this simulation.

Note that in the above equation, the particle trajectories are calculated using the time-average gas velocity, $\overline{\vec{v}}_g$, in a Reynolds Average Navier Stokes (RANS) approach, which neglects the turbulence's effect on particle's motion. In fact the local gas phase velocity contains the mean value, $\overline{\vec{v}}$, and its fluctuation, $\vec{v}'$:

$$\vec{v} = \overline{\vec{v}} + \vec{v}' \qquad (6.5)$$

Therefore, stochastic tracking and Discrete Random Walk (DRW) Model [229] was used for the particle dispersion due to turbulence. The particle is assumed to interact with a succession of fluid phase eddies over a time scale during its trajectory, where the fluctuation velocity is assumed as a function of the local turbulence kinetic energy, k, for instance, the velocity fluctuation in x direction is modeled as:

$$u' = \zeta\sqrt{\frac{2k}{3}} \qquad (6.6)$$

where ζ is a normally distributed random number. The particle-eddy interaction time is taken to be the minimum of the eddy lifetime, t_e, and the eddy-crossing time, t_{cross}, which are defined as:

$$t_e = 2C_L\frac{k}{\varepsilon} \qquad (6.7)$$

$$t_{cross} = -\tau\ln\left[1 - \left(\frac{L_e}{\tau\left|u - u_p\right|}\right)\right] \qquad (6.8)$$

where $\tau = \frac{\rho_p d_p^2}{18\mu_g}$ is the particle relaxation time, $L_e = C_L \frac{k^{1.5}}{\varepsilon}$ is the eddy length scale, and C_L is modeling constant. Based on a validation study conducted by Kumar and Ghoniem [174, 175] for swirling turbulent flow, C_L is taken to be 0.6 in this study.

Along the particle trajectories, the mass, momentum and heat exchanges between the particle phase and the gas phase are calculated using the "particle-source-in-cell" method.

6.3.3. Coupling the VOF and DPM methods

When a coal/char particle hits the boundary wall, it may be captured by the wall or the slag film, and form a slag layer in that location. If it is captured by the wall, its mass, momentum and sensible energy will be transferred to the slag phase by adding source terms in the volume fraction continuity equation, momentum equation, and energy equation. In this section, the capture criteria will be discussed, followed by an introduction to the modeling of source terms.

6.3.3.1. Ash Particle Capture Criteria

The particle capture submodel is to predict if a particle is captured to form slag or not when it reaches the wall boundary or the slag film. Two capture mechanisms were used in this study: the ash particle can either be captured by the reactor wall, or by the existing slag film. For the latter case, according to the order of magnitude analysis by Montagnaro and Salatino [230], under typical operating conditions of pulverized coal combustion, ash or char particles do not penetrate the slag surface due to the large surface tension and viscosity, and will captured or bounced by the slag film.

In this study, the particle capture criterion is based on the temperature of the particle and the combustor wall, as well as the carbon conversion of the particle. Ash or char particles are able to be trapped on the wall or in the slag film when the following criteria are satisfied:

- When there is no slag film on the wall, the particle is captured if the refractory wall internal surface

$$C > C \quad =$$

- If there is already slag film on the wall, the particle is captured if the particle char conversion is above the critical particle conversion factor ($C > C_{cr} = 0.88$).

6.3.3.2. Modeling the Source Terms

Once the ash particle is captured by the wall or by the slag film, it forms a slag film on the wall, or resolves into the existing slag film. This process is accomplished by adding the particle phase's mass, momentum and sensible heat into the slag phase. The mass source term S_{α_s}, momentum source term $\vec{S}_{ash}$, and energy source term S_h in Equation (6.1)-(6.3), are modeled as:

$$S_{\alpha_s} = \frac{\sum_V \dot{m}_p}{V_{cell}} \tag{6.9}$$

$$\vec{S}_{ash} = \frac{\sum_V \dot{m}_p \vec{v}_p}{V_{cell}} \tag{6.10}$$

$$S_h = \frac{\sum_V \dot{m}_p \int_{T_{ref}}^{T_p} c_{p,p} dT}{V_{cell}} \tag{6.11}$$

where $\dot{m}_p$ $\left[\mathrm{kg/s}\right]$ is the ash deposition rate that captured in the local cell, $c_{p,p}$ is the specific heat of ash, T_{ref} and T_p are the reference temperature for enthalpy calculation and temperature of the captured particle, respectively, and V_{cell} $\left[\mathrm{m}^3\right]$ is the volume of the cell.

6.3.4. Slag properties

Slag physical properties such as viscosity, density, specific heat and thermal conductivity are functions of the ash chemistry composition, oxidation or reduction atmosphere in the surrounding gas,

as well as slag temperature. Empirical correlations are used to predict these properties and solve the conservation equations [232]. **Table 6-1** and **Table 6-2** show the proximate and ultimate analysis of the raw coal and ash composition, respectively. Mean temperature in each of the computational cell is used to evaluate the properties.

The correlations for specific heat, thermal conductivity, density and surface tension are taken from Mills and Rhine [233, 234], whereas the slag viscosity is based on the Urbain and the Kalmanovitch-Frank models [235]. Of all the slag properties, the temperature of critical viscosity, T_{cv}, is the most critical property for slag modeling because it defines the interface between liquid and solid slag layers, and it is the most challenging property to predict. Based on the correlations presented in Vargas et al. [235] and Seggiani [219], we used a reference temperature $T_{cv} = 1480K$ in the current study. These physical properties are summarized in **Table 6-3**.

Table 6-1. Coal properties used in this study.

	Unit	Value
Proximate analysis (as received)		
HHV	kJ/kg	29153
Moisture	wt%	6.4
Ash	wt%	7.0
Volatile matter	wt%	33.1
Fixed carbon	wt%	53.5
Ultimate analysis (dry ash free)		
Carbon	wt%	82.1
Hydrogen	wt%	5.43
Oxygen	wt%	10.5
Nitrogen	wt%	1.39
Sulphur	wt%	0.58

Table 6-2. Oxide composition of the coal ash.

Ash composition	wt% as oxide
SiO_2	44.35
TiO_2	1.56
Al_2O_3	30.88
CaO	3.82
MgO	3.14
Na_2O	0.76
K_2O	0.67
P_2O_5	1.027
Mn_3O_4	0.1
SO_3	0.85
Fe_2O_3	4.51

Table 6-3. Physical properties of the coal slag.

Slag properties	Correlations in Ref.	Range
Temperature of critical viscosity T_{cv} (K)	[219, 235]	1480
Viscosity μ_s (Pa s)	[235]	1-20
Density ρ_s (kg/m^3)	[233, 234]	2779.9-2887.9
Specific heat c_p (kJ/kg K)	[233, 234]	1.3825
Thermal conductivity k_l (W/m K)	[233, 234]	1.73-1.80

6.3.5. Solution Strategies

Efforts have been made to develop and validate the CFD approaches in modeling oxy-coal combustion in a CO_2-rich environment [22, 236]. In this study, the slag model is implemented in a three-dimensional CFD simulation of the oxy-coal test facility in the form of UDFs. Mathematical submodels, such as standard $k-\varepsilon$ model, Eddy Dissipation model and Discrete Ordinate model, were used for modeling turbulence, chemistry-turbulence interaction and radiation heat transfer, respectively. The reader is referred to the previous reports for more details on the oxy-coal combustion CFD simulation [62, 193].

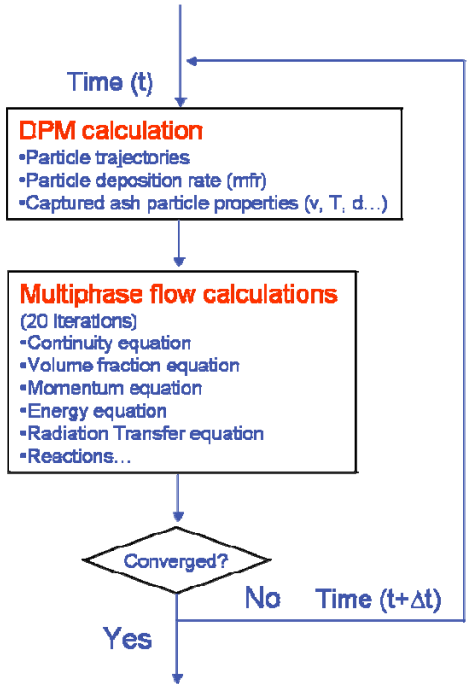

Figure 6-4. The algorithm of the slag model integration in the 3-D CFD framework.

Solving the slag flow with the reacting gas phase is challenging because of their different time scales, as well as the large physical property gradient such as viscosity and density at the gas/slag interfaces. In general, the best practice for VOF model is to use explicit formulation with Geo-Reconstruct method as the volume fraction discretization scheme. However, this

numerical method requires a very small time step (in millisecond) for the gas phase with high velocity, which is not affordable to solve the slag phase with flow time of several hours. In order to improve the sharpness at the interfaces and resolve the slag thickness accurately, transient calculation with implicit numerical scheme is recommended, which allows a large time step, which is taken to be 10 seconds based on the Courant number of the slag flow. The transient simulation results in the same solution as a steady-state calculation, but it combines with the Modified HRIC as the volume fraction spatial discretization scheme, and significantly improves the interface resolution.

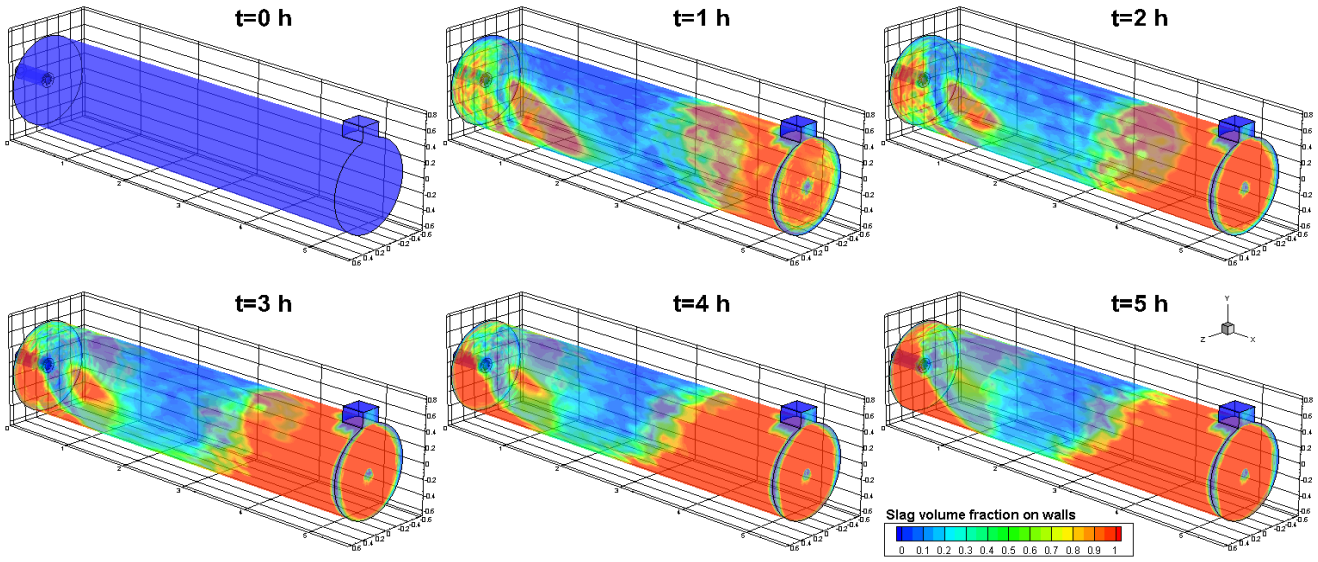

Figure 6-5. The slag buildup along with time in the transient calculation. Figure shows the slag volume fraction on the first layer of the mesh near the wall at time 0-5h.

The solving strategy is as follows: First, a converged steady-state solution of the coal combustion is achieved; then the slag model is loaded and implemented into the CFD calculation, and the problem is calculated using transient solver with a time step of 10 seconds. Figure 6-4 shows a flow chart of the algorithm and the coupling of the DPM and VOF model in the CFD calculation. In each of the time step, there is one DPM calculation, followed by 20 continuous

phase iterations. In a DPM iteration step, the particle trajectories are calculated, and the deposition rates with trapped particle properties were saved in User Defined Memories (UDM) corresponding to the deposition local volumetric cells. Following each DPM calculation, the conservation equations for continuity, species transport, slag volume fraction, momentum, and energy are solved iteratively using the UDM values as source terms. For the current study, steady state results are reached with a flow time of about 4-5 hours. Figure 6-5 shows the transient solution of the slag volume fraction on the wall during a convergence process. The slag flow rate, molten slag thickness, slag average velocity, heat loss and slag layer temperatures in each of the cells are analyzed and discussed in the following section.

6.4. Results and Discussions

In this section, the modeling results of the three-dimensional slag flow in the 5 MW_{th} reactor are analyzed. The turbulence is found to be important on particle's trajectory and deposition on the wall, and should be modeled correctly using the turbulence-particle interaction model. The slag flow behaviors in the reference operating condition are investigated in details, and the effects of coal throughput on the slagging behaviors are discussed.

6.4.1. Ash Deposition and the Effect of the Turbulence

The modeling of the coal char and ash particle trajectory in the CFD modeling is critical for deposition rate prediction, which determines the molten slag behaviors. Based on the particle's force balance Equation (6.4), we use the dimensionless Stokes number, Stk, to characterize the behavior of particles suspended in a fluid flow. It is defined as the ratio of the relaxation time, τ, to the flow time, $\frac{d_c}{u_g}$:

$$Stk = \frac{\tau}{d_c / u_g} = \frac{\rho_p d_p^2 u_g}{18 \mu_g d_c} \qquad (6.12)$$

where d_c is the characteristic length scale, u_g is the fluid velocity in far field. For the typical size of the pulverized coal particles (<100 um), and typical velocity field in the reactor, the Stk is much smaller than unity, which indicates that the particles follow the fluid streamlines well.

Therefore, the mean velocity, $\overline{\vec{v}}$, cannot resolve the turbulence's effect on the particle trajectories, while the fluctuation, $\vec{v}'$, has to be modeled in order to get an accurate particle deposition rate on the wall in the near-wall regions.

(a) (b)

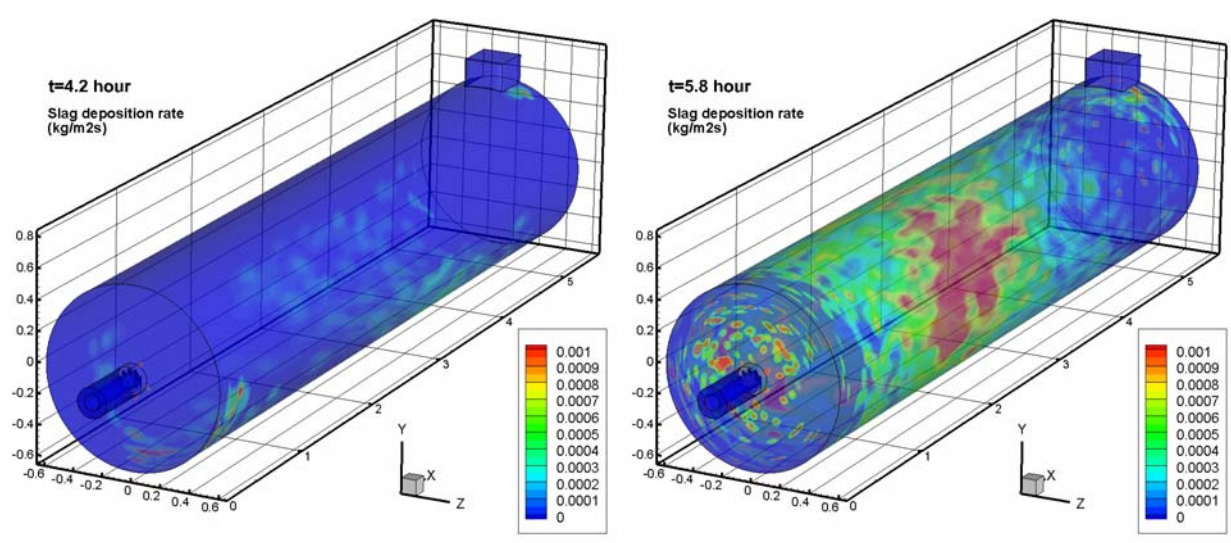

Figure 6-6. Char/Ash particle deposition flux (kg/m^{2}s) in each of the wall finite face, (a) without and (b) with the particle dispersion model.

Figure 6-6 shows the particle deposition flux ($\mathrm{kg}/\left(\mathrm{m}^2\mathrm{s}\right)$) distribution, defined as the captured particle mass flow rate per unit area, on the refractory wall, without and with the particle dispersion model (DRW model). The consideration of the turbulence-particle interaction

has a major impact on the predicted deposition flux: when the turbulence's effect on particle trajectory is considered, the particle deposition flux increases significantly, and the deposition location expands to both the top and the bottom of the reactor. The maximum particle deposition flux is in the range of 1×10^{-3} $\left(\mathrm{kg/m^2s}\right)$, and the maximum deposition flux is located between 2 and 3 meters away from the burner where char and ash particles impact the wall from the coal water slurry injector. It is noteworthy that the deposition flux is not uniformly distributed in the circumference direction on the cylinder wall due to the non-axisymmetric nature of the flowfield and particle trajectories in the combustor. As discussed in section 6.3.3.1, the fate of the ash particle (captured or not) varies depending on the particle temperature, carbon conversion, and the existing molten slag on the wall. Figure 6-7 shows the capture efficiency of coal ash on the reactor walls. With the particle dispersion model taken into account, about 80-90% of the total ash content in the coal is captured and can be discharged in the form of molten slag, which agrees with the experimental observations. To the contrary, only about 15% ash is captured when the particle dispersion is neglected. In both case, most of the ash is captured on the side wall.

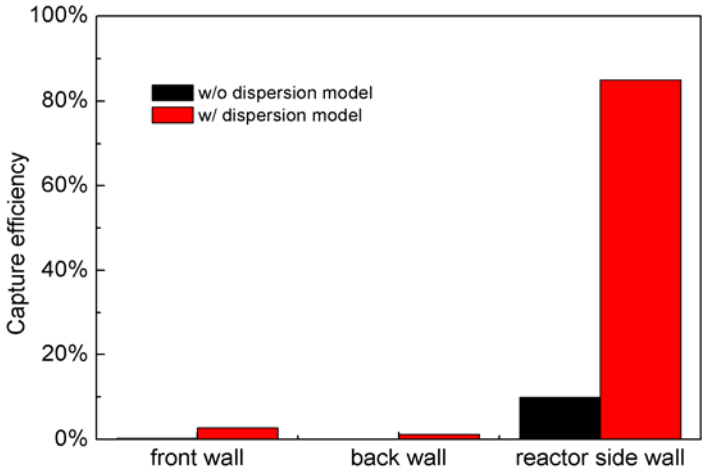

Figure 6-7. The ash capture efficiency on the reactor walls (including the front wall, back wall, and side wall), without and with the particle dispersion model.

(a) (b)

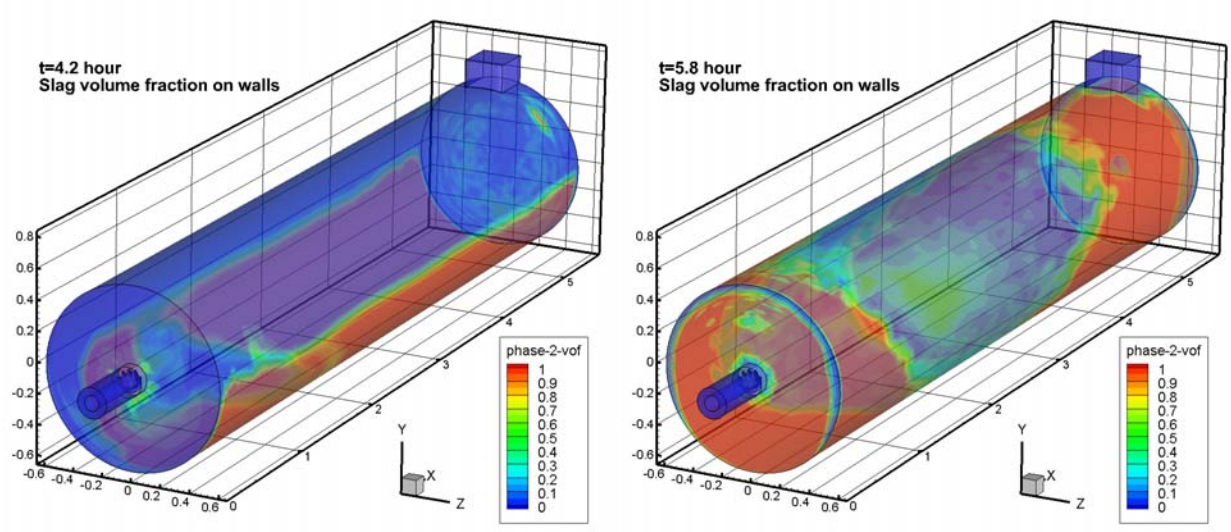

Figure 6-8. The slag volume fraction on the first layer of the mesh near the wall, (a) without and (b) with the particle dispersion model.

The significantly different deposition flux leads to different slagging behaviors. Figure 6-8 compares the calculated slag phase volume fraction on the wall without and with the particle dispersion (DRW) model. It can be seen that when the turbulence's effect on particle trajectory is neglected, the slag is only built on the bottom of the reactor, and slightly deposited the front and back wall. However, when considering the velocity's fluctuation on particle's motion, the slag is built on both the top and the bottom of the reactor, as well as the front and back walls, which agrees better with the experimental observations shown in Figure 6-1. Therefore, the simulation results with particle dispersion model are analyzed in the following sections.

6.4.2. Molten Slag Thicknesses and Flow Velocity

Figure 6-9 (a) shows the molten slag layer thickness and its flow velocity distribution on the wall. The molten slag layer covers most of the reactor walls, in particular at the bottom half, and its thickness increases from 0 to above 1 mm due to the accumulation of ash particle deposition.

Figure 6-9 (b) shows the slag surface velocity magnitude. The molten slag flows both downward the side wall, and toward the end of the reactor at the bottom due to the 1.5 degree slope. The slag flow is mainly driven by gravity and particle deposition momentum. Due to its high viscosity, the average velocity is generally around 0.1 mm/s.

(a) (b)

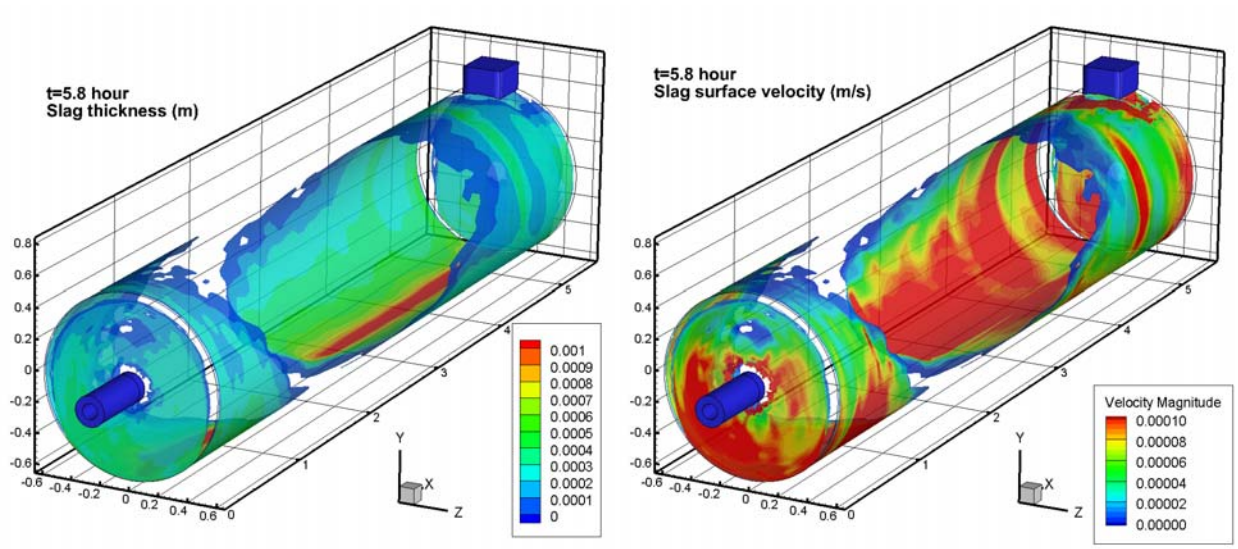

Figure 6-9. (a) The molten slag thickness (m), and (b) the slag surface flow velocity (m/s) in a steady state condition.

The slag thickness results at a cross section of the reactor at 4 m away from the burner are shown in Figure 6-10, with greater detail on the top, side and bottom locations. It can be seen that the slag film is thicker down to the bottom due to the slag accumulation along its path, and the slag thickness can be resolved by the local refined mesh at all locations. It should be noted that the slag dripping phenomenon at the top of the reactor that observed in experiment in Figure 6-1 is not well represented in the simulation results, probably due to the fact that the mesh on the perimeter is larger than the slag drip length scale. However, this does not affect the slag mass conservation and the slag behavior on the side and bottom of the reactor.

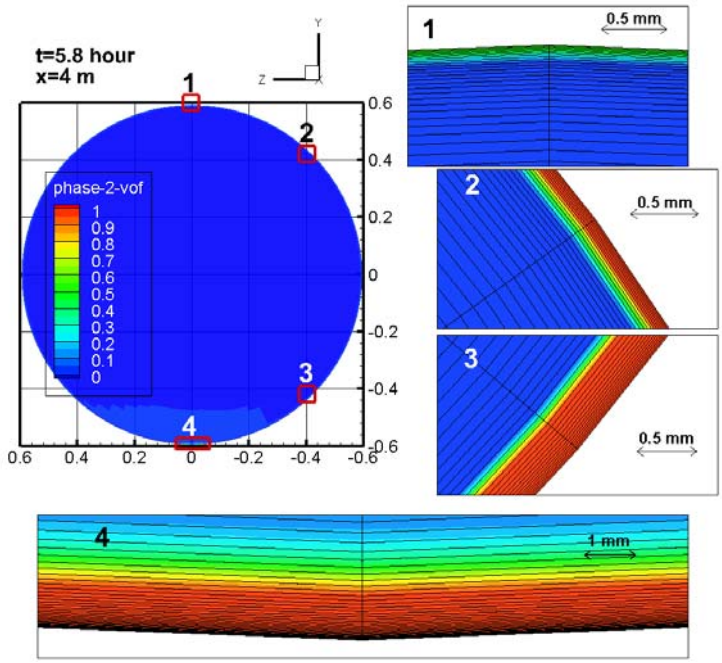

Figure 6-10. The slag thickness distribution at x=4 m, with local slag volume fraction distribution on the top, side and bottom of the reactor wall. The mesh is also shown with the results.

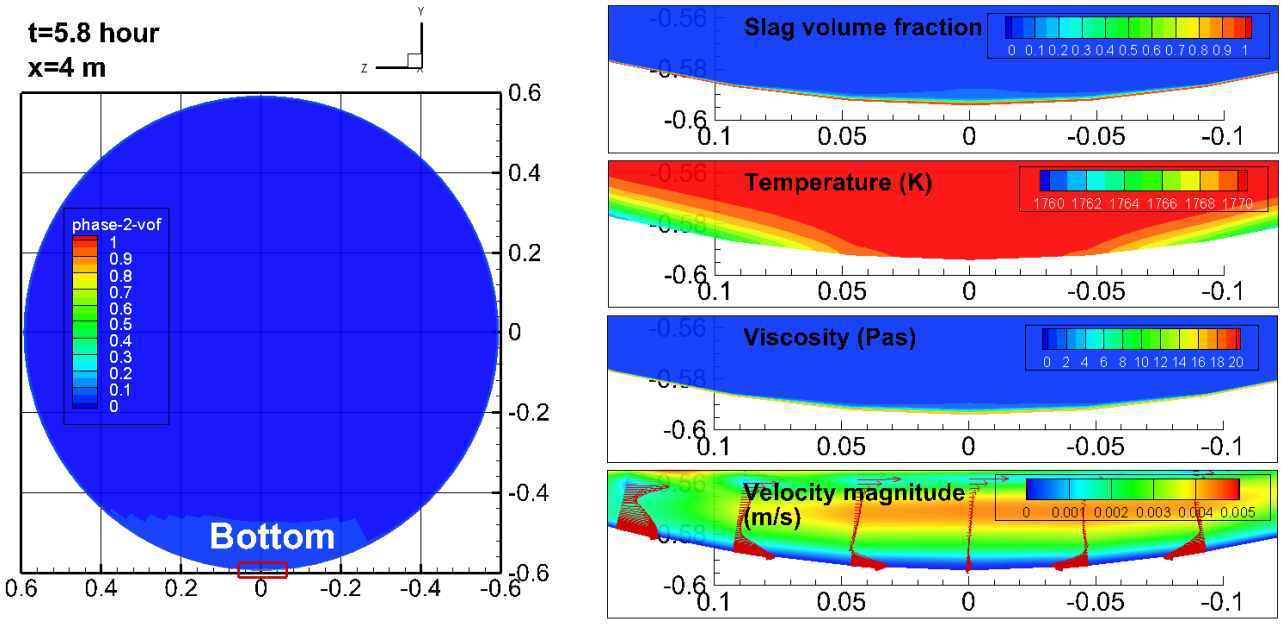

Figure 6-11. The slag volume fraction, temperature, viscosity and velocity distribution at the bottom of the reactor wall at x=4 m. The vector in the velocity distribution shows only the flow direction, and the velocity magnitude is shown in color.

Since the slag thickness reaches its maximum at the bottom of the reactor, its characteristics were analyzed in Figure 6-11, in which the slag volume fraction, temperature distribution, fluid viscosity, and velocity distribution are shown in details. The temperature gradient is high across the thin slag layer due to its low thermal conductivity; however, given the small slag thickness (~1 mm) on a relatively thick refractory wall (~200 mm), it would neither have a significant impact on the heat transfer through the wall, nor affect the combustion in the reactor. The situation would be different if the refractory wall is water-membrane lined, in which case the slag or fouling layer contributes to the thermal resistance in convective and conductive heat transfer, and can significantly reduce the radiation heat transfer. The viscosity of the molten slag is around 10-20 $Pa \cdot s$, about 6 order of magnitude higher than the gas viscosity, which results in a small slag velocity as shown in the bottom of the figure. Due to its high density, the slag flow is mainly driven by gravity, therefore, different from the gas velocity which is mainly in the axis direction, the slag flows downward along the wall as shown by the vectors.

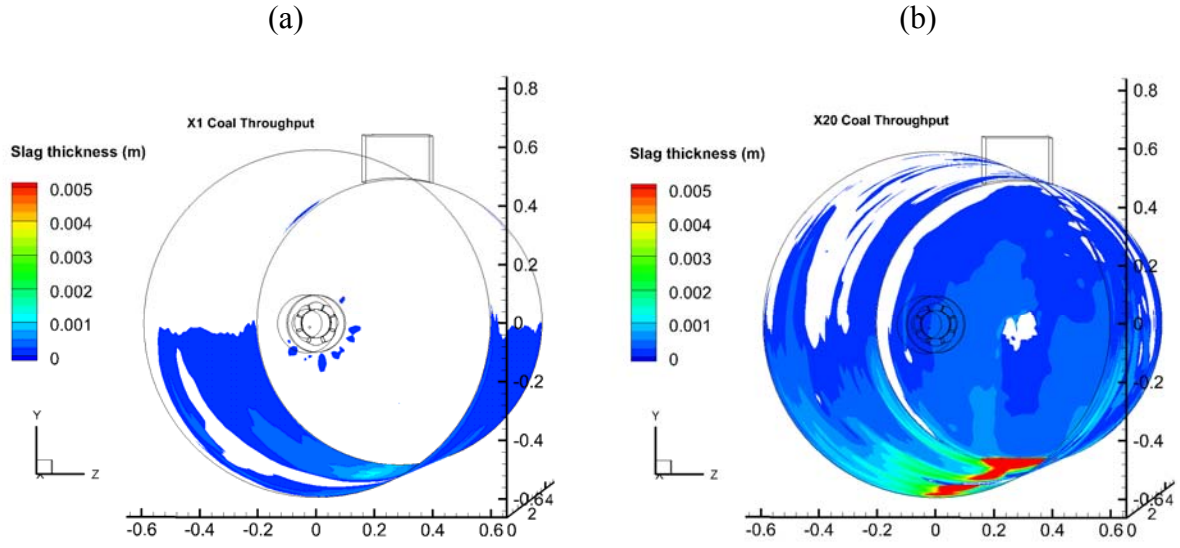

Figure 6-12. Coal throughput effect on the slagging behavior. (a) 4 bar 3MW_{th} case, and (b) 40 bar 60 MW_{th} case.

It should be noted that no solid slag layer is formed in this case when the reference T_{cv} is set to be 1480K, because the refractory wall internal surface temperature T_{wi} is above the slag melting temperature at all the locations covered by liquid slag layer. However, solid slag may begin to form or melt under the molten slag layer if the operating temperature or the feeding stock is changed, or in a different thermal wall boundary condition such as water membrane wall.

It should also be noted that coal ash consists of complex chemistry components, which have very different phase change temperatures. Some metal oxides with higher melting temperature may condense and accumulate on the refractory wall to form solid slag. Solid slag layers are also formed because of the temperature fluctuations in operating of slagging combustors or gasifiers. Time- and composition-varying models are required to capture these physics, which will be conducted as a future work.[237]

6.4.3. Effect of Coal Throughput on Slagging Behaviors

As discussed in our previous pressure study using the one-dimensional slag model [238], the slag thickness can be increased at higher operating pressure, because of the higher coal mass flow rate in the reactor. Figure 6-12 compares the simulation results of the slag thickness under 4 bar and 40 bar operating conditions, corresponding to 3 MW_{th} and 60 MW_{th} thermal loads. The slag thickness increases from about 1 mm to about 5 mm at the bottom of the reactor, due to the 20 times higher coal mass flow rate. Moreover, the slagging tendency becomes significant on the top, side and back walls.

6.5. Conclusion

A novel fully three-dimensional slag flow model is developed for slagging coal combustion

and gasification CFD simulation. The model couples two multiphase flow models, i.e., the DPM and VOF model, for the gas, slag and particle phases. The slag model was implemented as user defined functions (UDF) in a three-dimensional CFD code FLUENT, and applied in the simulation of a pilot scale slagging oxy-coal combustor.

The slag flow behaviors are obtained and compared with the experimental observations with good agreements. Results show that the turbulence has significant impact on particle trajectories and should be modeled correctly in order to achieve an accurate prediction of the particle deposition rate. Driven mainly by gravity, the molten slag flows down from the front, back and side walls and accumulates at the bottom of the reactor, forming a 1 mm slag stream which flows to the end of the reactor due to the slope. The slag velocity is around 0.1 mm/s due to its high viscosity. And the slagging behavior can be affected by the operating conditions such as pressure and coal throughput.

The slag model is quite general and can be used for slagging combustion modeling with any geometry. Solidification and melting submodel can be added to model the solid slag layer formation in the case with water-membrane walls in the future.

Page left intentionally blank

Chapter 7 Conclusions

In previous chapters, we have reviewed the characteristics and fundamentals of oxy-fuel combustion, due to the carbon dioxide's different physical properties and chemical effects. We have also discussed the sub-models of oxy-coal combustion in a CFD framework, and validated the CFD approach as a whole using experimental results from lab-scale tests. The CFD model was extrapolated to oxy-coal combustion under elevated pressures, which provides insights into its combustion characteristics. Finally, we introduced the development of a novel three-dimensional slag model which can be used as a design tool for slagging combustor or gasifier development, in particular at elevated operating pressures. The main conclusions in the study are summarized as follows.

7.1. Conclusions

Among all the sub-processes in oxy-coal combustion, turbulence is still the most important and challenging physics to model in oxy-coal combustion, because it couples with heat and mass transfer, and chemical reactions, in a fully dynamic manner. In the validation study on a 100 kW_{th} swirl oxy-coal burner (see Chapter 3), results show that although agreeing reasonably with the measured mean axial and tangential velocity, all the RANS turbulence models underestimate the internal recirculation zone size and the turbulence mixing intensity in the char combustion zone. The standard $k-\varepsilon$ and RNG $k-\varepsilon$ models with default model constants fail to predict accurately the flow and mixing process associated with the staging stream, and perform poorly on the oxygen concentration prediction. The SST $k-\omega$ model captures most of the flow regimes and improves the prediction of oxygen diffusion than other turbulent-viscosity models.

LES can resolve some of the large-scale turbulent structures of the swirling flow in the burner quarl and of the staging stream downstream of the burner, better matching the measured internal recirculation zone size, the entrainment of oxygen from the staging stream, and the overall flame length than the RANS approaches.

The chemical effects of CO_2 in oxy-coal combustion have been discussed in the CFD simulation. The carbon dioxide is not inert but participates in both the homogenous reactions (see Chapter 4) and the heterogeneous reactions (see Chapter 3). In the volatile or gaseous fuel diffusion flames, the reaction $H+CO_2 \rightleftarrows OH+CO$ enhances the CO formation in the fuel-rich side due to high CO_2 concentration, leading to a significantly higher CO concentration. High CO_2 concentration also impacts the reaction $OH+H_2 \rightleftarrows H+H_2O$ via OH radical and results in lower H_2 and higher H_2O concentrations. Therefore, as an intermediate product sensitive to reaction rates, reasonable CO predictions can only be obtained using appropriate finite-rate mechanisms, such as the Westbrook-Dryer multiple-step mechanism. In the oxy-char combustion process, simulation shows that oxidation reactions dominate char consumption in oxy-fuel combustion. However, gasification reactions between char and carbon dioxide can be important locally in the fuel-rich zone of the volatiles-flame and the char-combustion regions, where the temperature is high and the oxygen concentration is low.

Beyond the potential advances in net efficiency and capital cost in pressurized oxy-coal combustion system [34, 35], the study demonstrates that pressure is also beneficial to the coal combustion process (see Chapter 5). The high partial pressure of reactants, such as oxygen, carbon dioxide and steam, enhances combustion reaction significantly and leads to a shorter fuel conversion time under pressure. Therefore, a relatively higher burner velocity (and shorter residence time) can be used at higher operating pressure, which significantly increases the

thermal loads. It should be noted that, due to the lack of fuel chemistry and homogeneous kinetics data at elevated pressures, the homogeneous reaction rates were assumed to be controlled by turbulent mixing while neglecting the gas phase reaction kinetics, and only the char reaction kinetics were considered in the simulation. In fact, for coal combustion and gasification, the char conversion dominates the fuel conversion time. Therefore, the conclusion will not be affected even with consideration of the neglected homogeneous reaction kinetics.

A three-dimensional slag model has been developed to investigate the slag flow behaviors in the pressurized oxy-coal combustor (see Chapter 6). The slag model resolves the detailed physics of slag flow, including ash particle deposition, slag layer thickness, molten slag flow velocity, as well as its effects on the heat transfer. Results show that the slag is driven mainly by gravity; the molten slag flows down from the front, back and side walls and accumulates at the bottom of the reactor, forming a 1 mm slag stream which flows to the end of the reactor due to the slope. The slag velocity is around 0.1 mm/s due to its high viscosity. And the slagging behavior can be affected by the operating conditions such as pressure and coal throughput. Achieving good agreement with the experimental observations, the slag model can be further applied as a useful tool in slagging coal combustion or gasification studies with any reactor geometry.

7.2. Future Work

As the most promising carbon capture technology for existing coal-fired power plants, the oxy-fuel combustion have been advanced significantly in the past two decades, in particular on the fundamental understanding of the carbon dioxide's roles in transport and chemical phenomena. However, there are still engineering challenges before it reaches its full potential

and large-scale deployment in the power industry. In this study, the CFD simulation with appropriate sub-models has been demonstrated in oxy-coal combustion fundamental studies. Broader applications of the validated CFD models are expected in advanced oxy-burner and full scale furnace concept designs, such as:

- *Combustion dynamics and flame stability study using LES*: The challenges to maintaining oxy-coal combustion stability have been reported in early pilot scale experimental studies [77, 189]. These challenges stem from the lower adiabatic flame temperature, the delayed ignition and the lower burning rate of coal particles in a CO_2 diluted environment, among other fundamental issues discussed above. The LES approach resolves fluid dynamics properties in combustion, and can be used to study the flame stability characteristics, such as destabilization and blow off phenomena, with different burner geometry and operating windows.
- *Advanced oxy-burner designs*: Operating in the oxy-fuel regime provides more flexibility because the oxygen concentrations in the oxidizing streams are not restricted to 21%. This opens up opportunities for advanced oxy-coal burner design including various flue gas recycle ratio, flexible oxygen partition in different streams, re-distribution of gas volumes in different streams, etc. Moreover, following the single oxy-burner development, the performance of scale-up burners and multi-burner configurations should also be carried out using CFD.
- *Full scale furnace/reactor simulations*: A well-organized heat transfer characteristics is the most critical objective in furnace design. Although some efforts have been made to understand the combustion and heat transfer characteristics in full-scale boilers using CFD approaches [142, 176], much more remains to be done for a coupled simulation of the heat

- *Further applications of the three-dimensional slag model*: The slag model developed in Chapter 6 is quite general and can be used for slagging combustion modeling with any geometry. Solidification and melting submodel can be added to model the solid slag layer formation in the case with water-membrane walls in the future. In this case, the slag's effect on heat transfer becomes prominent and should be investigated carefully.

Due to its complexity, the combustion technology is still heavily dependent on experiments and operational experience, especially in its application in coal-fired power plants. Therefore, the CFD approach should be conducted along with experimental studies and on-site tests, in order to obtain insights and practical knowledge on oxy-coal combustion operation, heat transfer, its combustion dynamics and stability, as well as pollutant formation and control.

Page left intentionally blank

References

[1] IPCC. Contribution of Working Groups I, II and III to the Fourth Assessment Report of the Intergovernmental Panel on Climate Change. Intergovernmental Panel on Climate Change; 2007.
[2] Ghoniem AF. Needs, resources and climate change: Clean and efficient conversion technologies. Progress in Energy and Combustion Science. 2011;37:15-51.
[3] Pacala S, Socolow R. Stabilization Wedges: Solving the Climate Problem for the Next 50 Years with Current Technologies. Science. 2004;305:968-72.
[4] BP. Statistical Review of World Energy 2010. 2010.
[5] Annual Energy Review 2009. U.S. Energy Information Administration; 2010.
[6] Wall TF. Combustion processes for carbon capture. Proceedings of the Combustion Institute. 2007;31:31-47.
[7] Wang M, Lawal A, Stephenson P, Sidders J, Ramshaw C. Post-combustion CO2 capture with chemical absorption: A state-of-the-art review. Chemical Engineering Research and Design.In Press, Corrected Proof.
[8] Blamey J, Anthony EJ, Wang J, Fennell PS. The calcium looping cycle for large-scale CO2 capture. Progress in Energy and Combustion Science. 2010;36:260-79.
[9] Thiruvenkatachari R, Su S, An H, Yu XX. Post combustion CO2 capture by carbon fibre monolithic adsorbents. Progress in Energy and Combustion Science. 2009;35:438-55.
[10] Merkel TC, Lin H, Wei X, Baker R. Power plant post-combustion carbon dioxide capture: An opportunity for membranes. Journal of Membrane Science. 2010;359:126-39.
[11] Lyngfelt A, Leckner B, Mattisson T. A fluidized-bed combustion process with inherent CO2 separation; application of chemical-looping combustion. Chemical Engineering Science. 2001;56:3101-13.
[12] Hossain MM, de Lasa HI. Chemical-looping combustion (CLC) for inherent CO2 separations--a review. Chemical Engineering Science. 2008;63:4433-51.
[13] Fan L-S, Wiley InterScience (Online service). Chemical looping systems for fossil energy conversions. Hoboken, NJ: Wiley-AIChE; 2010.
[14] The future of coal: options for a carbon-constrained world: MIT; 2007.
[15] Haslbeck JL, Capicotto PJ, Juehn NJ, Lewis E, Rutkowski MD, Woods MC, et al. Pulverized Coal Oxycombustion Power Plants, Volume 1: Bituminous Coal to Electricity. Washington D.C.: DOE/NETL-2007/1291; 2007.
[16] Kanniche M, Gros-Bonnivard R, Jaud P, Valle-Marcos J, Amann J-M, Bouallou C. Pre-combustion, post-combustion and oxy-combustion in thermal power plant for CO2 capture. Applied Thermal Engineering. 2010;30:53-62.
[17] EIA-860 Annual Electric Generator Report. U.S. Energy Information Administration; 2010.
[18] DOE US. Secretary Chu Announces FutureGen 2.0; 2010, Aug 5th.http://www.energy.gov/9309.htm.
[19] Toftegaard MB, Brix J, Jensen PA, Glarborg P, Jensen AD. Oxy-fuel combustion of solid fuels. Progress in Energy and Combustion Science. 2010;36:581-625.
[20] Buhre BJP, Elliott LK, Sheng CD, Gupta RP, Wall TF. Oxy-fuel combustion technology for coal-fired power generation. Progress in Energy and Combustion Science. 2005;31:283-307.
[21] Wall T, Liu Y, Spero C, Elliott L, Khare S, Rathnam R, et al. An overview on oxyfuel coal combustion--State of the art research and technology development. Chemical Engineering Research and Design. 2009;87:1003-16.
[22] Chen L, Yong SZ, Ghoniem AF. Oxy-fuel combustion of pulverized coal: Characterization, fundamentals, stabilization and CFD modeling. Progress in Energy and Combustion Science. 2012;38:156-214.
[23] Wall T, Yu J. Coal-fired oxyfuel technology status and progress to deployment. The 34th International Technical Conference on Clean Coal & Fuel Systems. Clearwater, Florida, USA2009.

[24] Horn FL, Steinberg M. Control of carbon dioxide emissions from a power plant (and use in enhanced oil recovery). Fuel. 1982;61:415-22.
[25] Steinberg M. History of CO2 greenhouse gas mitigation technologies. Energy Conversion and Management. 1992;33:311-5.
[26] Abraham B, Asbury J, Lynch E, Teotia A. Coal-oxygen process provides carbon dioxide for enhanced recovery. Oil Gas Journal. 1982;80:68-70.
[27] Abele AR, Kindt GS, Clark WD, Payne R, Chen SL. An experimental program to test the feasibility of obtaining normal performance from combustors using oxygen and recycled gas instead of air. Argonne National Lab Report ANL/CNSV-TM-204; 1988.
[28] Wang CS, Berry GF, Chang KC, Wolsky AM. Combustion of pulverized coal using waste carbon dioxide and oxygen. Combustion and Flame. 1988;72:301-10.
[29] Payne R, Chen SL, Wolsky AM, Richter WF. CO2 Recovery via Coal Combustion in Mixtures of Oxygen and Recycled Flue Gas. Combustion Science and Technology. 1989;67:1 - 16.
[30] Herzog H. CCS project database; 2011.http://sequestration.mit.edu/tools/projects/index.html.
[31] Zheng L, Pomalis R, Clements B, Herage T. Optimization of a High Pressure Oxy-fuel Combustion Process for Power Generation and CO2 Capture. The 35th international technical conference on clean coal & fuel systems. Clearwater, FL2010.
[32] Fassbender AG, Henry RS, Tao L. Analysis of ThermoEnergy Integrated Power System for New Power Facilities Using Alaskan and Reference Coal Types. AEA Report, AEA Grant Number - AEA 07-014; 2009.
[33] Hong J. M.S. Thesis: Techno-Economic analysis of pressurized oxy-fuel combustion power cycle for CO2 capture. Cambridge: Massachusetts Institute of Technology; 2009.
[34] Hong J, Chaudhry G, Brisson JG, Field R, Gazzino M, Ghoniem AF. Analysis of oxy-fuel combustion power cycle utilizing a pressurized coal combustor. Energy. 2009;34:1332-40.
[35] Hong J, Field R, Gazzino M, Ghoniem AF. Operating pressure dependence of the pressurized oxy-fuel combustion power cycle. Energy. 2010;35:5391-9.
[36] Yang T, Hunt P, Lisauskas R, Ballas EN, Vitalis B. Pressurized Oxycombustion Carbon Capture Power System. The 35th international technical conference on clean coal & fuel systems. Clearwater, FL2010.
[37] Andersen RE, MacAdam S, Viteri F, Davies DO, Downs JP, Paliszewski A. Adapting gas turbines to zero emission oxy-fuel power plants. Proceedings of ASME Turbo Expo 2008: Power for Land, Sea and Air. Berlin, Germany2008.
[38] BERR Carbon Abatement Technologies Programme: Future CO2 capture technology options for the Canadian market. AEA Energy & Environment, COAL R309 BERR/Pub URN 07/1251; 2007.
[39] Darde A, Prabhakar R, Tranier J-P, Perrin N. Air separation and flue gas compression and purification units for oxy-coal combustion systems. Energy Procedia. 2009;1:527-34.
[40] Andersson K, Johnsson F. Process evaluation of an 865 MWe lignite fired O2/CO2 power plant. Energy Conversion and Management. 2006;47:3487-98.
[41] Okawa M, Kimura N, Kiga T, Takano S, Arai K, Kato M. Trial design for a CO2 recovery power plant by burning pulverized coal in O2/CO2. Energy Conversion and Management. 1997;38:S123-S7.
[42] Varagani R, Chatel-Pelage F, Pranda P, Rostam-Abadi M, Lu Y, Bose A. Performance simulation and cost assessment of oxy-combustion processs for CO2 capture from coal-fired power plants. The 4th Annual Conference on Carbon Sequestration. Alexandria, VA2005.
[43] Nakayama S, Noguchi Y, Kiga T, Miyamae S, Maeda U, Kawai M, et al. Pulverized coal combustion in O2/CO2 mixtures on a power plant for CO2 recovery. Energy Conversion and Management.33:379-86.
[44] Dillon DJ, White V, Allam RJ, Wall RA, Gibbins J. Oxy-combustion processes for CO2 capture from power plant. Engineering investigation report IEA greenhouse gas R&D research and development programme; 2005.
[45] Zheng L, Pomalis R, Clements B. Technical and economic feasibility study of a pressurized oxy-fuel approch to carbon capture: Part 1 - Technical feasibility study and comparison of the thermoEnergy Integrated Power System (TIPS) with a conventional power plant and other carbon capture processes.

CANMET Energy Research Centre, Natural Resources Canada; 2007.
[46] Fassbender AG. Pressurized oxy-fuel combustion for multi-pollutant capture. The 30th International Technical Conference on Coal Utilization & Fuel Systems. Clearwater, FL2005.
[47] Badzioch S, Hawksley PGW. Kinetics of Thermal Decomposition of Pulverized Coal Particles. Industrial & Engineering Chemistry Process Design and Development. 1970;9:521-30.
[48] Gazzino M, Benelli G. Pressurised Oxy-Coal Combustion Rankine-Cycle for Future Zero Emission Power Plants: Process Design and Energy Analysis. Proceedings of ASME ES2008. Jacksonville, Florida, USA2008.
[49] CANMET. Clean Fossil Fuels: Carbon Capture & Storage, High Pressure Oxy-fuel (HiPrOx); 2009.http://canmetenergy-canmetenergie.nrcan-rncan.gc.ca/eng/clean_fossils_fuels/carbon_capture_storage/hiprox.html.
[50] Rossetti E, Malavasi M. Method and Plant for the Treatment of Materials in Particular Waste Materials and Refuse. 2004.
[51] Malavasi M, Rossetti E. High-efficiency Combustors with Reduced Environmental Impact and Processes for Power Generation Derivable Therefrom. 2005.
[52] Malavasi M, Di Salvia G, Rossetti E. Combustion process. 2009.
[53] White V, Torrente-Murciano L, Sturgeon D, Chadwick D. Purification of oxyfuel-derived CO2. Energy Procedia. 2009;1:399-406.
[54] Fogash K, White V. Oxycoal Combustion: Opportunities and Challenges - Purification of Oxyfuel-Derived CO2. AIChE 2007 Annual Meeting. Salt Lake City, UT2007.
[55] Iloeje C, Field R, Gazzino M, Ghoniem A. Process modeling and analysis of CO2 purification for pressurized oxy-coal combustion. The 35th International Technical Conference on Clean Coal and Fuel Systems. Clearwater, FL2010.
[56] Pomalis R, Zheng L, Clements B. ThermoEnergy Integrated Power System Economics. 32nd International Technical Conference on Coal Utilization & Fuel Systems. Clearwater FL2007.
[57] Henry RS. Modeling of pressurized oxy-fuel for recovery of latent heat and carbon capture using usibelli coal. 32nd International Technical Conference on Coal Utilization & Fuel Systems. Clearwater FL2007.
[58] NIST Chemistry WebBook: Thermophysical Properties of Fluid Systems; 2009.http://webbook.nist.gov/chemistry/.
[59] IAPWS Release on Surface Tension of Ordinary Water Substance. International Association for the Properties of Water and Steam; 1994.
[60] Incropera FP, DeWitt DP. Fundamentals of heat and mass transfer. 5th ed. New York: Wiley; 2002.
[61] Chun B-S, Wilkinson GT. Interfacial tension in high-pressure carbon dioxide mixtures. Industrial & Engineering Chemistry Research. 1995;34:4371-7.
[62] Chen L, Gazzino M, Ghoniem AF. Characteristics of pressurized oxy-coal combustion under increasing swirl number. The 35th international technical conference on clean coal & fuel systems. Clearwater, FL2010.
[63] Herwig H. Warmeubertragung A-Z: Systematische und ausführliche Erläuterungen wichtiger Größen und Konzepte: Springer-Verlag Berlin and Heidelberg GmbH & Co. K; 2000.
[64] Edwards DK. Radiation heat transfer notes. Washington D.C.: Hemisphere; 1981.
[65] Andersson K, Johansson R, Hjartstam S, Johnsson F, Leckner B. Radiation intensity of lignite-fired oxy-fuel flames. Experimental Thermal and Fluid Science. 2008;33:67-76.
[66] Gupta RP, Wall TF. The optical properties of fly ash in coal fired furnaces. Combustion and Flame. 1985;61:145-51.
[67] Wall TF, Stewart IM. The measurement and prediction of solids- andsoot-absorption coefficients in the flame region of an industrial P.F. chamber. Symposium (International) on Combustion. 1973;14:689-97.
[68] Andersson K, Johnsson F. Flame and radiation characteristics of gas-fired O2/CO2 combustion. Fuel. 2007;86:656-68.
[69] Andersson K, Johansson R, Johnsson F, Leckner B. Radiation Intensity of Propane-Fired Oxy-Fuel

Flames: Implications for Soot Formation. Energy & Fuels. 2008;22:1535-41.
[70] Hjartstam S, Andersson K, Johnsson F, Leckner B. Combustion characteristics of lignite-fired oxy-fuel flames. Fuel. 2009;88:2216-24.
[71] Woycenko D, Ikeda I, van de Kamp W. Combustion of pulverized coal in a mixture of oxygen and recycled flue gas. Technical Report Doc F98/Y/1: International Flame Research Foundation; 1994.
[72] Woycenko D, van de Kamp W, Roberts P. Combustion of pulverized coal in a mixture of oxygen and recycled flue gas. Tenical Report Doc F98/y/2: International Flame Research Foundation; 1995.
[73] Smart JP, O'Nions P, Riley GS. Radiation and convective heat transfer, and burnout in oxy-coal combustion. Fuel. 2010;89:2468-76.
[74] Weller AE, Rising BW, Boiarski AA, Nordstrom RJ, Barrett RE, Luce RG. Experimental evaluation of firing pulverized coal in a CO2/O2 atmosphere. Argonne National Laboratory, Report ANL/CNSV-TM-168; 1985. p. 342.
[75] Liu H, Zailani R, Gibbs BM. Comparisons of pulverized coal combustion in air and in mixtures of O2/CO2. Fuel. 2005;84:833-40.
[76] Liu H, Zailani R, Gibbs BM. Pulverized coal combustion in air and in O2/CO2 mixtures with NOx recycle. Fuel. 2005;84:2109-15.
[77] Nozaki T, Takano S-i, Kiga T, Omata K, Kimura N. Analysis of the flame formed during oxidation of pulverized coal by an O2---CO2 mixture. Energy. 1997;22:199-205.
[78] Rehfeldt S, Kuhr C, Ehmann M, Bergins C, Scheffknecht G, Maier J, et al. Basic experiments and CFD calculations of air and oxyfuel firing of lignite and bituminous coals in 0.5 and 1 MW scale combustion test facilities. The 34th International Technical Conference on Clean Coal and Fuel Systems. Clearwater, FL2009.
[79] Tan Y, Croiset E, Douglas MA, Thambimuthu KV. Combustion characteristics of coal in a mixture of oxygen and recycled flue gas. Fuel. 2006;85:507-12.
[80] Croiset E, Thambimuthu K, Palmer A. Coal combustion in O2/CO2 mixtures compared with air. The Canadian Journal of Chemical Engineering. 2000;78:402-7.
[81] Turns SR. An introduction to combustion : concepts and applications. 2nd ed. Boston: McGraw-Hill; 2000.
[82] Cen K, Yao Q, Cao X, Zhao X, Huang Z, Zhou J, et al. Theory and application of combustion, flow, heat transfer and gasification of coal slurry. Hangzhou: Zhejiang University Press; 1997.
[83] Law CK, Williams FA. Kinetics and convection in the combustion of alkane droplets. Combustion and Flame. 1972;19:393-405.
[84] Suuberg EM, Peters WA, Howard JB. Product compositions in rapid hydropyrolysis of coal. Fuel. 1980;59:405-12.
[85] Anthony DB, Howard JB, Hottel HC, Meissner HP. Rapid devolatilization and hydrogasification of bituminous coal. Fuel. 1976;55:121-8.
[86] Bautista JR, Russel WB, Saville DA. Time-resolved pyrolysis product distributions of softening coals. Ind Eng Chem Fund. 1986;25:536-44.
[87] Serio MA, Hamblen DG, Markham JR, Solomon PR. Kinetics of volatile product evolution in coal pyrolysis: experiment and theory. Energy Fuels. 1987;1:138-52.
[88] Gibbins-Matham J, Kandiyoti R. Coal pyrolysis yields from fast and slow heating in a wire-mesh apparatus with a gas sweep. Energy Fuels. 1988;2:505-11.
[89] Ko GH, Sanchez DM, Peters WA, Howard JB. Correlations for effects of coal type and pressure on tar yields from rapid devolatilization. Symposium (International) on Combustion. 1989;22:115-24.
[90] Li C-Z. Advances in the science of Victorian brown coal. Amsterdam ; London: Elsevier; 2004.
[91] Chen L, Zeng C, Guo X, Mao Y, Zhang Y, Zhang X, et al. Gas evolution kinetics of two coal samples during rapid pyrolysis. Fuel Processing Technology. 2010;91.
[92] Donald B. Anthony JBH. Coal devolatilization and hydrogastification. AIChE Journal. 1976;22:625-56.
[93] Rathnam RK, Elliott LK, Wall TF, Liu Y, Moghtaderi B. Differences in reactivity of pulverised coal in air (O2/N2) and oxy-fuel (O2/CO2) conditions. Fuel Processing Technology. 2009;90:797-802.

[94] Borrego AG, Alvarez D. Comparison of Chars Obtained under Oxy-Fuel and Conventional Pulverized Coal Combustion Atmospheres. Energy & Fuels. 2007;21:3171-9.
[95] Al-Makhadmeh L, Maier J, Scheffknecht G. Coal pyrolysis and char combustion under oxy-fuel conditions. The 34th International Technical Conference on Coal Utilization & Fuel Systems. Clearwater, FL2009.
[96] Brix J, Jensen PA, Jensen AD. Coal devolatilization and char conversion under suspension fired conditions in O2/N2 and O2/CO2 atmospheres. Fuel. 2010;89:3373-80.
[97] Howard JB, Essenhigh RH. Pyrolysis of Coal Particles in Pulverized Fuel Flames. Industrial & Engineering Chemistry Process Design and Development. 1967;6:74-84.
[98] Howard JB, Essenhigh RH. Mechanism of solid-partical combustion with simultaneous gas-phase volatiles combustion. Symposium (International) on Combustion. 1967;11:399-408.
[99] Essenhigh RH, Misra MK, Shaw DW. Ignition of coal particles: A review. Combustion and Flame. 1989;77:3-30.
[100] Ponzio A, Senthoorselvan S, Yang W, Blasiak W, Eriksson O. Ignition of single coal particles in high-temperature oxidizers with various oxygen concentrations. Fuel. 2008;87:974-87.
[101] Levendis YA, Joshi K, Khatami R, Sarofim AF. Combustion behavior in air of single particles from three different coal ranks and from sugarcane bagasse. Combustion and Flame. 2011;158:452-65.
[102] Molina A, Shaddix CR. Ignition and devolatilization of pulverized bituminous coal particles during oxygen/carbon dioxide coal combustion. Proceedings of the Combustion Institute. 2007;31:1905-12.
[103] Shaddix CR, Molina A. Particle imaging of ignition and devolatilization of pulverized coal during oxy-fuel combustion. Proceedings of the Combustion Institute. 2009;32:2091-8.
[104] Molina A, Hecht ES, Shaddix CR. Ignition of a group of coal particles in oxyfuel combustion with CO2 recirculation. The 34th International Technical Conference on Coal Utilization and Fuel Systems. Clearwater, FL, USA2009.
[105] Stivers C, Levendis YA. Ignition of sigle coal particles in O2/N2/CO2 atmospheres. The 35th International Technical Conference on Clean Coal & Fuel Systems. Clearwater, FL2010.
[106] Harris DJ, Smith IW. Intrinsic reactivity of petroleum coke and brown coal char to carbon dioxide, steam and oxygen. Symposium (International) on Combustion. 1991;23:1185-90.
[107] Mann AP, Kent JH. A computational study of heterogeneous char reactions in a full-scale furnace. Combustion and Flame. 1994;99:147-56.
[108] Stanmore BR, Visona SP. The Contribution to Char Burnout from Gasification by H2O and CO2 During Pulverized-Coal Flame Combustion. Combustion and Flame. 1998;113:274-6.
[109] Kajitani S, Hara S, Matsuda H. Gasification rate analysis of coal char with a pressurized drop tube furnace. Fuel. 2002;81:539-46.
[110] Bejarano PA, Levendis YA. Single-coal-particle combustion in O2/N2 and O2/CO2 environments. Combustion and Flame. 2008;153:270-87.
[111] Shaddix CR, Molina A. Effect of O2 and high CO2 concentrations on PC char burning rates during oxy-fuel combustion. The 33rd International Technical Conference on Coal Utilization and Fuel Systems. Clearwater, FL, USA2008.
[112] Shaddix CR, Hecht ES, Geier M, Molina A, Haynes BS. Effect of gasificaiton reactions on oxy-fuel combustion of pulverized coal char. The 35th International Technical Conference on Clean Coal & Fuel Systems. Clearwater, FL2010.
[113] !!! INVALID CITATION !!!
[114] Liu H. Combustion of Coal Chars in O2/CO2 and O2/N2 Mixtures: A Comparative Study with Non-isothermal Thermogravimetric Analyzer (TGA) Tests. Energy & Fuels. 2009;23:4278-85.
[115] Liu H. A comparison of combustion of coal chars in O2/CO2 and O2/N2 mixtures - Isothermal TGA studies. International Journal of Reactor Engineering. 2009;7.
[116] Varhegyi G, Szabo P, Jakab E, Till F, Richard JR. Mathematical Modeling of Char Reactivity in Ar-O2 and CO2-O2 Mixtures. Energy Fuels. 1996;10:1208-14.
[117] Singer SL, Chen L, Ghoniem AF. The Influence of Gasification Reactions on Char Consumption under Oxy-Combustion Conditions: Effects of Particle Trajectory and Conversion. Proceedings of the

Combustion Institute. 2012;DOI:10.1016/j.proci.2012.07.042.
[118] Zhu DL, Egolfopoulos FN, Law CK. Experimental and numerical determination of laminar flame speeds of methane/(Ar, N2, CO2)-air mixtures as function of stoichiometry, pressure, and flame temperature. Symposium (International) on Combustion. 1989;22:1537-45.
[119] Kiga T, Takano S, Kimura N, Omata K, Okawa M, Mori T, et al. Characteristics of pulverized-coal combustion in the system of oxygen/recycled flue gas combustion. Energy Conversion and Management. 1997;38:S129-S34.
[120] Suda T, Masuko K, Sato Ji, Yamamoto A, Okazaki K. Effect of carbon dioxide on flame propagation of pulverized coal clouds in CO2/O2 combustion. Fuel. 2007;86:2008-15.
[121] Liu F, Guo H, Smallwood GJ. The chemical effect of CO2 replacement of N2 in air on the burning velocity of CH4 and H2 premixed flames. Combustion and Flame. 2003;133:495-7.
[122] Westbrook CK, Dryer FL. Chemical kinetic modeling of hydrocarbon combustion. Progress in Energy and Combustion Science. 1984;10:1-57.
[123] Zheng L, Furimsky E. Assessment of coal combustion in O2+CO2 by equilibrium calculations. Fuel Processing Technology. 2003;81:23-34.
[124] Glarborg P, Bentzen LLB. Chemical Effects of a High CO2 Concentration in Oxy-Fuel Combustion of Methane. Energy & Fuels. 2008;22:291-6.
[125] Andersson K, Normann F, Johnsson F, Leckner B. NO Emission during Oxy-Fuel Combustion of Lignite. Industrial & Engineering Chemistry Research. 2008;47:1835-45.
[126] Croiset E, Thambimuthu KV. NOx and SO2 emissions from O2/CO2 recycle coal combustion. Fuel. 2001;80:2117-21.
[127] Wendt JF, Anderson JD, Von Karman Institute for Fluid Dynamics. Computational fluid dynamics : an introduction. 2nd ed. Berlin ; New York: Springer; 1996.
[128] Smith PJ, Smoot LD. One-Dimensional Model for Pulverized Coal Combustion and Gasification. Combustion Science and Technology. 1980;23:17 - 31.
[129] Khare SP, Wall TF, Farida AZ, Liu Y, Moghtaderi B, Gupta RP. Factors influencing the ignition of flames from air-fired swirl pf burners retrofitted to oxy-fuel. Fuel. 2008;87:1042-9.
[130] Patankar SV, Spalding DB. A computer model for three-dimensional flow in furnaces. Symposium (International) on Combustion. 1973;14:605-14.
[131] Lockwood FC, Salooja AP, Syed SA. A prediction method for coal-fired furnaces. Combustion and Flame. 1980;38:1-15.
[132] Chui EH, Douglas MA, Tan Y. Modeling of oxy-fuel combustion for a western Canadian sub-bituminous coal. Fuel. 2003;82:1201-10.
[133] Toporov D, Bocian P, Heil P, Kellermann A, Stadler H, Tschunko S, et al. Detailed investigation of a pulverized fuel swirl flame in CO2/O2 atmosphere. Combustion and Flame. 2008;155:605-18.
[134] Dryer FL, Glassman I. High-temperature oxidation of CO and CH4. Symposium (International) on Combustion. 1973;14:987-1003.
[135] Andersen J, Rasmussen CL, Giselsson T, Glarborg P. Global Combustion Mechanisms for Use in CFD Modeling under Oxy-Fuel Conditions. Energy & Fuels. 2009;23:1379-89.
[136] Westbrook CK, Dryer FL. Simplified Reaction Mechanisms for the Oxidation of Hydrocarbon Fuels in Flames. Combustion Science and Technology. 1981;27:31 - 43.
[137] Jones WP, Lindstedt RP. Global reaction schemes for hydrocarbon combustion. Combustion and Flame. 1988;73:233-49.
[138] Vascellari M, Cau G. Numerical simulation of pulverized coal oxy-combustion with exhaust gas recirculation. Proceeding of CCT2009 Fourth International Conference on Clean Coal Technologies. Dresden, Germany2009.
[139] Kim JP, Schnell U, Scheffknecht G. Comparison of Different Global Reaction Mechanisms for MILD Combustion of Natural Gas. Combustion Science and Technology. 2008;180:565 - 92.
[140] Muller M, Lemp O, Leiser S, Schnell U, Grathwohl S, Maier J, et al. Advanced modeling of pulverized coal combustion under oxy-fuel conditions. The 35th International Technical Conference on Clean Coal and Fuel Systems. Clearwater, FL2010.

[141] Leckner B. Spectral and total emissivity of water vapor and carbon dioxide. Combustion and Flame. 1972;19:33-48.
[142] Nikolopoulos N, Nikolopoulos A, Karampinis E, Grammelis P, Kakaras E. Numerical investigation of the oxy-fuel combustion in large scale boilers adopting the ECO-Scrub technology. Fuel. 2011;90:198-214.
[143] Edge P, Gubba SR, Ma L, Porter R, Pourkashanian M, Williams A. LES modelling of air and oxy-fuel pulverised coal combustion - Impact on flame properties. Proceedings of the Combustion Institute. 2011;33:2709-16.
[144] Migdal D, Agosta VD, American Society of Mechanical E. A source flow model for continuum gas-particle flow. New York, N.Y.: ASME; 1967.
[145] FLUENT 6.3 user's guide. Fluent Inc.; 2006.
[146] Porter R, Liu F, Pourkashanian M, Williams A, Smith D. Evaluation of solution methods for radiative heat transfer in gaseous oxy-fuel combustion environments. Journal of Quantitative Spectroscopy and Radiative Transfer. 2010;111:2084-94.
[147] Rehfeldt S, Kuhr C, Ehmann M, Bergins C, Tigges KD, Wu S. Modeling of radiative heat transfer in an oxyfuel atmosphere with a wide band model and a weighted sum of gray gases. The 35th International Technical Conference on Clean Coal and Fuel Systems. Clearwater, FL2010.
[148] Smith TF, Shen ZF, Friedman JN. Evaluation of Coefficients for the Weighted Sum of Gray Gases Model. The ASME Journal of Heat Transfer. 1982;104:602-8.
[149] Viskanta R, Menguc MP. Radiation heat transfer in combustion systems. Progress in Energy and Combustion Science. 1987;13:97-160.
[150] Edwards DK, Menard WA. Comparison of Models for Correlation of Total Band Absorption. Appl Opt. 1964;3:621-5.
[151] Johansson R, Andersson K, Leckner B, Thunman H. Models for gaseous radiative heat transfer applied to oxy-fuel conditions in boilers. International Journal of Heat and Mass Transfer. 2010;53:220-30.
[152] Annamalai K, Puri IK. Combustion science and engineering. Boca Raton: CRC Press/Taylor & Francis; 2007.
[153] Mitchell RE, Kee RJ, Glarborg P, Coltrin ME. The effect of CO conversion in the boundary layers surrounding pulverized-coal char particles. Symposium (International) on Combustion. 1991;23:1169-76.
[154] Murphy JJ, Shaddix CR. Combustion kinetics of coal chars in oxygen-enriched environments. Combustion and Flame. 2006;144:710-29.
[155] Tognotti L, Longwell JP, Sarofim AF. The products of the high temperature oxidation of a single char particle in an electrodynamic balance. Symposium (International) on Combustion. 1991;23:1207-13.
[156] Field MA. Rate of combustion of size-graded fractions of char from a low-rank coal between 1 200 K and 2 000 K. Combustion and Flame. 1969;13:237-52.
[157] Hecht ES, Shaddix CR, Molina A, Haynes BS. Effect of CO2 gasification reaction on oxy-combustion of pulverized coal char. Proceedings of the Combustion Institute. 2011;33:1699-706.
[158] Kuhr C, Ehmann M, Rehfeldt S, Bergins C, Maier J, Scheffknecht G, et al. Modeling of char combustion in CO2/O2 and N2/O2 atmospheres. The 35th International Technical Conference on Clean Coal and Fuel Systems. Clearwater, FL2010.
[159] Smith IW. The combustion rates of coal chars: A review. Symposium (International) on Combustion. 1982;19:1045-65.
[160] Zhang M, Yu J, Xu X. A new flame sheet model to reflect the influence of the oxidation of CO on the combustion of a carbon particle. Combustion and Flame. 2005;143:150-8.
[161] Yin C, Kar SK, Rosendahl L, Hvid SL. Co-firing straw with coal in a swirl-stabilized dual-feed burner: Modelling and experimental validation. Bioresource Technology. 2010;101:4169-78.
[162] Kumar M, Zhang C, Monaghan RFD, Singer SL, Ghoniem AF. CFD simulation of entrained flow gasification with improved devolatilization and char consumption submodels. ASME 2009 International Mechanical Engineering Congress & Exposition. Lake Buena Vista, FL2009.
[163] Magnussen BF, Hjertager BH. On mathematical modeling of turbulent combustion with special emphasis on soot formation and combustion. Symposium (International) on Combustion. 1977;16:719-29.

[164] Spalding DB. Mixing and chemical reaction in steady confined turbulent flames. Symposium (International) on Combustion. 1971;13:649-57.
[165] Breussin F, Lallemant N, Weber R. Computing of Oxy-Natural Gas Flames using Both a Global Combustion Scheme and a Chemical Equilibrium Procedure. Combustion Science and Technology. 2000;160:369 - 97.
[166] Magnussen BF. On the Structure of Turbulence and a Generalized Eddy Dissipation Concept for Chemical Reaction in Turbulent Flow. 19th AIAA Aerospace Science Meeting. St.Louis, Missouri1981.
[167] Brink A, Kilpinen P, Hupa M, Kjäldman L. Study of Alternative Descriptions of Methane Oxidation for CFD Modeling of Turbulent Combustors. J Combustion Science and Technology. 1999;141:59 - 81.
[168] Fortsch D, Kluger F, Schnell U, Spliethoff H, Hein KRG. A kinetic model for the prediction of no emissions from staged combustion of pulverized coal. Symposium (International) on Combustion. 1998;27:3037-44.
[169] Launder BE, Spalding DB. Lectures in Mathematical Models of Turbulence. London, England: Academic Press; 1972.
[170] Orszag SAY, Yakhot V, Flannery WS, Boysan F, Choudhury D, Maruzewski J, et al. Renormalization Group Modeling and Turbulence Simulations. International Conference on Near-Wall Turbulent Flows. Tempe, Arizona1993.
[171] Chui EH, Majeski AJ, Douglas MA, Tan Y, Thambimuthu KV. Numerical investigation of oxy-coal combustion to evaluate burner and combustor design concepts. Energy. 2004;29:1285-96.
[172] Al-Abbas AH, Naser J, Dodds D. CFD modelling of air-fired and oxy-fuel combustion of lignite in a 100 KW furnace. Fuel. 2011;90:1778-95.
[173] Pope SB. Turbulent flows. Cambridge ; New York: Cambridge University Press; 2000.
[174] Kumar M, Ghoniem AF. Multiphysics Simulations of Entrained Flow Gasification. Part I: Validating the Nonreacting Flow Solver and the Particle Turbulent Dispersion Model. Energy & Fuels. 2011;26:451-63.
[175] Kumar M, Ghoniem AF. Multiphysics Simulations of Entrained Flow Gasification. Part II: Constructing and Validating the Overall Model. Energy & Fuels. 2011;26:464-79.
[176] Gharebaghi M, Irons RMA, Ma L, Pourkashanian M, Pranzitelli A. Large eddy simulation of oxy-coal combustion in an industrial combustion test facility. International Journal of Greenhouse Gas Control. 2011;5, Supplement 1:S100-S10.
[177] Heil P, Toporov D, Stadler H, Tschunko S, Forster M, Kneer R. Development of an oxycoal swirl burner operating at low O2 concentrations. Fuel. 2009;88:1269-74.
[178] Beer JM, Chigier NA. Combustion aerodynamics. Malabar, Fla.: Krieger; 1983.
[179] Wilcox DC. Turbulence modeling for CFD. La Cãnada, CA: DCW Industries, Inc.; 1993.
[180] Menter FR. Two-Equation Eddy-Viscosity Turbulence Models for Engineering Applications. AIAA Journal. 1994;32:1598-605.
[181] ANSYS FLUENT 12.0 Theory Guide. 2009.
[182] Smagorinsky J. GENERAL CIRCULATION EXPERIMENTS WITH THE PRIMITIVE EQUATIONS. Monthly Weather Review. 1963;91:99-164.
[183] Wall T, Rhelan W, Bartz S. Doc. F388/a/3. Livorno (Italy): International Flame Research Foundation; 1976.
[184] Brown BW, Smoot LD, Smith PJ, Hedman PO. Measurement and prediction of entrained-flow gasification processes. AIChE Journal. 1988;34:435-46.
[185] Raithby GD, Chui EH. A Finite-Volume Method for Predicting a Radiant Heat Transfer in Enclosures With Participating Media. Journal of heat transfer. 1990;112:415-23.
[186] Chui EH, Raithby GD. COMPUTATION OF RADIANT HEAT TRANSFER ON A NONORTHOGONAL MESH USING THE FINITE-VOLUME METHOD. Numerical Heat Transfer, Part B: Fundamentals. 1993;23:269-88.
[187] Hottel HC, Sarofim AF. Radiative transfer. New York,: McGraw-Hill; 1967.
[188] Kangwanpongpan T, Corrêa da Silva R, Krautz HJ. Prediction of oxy-coal combustion through an optimized weighted sum of gray gases model. Energy. In press.

[189] Kimura N, Omata K, Kiga T, Takano S, Shikisima S. The characteristics of pulverized coal combustion in O2/CO2 mixtures for CO2 recovery. Energy Conversion and Management. 1995;36:805-8.
[190] Zhang J, Kelly KE, Eddings EG, Wendt JOL. Ignition in 40 kW co-axial turbulent diffusion oxy-coal jet flames. Proceedings of the Combustion Institute. 2011;33:3375-82.
[191] Fry A, Adams B, Shan J. Oxy-burner retrofit principles for existing coal-fired utility biolers. The 35th International Technical Conference on Clean Coal & Fuel Systems. Clearwaer, FL2010.
[192] Liu F, Guo H, Smallwood GJ, Gülder ÖL. The chemical effects of carbon dioxide as an additive in an ethylene diffusion flame: implications for soot and NOx formation. Combustion and Flame. 2001;125:778-87.
[193] Chen L, Ghoniem AF. Simulation of Oxy-Coal Combustion in a 100 kWth Test Facility Using RANS and LES: A Validation Study. Energy & Fuels. 2012;26:4783-98.
[194] Barlow RS, Frank JH. Effects of turbulence on species mass fractions in methane/air jet flames. Symposium (International) on Combustion. 1998;27:1087-95.
[195] Sandia/TUD piloted CH4/Air jet flames.http://www.sandia.gov/TNF/DataArch/FlameD.html.
[196] Barlow RS, Frank JH, Karpetis AN, Chen JY. Piloted methane/air jet flames: Transport effects and aspects of scalar structure. Combustion and Flame. 2005;143:433-49.
[197] Chen L, Ghoniem AF. Simulation of oxy-coal combustion in a 100 kWth test facility using RANS and LES: A validation study. Energy & Fuels. 2012;DOI:10.1021/ef3006993.
[198] Khan IM, Greeves G. A method for calculating the formation and combustion of soot in diesel engines. In: Afgan NH, Beer JM, editors. Heat Transfer in Flames. Washington: Scripta Book Co.; 1974.
[199] Pope SB. Computationally efficient implementation of combustion chemistry using in situ adaptive tabulation. Combustion Theory and Modelling. 1997;1:41-63.
[200] Gregory P. Smith, David M. Golden, Michael Frenklach, Nigel W. Moriarty, Boris Eiteneer, Mikhail Goldenberg, et al. GRI-Mech 3.0; 2009.http://www.me.berkeley.edu/gri_mech/.
[201] Bilger RW, Stårner SH, Kee RJ. On reduced mechanisms for methane air combustion in nonpremixed flames. Combustion and Flame. 1990;80:135-49.
[202] Hjärtstam S, Johansson R, Andersson K, Johnsson F. Computational Fluid Dynamics Modeling of Oxy-Fuel Flames: The Role of Soot and Gas Radiation. Energy & Fuels. 2012;26:2786-97.
[203] Benelli G, Malavasi M, Girardi G. Oxy-coal Combustion Process Suitable for Future and more Efficient Zero Emission Power Plants. PowerGen Europe Conference and Exhibition. Madrid, Spain2007.
[204] Benelli G. Isotherm: a new oxy-combustion process to match the zero emission challenge in power generation. 7th high temperature air combustion and gasification international symposium. Phuket, Thailand2008.
[205] Mills AF. Heat transfer. Homewood, IL: Irwin; 1992.
[206] Wu Y, Zhang J, Smith PJ, Zhang H, Reid C, Lv J, et al. Three-Dimensional Simulation for an Entrained Flow Coal Slurry Gasifier. Energy & Fuels. 2010;24:1156-63.
[207] Sojka PE, Lefebvre AH. A novel method of atomizing coal-water slurry fuels: Final report for Grant No. DE-FG22-87PC79931 US DOE. West Lafayette, IN: Thermal Sciences and Propulsion Center, School of Mechanical Engineering, Purdue University; 1990. p. 1-116.
[208] Sovani SD, Chou E, Sojka PE, Gore JP, Eckerle WA, Crofts JD. High pressure effervescent atomization: effect of ambient pressure on spray cone angle. Fuel. 2001;80:427-35.
[209] Miller SF, Schobert HH. Effect of fuel particle and droplet size distribution on particle size distribution of char and ash during pilot-scale combustion of pulverized coal and coal-water slurry fuels. Energy & Fuels. 1993;7:520-31.
[210] Dunn-Rankin D, Hoornstra J, Gruelich FA, Holve DJ. Combustion of coal--water slurries: Evolution of particle size distribution for coals of different rank. Fuel. 1987;66:1139-45.
[211] Fletcher TH, Kerstein AR, Pugmire RJ, Solum M, Grant DM. A chemical percolation model for devolatilization: summary. Combustion Research Facility, Sandia National Laboratories
Department of Fuels Engineering and Chemistry, University of Utah.
[212] Haider A, Levenspiel O. Drag coefficient and terminal velocity of spherical and nonspherical

particles. Powder Technology. 1989;58:63-70.
[213] Srinivasachar S, Kang SW, Timothy LD, Froelich D, Sarofim AF, Beér JM. Fundamentals of coal-water fuel combustion. 8th International Symposium on coal slurry preparation and utilization. Orlando, FL1986.
[214] Beér JM. Combustion technology developments in power generation in response to environmental challenges. Progress in Energy and Combustion Science. 2000;26:301-27.
[215] Feng J, Shen Y, Yang R. Principles and calculations of boilers. 3rd edition ed. Beijing: Science press; 2003.
[216] Tampa Electric Company: Tampa Electirc Polk Power Station Integrated Gasification Combined Cycle Project, Final technical report. U.S. DOE, DE-FC-21-91MC27363; 2001.
[217] Rawers J, Kwong J, Bennett J. Characterizing coal-gasifier slag-refractory interactions. Materials at High Temperatures. 1999;16:219-22.
[218] Shannon GN, Rozelle PL, Pisupati SV, Sridhar S. Conditions for entrainment into a FeOx containing slag for a carbon-containing particle in an entrained coal gasifier. Fuel Processing Technology. 2008;89:1379-85.
[219] Seggiani M. Modelling and simulation of time varying slag flow in a Prenflo entrained-flow gasifier. Fuel. 1998;77:1611-21.
[220] Wang XH, Zhao DQ, He LB, Jiang LQ, He Q, Chen Y. Modeling of a coal-fired slagging combustor: Development of a slag submodel. Combustion and Flame. 2007;149:249-60.
[221] Ni J, Zhou Z, Yu G, Liang Q, Wang F. Molten slag flow and phase transformation behaviors in a slagging entrained flow coal gasifier. Ind Eng Chem Res. 2010;49:12302-10.
[222] Wang X, Zhao D, Jiang L, Yang W. The Deposition and Burning Characteristics During Slagging Co-Firing Coal and Wood: Modeling and Numerical Simulation. Combustion Science and Technology. 2009;181:710-28.
[223] Li S, Wu Y, Whitty KJ. Ash Deposition Behavior during Char-Slag Transition under Simulated Gasification Conditions. Energy & Fuels. 2010;24:1868-76.
[224] Shimizu T, Tominaga H. A model of char capture by molten slag surface under high-temperature gasification conditions. Fuel. 2006;85:170-8.
[225] Bockelie MJ, Denison MK, Chen Z, Linjewile T, Senior CL, Sarofim AF. CFD Modeling for entrained flow gasifiers in vision 21 systems. Pittsburgh Coal Conference. Pittsburgh, PA2002.
[226] Chen L, Yong SZ, Ghoniem AF. Modeling the slag behavior in three dimensional CFD simulation of a vertically-oriented oxy-coal combustor. The 37th International Technical Conference on Clean Coal & Fuel Systems. Clearwater FL2012.
[227] Liu S, Hao Y. Numerical Study on Slag Flow in an Entrained-Flow Gasifier. ASME Conference Proceedings. 2007;2007:793-800.
[228] Hirt CW, Nichols BD. Volume of fluid (VOF) method for the dynamics of free boundaries. Journal of Computational Physics. 1981;39:201-25.
[229] Thomson DJ. Criteria for the selection of stochastic models of particle trajectories in turbulent flows. Journal of Fluid Mechanics. 1987;180:529-56.
[230] Montagnaro F, Salatino P. Analysis of char–slag interaction and near-wall particle segregation in entrained-flow gasification of coal. Combustion and Flame. 2010;157:874-83.
[231] Richards GH, Slater PN, Harb JN. Simulation of ash deposit growth in a pulverized coal-fired pilot scale reactor. Energy & Fuels. 1993;7:774-81.
[232] Yong SZ, Gazzino M, Ghoniem A. Modeling the slag layer in solid fuel gasification and combustion – Formulation and sensitivity analysis. Fuel. 2012;92:162-70.
[233] Mills KC, Rhine JM. The measurement and estimation of the physical properties of slags formed during coal gasification: 1. Properties relevant to fluid flow. Fuel. 1989;68:193-200.
[234] Mills KC, Rhine JM. The measurement and estimation of the physical properties of slags formed during coal gasification: 2. Properties relevant to heat transfer. Fuel. 1989;68:904-10.
[235] Vargas S, Frandsen FJ, Dam-Johansen K. Rheological properties of high-temperature melts of coal ashes and other silicates. Progress in Energy and Combustion Science. 2001;27:237-429.

[236] Edge P, Gharebaghi M, Irons R, Porter R, Porter RTJ, Pourkashanian M, et al. Combustion modelling opportunities and challenges for oxy-coal carbon capture technology. Chemical Engineering Research and Design. 2011;89:1470-93.
[237] Natural gas- determination of water by the Karl Fischer method- Part 3: Coulometric procedure. ISO 10101-3:1993.
[238] Chen L, Ghoniem A. CFD simulation of oxy-coal combustion: the effect of pressure on coal conversion and optimal operating conditions at elevated pressures. MIT; 2012.